Kinetic Studies of Halogen Oxide Free Radical Reactions of Importance in the Atmosphere

Kate Susan Gawler

University College London

A thesis submitted in partial fulfilment for the degree of Doctor of Philosophy

ProQuest LLC
789 East Eisenhower Parkway
P.O. Box 1346
Ann Arbor, MI 48106-1346

Abstract

The aim of this research was to characterise the kinetics of key gas phase reactions between free radicals which occur in the atmosphere. In particular, the reactions that have been focused on are reactions where uncertainties are apparent in the reported kinetics and are:

$$ClO + ClO + M \rightarrow Cl_2O_2 + M$$

$$ClO + HO_2 \rightarrow HOCl + O_2$$

$$BrO + BrO \rightarrow \text{Products}$$

In the atmosphere, subsequent production of halogen atoms (X = Cl, Br) following these reactions leads to ozone loss:

$$X + O_3 \rightarrow XO + O_2$$

and repetition of these radical reactions renders this ozone loss process catalytic. Under sunlit conditions the self or cross-reactions of ClO or BrO constitute the rate limiting step in the ozone loss process. Consequently, accurate knowledge of the rate coefficients and products of these reactions under appropriate atmospheric conditions is essential when assessing the extent of halogen-induced atmospheric ozone depletion.

These reactions were studied using flash photolysis coupled with UV absorption spectroscopy. The spectroscopy incorporated charge coupled device (CCD) technology, which facilitated rapid timescale broad band data acquisition giving rise to accurate and unequivocal monitoring of multiple species. Classical or numerical models were used to simulate experimental data by optimising kinetic parameters. The improvements in both accuracy and precision of radical monitoring associated with the CCD studies have led to a considerable improvement in our understanding of the roles of these free radical reactions in the Earth's atmosphere.

Acknowledgements

First, I would like to thank my family and friends for their help and support in whatever I do and in particular over the last few years, they would have been a lot tougher without you. I am eternally grateful to my fiancé, Emerson King, who always finds the good in me and has helped me to see the bigger picture. Special thanks also go out to my friend and colleague Daniel Stone for being ever present and ever willing to listen to my many woes and put right my many misunderstandings, I hope I can return the favour some day soon.

The experiments would not have got off the ground without the sound advice and expert knowledge of the UCL chemistry technical staff. In particular my sincere gratitude goes to Dick Waymark and Roy Northeast, who always managed to interpret my confused ramblings into something productive and fix many a problem.

Finally, I must thank my supervisor, David Rowley, for setting me this immense challenge and helping me see it through to a truly worthwhile end.

Table of Contents

Table of Figures

Table of Tables

Chapter 1
Physics and Chemistry of the Earth's Atmosphere

Understanding the Earth's atmosphere has been a quest for scientists since ancient times. Atmospheres vary greatly throughout the solar system and the Earth's atmosphere is apparently unique in its ability to support life forms. The Greeks' early rationalisations for the gaseous layer around the planet assumed air to be one of four elements making Earthly matter. It was not until the seventeenth century that air was recognised as a mixture of gases and in turn nitrogen and oxygen were determined to be the major components.

During the twentieth century, studies of the Earth's atmosphere have developed a fundamental understanding of atmospheric physics and chemistry to incorporate man's impact upon atmospheric composition and processes. Most widely publicised are the environmental issues resulting from changes in atmospheric composition, such as ozone depletion and climate change.

1. 1 Physics of the Atmosphere

1. 1. 1 Pressure Profile

The vertical pressure profile of a planet's atmosphere results from the relationship between the total atmospheric weight and the surface area. This relationship can be rationalised in the following way. For an incremental change (an increase) in altitude, dz, the corresponding change in pressure, dp, is given by:

(E1. 1) $$dp = -\rho(z).g.dz$$

where g represents acceleration due to gravity and $\rho(z)$ is the ambient air density.

This equation can be rationalised since, if dm is the incremental change in mass of a uniform volume of air with a cross-sectional area A,

(E1. 2) $$dp = -\frac{dm.g}{A}$$

and, using the definition of density and the volume of air beneath the incremental increase in altitude:

(E1. 3) $$dm = \rho(z).A.dz$$

which substitutes into (E1. 2) to give (E1. 1).

For an ideal gas $pV = nRT$ and therefore the density may be expressed as:

(E1. 4) $$\rho(z) = \frac{Mp}{RT}$$

where M is the mass of 1 mole of air (*ca.* 0.0288 kg), T is temperature and R is the gas constant.

Hence, in equation (E1. 1):

(E1. 5) $$dp = -\frac{Mpg}{RT}dz$$

Defining the factor H, the *scale height*, as $H = \frac{RT}{Mg}$, rearranging to separate variables and integrating between altitudes 0 and z leads to the *hydrostatic equation* (E1. 6):

(E1. 6) $$p_z = p_0 \exp\left(-\frac{z}{H}\right)$$

where p_z and p_0 are the atmospheric pressures at altitudes z and 0 respectively.

Equation (E1. 6) shows that atmospheric pressure falls exponentially with increasing altitude. Consequently, the majority of the mass of the atmosphere resides at low altitudes. Indeed, more than 99% of atmospheric mass is made up by the lowest 50 km closest to the Earth's surface. The scale height, H, is typically 6-8.5 km, and is defined as the vertical distance over which the pressure drops by a factor of $1/e$.

Upon initial inspection of (E1. 6), it appears that the vertical distribution of a gas is governed by its molar mass. However, at altitudes below approximately 100 km, a region termed the *homosphere*, local mixing processes such as turbulence and convection are not mass specific and disrupt gravitational settling and separation of the air. Hence, the homosphere is comparatively well mixed with an averaged bulk composition. The gravitationally separated region above 100 km is known as the *heterosphere*. This dissertation describes studies pertinent to the homosphere. It is often convenient to refer to the regions of the homosphere determined by the typical vertical temperature profile.

1. 1. 2 Temperature Profile

The vertical temperature profile of the atmosphere is much more complex than the pressure profile, which falls continuously with increasing altitude. The nature of the temperature profile is such that it is used to segment the atmosphere into distinct vertical regions. These regions are highlighted on the schematic diagram of the temperature profile of the atmosphere, shown in Figure 1. 1.

In the lowermost region of the atmosphere, from ground level to approximately 12-15 km (depending on the latitude and season), atmospheric temperature generally decreases with increasing altitude. This region is known as the *troposphere*. The lowermost region of the troposphere lies 0.5-2 km above the Earth's surface and is known as the *boundary layer*. Here, air repeatedly comes into contact with the surface, a process that influences many of the chemical processes which take place. Above this is termed the *free troposphere* and the upper boundary of the troposphere lies around 12-15 km and is known as the *tropopause*.

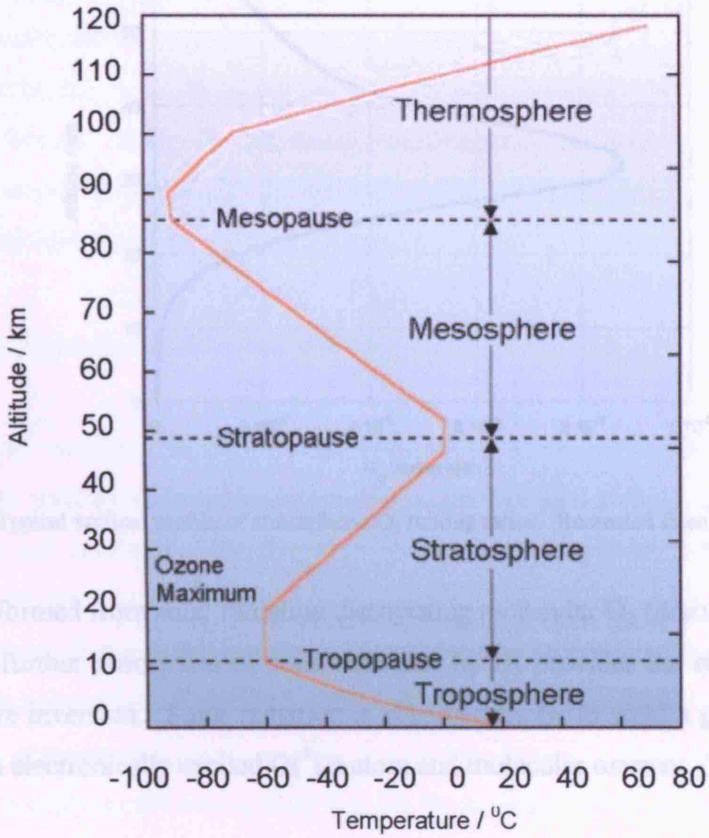

Figure 1. 1 Schematic diagram of the temperature profile of the Earth's atmosphere. Diagram adapted from reference 1.

Above the tropopause there is a temperature profile inversion, consequently the temperature of the atmosphere is seen to *increase* with increasing altitude. This continues to an altitude of approximately 50 km and defines a second region of the atmosphere known as the *stratosphere*. The contrasting temperature profile is brought about due to the interaction of solar radiation with atmospheric ozone, O_3, discussed below. The typical vertical profile of atmospheric O_3 is shown in Figure 1. 2 below.

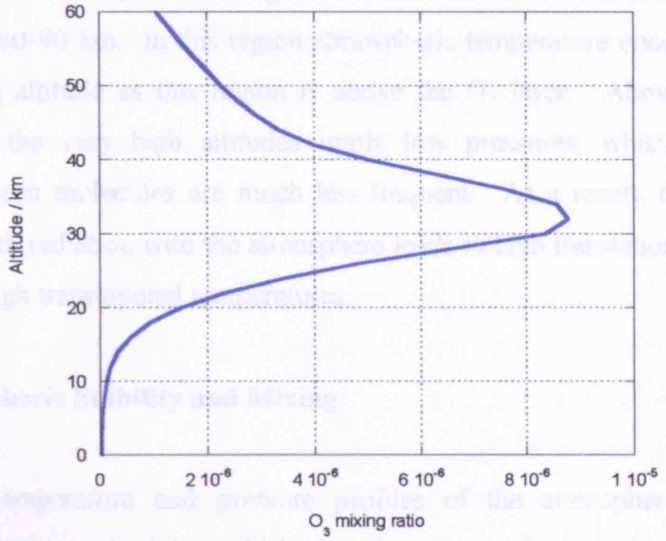

Figure 1. 2 Typical vertical profile of atmospheric O_3 mixing ratios. Recreated from Brasseur *et al.*[2]

The O_3 is formed from solar radiation dissociating molecular O_2 (discussed in Section 1. 3. 1) and further absorption of solar radiation by O_3 provides the energy to drive the temperature inversion. Solar radiation is absorbed by O_3 to yield a ground state $O(^3P)$ atom or an electronically excited $O(^1D)$ atom and molecular oxygen:

(1. 1a) $O_3 + h\nu\ (\lambda < 1180\ nm) \rightarrow O(^3P) + O_2(^3\Sigma_g)$

(1. 1b) $O_3 + h\nu\ (\lambda < 310\ nm) \rightarrow O(^1D) + O_2(^1\Delta_g)$

Any excited oxygen atoms can be collisionally quenched to give ground state oxygen atoms, which recombine with molecular oxygen to form O_3:

(1. 2) $O(^1D) + M \rightarrow O(^3P) + M \quad (\Delta_r H = -190\ kJ\ mol^{-1})$[3]

(1. 3) $O(^3P) + O_2 + M \rightarrow O_3 + M \quad (\Delta_r H = -106\ kJ\ mol^{-1})$[3]

In both cases, the transfer of energy to a third body, M (where M is any other molecule), increases the thermal energy of M. Furthermore, both processes are exothermic, therefore the local atmosphere is heated ensuring the observed increase in the temperature.

The next vertical temperature region, known as the *mesosphere*, extends to approximately 80-90 km. In this region atmospheric temperature once again decreases with increasing altitude as this region is above the O_3 layer. Above 90 km, in the *thermosphere*, the very high altitudes imply low pressures, which mean that the collisions between molecules are much less frequent. As a result, the interaction of short wavelength radiation with the atmosphere leads to high translational velocities and consequently high translational temperatures.

1. 1. 3 Atmospheric Stability and Mixing

The vertical temperature and pressure profiles of the atmosphere determine the atmospheric stability and mixing, which are referred to as dynamical parameters. When comparing and contrasting the dynamics of the troposphere and the stratosphere it is often convenient to consider an imaginary air parcel, initially in thermal equilibrium with its surroundings, and its response to small perturbations in altitude. At any given point in the atmosphere, if the air parcel is displaced vertically it will expand, due to the decreasing atmospheric pressure with increasing altitude. In the gas phase thermal transfer is usually inefficient and as a result the expansion with increasing altitude can be assumed to be adiabatic and the parcel must therefore lose internal energy (as governed by the First Law of thermodynamics). Consequently, upon vertical displacement the air parcel cools.

Considering the situation in the troposphere, the atmospheric temperature also falls with increasing altitude. If this cooling over the same vertical distance is greater than that of the air parcel, following displacement the parcel will be warmer than its local surroundings at the same pressure, it will therefore continue to rise. Similarly, if the parcel were perturbed downwards in altitude it would continue to sink. Such a situation is commonplace in the troposphere and as a result the troposphere is often characterised by rapid vertical mixing and convection.

Once in the stratosphere the air parcel faces a contrasting situation. Here the atmospheric temperature increases with increasing temperature. As the parcel rises it once again expands and cools, but at these altitudes it will encounter warmer local

surroundings at the same pressure. The air parcel will consequently be more dense than the surroundings after perturbation and will experience a restoring force, returning it to its original altitude. Consequently, the stratosphere is resistant to vertical transport and the region is characteristically layered or *stratified.*

Despite this resistance to vertical transport in the stratosphere there is still global circulation, which results in exchange between the troposphere and the stratosphere. This occurs because typically at low latitudes the troposphere undergoes heating, which is driven by outgoing IR radiation emitted by the Earth, exceeding absorbed solar radiation. This imbalance is compensated by a net cooling at high latitudes leading to what is known as the Meridonial or Brewer-Dobson circulation.

Aside from vertical mixing in different regions of the atmosphere it should be noted that air is moved horizontally, North-South and East-West around the planet, as a result of the rotation of the Earth, coupled with local temperature and pressure gradients. In the lowermost atmosphere weather systems show great dynamical complexity. At other altitudes similar prevailing conditions exist and naturally govern the geographical distribution of trace gases. A full description of atmospheric dynamics is beyond the scope of this work, but the behaviour of the atmosphere as a fluid medium should always be borne in mind.

1. 1. 4 Radiative Balance

Because the air in the troposphere (*i.e.* most of the mass of the atmosphere) is relatively well mixed, any changes to atmospheric temperatures also become uniformly distributed. As a result the exact location of the supply or removal of heat from the Sun need not be known, provided the amount of heat is known. It is therefore possible to use very simple models to give accurate estimates of surface temperatures.

The Earth's radiative balance, the balance between incident solar radiation and emitted terrestrial radiation, gives rise to surface temperature and is controlled by the Earth's ability to absorb radiation. This can be modelled simply by assuming that the Earth is a black body with a non-absorbing atmosphere. In such a model the temperature of the

Earth's surface can be related to the energy flux, which may in turn be calculated using the following simple relationship:

(E1. 7) Energy absorbed = Energy emitted

The total energy absorbed per unit time results from the solar energy reaching the top of the atmosphere *per* unit area, which is given by the solar constant, S = 1368 W m^{-2}. This energy is absorbed by the cross-sectional area of the solar radiation beam, which impinges the Earth's surface *i.e.* a disc with radius R, the radius of the Earth. This value is then adjusted to account for cloud and surface backscatter of incoming radiation, known as albedo, A. A is often approximated to 30%.[4] Calculation of the outgoing energy then results from assuming that the Earth emits over its entire surface, *i.e.* the surface area of a sphere, and knowing that a black body at temperature T_e emits a known amount of energy *per* unit time given by the Stefan-Boltzmann law, where radiated flux *per* unit area, $F = \sigma T_e^4$ (Stefan's constant, $\sigma = 5.67 \times 10^{-8}$ W m^{-2} K^{-4}). Hence, using (E1. 8):

(E1. 8) $$(1-A)\times S \times \pi R^2 = \sigma T_e^{\,4} \times 4\pi R^2$$

This calculation results in an average Earth's surface temperature of 256 K. In reality we know that this is not the case since the mean surface temperature of the Earth is a more habitable 288 K. This discrepancy can be resolved if the spectral distributions of the Sun and the Earth's surface are considered. The mean surface temperature of the Sun is approximately 5780 K, which gives rise to a peak emission in the visible part of the electromagnetic spectrum. In contrast the peak emission at the Earth's surface is somewhat shifted and falls in the IR region of the spectrum. This is illustrated in Figure 1. 3 where the Planck black body curves for both 5780 K and 256 K have been plotted as a function of emission wavelength.

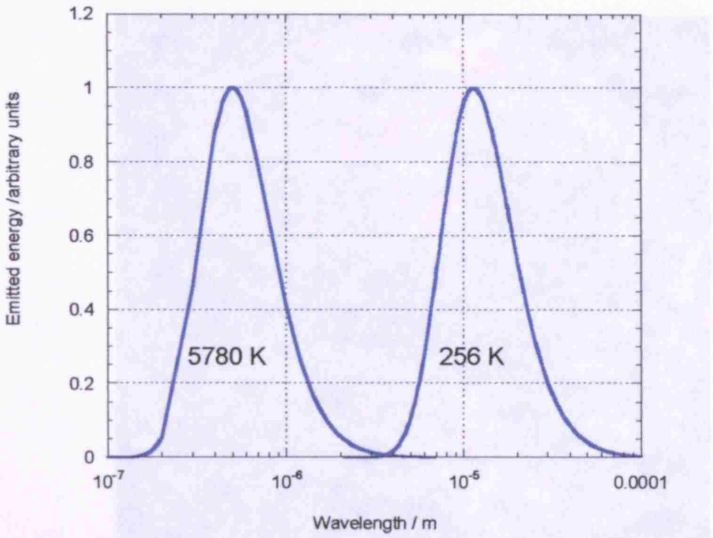

Figure 1. 3 Planck black body emission curves (normalised) plotted as a function of wavelength for a temperature representing the Sun, 5780 K, and the Earth's mean temperature, 256 K.

This difference in the spectral profiles, of the incoming and outgoing radiation interacting with Earth, explains the discrepancy between modelled and measured temperatures when the initial assumption of a completely transparent atmosphere is examined. In the UV/visible region atmospheric gases (with the exception of O_3) absorb weakly. In contrast, in the IR spectral region characterising the outgoing radiation, atmospheric trace species such as CH_4, H_2O, O_3 and CO_2 absorb and re-emit energy. This is apparent since, if the Earth is observed at IR wavelengths, the atmosphere appears somewhat opaque, as shown in Figure 1. 4.

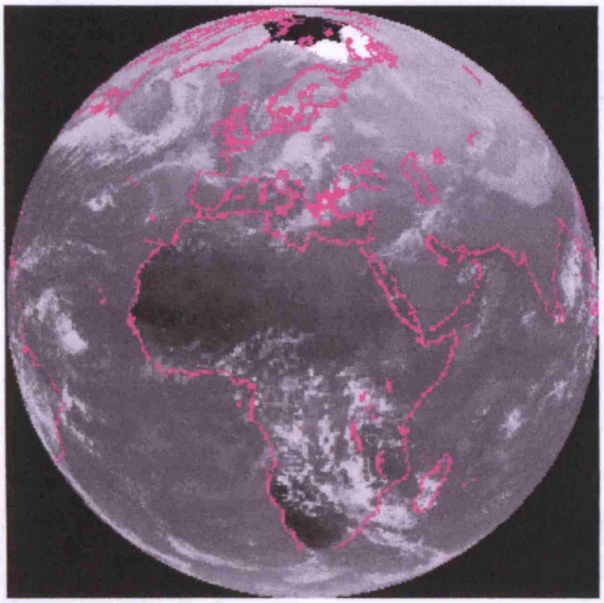

Figure 1. 4 Satellite image of the Earth viewed in the IR.[5]

It is this absorption of outgoing IR radiation by the atmosphere that prevents some of the radiation emitted at the surface leaving the planet and effectively heats the Earth's surface to a habitable temperature. This effect is known as the natural greenhouse effect and the IR absorbing gases responsible for it are termed greenhouse gases. Since the industrial revolution an increase in anthropogenic sources of greenhouse gases have threatened to upset this natural radiative balance. This potential imbalance is one of the main arguments in the concern and debate about climate change.

1. 1. 5 Photochemical Environment

It is clear from the preceding discussion that irradiation of the Earth's atmosphere by the Sun results in the physical conditions and compositional features present. As radiation penetrates the atmosphere further, a greater fraction is absorbed and scattered by atmospheric species. These effects are reflected in features of the solar spectrum, which are altitude dependent, shown in Figure 1. 5.

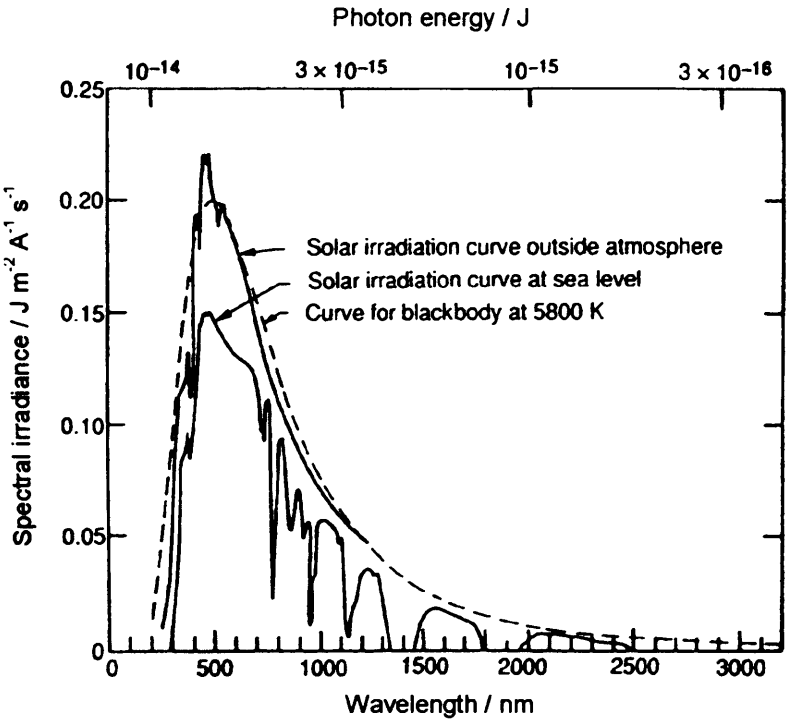

Figure 1. 5 Solar radiation experienced at the top of the Earth's atmosphere compared to that experienced at ground level.[6]

Whilst in principle the solar spectrum at a given altitude will be dependent upon all absorbing species above that altitude, in practice absorption of solar radiation in the UV/visible is dominated by O_2 and O_3. Absorption of UV and visible radiation at high altitudes by O_2 and O_3 (below 242 nm for O_2 and principally below 330 nm for O_3) means that very little short wavelength radiation reaches altitudes below the mid-stratosphere. The attenuation of harmful UV radiation by the stratospheric O_3 layer, in addition to atmospheric N_2, has enormous consequences for life at the Earth's surface, in the biosphere. UV-B radiation (290-320 nm) has been shown to be biologically active (meaning it may modify or destroy DNA), and as a result exposure to radiation of these wavelengths is linked to conditions such as erythema (skin cancer) and cataracts.[4] It can also be lethal to plant surface cells proving devastating for crop yields, with potentially grave cost to human welfare. The relative UV wavelengths at which some of these effects can occur are shown in the spectrum in Figure 1. 6.

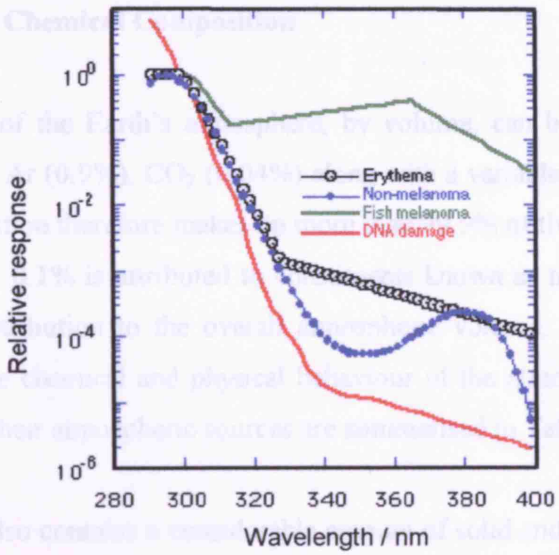

Figure 1. 6 Action spectra for UV related effects, including erythema (normalised to unity at 300 nm).[7]

Solar radiation can result in photodissociation of atmospheric molecules provided the wavelength of the incident photon is suitably short (*i.e.* the photon has enough energy), the molecule absorbs the photon and this absorption leads to dissociation. Some species may be photolysed by relatively long (visible) wavelengths throughout the atmosphere, for example NO_2 ($\lambda < 398$ nm). Other species may only undergo photodissociation at shorter wavelengths, present only at certain altitudes of the atmosphere. A prime example of this is the formation of atmospheric O_3. Atmospheric O_2 is only dissociated by radiation at wavelengths shorter than 242 nm, forming oxygen atoms. O_3 is then formed through combination of oxygen atoms and molecular O_2. Attenuation of this short wavelength radiation with increasing atmospheric depth, by O_2 and O_3, then results in limiting this process and defines the lower boundary of the O_3 layer. Similarly, species such as chlorofluorocarbons (CFCs) are chemically inert in the troposphere but may pass by slow vertical transport into the stratosphere where they are more readily photolysed. In all cases, chemical change in the atmosphere that affects composition (as discussed in the following section) is initiated by absorption of solar radiation and photolysis.

1. 2 Atmospheric Chemical Composition

The composition of the Earth's atmosphere, by volume, can be approximated to N_2 (78%), O_2 (21%), Ar (0.9%), CO_2 (0.04%) along with a variable water vapour content. This bulk composition therefore makes up more than 99.9% of the atmospheric volume. The remaining *ca.* 0.1% is attributed to constituents known as trace gases. In spite of their minimal contribution to the overall atmospheric volume, these trace gases play crucial roles in the chemical and physical behaviour of the atmosphere. A number of trace species and their atmospheric sources are summarised in Table 1.1 below.

The atmosphere also contains a considerable amount of solid and liquid material, which along with condensed water can form aerosol particles with radii ranging from <1 nm - 100 μm. These aerosols can enter the atmosphere directly, either by being picked up by convection, or they can be emitted *e.g.* by volcanoes. Alternatively, aerosols may be formed chemically in the atmosphere *e.g.* the formation of sulfate aerosols (H_2SO_4/H_2O droplets) in the stratosphere following the oxidation of SO_2. Atmospheric aerosols can affect the Earth's radiative balance directly by absorbing and scattering light, as well as acting as cloud condensation nuclei and hence enhancing cloud formation. They may also provide a surface for heterogeneous chemical reactions and therefore can play an important role in atmospheric chemistry.

The formation of aerosols in the lower atmosphere commonly requires the presence of water vapour. Water vapour enters the atmosphere *via* evaporation. The majority of this water vapour resides in the troposphere where it therefore plays a key role in cloud content and radiative balance. The water vapour content of the stratosphere is much lower. This is thought to be due to an effective freeze-drying of the atmosphere as it passes through the equatorial tropopause, at temperatures of around 190 K. Water vapour may also be formed *in situ* in the stratosphere through the oxidation of methane.

One of the key trace gases of the Earth's atmosphere is O_3. The chemistry and atmospheric importance, as well as observed trends in atmospheric O_3 are discussed in the following sections.

Compound	Natural sources	Anthropogenic sources
Methane (CH_4)	Emissions from swamps, bogs, wetlands and oceans, enteric fermentation in wild animals	Natural gas leakage, enteric fermentation in domesticated animals, emissions from paddies, combustion
Hydrocarbons (HCs) and volatile organic compounds (VOCs)	Vegetation, aerobic biological processes, forest fires	Natural gas leakage, combustion, vehicle exhausts, paints and solvents.
Carbon monoxide (CO)	Oxidation of natural methane (and larger HCs) and VOCs, emission from oceans and forest fires	Oxidation of anthropogenic HCs and VOCs, incomplete combustion (especially in motor vehicles), blast furnaces.
Nitric oxide (NO)	Anaerobic processes in soil, forest fires, electric storms	High temperature combustion of fossil fuels, aircraft
Nitrous oxide (N_2O)	Denitrifying bacteria in soil, oceans	Combustion of oil and coal, industrial processes
Ammonia (NH_3)	Aerobic biological processes in soil, breakdown of amino acids in organic waste material	Coal and oil combustion, waste treatment
Hydrogen sulphide (H_2S)	Anaerobic fermentation, volcanoes	Oil refining, combustion, animal manure
Dimethyl sulphide (CH_3SCH_3)	Aerobic biological sources	Animal manure, pulp and paper mills, brick manufacture, oli refining
Sulphur dioxide (SO_2)	Oxidation of H_2S, volcanic activity	Combustion of oil and coal
Methyl chloride (CH_3Cl)	Biological processes in oceans, algae	PVC manufacture and degradation, tobacco consumption
Methyl bromide (CH_3Br)	Aerobic biological processes	Soil fumigation, fire retardants
Chlorofluorocarbons (CFCs)	None	Solvents, aerosol propellants, refrigerants

Table 1. 1 Typical sources of trace constituents of the atmosphere. Adapted from reference 4.

1. 3 Chemistry of Atmospheric Ozone

Christian Friedrich Schönbein first discovered O_3 in 1840.[8] Subsequent chemical investigations by Houzeau, and spectroscopic studies at UV/visible wavelengths by Hartley, led to the conclusion that O_3 is present in the atmosphere, and furthermore that atmospheric concentrations of O_3 are greater at higher altitudes than they are at ground level.[9, 10] Dobson and Fabry were able to demonstrate the existence of a distinct O_3 layer in the lower stratosphere in the early 1900s.[11] Around the same time, Sidney Chapman was working towards a proposal to explain this observed vertical distribution of O_3 in terms of photochemical kinetics.

1. 3. 1 Stratospheric Ozone

In 1930 Chapman published his proposal of a theoretical explanation for the observed stratospheric profile of O_3.[12] The theory included a series of reactions involving only the chemistry of oxygen, since termed the 'oxygen only' model:

(1. 4) $O_2 + h\nu\ (\lambda < 242\ nm) \rightarrow O + O$

(1. 3) $O + O_2 + M \rightarrow O_3 + M$

(1. 1a) $O_3 + h\nu\ (\lambda < 1180\ nm) \rightarrow O_2 + O$

(1. 5) $O + O_3 \rightarrow O_2 + O_2$

(1. 6) $O + O + M \rightarrow O_2 + M$

The vertical distribution arises due to the variation of the rates of O_3 formation in this model as a function of altitude. Simplistically, O_3 production will be optimal at a cross over altitude where both the concentration of O_2 and the intensity of radiation at wavelengths less than 242 nm are both high.

Taking into account the observed abundances of O_2 and O_3 in the atmosphere, reaction (1. 6) is too slow to compete with reactions (1. 3) and (1. 5) and is therefore unlikely to occur. However, the interconversion of oxygen atoms and O_3 in reactions (1. 3) and

(1. 1a) is rapid compared to reactions (1. 4) and (1. 5), O and O_3 can therefore be treated using the steady-state approximation and the combined concentrations of O and O_3 termed the 'odd-oxygen' family, O_x ($O_x = O + O_3$). The overall production and loss processes for odd oxygen are therefore reactions (1. 4) (production) and (1. 5) (loss).

With the advent of more sophisticated atmospheric modelling, accurate *in situ* and remote sensing measurements of absolute atmospheric O_3 concentrations and accurate laboratory measurements of rate coefficients, it became apparent that whilst this oxygen only model could account qualitatively for stratospheric O_3 production, the model alone could not account for observed amounts.[4] Furthermore, this simplified model was modified to take into account factors such as latitudinal and seasonal variations of solar intensity, atmospheric temperature and solar zenith angle. This adaptation showed that the regions where the highest O_2 photolysis rates occur do not correlate with the highest O_3 concentrations. Photolysis rates are highest near the equator but O_3 concentrations were observed to maximise in Northern regions.[4] Furthermore, at the poles, the maximum photolysis rates are at high altitudes while the maximum O_3 concentrations were observed at lower altitudes. Evidently, the Chapman model does not account for horizontal and vertical mixing, which is significant in some regions of the atmosphere. If however, allowances for transport are included in the oxygen only model, the model can match the shape of observed O_3 vertical profiles but it still fails to predict the absolute concentrations observed. The oxygen only model typically predicts atmospheric odd-oxygen concentrations to be almost double those actually observed.

The discrepancies between observed O_3 profiles and those predicted by the oxygen only model imply that the model either overestimates O_3 production or underestimates O_3 destruction. Reaction (1. 4) is the major source of odd-oxygen in the atmosphere. The rate of this reaction is determined by the solar radiation profile of UV radiation capable of photolysing O_2 and the atmospheric O_2 concentrations, both of which are well determined. The primary loss route for odd-oxygen, according to the Chapman model, is reaction (1. 5). This reaction has been shown to have an unusually high activation energy (E_a = 17 kJ mol^{-1}).[3] As a result, at stratospheric temperatures, reaction (1. 5) is too slow to account for the observed profile. Additional odd-oxygen loss processes must be present.

Additional reaction schemes do exist and take the form of catalytic O_3 loss cycles. O_3 and oxygen atoms, which are both highly reactive, react with many trace atmospheric species forming O_2. Molina and Rowland proposed a reaction scheme where a trace species, X, can react with O_3 destroying it, but is itself reformed during the cycle *via* the reaction of a co-product of reaction (1. 7) with oxygen atoms:[13]

(1. 7) $X + O_3 \rightarrow XO + O_2$

(1. 8) $XO + O \rightarrow X + O_2$

Net: $O + O_3 \rightarrow 2O_2$

These cycles provide a more efficient route for the loss of odd-oxygen than the direct loss in reaction (1. 5), but have the same net result. As a consequence of the cycles' catalytic nature, even if X is only present in very small quantities it can be responsible for large perturbations in the, somewhat higher, mixing ratios of odd-oxygen.

The most common candidates for X/XO in the stratosphere are NO/NO_2, OH/HO_2, H/OH, Cl/ClO, Br/BrO and I/IO, all of which are trace atmospheric constituents. Different odd-oxygen loss cycles will dominate at different latitudes and altitudes. The efficiency at which these catalytic cycles can operate will be dependent upon a number of competing reactions, which may or may not perturb the destruction cycle. For example, the formation of so called *reservoir species* (named because they temporarily render X inactive with respect to O_x destruction) can break the catalytic cycle until the reservoirs themselves are broken down and the active form of X or XO is re-released. Therefore, for chlorine, $ClONO_2$ and HCl are important reservoir species:

(1. 9) $ClO + NO_2 + M \rightarrow ClONO_2 + M$

(1. 10) $Cl + CH_4 \rightarrow HCl + CH_3$

and the effect that chlorine can have on O_3 destruction is dependent upon the stability of these reservoirs. Indeed, some reservoirs may be so stable that they are be removed

from the atmosphere in deposition processes such as precipitation. Alternatively, the reservoirs may themselves be photolysed or undergo chemical reaction to release active species. In the polar stratosphere in wintertime, heterogeneous reactions of reservoir species on polar stratospheric cloud particles are now recognised as a source of elevated levels of molecular chlorine:[14]

(1. 11) $ClONO_2 + HCl \rightarrow Cl_2 + HNO_3$

(1. 12) $HOCl + HCl \rightarrow Cl_2 + H_2O$

At the onset of polar springtime, solar photolysis of this photolabile molecular chlorine releases enhanced levels of active Cl and increased O_3 destruction inevitably ensues. Polar O_3 loss is discussed in more detail in Section 1. 4.

Alternatively, competing reactions to O_3 destruction or reservoir formation may result in no overall effect on O_3 loss. In the stratosphere, the catalytic O_3 destruction cycle involving NO/NO_2 is thought to account for up to 50% of O_3 loss. However, one of the most significant competing processes for this cycle, in the sunlit atmosphere, is NO_2 photolysis. NO_2 photolysis results in odd-oxygen production so despite the destruction of O_3 in forming NO_2 in reaction (1. 13), no net perturbation of odd-oxygen destruction is observed. The overall cycle is, in this case, is termed a 'null cycle':

(1. 13) $NO + O_3 \rightarrow NO_2 + O_2$

(1. 14) $NO_2 + h\nu \rightarrow NO + O$

(1. 3) $O + O_2 + M \rightarrow O_3 + M$

Net: $(O_3 + O + O_2 \rightarrow O_3 + O + O_2)$ No change

At low altitudes in the stratosphere, where oxygen atom concentrations are low, the catalytic cycles involving oxygen atoms become less efficient (reaction (1. 3) becomes efficient at low altitude due to high concentrations of O_2 and M). Under these conditions coupling between different chemical families can become the dominant O_3

loss cycles.[15] One example of this is the formation and solar photolysis of hypochlorous acid, HOCl:

(1. 15)		$ClO + HO_2$	$\rightarrow$	$HOCl + O_2$
(1. 16)		$HOCl + h\nu$	$\rightarrow$	$OH + Cl$
(1. 17)		$Cl + O_3$	$\rightarrow$	$ClO + O_2$
(1. 18)		$OH + O_3$	$\rightarrow$	$HO_2 + O_2$
	Net:	$2O_3$	$\rightarrow$	$3O_2$

Such couplings, to form weakly bound and readily photolysed reservoir species such as HOCl, can be thought of as mid-way between direct O_3 loss and reservoir formation.

In all cases, successful modelling of stratospheric O_3 abundances requires identification of the rate determining step of the process and characterisation of the rate of this process under appropriate experimental conditions. This is also true for the troposphere, where the role of O_3 is also important, as discussed in the following section.

1. 3. 2 Tropospheric Ozone

The tropospheric environment is very different to that of the stratosphere. As discussed above, the troposphere undergoes rapid vertical mixing compared to the layered stratosphere. The troposphere also has a much higher water vapour content than the stratosphere and, since short wavelength solar radiation is absorbed by the O_3 layer above, a milder photochemical environment. As a result of this latter feature, O_2 photolysis does not occur to the same extent as in the stratosphere and O_3 formation in the troposphere, *via* reactions (1. 3) and (1. 4), is negligible. Some O_3 is present in the troposphere however, and has been attributed to slow stratosphere-troposphere exchange, along with some chemical *in situ* production.

Short wavelength photolysis of O_3 produces both $O(^1D)$ and $O(^3P)$. Any reactive $O(^1D)$ that is formed however, is more likely to be quenched to $O(^3P)$ by the increased atmospheric density relative to higher altitudes. For this reason, initial studies of

atmospheric chemistry considered the troposphere to be an unreactive atmospheric region compared to the stratosphere. However, because of the high water content of the troposphere, some competition for the small amount of $O(^1D)$ formed from short wavelength O_3 photolysis does take place. The reaction of water with $O(^1D)$ results in the formation of OH radicals:[16]

(1. 19) $$O(^1D) + H_2O \rightarrow OH + OH$$

This process is profoundly important since OH radicals facilitate the removal of many atmospheric species through oxidation cycles. Without these oxidation processes, atmospheric concentrations of species such as CO, CH_4 and many other species (such as those shown in Table 1. 1) could build up to dangerous levels.

Many of these oxidation cycles will have differing outcomes depending on the chemistry of the local environment. For example in the unpolluted troposphere, where short lived pollutant concentrations such as nitrogen oxides, NO_x ($NO_x = NO + NO_2$), are low, CO may undergo the following oxidation cycle involving OH:[17]

(1. 20) $$CO + OH \rightarrow H + CO_2$$

(1. 21) $$H + O_2 + M \rightarrow HO_2 + M$$

The hydroperoxy radical, HO_2, formed in this sequence may then react with any O_3 present:

(1. 22) $$HO_2 + O_3 \rightarrow OH + 2O_2$$

This cycle sets up an interconversion of OH and HO_2 radicals, often defined as the odd-hydrogen family, HO_x ($HO_x = OH + HO_2$), as they enter effective equilibrium. The above cycle, involving CO, accounts for approximately 70% of HO_x chemistry in the background troposphere. The remaining 30% is described by a more complex chain of reactions initiated by OH reacting with methane:

(1. 23) $$OH + CH_4 \rightarrow H_2O + CH_3$$

HO_x may be removed from the troposphere by reactions that form soluble species, with subsequent heterogeneous uptake and removal. For example, the HO_2 self-reaction, reaction (1. 24), forms H_2O_2, which can be readily removed *via* precipitation, a process termed wet deposition.

(1. 24) $HO_2 + HO_2 \rightarrow H_2O_2 + O_2$

The oxidation of hydrocarbons, including CH_4, and CO in the troposphere by OH, has important consequences for tropospheric O_3. For example, in the absence of NO_x the set of reactions initiated by oxidation of CO, reactions (1. 20)-(1. 22), results in net *loss* of O_3:

Net: $CO + O_3 \rightarrow CO_2 + O_2$

Oxidation of hydrocarbons under these conditions also results in net *loss* of HO_x:

(1. 23) $OH + CH_4 \rightarrow H_2O + CH_3$

(1. 25) $CH_3 + O_2 + M \rightarrow CH_3O_2 + M$

where the principal fate of the methylperoxy radical, CH_3O_2, is reaction with HO_2, analogous to the HO_2 self-reaction:

(1. 26) $CH_3O_2 + HO_2 \rightarrow CH_3OOH + O_2$

However, in the polluted atmosphere, where short lived pollutants such as NO_x are present, this interconversion of OH and HO_2 can be perturbed significantly. For example NO can compete with O_3 for HO_2:

(1. 27) $HO_2 + NO \rightarrow OH + NO_2$

NO_2 is readily photolysed at visible wavelengths, reforming NO. In addition, the co-product is an oxygen atom, resulting in the formation of O_3:

(1. 14) $NO_2 + h\nu \rightarrow NO + O(^3P)$

(1. 3) $O(^3P) + O_2 + M \rightarrow O_3 + M$

(1. 13) $NO + O_3 \rightarrow NO_2 + O_2$

Therefore, under these conditions, O_3 is *produced* in the overall oxidation of CO and consequently increases HO_x *via* subsequent photolysis of O_3. Furthermore, NO, OH and NO_2 are all regenerated in the above catalytic cycle. Analogous cycles occur for larger peroxy radicals (where the more CH_2 groups there are the greater the number of O_3 molecules formed *per* cycle, provided that concentrations of NO_x are suitably high).

The presence of NO_x thus completely shifts the balance of the oxidaiton process of hydrocarbons in favour of production of O_3 and HO_x. The degree to which this shift occurs will be dependent upon the relative rates of (1. 22) and (1. 27). Modelling studies have shown that if the tropospheric ratio of $[NO]/[O_3]$ typically exceeds 2×10^{-4} then net O_3 production will occur.[18] This is indeed the case in many industrialised areas where NO_x emissions, primarily from motor vehicle exhausts, lead to the formation of O_3 *via* hydrocarbon oxidation in cycles similar to those discussed above. The production of O_3 at ground level has been associated with the formation of what is commonly termed photochemical smog, itself linked with adverse effects on health as well as the natural and built environment.

1. 4 Trends in Atmospheric Ozone

1. 4. 1 Polar Stratospheric Ozone

Perhaps the most dramatic and certainly the most widely publicised change in atmospheric O_3 abundances are the polar stratospheric O_3 'holes' observed in springtime over Antarctic and more recently Arctic regions.

The British Antarctic Survey first reported significant stratospheric O_3 depletion during routine long term monitoring of O_3 column densities (*i.e.* the total O_3 abundance above a fixed area) from ground based measurements at Halley Bay, Antarctica, as shown in Figure 1. 7 below.

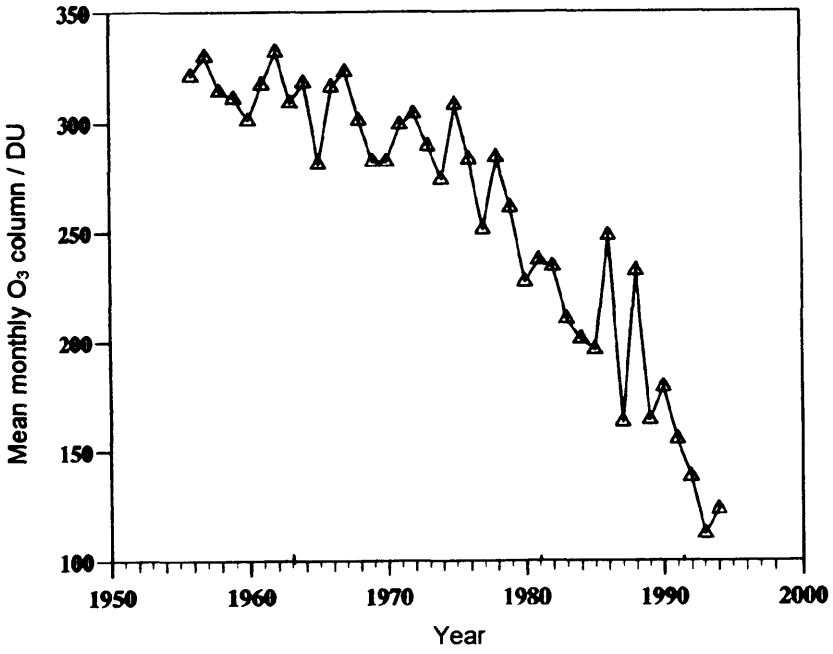

Figure 1. 7 Mean October value of column O_3 over Halley Bay, Antarctica, reported by Farman *et al.*[19,20]

A series of measurements made using a variety of remote sensing techniques, including the satellite TOMS (Total Ozone Mapping Spectrometer),[21] over the following years reaffirmed these findings. Furthermore, these subsequent readings suggested that the magnitude of this depletion was increasing each year. Indeed, measurements have shown that the total column O_3 is typically depleted by 80% during the Antarctic springtime and at some altitudes up to 100% depletion occurs, as shown from the O_3 vertical profile in Figure 1. 8. More recently, O_3 'holes' have also been recorded at the Arctic by field campaigns such as THESEO (Third European Stratospheric Experiment on Ozone).[22] Arctic and Antarctic O_3 holes appear as severe reductions in the stratospheric O_3 layer at the onset of polar springtime. Gradual recovery of the O_3 layer takes place early in the local summer.

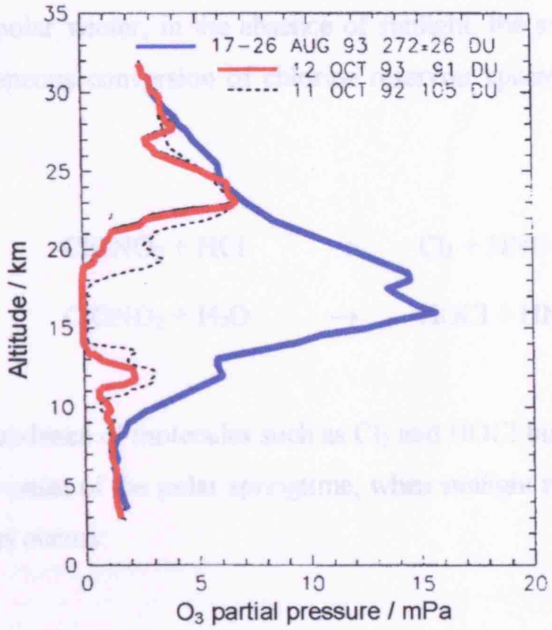

Figure 1. 8 O_3 profiles over the South Pole in the winter (blue) and springtime (red) of 1993.[23]

It is now widely accepted that O_3 hole events arise from a combination of chemical and meteorological factors, which are unique to polar regions. During the polar winter strong Westerly winds inhibit North-South mixing of air, resulting in an intense circulatory system around the pole, known as the polar vortex. This vortex is most extreme in the Southern Hemisphere, but does occur to some extent in the Arctic. The isolated vortex has two main features congruent with O_3 hole events. First, temperatures within the vortex can fall as low as 180 K, as air is isolated from warmer mid-latitudes. Secondly, during the polar winter, the region is dark. When the temperature within the vortex falls below *ca.* 194 K the formation of polar stratospheric clouds (PSCs) through nucleation is favoured. Some PSCs are known to be liquid particles of a solution of sulphuric acid, nitric acid and water. Others are formed from the co-condensation of water and nitric acid, giving rise to particles of $HNO_3.3H_2O$ (Type I PSCs).[24] Once temperatures drop below *ca.* 188 K rapid condensation of water on the surface of PSC particles results in particle growth until gravitational settling occurs (Type II PSCs). HNO_3 can be permanently removed from the atmosphere *via* sedimentation of large PSC particles and consequently the stratosphere becomes denitrified.[25] Denitrification removes gaseous NO_x as HNO_3, which would otherwise interrupt O_3 loss cycles by forming reservoir species such as $ClONO_2$.

Throughout the polar winter, in the absence of sunlight, the surfaces of PSCs provide sites for heterogeneous conversion of chlorine reservoir species into more photolabile chlorine forms:[26]

(1. 11) $ClONO_2 + HCl \rightarrow Cl_2 + HNO_3$

(1. 28) $ClONO_2 + H_2O \rightarrow HOCl + HNO_3$

Therefore, an abundance of molecules such as Cl_2 and HOCl builds up through the polar winter and at the onset of the polar springtime, when sunlight returns, photolytic release of active Cl atoms occurs:

(1. 29) $Cl_2 + h\nu \rightarrow 2Cl$

(1. 16) $HOCl + h\nu \rightarrow Cl + OH$

Cl atoms react rapidly with O_3 resulting in an increase in ClO and consequent decrease in O_3 mixing ratios.

(1. 17) $Cl + O_3 \rightarrow ClO + O_2$

In the spring of 1987, aircraft measurements simultaneously monitored O_3 and ClO mixing ratios in the Antarctic stratosphere.[27] These measurements showed an obvious anti-correlation between elevated ClO concentrations and depleted amounts of O_3, as shown in Figure 1. 9, providing the first conclusive evidence for the involvement of chlorine in O_3 destruction.

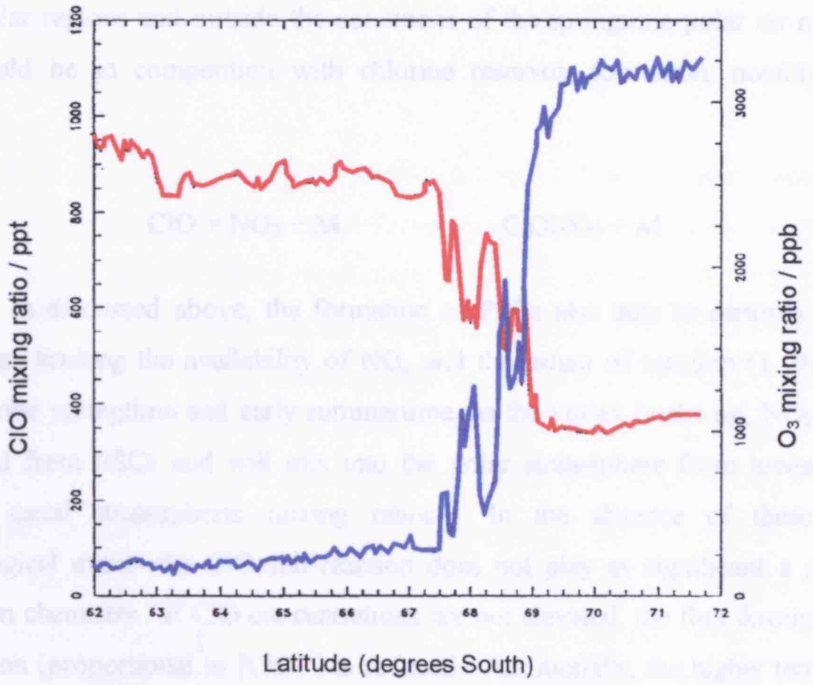

Figure 1. 9 Latitude dependence of O_3 (red) and ClO (blue) recorded simultaneously near the South Pole during springtime.[28]

The measurements also showed that the ClO mixing ratios were much smaller than the amount of O_3 destroyed, indicating that the O_3 depletion is a catalytic process of a similar form to those described in Section 1. 3. 1 above. One problem with this proposal however, was that the concentrations of oxygen atoms in the lowermost stratosphere, where depletion occurred, were too small for such cycles to be efficient. This led to the suggestion that as a result of the high ClO content the ClO self-reaction could become a favourable process. This reaction reversibly forms the Cl_2O_2 dimer, which, if sufficiently stable with respect to thermal decomposition, could be photolysed in sunlight to produce Cl atoms, either directly, or through formation and decomposition of the ClOO product:[29]

(1. 17) $2 \times (Cl + O_3 \rightarrow ClO + O_2)$

(1. 30) $ClO + ClO + M \leftrightarrow Cl_2O_2 + M$

(1. 31) $Cl_2O_2 + h\nu \rightarrow ClOO + Cl$

(1. 32) $ClOO + M \rightarrow Cl + O_2 + M$

Net: $2O_3 \rightarrow 3O_2$

In non-polar regions and outside the conditions of the springtime polar air masses this cycle would be in competition with chlorine reservoir formation, notably chlorine nitrate:

(1. 9) $ClO + NO_2 + M \rightarrow ClONO_2 + M$

However, as discussed above, the formation of PSCs also acts to denitrify the polar stratosphere limiting the availability of NO_x and the extent of reaction (1. 9). During the late polar springtime and early summertime, as the vortex beaks up, NO_2 could be re-released from PSCs and will mix into the polar stratosphere from lower latitudes restoring usual stratospheric mixing ratios. In the absence of these extreme meteorological events the ClO self-reaction does not play as significant a role in O_3 destruction chemistry. If ClO concentrations are not elevated, the flux through the ClO self-reaction (proportional to $[ClO]^2$) is reduced. Additionally, the higher temperatures as the vortex breaks down lead to thermal dissociation of the ClO dimer back to ClO radicals (depending upon the thermal stability of the dimer), hence active chlorine is no longer released and extreme O_3 depletion events are no longer observed.

Supplementary catalytic cycles coupling other halogens are thought to complement the ClO cycle described above. One of the most important additional cycles has the reaction ClO + BrO as the rate determining step, but does not proceed *via* the association of radicals:

(1. 33a) $ClO + BrO \rightarrow Cl + Br + O_2$

(1. 33b) $ClO + BrO \rightarrow Br + OClO$

(1. 33c) $ClO + BrO \rightarrow BrCl + O_2$

Together with the ClO cycle these reactions form the major gas phase processes responsible for the formation of polar O_3 holes.[23] An important contrast to the cycle involving the ClO self-reaction is that in the ClO + BrO cycle active halogen atoms are directly formed, as opposed to adduct formation in the former cycle. The importance of this cycle is however perturbed by the formation of OClO in channel (1. 33b). OClO

readily photolyses to give oxygen atoms which will offset the degree of O_3 loss caused by this cycle.

The extent of these annual O_3 hole events is expected to decrease thanks to the restrictions brought in by the Montreal Protocol and subsequent amendments.[30] The protocol does however only limit *production* of specific halogen containing species. It does not prohibit the use of chemicals already stockpiled. Although many developed countries have agreed to restrict usage of these chemicals it is possible that the reserved stocks will be used at some point in the future by less well developed countries. Consequently, it is very difficult to predict with any certainty when polar O_3 levels are going to recover significantly. A further complication to this debate is the suggestion that stratospheric cooling associated with global warming may increase the stability of the polar vortices enhancing all the chemistry discussed above, including the crucial radical-radical reaction rates. If this were the case, recovery of O_3 levels to pre-ozone hole values (which is expected to occur by the middle of the 21st century[30]) may be delayed by as much as 10-15 years.[31]

1. 4. 2 Mid-Latitude Stratospheric Ozone

In the mid-latitudes, observed trends in O_3 mixing ratios are much less extreme than those of the polar regions described above. Nevertheless, O_3 records from both satellite and ground based measurements have shown that depletion does take place and therefore presents a significant environmental threat as such regions are populated.[30] Some of the most comprehensive atmospheric measurements of O_3 and other trace gases in the middle latitudes were taken over the period 1979-1991 during the SAGE (Stratospheric Aerosol and Gas Experiment) campaign.[30] Results from these remote sensing measurements suggested that O_3 destruction was taking place in these regions. Indeed, some results suggest reductions of O_3 of $(20 \pm 8)\%$ *per* decade at altitudes 16-17 km for the middle latitudes, as shown in Figure 1. 10.

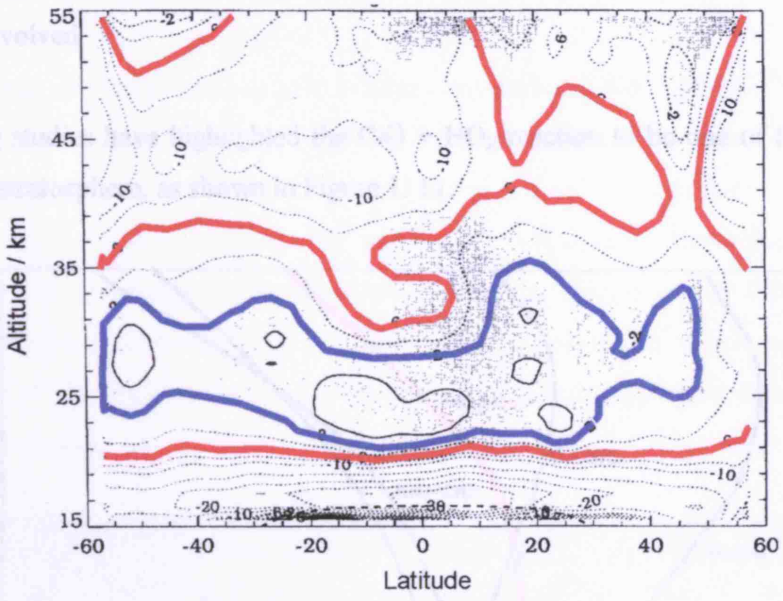

Figure 1. 10 Spatial mapping of O_3 trend (% loss *per* decade) at mid-latitudes from 1979-1991.[30] Highlighted are the areas with 6% loss (red) and 2% loss (blue).

O_3 destruction in mid-latitude regions has been attributed not only to out mixing of polar O_3 depleted air but also to *in situ* free radical chemistry. The conditions in the middle latitudes do not promote elevated ClO and BrO radical concentrations *via* PSC activation. As a result the important O_3 destruction cycles become those *between* radical families, for example:

(1. 34)	$OH + O_3$	$\rightarrow$	$HO_2 + O_2$	
(1. 7)	$X + O_3$	$\rightarrow$	$XO + O_2$	(X = Cl, Br)
(1. 35)	$XO + HO_2$	$\rightarrow$	$HOX + O_2$	
(1. 36)	$HOX + h\nu$	$\rightarrow$	$OH + X$	(rapid)
Net:	$2O_3$	$\rightarrow$	$3O_2$	

In sunlit conditions where reaction (1. 36) is fast, $XO + HO_2$ is the rate limiting step for this cycle. As a consequence, provision of kinetic and mechanistic data for $XO + HO_2$ reactions are a priority for atmospheric studies. Laboratory studies of free radical cross-

reactions will also inevitably require accurate knowledge of the self-reactions of the radicals involved.

Modelling studies have highlighted the ClO + HO_2 reaction to be one of the fastest in the lower stratosphere, as shown in Figure 1. 11.

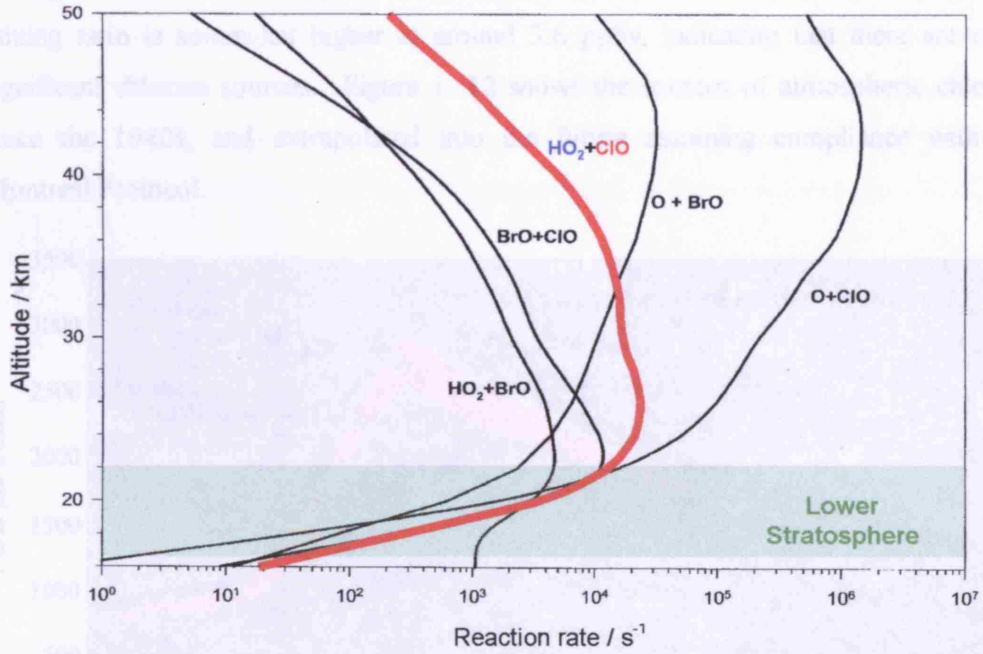

Figure 1. 11 Reaction rate as a function of altitude for the main cross radical reactions, showing that in the lower stratosphere the ClO + HO_2 reaction dominates (red line). Adapted from reference 3.

Despite the relative importance of this reaction there have been very few comprehensive studies under atmospheric conditions.

Work carried out in this dissertation has attempted to address discrepancies in the literature concerning reactions between halogen monoxide free radicals, both within radical families, so called self-reactions (discussed in Chapters 4 and 6), and between different radical families, termed cross-reactions (discussed in Chapter 5). The sources of atmospheric halogens and trends in halogen abundance are discussed in the following section.

1. 5 Sources of Atmospheric Halogens

The principal sources of atmospheric halogens are methyl halides, CH_3X (X=Cl, Br, I). Whilst significant natural resources of CH_3Cl include release from oceans and tropical plants, dominant sources are also biomass burning and industrial release. CH_3Cl has a mixing ratio of about 0.6 ppbv at the tropopause, but the total stratospheric chlorine mixing ratio is somewhat higher at around 3.6 ppbv, indicating that there are other significant chlorine sources. Figure 1. 12 shows the sources of atmospheric chlorine since the 1940s, and extrapolated into the future assuming compliance with the Montreal Protocol.

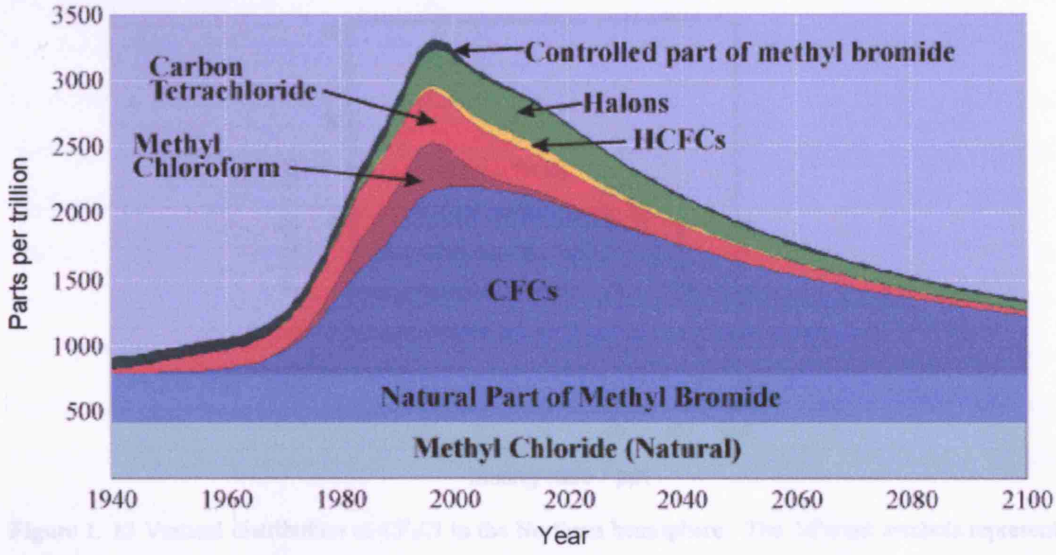

Figure 1. 12 Halogen loading as Equivalent Effective Stratospheric Chlorine.[32]

From the mid 1960s to the early 1990s an increase of around 3 ppbv of atmospheric chlorine occurred. The major stratospheric sources of chlorine are chlorofluorocarbons (CFCs), including CCl_2F_2 and CCl_3F. These compounds were developed at General Motors in the 1930s, in an attempt to replace ammonia and sulfur dioxide as refrigerants with less/non-toxic counterparts. In the 1960s, CFC production was increased as they began to be used as propellants and blowing agents in foam production, hence a further increase in atmospheric abundances occurred. Although the CFCs' non-toxicity and inertness were heralded an industrial success at ground level, it was precisely their unreactive nature that proved disastrous once released into the atmosphere.

In 1973, James Lovelock observed halogenated hydrocarbons in the lower atmosphere demonstrating that these compounds are photostable and very unreactive towards oxidation at these altitudes.[33] With some CFCs, such as CCl_2F_2, having atmospheric lifetimes of up to 100 years Molina and Rowland suggested that these compounds could undergo vertical transport into the stratosphere.[13] Once subjected to the harsher photochemical conditions at these higher altitudes the compounds may be photolysed, releasing halogen atoms into an environment rich in O_3. Inevitably rapid O_3 destruction would be possible. These proposals were confirmed in a number of field measurements that followed, showing that the abundance of CFCs, although constant throughout the troposphere, drops dramatically above the tropopause, as shown in Figure 1. 13.

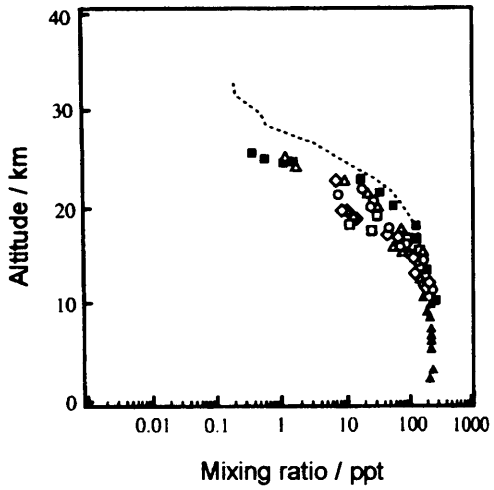

Figure 1. 13 Vertical distribution of CF_3Cl in the Northern hemisphere. The different symbols represent particular experiments performed on different days over the period 1987 to 1990.[23]

The major source of atmospheric bromine is methyl bromide, CH_3Br, contributing up to 50% of the total inorganic bromine content in the upper troposphere. CH_3Br has both natural and anthropogenic sources. Natural sources, principally production by marine algae, make up about 50% of its atmospheric release.[30] The anthropogenic sources include use as a soil fumigant and as an anti-knocking agent in fuel. Another considerable source (*ca.* 40%) of atmospheric bromine comes from halons, bromine analogues of CFCs, used mainly in fire extinguishers. Although bromine source gases are much less abundant than chlorine counterparts they are much less stable. As a result, the partitioning between active and reservoir forms of atmospheric bromine will favour active forms to a greater extent than the chlorine counterparts. Indeed, bromine

has been estimated to be up to 50 times more efficient *per* molecule than chlorine at destroying atmospheric O_3.[34] By analogy, the O_3 destroying efficiency of iodine is thought to be even greater, but this value depends upon key chemical/photochemical parameters which are to date, sparse.[35, 36] Furthermore, at present transport of iodine into the stratosphere is thought to be minimal.

1. 5. 1 CFC Control Measures

During the 1970s the potential hazardous consequences of increased halogen loading in the atmosphere on atmospheric O_3 featured heavily in the media of developed countries and began to influence consumer behaviour.[19] The United States market for spray cans fell by almost two-thirds due to public concern for the environment. With increasing pressure to act upon these concerns in 1978, the USA, and subsequently Canada, Norway and Sweden, banned the use of CFCs as spray can propellants in nonessential applications.[19] CFCs began to be replaced by transitional substances such as HCFCs. These substances, although not a permanent solution, as they still pose some threat to atmospheric O_3 levels, were necessary in the short term in order to permit rapid phase-out of the more dangerous alternatives. HCFCs have C-H bonds, which make them more reactive towards OH, allowing rapid atmospheric degradation in the troposphere, limiting their transport to the stratosphere. The dramatic discovery of the Antarctic O_3 hole by Farman *et al.*[20] in 1985, indicated that more extreme action needed to be taken in order to avoid a serious environmental disaster. In 1987, 25 countries accepted the Montreal Protocol on Substances that Deplete the Ozone Layer. As of the 1st January 1989 the treaty required all members to reduce production and emission of CFCs and halons. Subsequent damning evidence produced by Anderson *et al.*[28] linking CFC emissions with rapid, catalytic O_3 loss forced amendment of this original agreement to phase out CFCs, halons and HCFCs much more rapidly and on a much wider scale. The reductions in atmospheric halogen containing compound emissions brought about due to these policies can be seen in Figure 1. 14 below.

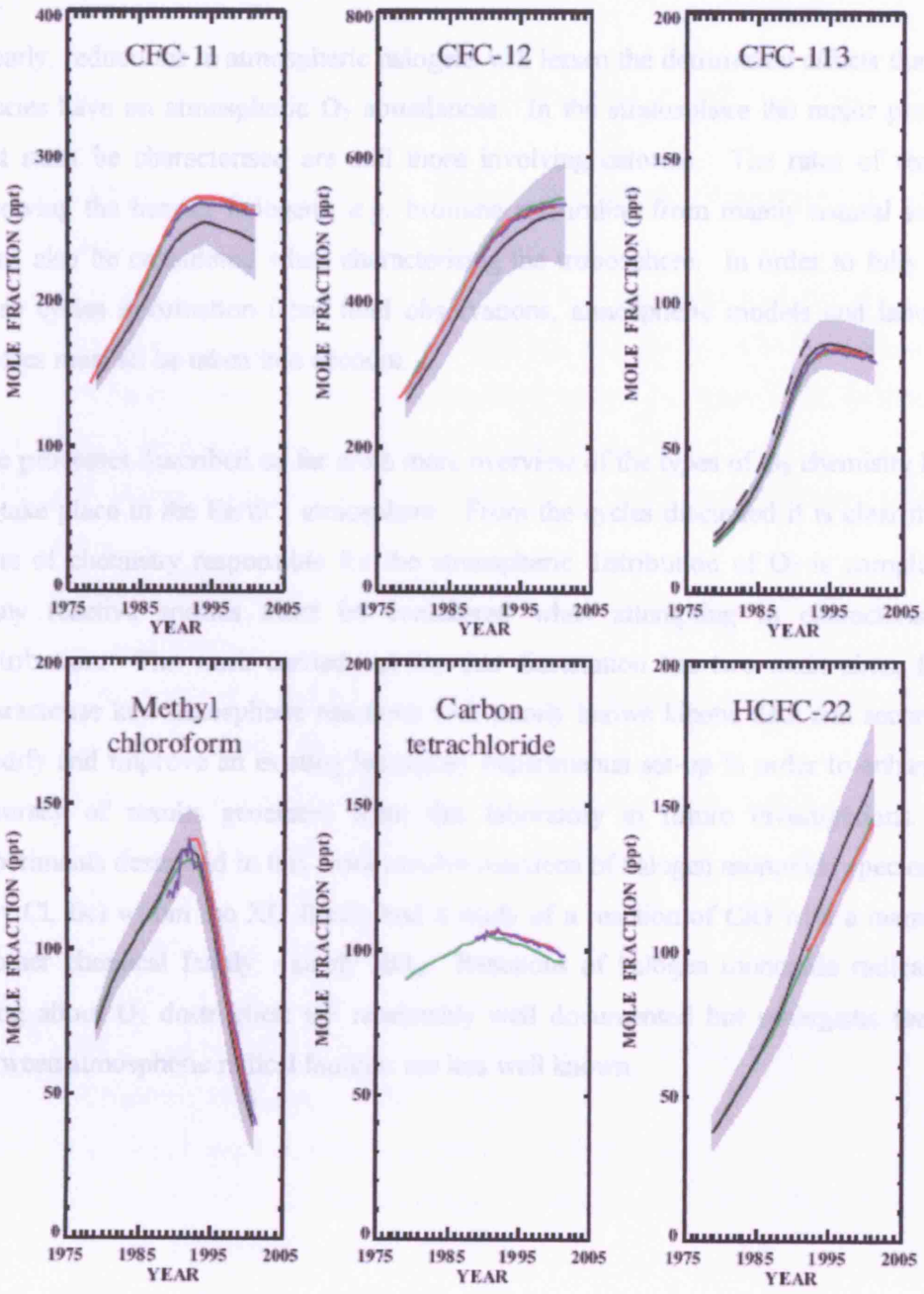

Figure 1. 14 Measured and calculated global mean surface mixing ratios for the major CFCs, methyl chloroform, carbon tetrachloride and HCFC-22. The different coloured lines represent measurements from different field campaigns, the black lines represent ratios calculated using atmospheric box models and the shaded grey areas represent the uncertainties in these model calculations.[30]

1. 6 Summary

Clearly, reductions in atmospheric halogens will lessen the detrimental effects that these species have on atmospheric O_3 abundances. In the stratosphere the major processes that must be characterised are still those involving chlorine. The rates of reactions involving the heavier halogens, *e.g.* bromine and iodine from mainly natural sources, must also be considered when characterising the troposphere. In order to fully assess these cycles information from field observations, atmospheric models and laboratory studies must all be taken into account.

The processes described so far are a mere overview of the types of O_3 chemistry known to take place in the Earth's atmosphere. From the cycles discussed it is clear that the suite of chemistry responsible for the atmospheric distribution of O_3 is complex and many reactive species must be considered when attempting to characterise this distribution. The work carried out for this dissertation has two main aims, first to characterise key atmospheric reactions with poorly known kinetic data and secondly to modify and improve an existing laboratory experimental set-up in order to enhance the accuracy of results generated from this laboratory in future investigations. The experiments described in this work involve reactions of halogen monoxide species (XO, X = Cl, Br) within the XO family and a study of a reaction of ClO with a member of another chemical family, namely HO_x. Reactions of halogen monoxide radicals that bring about O_3 destruction are reasonably well documented but synergistic reactions between atmospheric radical families are less well known.

1. 7 References

1. Taken from: *The Earth and its Atmosphere*, http://www.physics.isu.edu/weather/kmdbbd/unit1_images.htm, Idaho State University.
2. G. Brasseur, J. Orlando, and G. Tyndall, *Atmospheric Chemistry and Global Change*, **1999**, Oxford: Oxford University Press.
3. W.B. DeMore, S.P. Sander, D.M. Golden, R.F. Hampson, M.J. Kurylo, C.J. Howard, A.R. Ravishankara, C.E. Kolb, and M.J. Molina, *Chemical Kinetics and Photochemical Data for Use in Stratospheric Modelling*, JPL Publication 02-25, Jet Propulsion Laboratory, Pasadena, CA, **1997**.
4. R.P. Wayne, *Chemistry of Atmospheres*, 3rd ed, **2002**, Oxford: Oxford University Press.
5. Taken from: *Earth and Moon Viewer*, http://www.fourmilab.ch/cgi-bin/uncgi/Earth,
6. G. Brasseur and S. Solomon, *Aeornomy of the Middle Atmosphere*, 2nd ed, **1986**, Dordecht: D. Reidel Pub. Co.
7. Taken from: *Action Spectra*, http://sedac.ciesin.org/ozone/docs/AS.html, Stratospheric Ozone and Human Health Project.
8. C. Schonbein, *C. R. Acad. Sci. Paris*, **1840**, 10, 706.
9. A. Houzeau, *C. R. Acad. Sci. Paris*, **1858**, 46, 89.
10. W. Hartley, *J. Chem. Soc.*, **1881**, 39, 111.
11. G.M.B. Dobson, *Proc. Roy. Soc. London, Sec. A*, **1930**, 129, 411.
12. S. Chapman, *Phil. Mag.*, **1930**, 10, 369.
13. M.J. Molina and F.S. Rowland, *Nature*, **1974**, 249, 810.
14. D.R. Hanson and A.R. Ravishankara, *J. Geophys. Res.*, **1993**, 98, 22931.
15. Y. Yung, *J. Atmos. Sci.*, **1980**, 37, 339.
16. B. Weinstock, *Science*, **1969**, 166, 224.
17. H. Levy II, *Science*, **1971**, 173, 141.
18. P. Crutzen, *Topics in Atmospheric and Interstellar Physics and Chemistry*, **1994**, Les Editions de Physique, Les Ulis.
19. R. Harrison, *Pollution: Causes, Effects and Control*, 3rd ed, **1996**, Cambridge: Royal Society of Chemistry.

20. J.C. Farman, B.G. Gardiner, and J.D. Shanklin, *Nature*, **1985**, 315, 207.
21. Taken from: *Total Ozone Mapping Spectrometer*, http://toms.gsfc.nasa.gov/, NASA.
22. M.R. Schoeberl, P.A. Newman, L.R. Lait, T.J. McGee, J.F. Burris, E.V. Browell, W.B. Grant, E.C. Richard, P. von der Gathen, R. Bevilacqua, and I.S. Mikkelsen, *J. Geophys. Res. Atmos.*, **2002**, 107, D20, 8261.
23. WMO, *Scentific Assessment of Ozone Depletion: 1994*, World Meteorological Association, Geneva, **1994**.
24. P.J. Crutzen and F. Arnold, *Nature*, **1986**, 324, 651.
25. D.W. Fahey, S. Solomon, S.R. Kawa, M. Loewenstein, J.R. Podolske, S.E. Strahan, and K.R. Chan, *Nature*, **1990**, 345, 698.
26. S. Solomon, R. Garcia, F. Rowland, and D. Weubbles, *Nature*, **1986**, 321, 755.
27. J. Anderson, *J. Geophys. Res.*, **1989**, 94, 11465.
28. J.G. Anderson, W.H. Brune, and M.H. Proffitt, *J. Geophys. Res.*, **1989**, 95, 15129.
29. L. Molina and M. Molina, *J. Phys. Chem.*, **1987**, 91, 433.
30. WMO, *Scientific Assessment of Ozone Depletion: 2002*, World Meteorological Association, Geneva, **2002**.
31. D.T. Shindell, D. Rind, and P. Lonergan, *J. of Climate*, **1998**, 11, 895.
32. Taken from: *Atmospheric Chlorine: CFCs and Alternative Fluorocarbons*, http://www.afeas.org/atmospheric_chlorine.html, Alternative Fluorocarbon Environmental Acceptability Study.
33. J.E. Lovelock, R.J. Maggs, and R.J. Wade, *Nature*, **1973**, 241, 194.
34. S. Wofsy, M. McElroy, and Y. Yung, *Geophys. Res. Lett.*, **1975**, 2, 215.
35. S. Solomon, R. Garcia, and A.R. Ravishankara, *J. Geophys. Res.*, **1994**, 99, 20491.
36. D. M. Rowley, J. Mossinger, R. Cox, and R. L. Jones, *J. Atmos. Chem.*, **1999**, 34, 137.

Chapter 2
Photochemistry and Gas Kinetics

In order to characterise the chemistry and composition of the atmosphere it is essential to have an understanding of the processes affecting trace gases. As a result, knowledge of the kinetics and mechanisms of interactions of these species with light (photochemistry), in particular sunlight, and the rapidity of reaction of their breakdown products (kinetics) is crucial. The main principles of these disciplines are discussed in this chapter.

2. 1 Photochemical Processes

2. 1. 1 Absorption

Absorption of radiation by a molecule may occur if the incident energy of the photons is equal to a difference between the energy levels of the molecule. The extent of this absorption will be determined by the absorption cross-section, σ, of the absorbing species at a given wavelength, λ. The absorbance, A, of radiation through a sample of length, l, and concentration, c, is described by the Beer-Lambert law:

(E2. 1) $$A_\lambda = \ln\left[\frac{I_0}{I_t}\right] = \sigma_\lambda \cdot c \cdot l$$

where I_0 is the incident intensity and I_t the transmitted intensity.

Absorption cross-sections are photon energy, and hence wavelength, dependent. For a number of atmospheric species, absorption of photons of UV and visible wavelengths (typical of solar radiation) results in electronic transitions. Rotational and vibrational excitation will accompany the electronic transition if the transition is below the dissociation limit of a bound upper state. As a result the observed spectra will exhibit distinguishing structural features. If these features are observed at sufficiently high resolution they can assist the identification and quantification of the species. Such phenomena (in this case vibrational transitions superimposed on an electronic

transition) are observed for many small molecules including the halogen monoxide radicals ClO and BrO, as shown for ClO in Figure 2. 1.

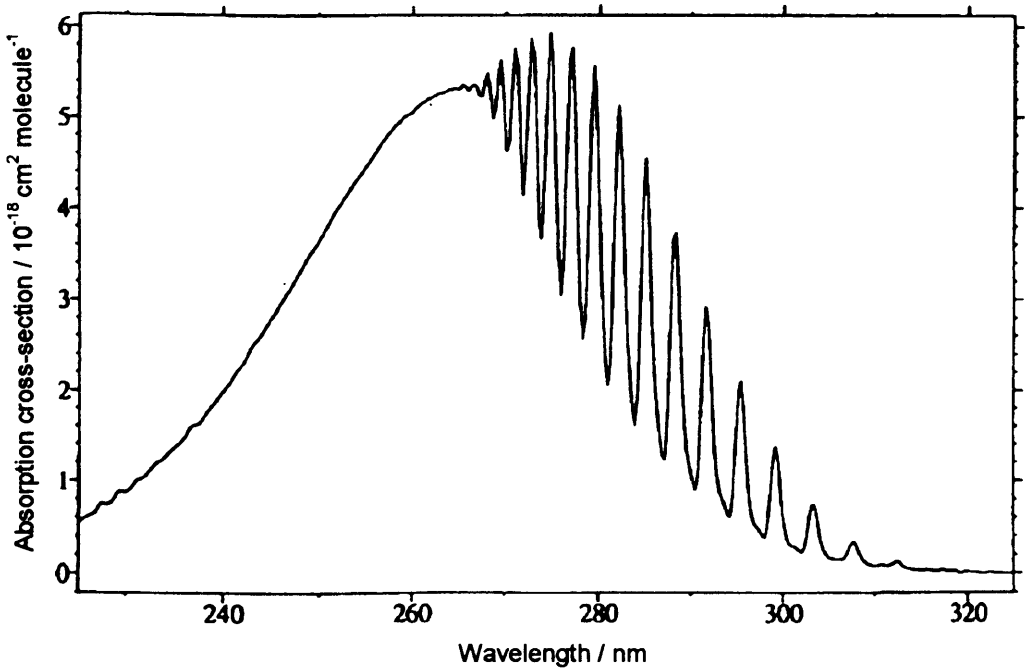

Figure 2. 1 Absorption cross-section of ClO.[1]

Figure 2. 1 clearly shows a portion of the spectrum ($\lambda < 270$ nm) with continuum absorption. This absorption results from excitation to an upper electronic state above the dissociation asymptote, as discussed in Section 2. 1. 2 below. At longer wavelengths ($\lambda > 270$ nm) the spectrum is banded resulting from absorption to discrete vibrational energy levels at energies below the dissociation limit.

Knowledge of suitable absorption cross-sections and application of the Beer-Lambert law (E2. 1) can be used to measure concentrations of absorbing species. However, absorption cross-sections are temperature, pressure, instrument function and resolution dependent. Given this, great care must be taken to make sure that cross-sections employed for a particular measurement are appropriate for those experimental conditions. The effect that the instrument function and resolution has on the measured cross-section is discussed in detail in Appendix 1 and in Chapter 6.

2. 1. 2 Fate of Excited Species

Absorption of a quantum of radiation by a species AB results in excitation of this species to form an excited molecule, AB*:

(2. 1) $AB + h\nu \rightarrow AB^*$

This excited state now faces one of a number of possible fates, many of which have atmospheric significance. These fates include dissociation, which results in fragmentation of AB*, luminescence (fluorescence or phosphorescence), which results in the re-emission of radiation or the species may undergo an internal energy transfer, an energy transfer in a collision or a chemical reaction.[2] The number of excited species, which undergo each pathway *per* photon absorbed, is defined as the quantum yield, ϕ, for that process. In atmospheric chemistry by far the most important of these processes is dissociation upon absorption of radiation, known as photolysis. If the energy of the absorbed photon or photons is greater than that of the bond energy of AB* then photodissociation will occur. This dissociation is said to be direct if absorption to a repulsive (non-bonding) upper state occurs. In this case, the observed spectrum would be continuous since photon energies need only equal or exceed the binding energy and not match specific quanta. Alternatively, absorption may initially occur to an upper state which is bound, followed by an internal conversion (IC) or an intersystem crossing (ISC) to a repulsive state which allows dissociation. In this case, some structural features may be apparent in the spectrum of the photolabile species.

The rate coefficient, J, for a photodissociation event is given by the product of local light intensity, I_λ, the absorption cross-section, σ_λ, and the quantum yield for that photodissociation, ϕ_λ, integrated over all wavelengths:

(E2. 2) $$J = \int_0^\infty I_\lambda \sigma_\lambda \Phi_\lambda d\lambda$$

2. 2 Gas Phase Kinetics

Many reactive species are produced in the atmosphere by photodissociation, and the nature and rapidity of their subsequent chemistry governs their atmospheric impact. Quantification of the reactivity of gas phase species *i.e.* kinetics, is discussed in the following section.

2. 2. 1 Fundamentals of Gas Phase Kinetics

For a generic species Q, in a gas phase chemical reaction, the extent of reaction, $\delta\xi$, is given by:

(E2. 3) $$\delta\xi = \frac{\delta n_Q}{\nu_Q}$$

where δn_Q is the change in number of moles of species Q in any reaction and ν_Q is the stoichiometric number for this species in the reaction. ν_Q is defined as negative for reactants and positive for products. Thus, considering the general reaction:

(2. 2) $$a\mathrm{A} + b\mathrm{B} \quad = \quad c\mathrm{C} + d\mathrm{D}$$

where a, b, c and d are the stoichiometric numbers for species A, B, C and D respectively, the extent of reaction can be expressed as:

(E2. 4) $$\delta\xi = \frac{\delta n_A}{-a} = \frac{\delta n_B}{-b} = \frac{\delta n_C}{c} = \frac{\delta n_D}{d}$$

The rate of reaction, $\tilde{r}$, is formally defined as:

(E2. 5) $$\tilde{r} = \frac{d\xi}{dt} = \frac{1}{\nu_Q} \cdot \frac{dn_Q}{dt}$$

Often it is convenient to refer to the intensive quantity (rate/volume) and consider this as the rate of reaction, r:

(E2. 6) $$r = \frac{1}{\nu_Q}\frac{d}{dt}\left(\frac{n_Q}{V}\right) = \frac{1}{\nu_Q}\frac{d}{dt}[\mathrm{Q}]$$

where [Q] is the concentration of any species Q.

Experimentally it is found that, for cases where product formation does not affect the reaction rate, the observed rate of reaction is given by:

(E2. 7) $$r = k_{obs}[\mathrm{A}]^{\alpha}[\mathrm{B}]^{\beta}$$

The observed rate coefficient, k_{obs} and the orders of reaction α and β, for species A and B respectively, cannot be predicted from the overall reaction rate but can be determined experimentally.

If however, the reaction proceeds *via* a series of known elementary or single step reactions, the overall rate equation may be predicted. In contrast to (E2. 7), the rate at which each elementary step proceeds *is* determined by the product of the reactant concentrations raised to the power of their stoichiometric number, known as molecularity, and the rate constant of the reaction, k. Hence, for example, if reaction (2. 2) is known to proceed by the elementary reactions (2. 3) and (2. 4) then a series of rate equations can be established, (E2. 8)-(E2. 10).

(2. 3) $\mathrm{A + B} \rightarrow \mathrm{AB}$

(2. 4) $\mathrm{AB} \rightarrow \mathrm{C + D}$

(E2. 8) $$-\frac{d[\mathrm{A}]}{dt} = -\frac{d[\mathrm{B}]}{dt} = k_{2.3}[\mathrm{A}][\mathrm{B}]$$

(E2. 9) $$\frac{d[\mathrm{AB}]}{dt} = k_{2.3}[\mathrm{A}][\mathrm{B}] - k_{2.4}[\mathrm{AB}]$$

(E2. 10) $$\frac{d[\mathrm{C}]}{dt} = \frac{d[\mathrm{D}]}{dt} = k_{2.4}[\mathrm{AB}]$$

If these differential equations are soluble then they can be used to measure the overall rate constant of the reaction from the time dependence of the concentrations of reactants A and B, or products C and D.

In many cases, in reaction sequences such as (2. 3)-(2. 4), AB is short lived and may therefore be described as a reactive intermediate. Consequently, the concentration of AB at any given time is small and invariant and as a result the following approximation may be made:

(E2. 11) $$\frac{d[\mathrm{AB}]}{dt} \approx 0$$

In this case, known as the steady state approximation, the overall rate of product formation can be expressed solely in terms of the primary reactant concentrations [A] and [B], since combining equations (E2. 9), (E2. 10) and (E2. 11) gives:

(E2. 12) $$\frac{d[\mathrm{C}]}{dt} = \frac{d[\mathrm{D}]}{dt} = k_{2.3}[\mathrm{A}][\mathrm{B}]$$

If exact solutions to the rate equations are not available then numerical integration can be employed to simulate species concentration as a function of time from the governing differential equations. In this case, reaction rate constants may be obtained from fitting simulated to observed temporal profiles, with variation of individual reaction rate constants to optimise the fit.

2. 3 Temperature Dependence of Reaction Rates

Rate coefficients for many gas phase reactions, including reactions shown to have atmospheric significance, can be dependent upon temperature and pressure as well as being perturbed by other species present. The effect temperature has on rate coefficients was first shown experimentally, in many cases, to take the form $k = Ae^{-B/T}$ where A and B are constants.[3] By considering the energetics of these reactions, suggesting that activated species were formed within the system and it was these species that reacted to form products, Arrhenius and van't Hoff stated that $B = E_a/R$, R being the gas constant and E_a the amount of energy required for the activated species to form from reactants. Thus, combination of these ideas and the empirical description of rate coefficients as a function of temperature resulted in the Arrhenius expression:[4]

(E2. 13) $$k = A\exp\left(\frac{-E_a}{RT}\right)$$

where E_a is the experimental activation energy and A is the pre-exponential factor.

Reactions involving radicals often have negative activation energies, resulting in a negative temperature dependence. Such behaviour is attributable to the formation of a reactive intermediate with an energetic barrier to products that lies lower in energy than the energy of the reactant entrance channel. Consequently, the rate coefficients of radical-radical reactions with negative activation energies become larger at low temperatures prevalent in the atmosphere.

2. 4 Theories of Reaction Rates

Several theories have been developed to account in detail for the dependencies of the rate coefficients that are observed, most of which give expressions similar to the Arrhenius expression. A number of these theories will now be summarised.

2. 4. 1 Bimolecular Reaction Theories

Simple Collision Theory (SCT) is the most basic model used to describe the behaviour of bimolecular gas phase rate coefficients with temperature. This model uses the kinetic theory of gases and treats reactant molecules as hard spheres, which only interact upon collision. The model will only allow a reaction to occur if the translational energy along a line centred through the spheres is greater than a critical 'activation energy', E_a. In effect, the model therefore deduces a collision frequency, and calculates the fraction of these collisions that results in reaction.

For the reaction:

(2. 5) $\quad A + B \quad \rightarrow \quad$ Products

By stating Z_{AB} as the collision frequency between A and B and F as the fraction of collisions with sufficient energy to react, SCT would therefore commence with the basic model:

(E2. 14) $$Rate = Z_{AB} \times F$$

Z_{AB} can be expressed, from kinetic theory, as:

(E2. 15) $$Z_{AB} = \sigma_{AB} \bar{v}_{AB} [A][B]$$

where σ_{AB} is the collisional cross-section, itself given by πd^2 where d is the sum of the reactant radii, $\bar{v}_{AB}$ is the relative mean velocity of molecules A and B given by $(8k_BT/\pi\mu)^{1/2}$, where k_B represents the Boltzmann constant, T is temperature and μ is the reduced mass of the reactants.

The fraction of molecules with sufficient energy to react, F, is determined by the Maxwell-Boltzmann energy distribution law, resulting in:

(E2. 16) $$F = \exp\left(\frac{-E_a}{RT}\right)$$

Consequently, combining (E2. 14)-(E2. 16) the expression for the rate becomes:

(E2. 17) $$Rate = \sigma_{AB}\bar{\nu}_{AB}\left\{\exp\left(\frac{-E_a}{RT}\right)\right\}[A][B]$$

Given that the rate equation for an elementary process A + B $\rightarrow$ Products is $Rate = k[A][B]$, this expression for the rate can be compared to the Arrhenius expression, which predicts an exponential temperature dependence of the bimolecular rate constant, k_{bi}:

(E2. 18) $$k_{bi} = \sigma_{AB}\bar{\nu}_{AB}\exp\left(\frac{-E_a}{RT}\right)$$

In this case, the pre-exponential factor is $\sigma_{AB}\bar{\nu}_{AB}$ and is predicted to have a weak temperature dependence, E_a is the energy threshold or activation energy for reaction. Experiments show that (E2. 18) usually overestimates k_{bi}. The discrepancies between experiment and theory arise since SCT does not consider steric factors of the collisions (molecules are not hard spheres) or the internal energy distribution of the reactants and products. Furthermore, SCT assumes that reactions occur instantaneously rather than over a finite time period. As an improvement to this hard sphere model, Transition State Theory (TST) or Activated Complex Theory (ACT) has been developed incorporating a more realistic description of bimolecular reactions.

By considering that the total energy of the reactants and products is a function of the atomic co-ordinates in each and every reacting species, improvements could be made to SCT. Taking the co-linear reaction A + BC $\rightarrow$ AB + C as a simple example, the potential energy of the system is a function of both the A...B and B...C co-ordinates.

This can be represented as a three-dimensional potential energy surface (PES) shown in Figure 2. 2 below.

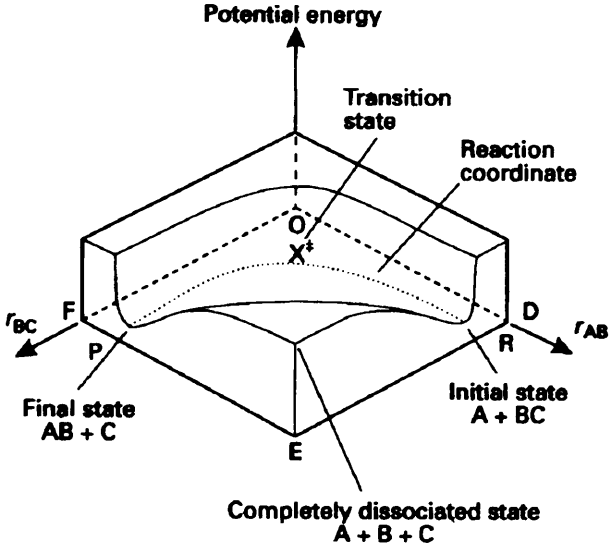

Figure 2. 2 Potential energy surface for the reaction A + BC → AB + C.[5]

As the reaction proceeds along the reaction coordinate the A...B separation decreases while the B...C bond weakens and consequently increases in length. This is accompanied by an increase in potential energy. At the 'saddle point' on the PES the separations A...B and B...C can be considered comparable. In this region, which will possess the greatest energy along the reaction coordinate, A...B...C can be considered a single entity know as the activated complex, and the point on the PES is known as the transition state. If the activated complex has enough energy to pass through this transition state towards products then the A...B separation will shorten resulting eventually in an A-B bond, lowering the energy. The B...C separation increases as C leaves the system.

TST interprets this motion across the PES as an equilibrium between reactants, A, BC and the activated complex, $ABC^{\ddagger}$. The overall rate of reaction is now expressed as the rate at which this transition state decomposes into products, AB and C, rate $k_{2.7}$.

(2. 6) $\quad A + BC \quad \leftrightarrow \quad ABC^{\ddagger}$

(2. 7) $\quad ABC^{\ddagger} \quad \rightarrow \quad AB + C$

(E2. 19) $$k_{bi} = \frac{d[\mathrm{AB}]}{dt} = k_{2.6}[\mathrm{A}][\mathrm{BC}] = k_{2.7}[\mathrm{ABC}^{\ddagger}]$$

Thus, in order to determine the overall rate of reaction it is necessary to calculate the rate of decay of the activated complex, $k_{2.7}$, and its concentration, $[\mathrm{ABC}^{\ddagger}]$.

For the activated complex to proceed through the product channel and consequently turn into products it needs to pass through the transition state. This can be viewed as having to undergo a critical vibration and thus the rate coefficient for this passage may be considered as equivalent to the critical vibrational frequency, υ. Since, realistically, not every oscillation may result in the activated complex passing through the transition state, the rate of decay is approximated by:

(E2.20) $$k_{2.7} = \kappa\nu$$

where κ, the transmission coefficient ($1 \geq \kappa \geq 0$), compensates for not every oscillation being critical.

Calculation of $[\mathrm{ABC}^{\ddagger}]$ makes use of the assumption that the reactants and activated complex are in equilibrium and hence the concentration of $\mathrm{ABC}^{\ddagger}$ is given by:

(E2. 21) $$[\mathrm{ABC}^{\ddagger}] = K[\mathrm{A}][\mathrm{BC}]$$

The equilibrium constant, K, between the activated complex and the reactants can be expressed in terms of total partition functions, Q_n, for reactants A and BC and the activated complex, $\mathrm{ABC}^{\ddagger}$, along with the Boltzmann constant, k_B, and the difference between the lowest energy levels in the reactants and the equivalent energy levels in the transition state, $\Delta\varepsilon_0$.

(E2. 22) $$K = \left(\frac{Q_{ABC^{\ddagger}}}{Q_A Q_{BC}}\right)\exp\left(-\frac{\Delta\varepsilon_0}{k_B T}\right)$$

Using this statistical expression for K the equilibrium concentration of $ABC^{\ddagger}$ becomes:

(E2. 23) $$[ABC^{\ddagger}] = \left(\frac{Q_{ABC^{\ddagger}}}{Q_A Q_{BC}}\right) \exp\left(-\frac{\Delta\varepsilon_0}{k_B T}\right)[A][BC]$$

The partition function of the activated complex $Q_{ABC^{\ddagger}}$ is given by the product of the partition function of the critical vibration Q_{RE}, taking the activated complex through the transition state, and the partition functions of the remaining non-critical oscillations, Q'.

(E2. 24) $$Q_{RE} = \frac{k_B T}{hc\omega_e}$$

Hence the overall partition function for the activated complex becomes:

(E2.25) $$Q_{ABC^{\ddagger}} = Q_{RE} Q' = \frac{k_B T}{hc\omega_e} Q'$$

Consequently (E2. 23) becomes:

(E2.26) $$[ABC^{\ddagger}] = \frac{k_B T}{hc\omega_e}\left(\frac{Q'}{Q_A Q_{BC}}\right) \exp\left(-\frac{\Delta\varepsilon_0}{k_B T}\right)[A][BC]$$

Combining (E2. 19), (E2. 20), (E2. 26) the overall expression for the rate constant for decay of the activated complex can therefore be expressed as:

(E2. 27) $$k_{bi} = \kappa\nu \frac{k_B T}{hc\omega_e}\left(\frac{Q'}{Q_A Q_{BC}}\right) \exp\left(-\frac{\Delta\varepsilon_0}{k_B T}\right)$$

which, given that $\nu = c\omega_e$ is simplified to the following expression:

(E2.28) $$k_{bi} = \kappa \frac{k_B T}{h}\left(\frac{Q'}{Q_A Q_{BC}}\right) \exp\left(-\frac{\Delta\varepsilon_0}{k_B T}\right)$$

Q_n may be calculated using statistical mechanics provided the rotational and vibrational constants are known. In practice, determining these parameters, spectroscopically, for polyatomic transition states is unfeasible. Consequently, quantum calculations of geometries of transition states are performed, and therefore spectroscopic constants are often used along with further assumptions in the theory to calculate k_{bi}.

To a first approximation, in the simplest cases where both reactants are monatomic, both SCT and TST simplify to the same expression. Thus, the existence of Arrhenius temperature dependencies of rate constants is accounted for by these theories.

If deviation from Arrhenius behaviour is observed experimentally, returning to TST but expressing the temperature dependence of each partition function as a power law results in the following modification:

(E2. 29) $$k_{bi} = A'T^{n} \exp\left(\frac{-E_a}{RT}\right)$$

This modified expression is likely to give rise to an improved parameterisation of the temperature dependent rate coefficients in cases where A has a strong temperature dependence and/or when large extrapolations are necessary.

2. 4. 2 Unimolecular and Termolecular Reaction Rate Theory

In contrast to pure bimolecular processes, which are often pressure independent, unimolecular (AB + M $\rightarrow$ Products) or termolecular (A + B + M $\rightarrow$ Products) reactions are usually pressure dependent, indicative of a mechanism including an additional species M. Such reactions also often exhibit a change in reaction order, further signifying a more complex mechanism.

The mechanism for the observed behaviour of unimolecular reactions, which show a change from second order at low pressure to limiting first order at high pressure, was first described by Lindemann.[6] The proposed mechanism suggested that unimolecular decomposition takes place *via* a series of elementary steps incorporating collisional

activation and deactivation of an energised species, in this example AB* in reactions (2. 8)-(2. 10).

(2. 8) $AB + M \rightarrow AB^* + M$

(2. 9) $AB^* + M \rightarrow AB + M$

(2. 10) $AB^* \rightarrow A + B$

where M is any surrounding molecule.

The theory makes the assumption that only the energised species will undergo a true elementary unimolecular reaction. Thus, the rate for the formation of products is given by:

(E2. 30) $$\frac{d[A]}{dt} = \frac{d[B]}{dt} = k_{2.10}[AB^*]$$

The rate for the describing the production and decomposition of the energised species AB* is given below. Since AB* may be considered a reactive intermediate this expression can be set equal to zero by application of the steady state approximation:

(E2. 31) $$\frac{d[AB^*]}{dt} = k_{2.8}[AB][M] - k_{2.9}[AB^*][M] - k_{2.10}[AB^*] = 0$$

therefore:

(E2. 32) $$[AB^*] = \frac{k_{2.8}[AB][M]}{k_{2.9}[M] + k_{2.10}}$$

substituting this into (E2. 30) gives:

(E2. 33) $$\frac{d[A]}{dt} = \frac{d[B]}{dt} = \frac{k_{2.10}k_{2.8}[AB][M]}{k_{2.9}[M] + k_{2.10}}$$

Considering (E2. 33) the observed change in reaction order as a function of pressure can be justified qualitatively.

In a low pressure regime ($k_{2.9}$ [M] << $k_{2.10}$) therefore,

(E2. 34) $$\frac{d[\mathrm{A}]}{dt} = \frac{d[\mathrm{B}]}{dt} = k_{2.8}[\mathrm{AB}][\mathrm{M}]$$

The rate of formation of A or B is second order and dependent upon pressure.

At high pressures ($k_{2.9}$ [M] >> $k_{2.10}$) leading to:

(E2. 35) $$\frac{d[\mathrm{A}]}{dt} = \frac{d[\mathrm{B}]}{dt} = \frac{k_{2.10}k_{2.8}[\mathrm{AB}]}{k_{2.9}}$$

The rate of reactant decay now tends towards limiting first order kinetics with a rate coefficient given by $\frac{k_{2.10}k_{2.8}}{k_{2.9}}$.

The pressure dependence of termolecular association reactions, which are third order and pressure dependent at low pressures and limiting second order and pressure independent at high pressures, may be described using a similar mechanistic scheme:

(2. 11) $\mathrm{A + B} \rightarrow \mathrm{AB^*}$

(2. 12) $\mathrm{AB^*} \rightarrow \mathrm{A + B}$

(2. 13) $\mathrm{AB^* + M} \rightarrow \mathrm{AB + M}$

If the steady state approximation is invoked once again for AB* the following expression for the rate of formation of AB is gained:

(E2. 36) $$\frac{d[\mathrm{AB}]}{dt} = \frac{k_{2.13}k_{2.11}[\mathrm{A}][\mathrm{B}][\mathrm{M}]}{k_{2.12} + k_{2.13}[\mathrm{M}]}$$

(E2. 36) is often expressed in terms of the termolecular rate constant, k_0, and the limiting high pressure bimolecular rate constant, k_∞:

(E2. 37)
$$\frac{d[AB]}{dt} = \frac{k_0 k_\infty [A][B][M]}{k_0[M] + k_\infty} \qquad k_0 = \frac{k_{2.13}k_{2.11}}{k_{2.12}}$$

$$k_\infty = k_{2.11}$$

Analogously to unimolecular dissociation at low pressures ($k_0[M] << k_\infty$) a pressure dependence is observed and at high pressures ($k_0[M] >> k_\infty$) the rate tends to a limiting value, k_∞. The form that this pressure dependence takes is shown schematically in Figure 2. 3 below.

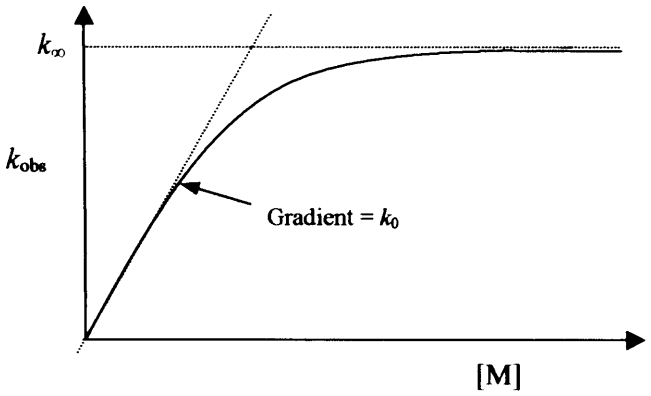

Figure 2. 3 Schematic diagram of the apparent second order rate coefficient, k_{obs}, as a function of [M]. The observed rate is third order at low pressures and tends to a limiting second order value at high pressures.

Discrepancies arise when theoretical results for the rate constant are compared to those generated experimentally, indicating a higher level of theory is required. The Lindemann mechanism overlooks that in reality the rates of formation and decomposition of the energised molecule, AB*, depend upon the internal degrees of freedom associated with AB*. A rigorous calculation of the overall rate constant should include a sum of rate coefficients for each vibrational and rotational energy level of AB* weighted to account for respective populations. These parameters have been included in an extension of the Lindemann mechanism developed by Rice, Ramsperger, Kassel and Marcus, RRKM theory.[7-9] RRKM theory can replicate experimental data to a high degree provided reliable thermodynamic constants can be acquired.

Accurate thermodynamic data are not, however, readily available for many reactive atmospheric species. As a result RRKM theory fails to predict rate coefficients reliably for reaction pathways involving these species. To address these problems Troe[10] demonstrated that the inclusion of a multiplying or 'broadening' factor, F, into expression (E2. 37), giving expression (E2. 38), results in a prediction of k that can replicate experimental data accurately as a function of pressure, over atmospheric pressure regimes.

(E2. 38) $$k_{ter} = \frac{k_0[\mathrm{M}]k_\infty}{k_0[\mathrm{M}]+k_\infty} \cdot F$$

where F is described by (E2. 39).

(E2. 39) $$F = F_c^{\left\{1+(\log_0\{k_0[\mathrm{M}]/k_\infty\})^2\right\}^{-1}}$$

F_c itself depends upon the specific reaction being considered although, in practice, when considering atmospheric reactions it is found that the value of 0.6 often results in an adequate description of k_{ter}. As a result, this value has been adopted by the NASA panel for data evaluation.[1]

2. 5 Summary

The field of photochemistry and kinetics has developed significantly in recent years. Theoretical tools have advanced to simulate accurately the behaviour of molecules' interaction with light or with other gas phase species. Fundamentally however, a test in these theories requires experiments that can monitor species concentration as a function of time. Principles of such experiments are considered in the following chapter.

2. 6 References

1. S.P. Sander, R.R. Friedl, D.M. Golden, M.J. Kurylo, R.E. Huie, V.L. Orkin, G.K. Moortgat, A.R. Ravishankara, C.E. Kolb, and M.J. Molina, *Chemical Kinetics and Photochemical Data for Use in Atmospheric Studies*, JPL Publication 02-25, Jet Propulsion Laboratory, Pasadena, CA, **2002**.
2. R.P. Wayne, *Chemistry of Atmospheres*, 3rd ed, **2002**, Oxford: Oxford University Press.
3. J.J. Hood, *Phil. Mag.*, **1878**, 6, 371.
4. S. Arrhenius, *Z. Phys. Chem.*, **1889**, 4, 226.
5. M. Pilling and P. W. Seakins, *Reaction Kinetics*, 1st ed, **1995**, Oxford: Oxford University Press.
6. F.A. Lindemann, *Trans. Faraday Soc.*, **1921**, 17, 598.
7. O.K. Rice and H.C. Ramsperger, *J. Am. Chem. Soc.*, **1927**, 49, 1617.
8. L.S. Kassel, *J. Phys. Chem.*, **1928**, 32, 255.
9. R.A. Marcus, *J. Chem. Phys.*, **1952**, 20, 359.
10. J. Troe, *J. Chem. Phys.*, **1977**, 66, 4745.

Chapter 3
Flash Photolysis with UV Absorption Spectroscopy

In order to monitor gas phase kinetics of reactive species successfully, an experiment must satisfy certain criteria. First, it is necessary to initiate the desired reaction, consequently the experiment needs to mix precursor gases and generate reactive species *i.e.* radicals/atoms. This reaction initiation must be followed by reactive species monitoring as a function of time. Thus, the monitoring technique must have a suitably fast temporal response, and in order to deconvolve initiation and subsequent reaction, radical generation must be on a timescale that is negligible to the reaction timescale. A further requirement for such experimental set-ups is the ability to control and measure reaction temperature and pressure. One such technique available, which satisfies all of these criteria, is flash photolysis coupled with time-resolved absorption spectroscopy.

This chapter describes the technique of flash photolysis coupled with UV absorption spectroscopy, which has been employed in the experiments for this dissertation. The technique offers many advantages when studying gas phase reactions of free radicals, such as those of importance in the atmosphere. Furthermore, the experimental set-up used for these experiments utilises a novel flash photolysis/UV absorption system that features charge coupled device (CCD) detection.

3. 1 The Flash Photolysis Technique

Flash photolysis employs an intense, short lived pulse of light, from a high-voltage flashlamp or a laser, to generate specific chemical species photolytically within a premixed gas mixture. These species may be generated directly, by photodissociation of precursor gases, or may be formed indirectly by subsequent rapid chemistry that has been photolytically induced. Regardless of the reactant source, it is crucial that the chemical species of interest are generated on a timescale that is negligible compared to their subsequent chemistry, so that formation and decay kinetics are decoupled, as shown schematically in Figure 3. 1. If this requirement is met, decay kinetics can be assumed correctly to represent only the reaction of the photolytically generated species of interest. Concentrations of, ideally, both reactants and products can be monitored using a variety of techniques and their temporal behaviour analysed to yield kinetic data.

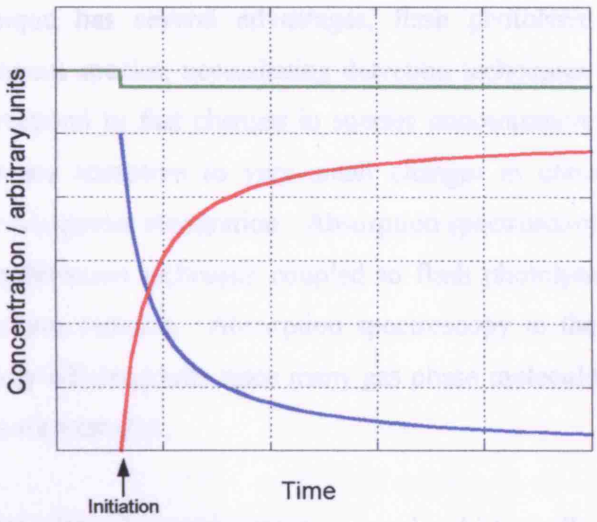

Figure 3. 1 Schematic representation of reactant (blue), product (red) and precursor (green) gas concentrations as a function of time in during a flash photolysis experiment.

In comparison to other techniques used for monitoring reactive gas species typical of the atmosphere, such as flow tubes, flash photolysis offers advantages. The use of premixed precursor gas mixtures overcomes problems with mixing and diffusion associated with flow systems. Such problems arise due to the necessity of using low pressures in flow tubes to attain rapid linear flow velocities. A further advantage of flash photolysis experiments is also, therefore, that they can be carried out over wide pressure ranges characteristic of the lower atmosphere. Also, since reacting species in flash photolysis experiments are generated throughout the reaction cell at moderate pressures, the possibility of cell wall reactions and associated heterogeneous loss of reactants are limited. A comparison of the main principles of real time techniques, such as flash photolysis, and the principles of elapsed time techniques, such as discharge flow, is given in Table 3.1 below.

Real time monitoring	Elapsed time monitoring
Rapid radical generation	Continuous radical generation
No mixing time	Mixing time required
High pressure (> 50 Torr)	Low pressure (< 10 Torr)
No wall reactions	Wall reactions likely

Table 3. 1 Comparison of the main principles of real time and elapsed time experimental techniques for measuring reaction kinetics.

Whilst the technique has several advantages, flash photolysis requires real time monitoring of transient species, necessitating detection techniques with response times rapid enough to respond to fast changes in species concentration. It is desirable that detection systems are receptive to very small changes in concentration and allow specific, unequivocal species recognition. Absorption spectroscopy fulfils these criteria and is a common detection technique coupled to flash photolysis when investigating reactions between free radicals. Absorption spectroscopy in the UV/visible spectral region is particularly advantageous since many gas phase molecules undergo electronic transitions at these wavelengths.

Time-resolved UV/visible absorption spectroscopy has historically been the monitoring tool chosen to accompany flash photolysis. In this work the monitoring of such absorption has advantages over previous work. Thus, a brief history of the technique and improvements undertaken since its inception is given below.

3. 1. 1 Historical Development

The flash photolysis/UV absorption technique was developed in the late 1940s and early 1950s by Porter, Norrish and co-workers in Cambridge.[1, 2] Early incarnations of the technique made use of ex-Royal Navy submarine capacitors charged to high voltages to power rare-gas flashlamps, illuminating the reaction vessel. Following a short delay, a second lamp was used to provide a pulsed analysis beam, which passed through the reaction vessel and into a spectrograph. From the spectrograph, wavelength-resolved light was imaged across a glass photographic plate. The delayed second light pulse afforded the time resolution of the experiment as, in successive experiments, it was initiated at different known delay times after the photolysis pulse. The intensities recorded onto the photographic plates were converted manually into absorptions by measuring the degree of darkening across the plates in comparison to an exposure recorded in the absence of the initial photolysis flash. A temporally resolved absorption profile could be built up by repeated experiments with varying delay times between photolysis and analysis pulses.

The development of electronic photodetectors, such as photomultiplier tubes (PMTs), permitted continuous, real time electronic monitoring of transmitted light intensity.[3]

Consequently, a continuous analysis beam could replace the pulsed analysis beam and a single experiment could produce an entire temporal decay profile. The analysis beam passed through the reaction cell and a single wavelength, selected by a monochromator, was imaged onto the PMT. Simultaneous monitoring of multiple wavelengths was however, prevented by the PMTs inability to distinguish between photons arriving at differing positions on the detector window, added to the physical size of the window relative the dispersion plane of typical spectrographs. Single wavelength monitoring compromised the ability to distinguish between multiple absorbing species resulting in corrections to kinetic analysis or repeated experiments to build up an absorption profile of the reacting mixture. Nonetheless, PMTs offer substantial advantages over the use of photographic plates and are widely used as photodetectors today.

In recent years, the advent of photodiode array detectors has allowed light intensity to be monitored with both temporal and spectral resolution. These detectors consist of a series of small, light-sensitive, pixels, which can be placed in the dispersive plane of the spectrograph. Diode array detection offers advantages when used in flash photolysis experiments. The ability to detect wavelength-resolved signal offers the opportunity to monitor multiple absorbing species. Additionally, the monitoring of whole absorption bands, as opposed to single peaks, improves the signal to noise ratio of experiments resulting in a more accurate determination of species concentration and consequently better constrained kinetic data. The time resolution for these experiments however, is limited by the readout time of the array, which for a linear array is typically milliseconds. Reactions that occur on faster timescales may still be studied by coupling the arrays to fast gating systems permitting time-resolved 'snapshots' of the spectrum at a certain time after photolysis. Multiple photolysis pulses are therefore required to build up a temporal profile, reminiscent of the photographic plate experiments.

Experiments described in this thesis have employed a two-dimensional light sensitive array, a charge coupled device (CCD), in order to overcome the limitations associated with both PMT and single dimension photodiode detection. Use of CCD detection maximises the quality and amount of information recorded in each experiment.[4] As with the photodiode array, the CCD consists of light sensitive pixels that convert incident light to photocharge. However, unlike the photodiode array, the CCD permits rapid and efficient transfer of charge across the device to a storage region, which is read

out later. It is now the rate of this charge transfer that limits the experimental time resolution and this is on a microsecond timescale. Since the data are not read until the entire storage region is full the read out process can occur on a much slower timescale and not compromise the efficiency of detection. A summary of the detection systems coupled to flash photolysis and their capability is given in Table 3. 2. The experimental set-up employed for experiments described in this thesis is discussed below.

Detection	Time resolution	Wavelength resolution	Read out
Photographic plates	×	✓	Manual
PMTs	✓	×	Electronic
Diode arrays	×	✓	Electronic
CCD	✓	✓	Electronic

Table 3. 2 Comparison of the different detection techniques often coupled to flash photolysis.

3. 2 Flash Photolysis Including Two Dimensional Array Detection

3. 2. 1 Charge Coupled Devices

CCDs are able to convert incident light into photocharge, and to move these charges rapidly and efficiently around the device. The 2-dimensional array consists of a grid of metal oxide semiconductor detector elements or pixels embedded into a silicon substrate. Each pixel can convert incident light into photocharge, which is then stored in an electrically generated potential well within the pixel. The quantum efficiency (QE) of this light-to-charge conversion is maximised around 700 nm, with a value of approximately 60%. Thus, to enable efficient detection of wavelengths below 400 nm, the pixels are covered in a fine phosphor coating. The coating luminesces when irradiated by radiation of wavelengths 180-400 nm, resulting in a QE of approximately 20%. The time resolution of the device remains undistorted since the coating has a fluorescence lifetime on the order of nanoseconds. Moreover, the thickness of the coating is negligible (0.3 μm) compared to the size of the pixel (22.5 μm square) thus preventing any significant cross talk between adjacent pixels.

The photocharge generated on the device can be moved from pixel to pixel along the axis of the array. Transfer is induced by applying a suitably phased voltage to a series of parallel electrodes aligned on the surface of the device, perpendicular to the axis of charge transfer. This process is shown schematically in Figure 3. 2 below.

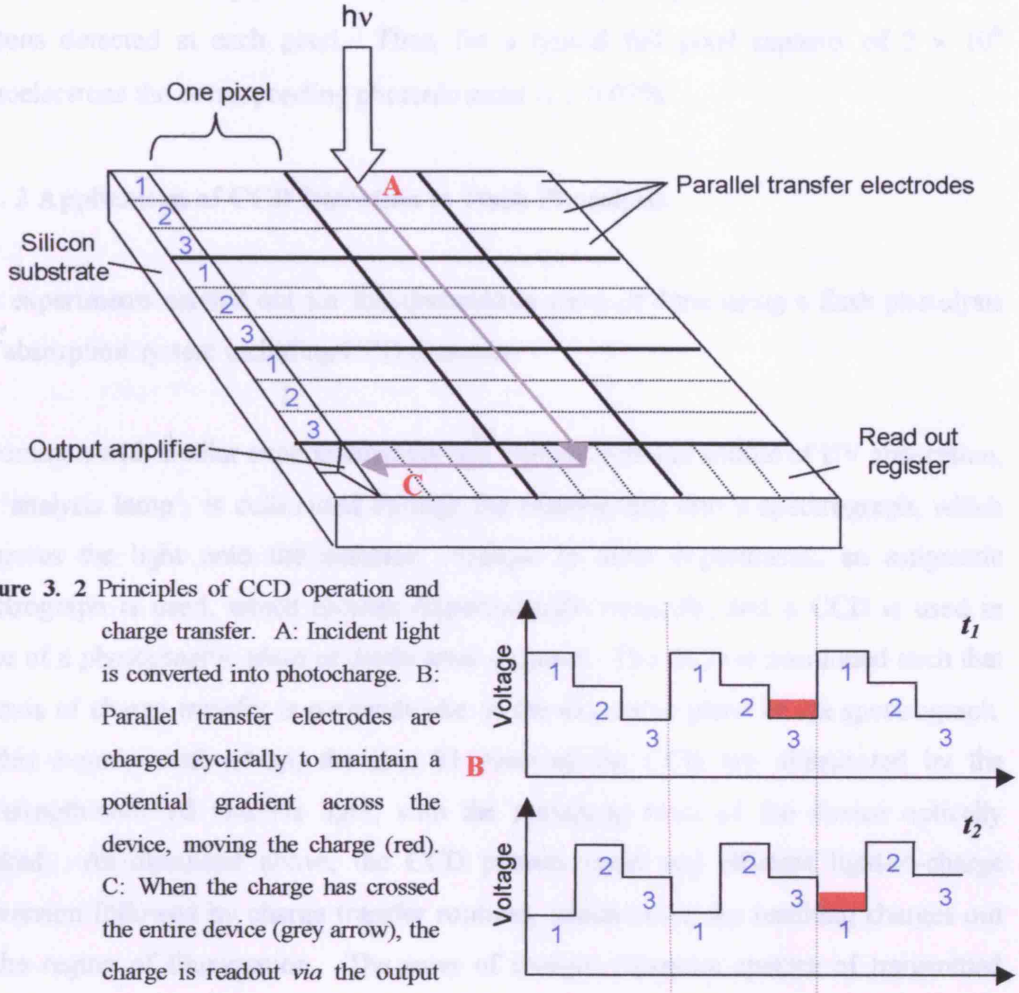

Figure 3. 2 Principles of CCD operation and charge transfer. A: Incident light is converted into photocharge. B: Parallel transfer electrodes are charged cyclically to maintain a potential gradient across the device, moving the charge (red). C: When the charge has crossed the entire device (grey arrow), the charge is readout *via* the output amplifier. Adapted from Rowley *et al.*[4]

The efficiency of each charge transfer typically exceeds 99.9999% *per* transfer, and transfer rates of up to 1 MHz (*i.e.* 1 μs time resolution) are feasible. Importantly, whole rows of photocharge are transferred simultaneously.

One of the major sources of noise for CCD detectors is dark current. This is produced within the CCD itself, arising from thermal electron-hole formation. The degree of dark current, and therefore spurious image, formed is reduced by Peltier cooling the device to

200 K. Additionally, housing the detector within a vacuum thermally isolates the device. Any remaining dark current must be recorded for each pixel prior to exposure and subtracted from measured light intensities. Another main source of noise is photonic noise, inherent to the incident light intensity. As photon flux typically exhibits a Poisson distribution, photonic noise is equivalent to the square root of the number of photons detected at each pixel. Thus, for a typical full pixel capacity of 2×10^6 photoelectrons the corresponding photonic noise is $\pm$ 0.07%.

3. 2. 2 Application of CCD Detection to Flash Photolysis

The experiments carried out for this dissertation were all done using a flash photolysis UV absorption system including CCD detection.

In common with similar experimental set-ups, output from the source of UV absorption, the 'analysis lamp', is collimated through the reaction cell into a spectrograph, which disperses the light onto the detector. Unique to these experiments, an astigmatic spectrograph is used, which focuses dispersed light vertically, and a CCD is used in place of a photographic plate or diode array detector. The CCD is positioned such that the axis of charge transfer is perpendicular to the dispersive plane of the spectrograph. In this experimental set-up, the first 31 rows of the CCD are illuminated by the wavelength-resolved analysis light, with the remaining rows of the device optically masked. As discussed above, the CCD permits rapid and efficient light-to-charge conversion followed by charge transfer routines, which move the resulting charges out of the region of illumination. The rows of charges represent spectra of transmitted intensity and rapidly moving rows down the CCD allows the acquisition of sequential spectra of the reaction mixture. This continuous process occurs until the full length of the CCD has been completed, wherein the first row of charges has reached the end of the device. On completion of charge transfer the recorded charges are readout, from the device to a computer, on a much slower timescale. The entire charge transfer process takes place between the opening and closing of a mechanical shutter in the analysis beam. The time between each charge transfer is known as the shift time or the (reciprocal of the) clocking rate. This time is selected prior to the experiment and the clocking axis represents the time-resolved axis of the detector, as shown in Figure 3. 3.

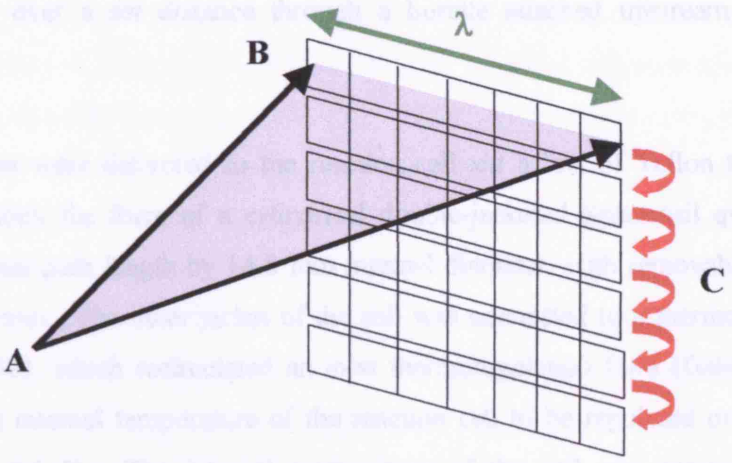

Figure 3. 3 Use of the CCD during kinetic experiments. A: Wavelength-resolved light from the spectrograph is imaged across the top 31 rows of the CCD array (one row shown for clarity); B: Incident light generates photocharge at the device; C: Rapid and efficient charge transfer permits recording of sequential spectra.

Incorporation of CCD detection into the flash photolysis experiment therefore confers the advantages of the wavelength coverage of a diode array without the associated loss of time resolution. Consequently, the CCD affords the recording of sequential spectra of the reaction mixture before, during and after photolysis in a single experiment.

3. 3 Description of the Flash Photolysis Experiment

3. 3. 1 Gas Handling

All gases were mixed with a carrier gas flow in a Pyrex mixing line equipped with Teflon taps (Young and Co.) prior to arrival at the reaction cell. The mixing line consisted of a cylindrical vessel with gas injectors at regular intervals, aligned against the carrier gas flow to ensure efficient mixing. Precursor gases were introduced directly to a carrier gas from pure or diluted mixtures in cylinders or, for vapours of condensed phase reagents, were taken up in a slow flow of carrier gas passed through a bubbler or a trap. Non-corrosive gases were passed into the mixing line, at known, set, flow rates, using mass flow controllers (MKS). Flow rates of corrosive gases were controlled using Teflon needle valves and measured using glass ball meters. Flow controllers and meters were routinely calibrated between experiments by measuring the flow rate of a

single bubble over a set distance through a burette attached upstream of a given controller.

Premixed gases were delivered to the reaction cell *via* a line of Teflon tubing. The reaction cell took the form of a cylindrical double-jacketed Spectrosil quartz vessel, 98.2 cm internal path length by 14.8 mm internal diameter, with removable Spectrosil quartz end pieces. The inner jacket of the cell was connected to a thermostatting unit (Huber, CC180), which recirculated an inert thermoregulation fluid (Galden, HT110) permitting the internal temperature of the reaction cell to be regulated over the range (206-373) ± 0.5 K. The internal temperature of the cell was measured using a ceramically enclosed, platinum resistance thermometer (Farnell, PT100), the internal temperature profile of the cell is discussed in detail in Appendix 2. The outer jacket and the end pieces of the reaction cell could be connected to a rotary pump and evacuated to improve thermal insulation and prevent any build up of condensation when operating at low temperatures. Experiments could be conducted over a pressure range, typically 100 to 760 Torr, by connecting the reaction cell exhaust to a rotary pump. The pressure within the cell was continuously monitored using a capacitance manometer (MKS Baratron).

During experiments, the gas mixture flowed continuously and slowly through the reaction cell ensuring a fresh gas mixture for each photolysis experiment. The timescale of this flow was much longer than the timescale of any of the kinetic processes being monitored.

3. 3. 2 Radical Generation

Free radicals and atoms were generated in the reaction cell *via* rapid photolysis. One of two photolysis sources could be employed to initiate photolysis, either a flashlamp or a laser. Flashlamp photolysis is described here and laser flash photolysis, implementation of which formed part of this work, is described in Section 3. 6. The flashlamp source was a 1m long xenon arc lamp (Perkin Elmer, QDX66) filled to a pressure of 50 Torr. This lamp was placed adjacent and parallel to the reaction cell, at an adjustable distance, typically held at 10 cm. Attenuation of short wavelength ($\lambda < 280$ nm) radiation could

be achieved by housing the lamp in a Pyrex jacket or by filling the outer jacket of the reaction cell with a suitable absorbing liquid or gas. The lamp was powered by a 25 kV, 2.6 μF rapid discharge capacitor (NWL Ltd.). This capacitor was charged to typically 20 kV by a high voltage power supply (Glassman High Voltage Ltd., EH100). Application of this voltage to the flashlamp initiated spontaneous breakdown in the lamp resulting in a flash. Thus, to control flash firing, a spark gap (EG&G, GP12B) isolated the flashlamp from the charged capacitor until triggering was required, thus preventing uncontrolled firing. Ionisation of the spark gap was controlled by a trigger module (EG&G, TM11A), which was itself initiated by a TTL pulse, converted into an optical pulse, from the control computer. The trigger module and computer were connected *via* an isolated fibre optic cable. The pulse energy of the flashlamp, typically 500 J, was completely discharged within 20 μs.

The reaction cell and flashlamp were contained within a fully sealed aluminium box, minimising escape of light. The box was earthed away from the CCD electronics to reduce radiofrequency interference. The steel box that enclosed the flashlamp circuit was earthed to the same point. Any electrical leads into these boxes were screened and integrity maintained with the earthed boxes at the interfaces. Mains power was supplied from a filtered unit, *via* a mains conditioner.

3. 3. 3 Species Monitoring

Transient species within the reaction vessel were characterised and monitored using UV absorption spectroscopy. Two possible sources of analysis light could be employed. For work in the wavelength region 200-300 nm a 30 W high-brightness deuterium lamp (Hamamatsu, L5499) was used and for higher wavelengths a 70 W continuous xenon arc lamp (Hamamatsu, L2174) was employed. A smoothed power supply unit powered both lamps. The deuterium lamp was situated along the analysis axis. The xenon lamp was positioned at 90° to the analysis axis and output was thus directed through the reaction cell using a high reflectivity mirror. A Spectrosil quartz lens collimated the lamp output, which was directed along the length of the cell before being focused, by a further lens, into the variable width entrance slit of a 25 cm focal length astigmatic

Czerny-Turner spectrograph (Chromex). The spectrograph subsequently imaged the wavelength-resolved light onto the CCD detector (Wright Instruments Ltd.).

The spectrograph was fitted with three interchangeable diffraction gratings, ruled at 600, 300 and 150 grooves/mm respectively. The gratings, along with the size of the detector array, gave rise to spectral coverages of approximately 30, 60 and 120 nm respectively. Each spectral coverage had an associated limiting dispersion (wavelength *per* pixel), which were determined to be 0.11, 0.22 and 0.45 nm correspondingly. The instrument function (the resolution) of the spectrograph was measured for each grating over a range of entrance slit widths, from 10-1000 μm. For each grating the spectrograph was wavelength and dispersion calibrated using spectral lines from a mercury pen-ray lamp, as described in Appendix 3.

The CCD consisted of a 298 (columns) × 1152 (rows) array of light sensitive pixels mounted within a Peltier cooled camera head. The camera head was attached to the spectrograph *via* a flange, allowing precise and repeatable alignment. The short axis of the array (perpendicular to the axis of charge transfer) was aligned in the dispersive plane of the spectrograph, representing the wavelength-resolved axis. Wavelength-resolved light from the spectrograph illuminated the top 31 rows of the device and the remaining rows were masked. The effect that the illumination of 31 rows as opposed to just one row has on the temporal resolution of each experiment is considered in Section 3. 5. 1. An optical shutter was situated in the optical line to prevent accumulation of photocharge between experiments. A schematic diagram of the experimental set-up employed during these experiments is given in Figure 3. 4 below.

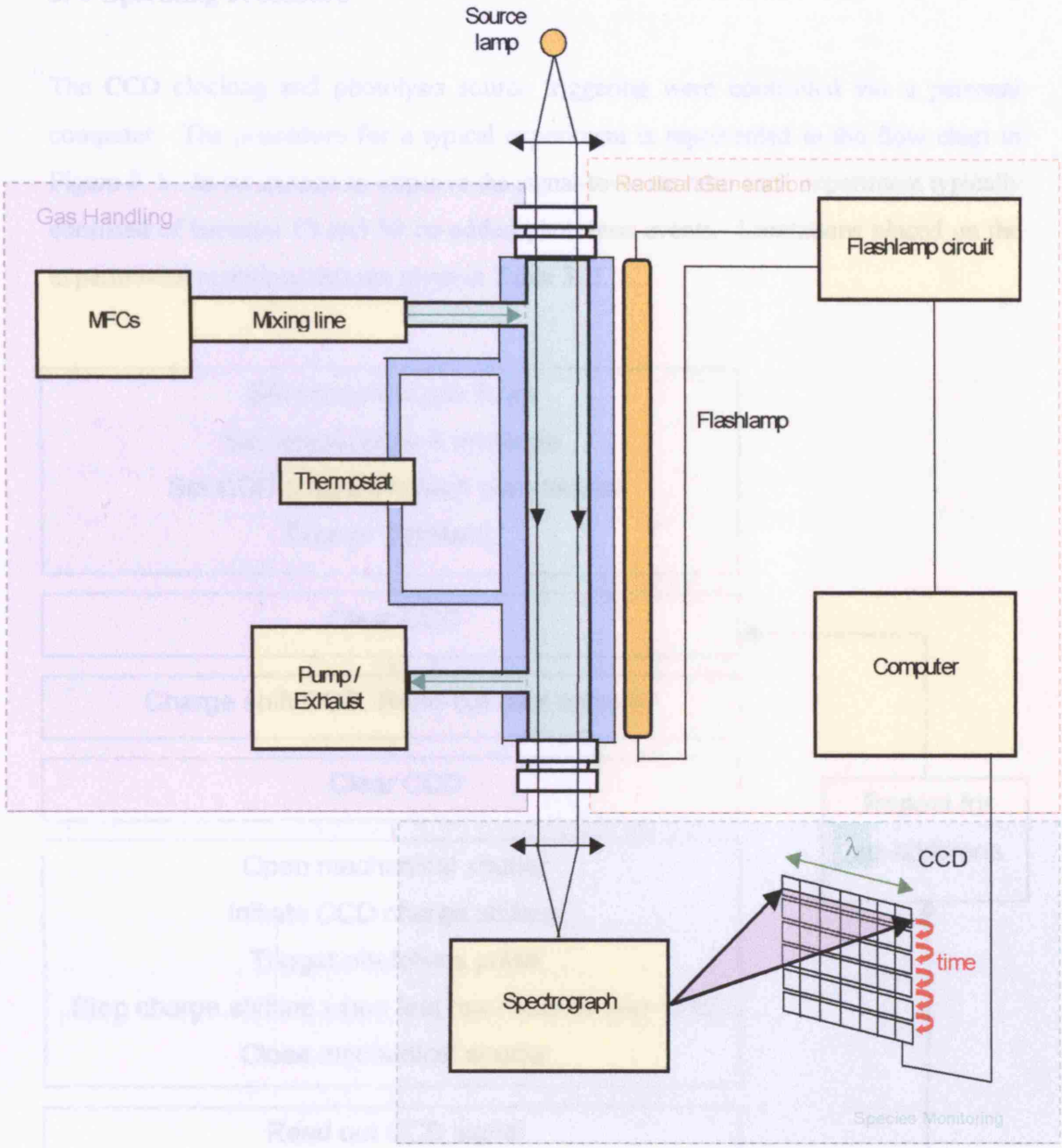

Figure 3. 4 Schematic diagram of the flash photolysis/UV absorption apparatus incorporating CCD detection used in this work.

3. 4 Operating Procedure

The CCD clocking and photolysis source triggering were controlled *via* a personal computer. The procedure for a typical experiment is represented in the flow chart in Figure 3. 5. In an attempt to improve the signal-to-noise ratio each experiment typically consisted of between 10 and 50 co-added photolysis events. Limitations placed on the experimental repetition rate are given in Table 3. 3.

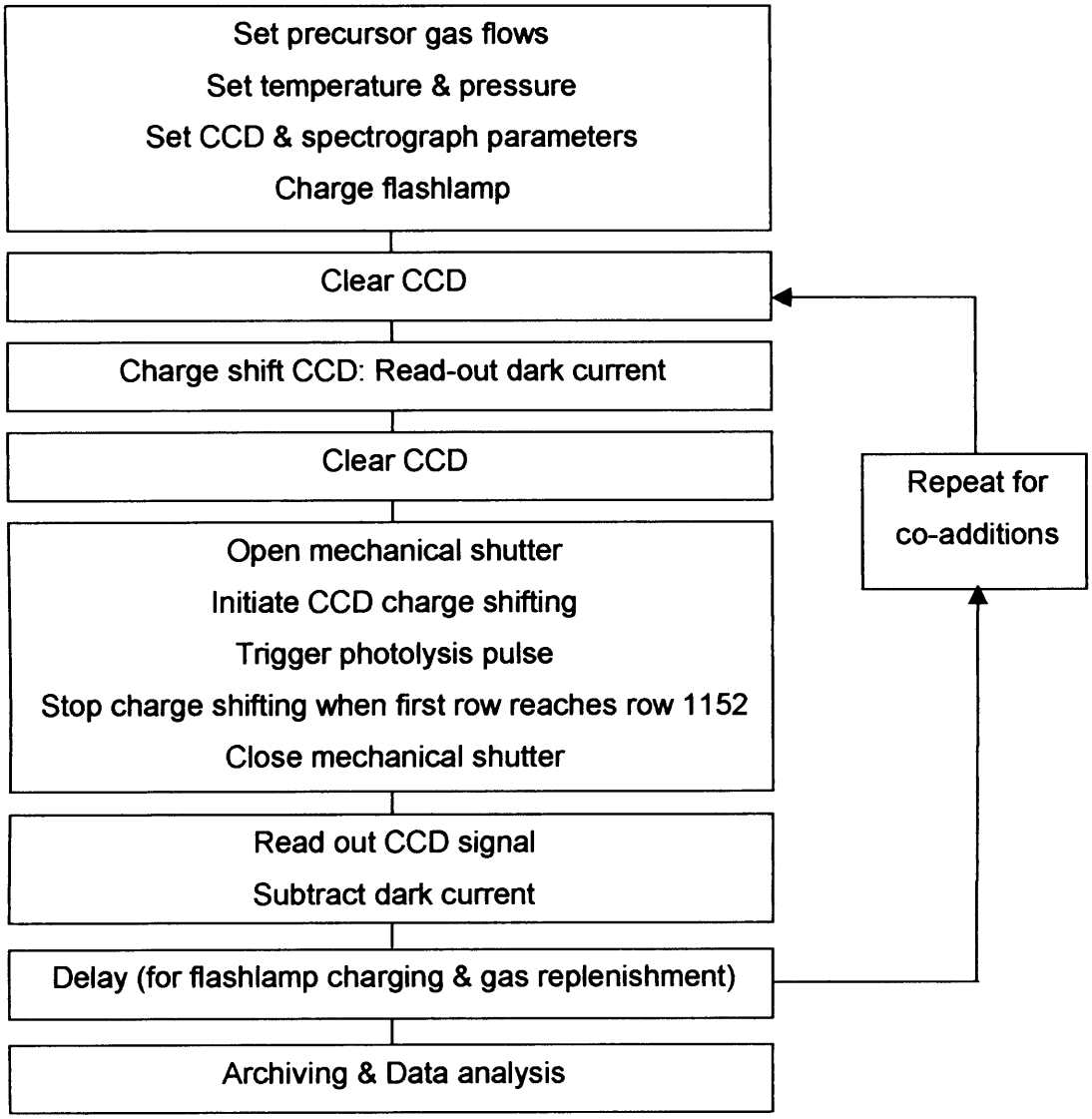

Figure 3. 5 Flowchart indicating operating procedure of a typical flash photolysis experiment.

Procedure	Approx. operation time / s
CCD read out	3
Gas replenishment	4-20 (flow dependent)
Capacitor recharge	15

Table 3. 3 Approximate timescales for experimental procedures.

3. 5 Analytical Procedures

For each kinetic experiment it was possible to generate a wavelength-resolved absorption spectrum for every time-resolved row on the CCD before, during and after photolysis. The charge, or light intensity, recorded on every pixel was related to absorbance of the reaction mixture at a given wavelength and time through application of the Beer-Lambert law:

(E3. 1) $$A_{\lambda,t} = \ln\left(\frac{\langle I_{0(\lambda,t)}\rangle}{I_{t(\lambda,t)}}\right)$$

where, for a given wavelength, λ, and time, t, A is absorbance, $\langle I_{0(\lambda,t)}\rangle$ is the average pre-photolysis intensity, and $I_{t(\lambda,t)}$ is the intensity at time t. Consequently, absorption spectra, calculated in this way, represent the change in absorbance brought about due to the photolysis pulse and subsequent chemistry. Preparation of sequential spectra allowed observation of changes in absorbance as a function of time.

The charge shifting routine employed by the CCD imparted a small complication upon this simple analysis. As a row of signal is shifted down the CCD, a small amount of additional charge, so called 'dark current', is acquired. This is a cumulative effect, consequently, in a given run, early data points will pick up more current than later points as these early points travel further along the length of the CCD. Uncorrected, this effect would result in a spurious apparent decrease in time-resolved intensities. Thus, by performing an identical experimental run but omitting the photolysis flash, known as a 'non-flashed' run, this phenomenon could easily be corrected by subtraction the results of this non-flashed experiment from the flashed experiment according to equation (E3. 2).

(E3. 2) $$A_{\lambda,t} = \ln\left(\frac{\langle I_{0(\lambda,t)}\rangle}{I_{t(\lambda,t)}}\right)_{\text{flashed}} - \ln\left(\frac{\langle I_{0(\lambda,t)}\rangle}{I_{t(\lambda,t)}}\right)_{\text{non-flashed}}$$

This type of correction was typically of the order 1×10^{-4} absorbance units (1/100 of typical initial experimental absorbance).

A further correction to data recorded by the CCD resulted from the simultaneous illumination of 31 rows of the device in experiments. This correction took place following conversion of the time-resolved absorbance to concentration, described in the following section, and details of the correction are presented subsequent to this.

3. 5. 1 Determination of Species Concentration

The absorbance of a gaseous mixture can be related to the concentrations of its components *via* the Beer-Lambert law:

(E3. 3) $$A_{\lambda} = \sum_{i} \sigma_{i}(\lambda)[i]l$$

where for species i, at wavelength λ, absorbance, A, is given by the product of the wavelength dependent absorption cross-section, $\sigma_i(\lambda)$, concentration, $[i]$, and the optical path length, l.

Experimental species concentration was determined by fitting known absorption cross-sections to experimental absorbance spectra, taking into account the known optical path length. This procedure was applied to each absorbance spectrum at every time point, hence the temporal concentration profile of multiple transient absorbers could in principle be determined. In practice, this process is often complicated by similarities and overlap of UV absorption of the species present in the wavelength region of interest. These problems can be overcome and an unequivocal and high signal-to-noise detection achieved if one or more absorbing species possess structural spectral features, as is the case with halogen monoxides. In these cases *differential* spectroscopy can be employed to isolate the unique structural features in the absorption spectrum and use the

magnitude of these features to quantify the absorbance. High-pass filtering the observed experimental spectrum isolates spectrally structured features. Analogous filtering of the reference absorption cross-section of the structured species can be used to generate a 'fingerprint' reference spectrum solely attributable to the structured species. Least squares fitting of the filtered reference spectrum to the filtered absorption cross-section then determines a factor, f, where:

(E3. 4) $$f = \text{concentration} \times \text{optical path length}$$

The concentration of the structured species can, in this way, be uniquely determined without spectral knowledge of other species present. Figure 3. 6 illustrates the method of differential fitting diagrammatically.

Differential spectroscopy gives rise to unequivocal identification and accurate quantification of structured absorbers in a manner that is unaffected by other absorbing species in overlapping wavelength regions. Furthermore, through subtraction of the quantified structured absorbance, deconvolution of the spectra is permitted revealing any other absorbance due to other smooth absorbers below the structure. If required, further fitting routines can be applied to quantify these spectrally smooth absorbers.

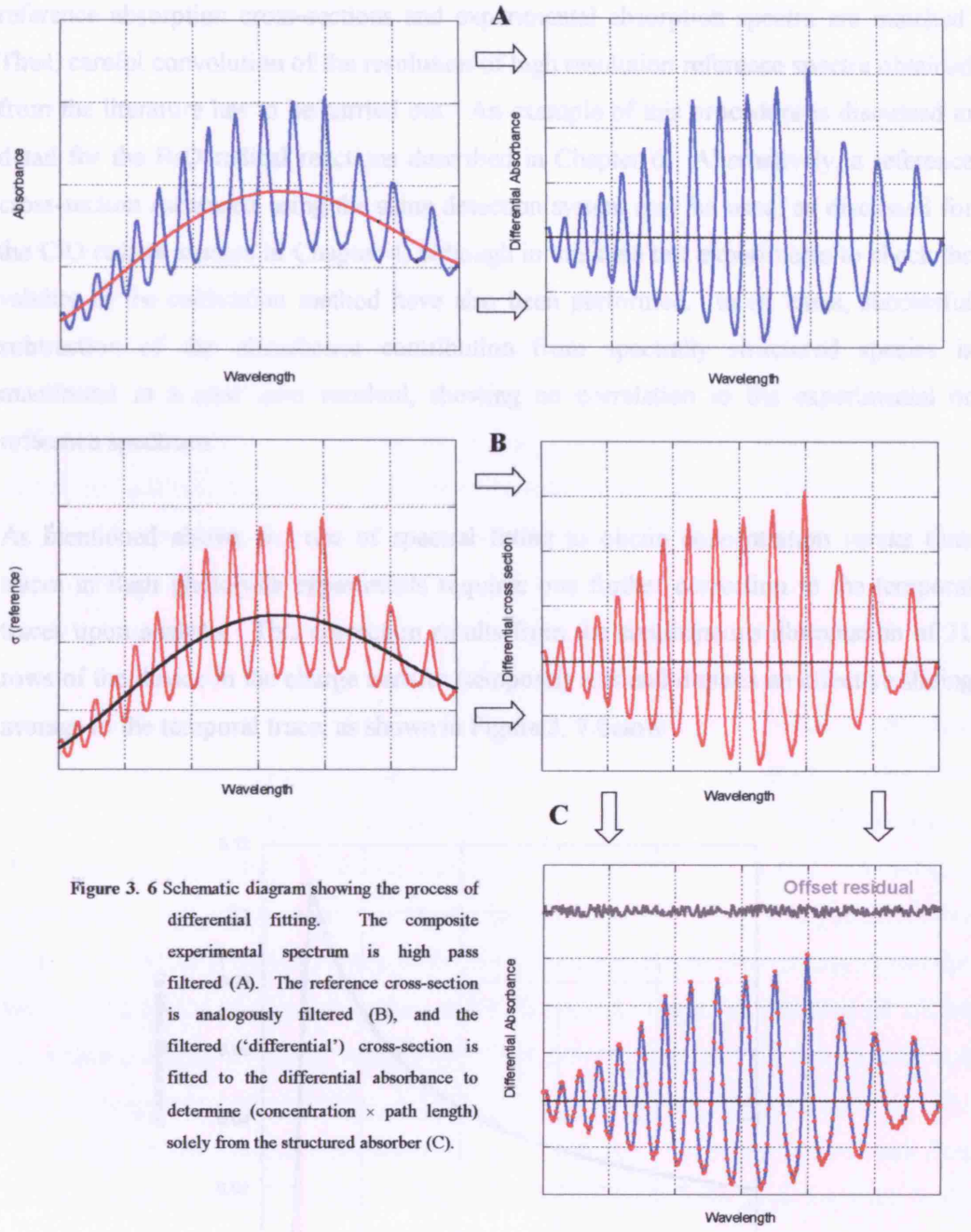

Figure 3. 6 Schematic diagram showing the process of differential fitting. The composite experimental spectrum is high pass filtered (A). The reference cross-section is analogously filtered (B), and the filtered ('differential') cross-section is fitted to the differential absorbance to determine (concentration × path length) solely from the structured absorber (C).

It is often the case that absorption cross-sections are taken from reference studies found in the literature. These studies will have been carried out using different equipment with differing instrument functions and potentially at much higher resolutions than in this experimental set-up, where a compromise between resolution and wavelength coverage needs to be invoked. Since absorption cross-sections of structured spectral features are highly resolution dependent it is imperative that the resolution of the

reference absorption cross-sections and experimental absorption spectra are matched. Thus, careful convolution of the resolution of high resolution reference spectra obtained from the literature has to be carried out. An example of this procedure is discussed in detail for the BrO radical reactions described in Chapter 6. Alternatively, a reference cross-section measured using the same detection system may be used, as discussed for the ClO radical studies in Chapter 4, although in this case test experiments to check the validity of the calibration method have also been performed. In all cases, successful subtraction of the absorbance contribution from spectrally structured species is manifested in a near zero residual, showing no correlation to the experimental or reference spectrum.

As mentioned above, the use of spectral fitting to obtain concentration *versus* time traces in flash photolysis experiments requires one further correction to the temporal traces upon analysis. This correction results from the simultaneous illumination of 31 rows of the device in the charge transfer (temporal) axis and imparts an effective sliding average to the temporal trace, as shown in Figure 3. 7 below.

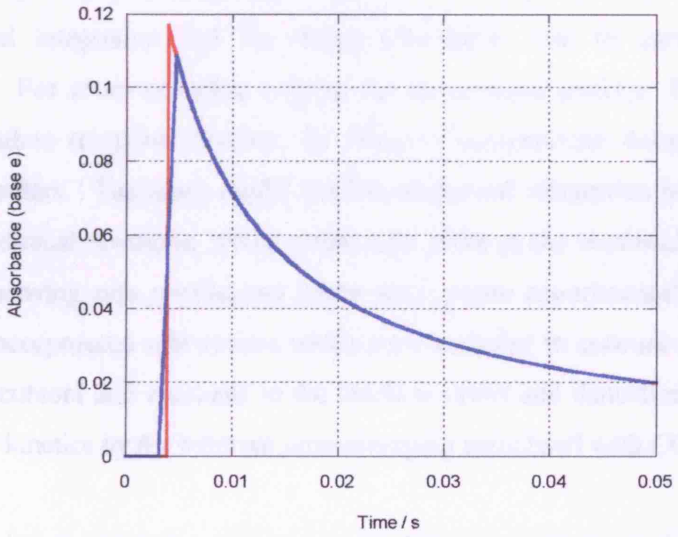

Figure 3. 7 The effect of 31 row sampling at the CCD. Simulated absorbance *versus* time trace (red) along with the temporal distortion to simulated trace imparted by temporal averaging from simultaneous illumination (blue).

Kinetic analysis of such concentration *versus* time traces, derived from recorded absorbances as described above, takes account this effect by applying an identical averaging effect to the classical or analytical solution of the relevant rate equations, discussed below.

3. 5. 2 Kinetic Analysis

Once species concentration *versus* time traces were generated, using the analytical procedures described above, kinetic analysis was carried out to determine the elementary rate constants governing the overall reaction. Where possible, and made easier by determination of unequivocal concentrations, classical solutions to the differential rate equations describing the overall reaction were derived. Such a solution is fitted to the observed kinetics, minimising the sum of squares between experimental and simulated traces by varying the rate constant of interest. In more complex chemical systems however, the resulting suite of differential equations became insoluble and use of numerical integration techniques became necessary in order to simulate observed decays. Again, least squares fitting of simulated to observed concentration *versus* time profiles subsequently permitted determination of kinetic parameters. For simple cases, the numerical integration and the fitting procedures may be carried out using a spreadsheet. For more complex systems the commercial package FACSIMILE[5] was used to simulate temporal profiles, fit these to experimental decays and determine kinetic parameters. The input model used in numerical integration included all known gas phase chemical reactions, which could take place in the chemical system used and their accompanying rate coefficients under appropriate experimental conditions. The model also incorporated subroutines which were included to account for the small flow in/out of precursors and reactants to the reaction vessel and distortions imparted to the experimental kinetics by the inherent time averaging associated with CCD detection.

In all cases, kinetic analysis was accompanied by a sensitivity study of the chemical system. This was to ensure that the derived kinetic parameter was correctly and independently determined from the experimental data. A typical sensitivity study involved the reanalysis of a representative concentration *versus* time trace after each rate coefficient, in the full kinetic model, had in turn been halved and then doubled and the effect on the observed kinetic parameter recorded. These sensitivity studies could

also be used to assess the effect of uncertainty in a given secondary reaction rate coefficient on the kinetic parameter being determined. Chemical models could also be simplified by using the sensitivity analysis to consider which reactions had no effect on the observed kinetics and could hence be excluded from the model. Other forms of sensitivity analysis were used to examine the goodness of fit of the simulated trace to the experimental trace. Details of each study are given in the appropriate results chapters that follow.

3. 6 Laser Flash Photolysis

The incorporation of an excimer laser photolysis source into the experimental set-up became available during this project and offered an alternative photolysis source to flashlamp photolysis. The choice of excimer laser or flashlamp photolysis was principally determined by the nature of photolysis required for the specific gas reaction system under investigation. The principal attributes of each photolysis source, as applied to flash photolysis, are summarised in Table 3. 4 below.

Attribute	Photolysis source	
	Flashlamp	**Laser**
Spectral output	Broad band Can photolyse multiple species at different wavelengths	Single wavelength Can selectively photolyse components of gas mixture
Optical path concentration gradient	No complications	Require low precursor mix OD at photolysis wavelength
Alignment	Facile	Precise alignment required
Repetition rate	Low (0.05 Hz)	High (10 Hz)
RF noise generation	High	Low

Table 3. 4 Flashlamp photolysis *versus* laser photolysis. RF = Radio frequency, OD = Optical depth.

Laser photolysis is preferred when only one species needs to be photolysed. Single wavelength photolysis can result in a much less complicated gas mixture compared to broad band photolysis and hence the need for knowledge of any complicating secondary chemistry is often reduced. Interpretation of results from laser photolysis experiments is also made easier by the reduced RF noise associated with the traces as compared to those taken using flashlamp photolysis. Whilst the laser itself contains a high voltage

flashlamp, the housing of this lamp in the highly screened laser chassis, compared to the necessity, in flashlamp photolysis, of having the flashlamp adjacent to the reaction cell probably accounts for this. Additionally, the high repetition rate for laser photolysis experiments means that many more co-additions can be achieved in the same experimental timescale further improving the quality of experimental traces. A typical radical concentration *versus* time trace generated using flashlamp photolysis is shown in comparison to one generated using laser photolysis, under otherwise analogous experimental conditions, in Figure 3. 8 below.

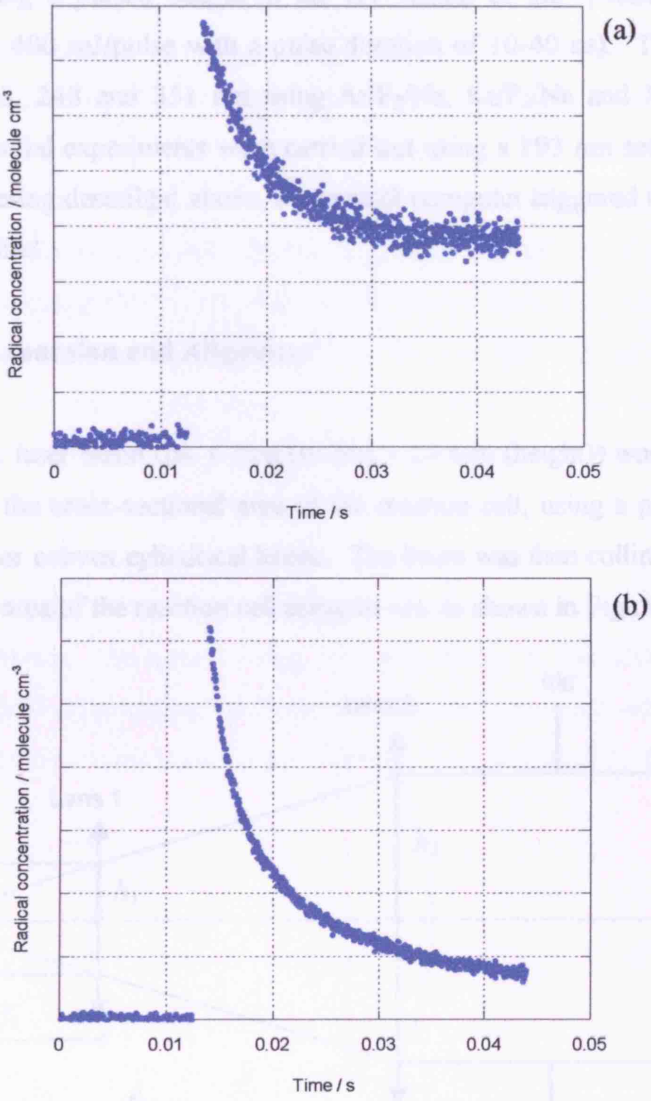

Figure 3. 8 A typical concentration *versus* time trace for a flashlamp photolysis system (a) and a laser photolysis system (b). Note that (a) and (b) are from two different chemical systems but otherwise analogous experimental conditions.

The requirement for a low optical depth precursor gas mixture at the laser photolysis wavelength does however, limit the range of experimental conditions that can be used in laser photolysis (given the only choice is passing the laser beam longitudinally along the reaction vessel), and is discussed below.

3. 6. 1 Laser Specifications

An excimer laser was chosen, for this experimental set-up, as the only available laser capable of giving a pulsed output in the UV region of the spectrum at high pulse energies (up to 400 mJ/pulse with a pulse duration of 10-40 ns). The laser could be operated at 193, 248 and 351 nm using $Ar/F_2/Ne$, $Kr/F_2/Ne$ and $Xe/F_2/Ne$ gas fills respectively. Initial experiments were carried out using a 193 nm set-up. As with the flashlamp triggering described above, the control computer triggered the laser pulse *via* a fibre optic cable.

3. 6. 2 Beam Expansion and Alignment

The rectangular laser beam (*ca.* 6 mm (width) × 20 mm (height)) was expanded in one axis to exceed the cross-sectional area of the reaction cell, using a pair of fused-silica plano-concave or convex cylindrical lenses. The beam was then collimated to match the cross-sectional area of the reaction cell using an iris, as shown in Figure 3. 9.

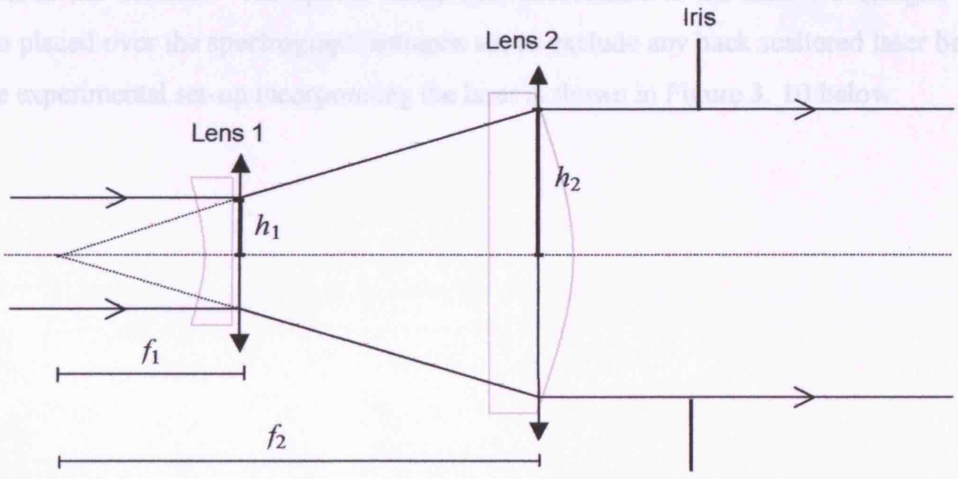

Figure 3. 9 Schematic diagram showing how the laser beam was expanded.

From Figure 3. 9 the magnification of the beam is determined by:

(E3. 5) $$magnification = \frac{h_2}{h_1} = \frac{f_2}{f_1}$$

and lenses with focal lengths of f_1 = 71 mm and f_2 = 223 mm, situated exactly 152 mm apart were used to expand and recollimate the beam.

To maximise the coupling of the photolysis laser to the cell, it was decided to direct the laser beam longitudinally along the analysis axis of the cell. It was considered prudent to have the photolysis laser beam travelling away from the light sensitive CCD detector, thus the laser was placed perpendicular to the axis of UV absorption and the expanded laser beam was directed along the reaction cell axis, counter propagating the analysis beam, using a dichroic reflector. Precise expansion and alignment of the laser beam (using a co-propagated He-Ne laser beam) ensured that the beam filled the entire cross-sectional area of the reaction cell. On passing through the reaction cell the beam was directed out of the analysis axis using a second dichroic reflector into a power meter. The production of extracellular O_3 (at 193 nm) in the analysis axis was minimised by placing the reflectors as close to the reaction cell end pieces as possible. The evacuated end pieces were also extended towards the dichroic reflection to minimise this, and angled windows on the end pieces minimised the back scatter of photolysis laser towards the detector. An optical filter, with absorbance at the laser wavelength, was also placed over the spectrograph entrance slit to exclude any back scattered laser beam. The experimental set-up incorporating the laser is shown in Figure 3. 10 below.

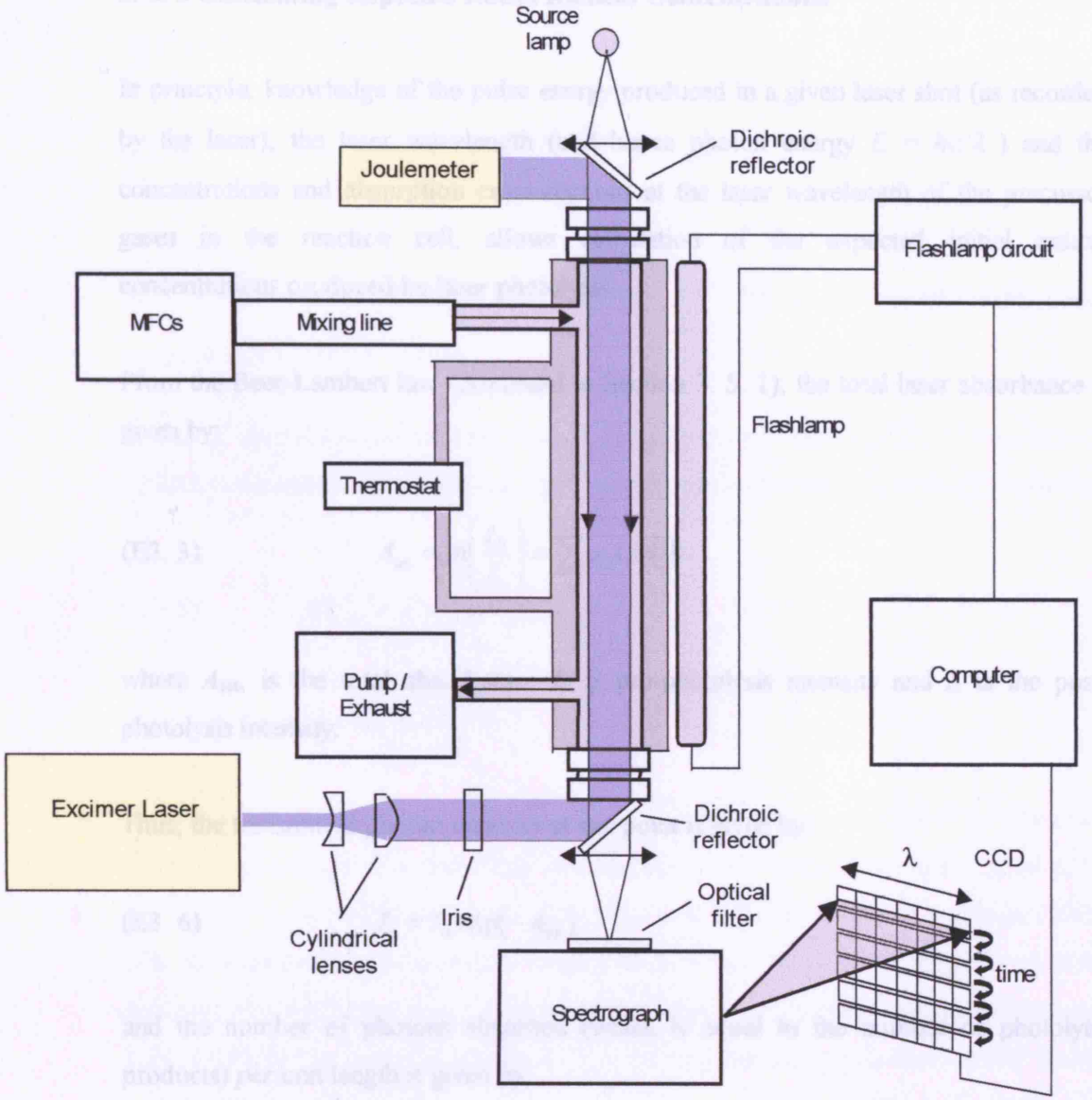

Figure 3. 10 Schematic diagram of the flash photolysis/UV absorption apparatus incorporating an excimer laser.

3. 6. 3 Calculating Expected Initial Radical Concentrations

In principle, knowledge of the pulse energy produced in a given laser shot (as recorded by the laser), the laser wavelength (and hence photon energy $E = hc/\lambda$) and the concentrations and absorption cross-sections at the laser wavelength of the precursor gases in the reaction cell, allows calculation of the expected initial radical concentrations produced by laser photolysis.

From the Beer-Lambert law (discussed in Section 3. 5. 1), the total laser absorbance is given by:

(E3. 3) $$A_{\text{tot}} = \ln\left(\frac{I_0}{I_t}\right) = \sum_i \sigma_i(\lambda)[i]l$$

where A_{tot}, is the total absorbance, I_0 is pre-photolysis intensity and I_t is the post-photolysis intensity.

Thus, the transmitted photon intensity at any point is given by:

(E3. 6) $$I_t = I_0 \exp(-A_{\text{tot}})$$

and the number of photons absorbed (which is equal to the number of photolytic products) *per* unit length is given by:

(E3. 7) $$I_{\text{abs,j}} = I_{\text{abs}} \frac{A_j}{A_{\text{tot}}} = \frac{A_j}{A_{\text{tot}}} I_0(1 - \exp(-A_{\text{tot}}))$$

where A_j is the absorbance of the precursor of interest, j, and A_{tot} is the total absorbance at the laser wavelength.

The I_0 value used has to be corrected for losses of laser fluence after exiting the laser. The expansion of the beam to fill the cross-sectional area of the reaction cell evidently

reduces the laser fluence, *per* unit area, by a geometrical multiplier. Thus, photon flux exiting the laser is given by:

$$(E3.\ 8) \qquad flux_{exit} = \frac{\text{total number of photons}}{0.6 \times 2}\ \text{cm}^{-2}$$

where the total number of photons is given by $\frac{E_{total}}{E_{photon}}$ and the denominator is the cross-sectional area of the beam in cm^2.

Losses of laser fluence through scattering and reflection at each surface of transmission optics are estimated at *ca.* 10% *per* surface, thus, the laser fluence is further reduced by:

$$(E3.\ 9) \qquad flux_{cell} = flux_{exit}\left((0.9)^9\left(\frac{f_1}{f_2}\right)\right)$$

providing the I_0 for use in (E3. 7).

If laser attenuation in the cell is very high, due to high concentrations of precursor gases, the possibility also arises that the laser beam will be significantly absorbed in the first part of the precursor mixture it encounters and a significant photogenerated radical concentration gradient could result. Such a gradient could lead to a spuriously enhanced apparent rate coefficient being observed, since high (fast reacting) concentration in one part of the reaction vessel is averaged with low concentration in another. Thus, for the preliminary laser photolysis experiments, chosen to be the generation and self-reaction of BrO radicals, calculations were performed to quantify possible effects of such a gradient.

3. 6. 4 Preliminary Experiments

Initial experiments were designed and carried out using a $N_2O/Br_2/N_2$ gas mixture photolysed at 193 nm, with resulting kinetics of the BrO self-reaction at 298 K and 760 Torr. N_2O photolyses at 193 nm to give:

(3. 1) $N_2O + h\nu\ (193\ nm) \rightarrow N_2 + O(^1D)$

(3. 2) $O(^1D) + M \rightarrow O(^3P) + M$

In the presence of excess Br_2, these $O(^3P)$ atoms react rapidly and exclusively with Br_2 to form BrO radicals, which then self react:

(3. 3) $Br_2 + O(^3P) \rightarrow BrO + Br$

(3. 4) $BrO + BrO \rightarrow$ Products

Initial N_2O precursor concentrations were designed to give a large oxygen atom concentration and therefore a large initial BrO concentration of *ca.* 7×10^{14} molecule cm^{-3}, requiring a laser fluence of typically 200 mJ/pulse. The effects of varying the N_2O concentration in the reaction cell were simulated by splitting the cell length into notional 10 cm lengths. The 10 resulting simulated traces were averaged to represent the line-of-sight view along the reaction cell and analysed to give a distortion (enhancement in the determined rate constant) from the known input parameters. The degree of distortion as a function of optical depth is shown in Figure 3. 11 below.

Taking a tolerable distortion of 10% an optical depth of up to 2.36 at the laser wavelength can be present. Lower optical depths will minimise this gradient but in turn the concentration of radicals generated, and associated signal-to-noise ratio, will be compromised directly.

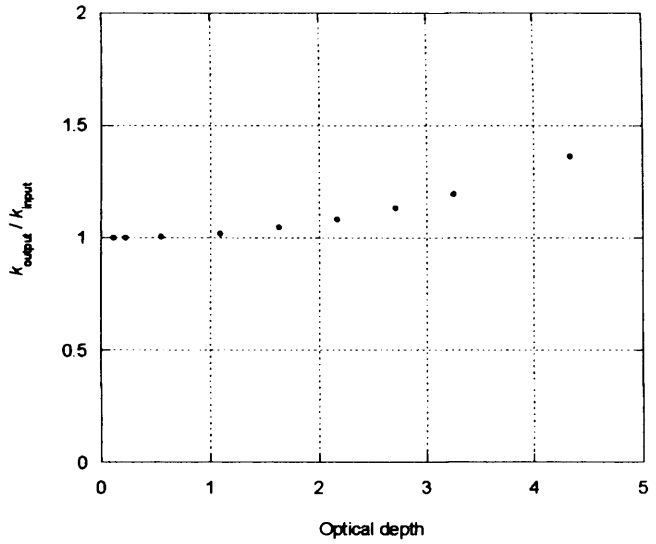

Figure 3. 11 Ratio of k_{output} to k_{input} as a function of optical depth, showing the distortion to k_{input} resulting from an increase in optical depth.

3. 7 Summary

In summary, this chapter has described the principles and operation of the flash photolysis/UV absorption technique used in this work. In particular the advantages of 'broad band' CCD detection of time-resolved transmission, and therefore absorption, have been described, and hopefully some of the advantages of this monitoring scheme (especially for spectrally structured absorbers, such as halogen oxides) should be evident in the results described in Chapters 4, 5 and 6. The implementation of excimer laser photolysis as a 'cleaner', more controllable radical source has also been described, along with some potential drawbacks, and elements of the studies described in succeeding chapters should reflect this technical development. Photographs of the apparatus in the laboratory are shown in Figures 3. 12 and 3. 13 below.

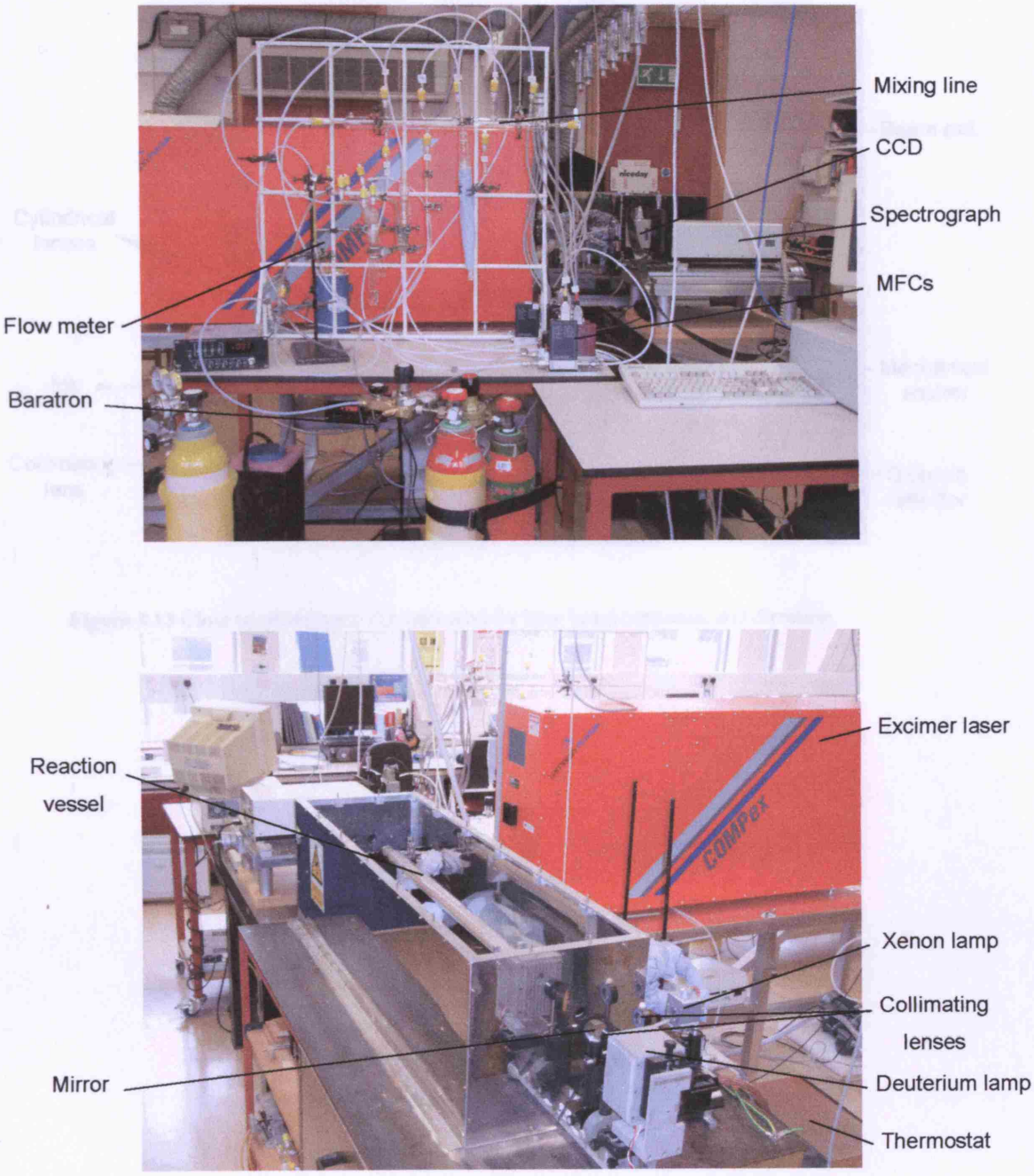

Figure 3.12 Photographs of the flash photolysis/UV absorption apparatus used for this work.

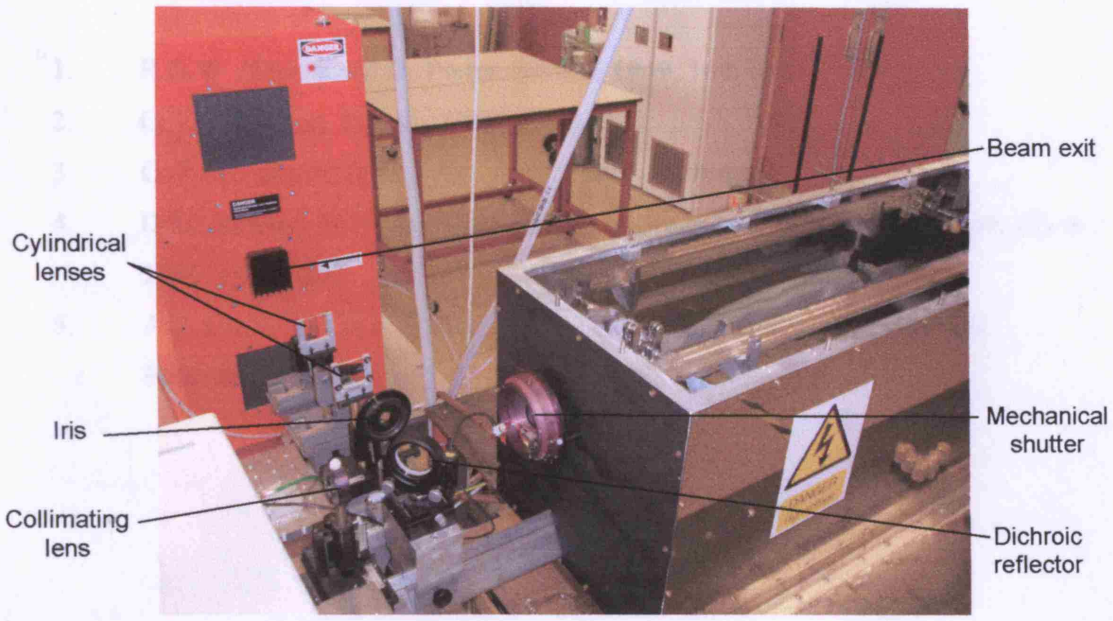

Figure 3.13 Close up photograph of lenses used for laser beam expansion and direction.

3. 8 References

1. R.G.W. Norrish and G. Porter, *Nature*, **1949**, 164, 658.
2. G. Porter, *Proc. R. Soc.*, **1950**, A200, 284.
3. G. Porter and P. West, *Proc. R. Soc. Ser. A*, **1964**, 279, 302.
4. D.M. Rowley, M.H. Harwood, R.A. Freshwater, and R.L. Jones, *J. Phys. Chem.*, **1996**, 100, 3020.
5. A.R. Curtis and W.P. Sweetenham, *FACSIMILE*. **1987**, AERE Harwell Publication: Oxford.

Chapter 4
The ClO + ClO Reaction

It is well established that the ClO radical plays a central role in human induced polar O_3 depletion.[1] As discussed in Chapter 1, within the polar vortices the primary route to O_3 destruction is thought to be the catalytic cycle involving the self-reaction of the ClO radical and subsequent photolysis of the ClO dimer, Cl_2O_2:[2]

(4. 1)		$2(Cl + O_3$	$\rightarrow$	$ClO + O_2)$
(4. 2a, -4. 2a)		$ClO + ClO + M$	$\leftrightarrow$	$Cl_2O_2 + M$
(4. 3)		$Cl_2O_2 + h\nu$	$\rightarrow$	$ClOO + Cl$
(4. 4)		$ClOO + M$	$\rightarrow$	$Cl + O_2 + M$
	Net:	$2O_3$	$\rightarrow$	$3O_2$

Accurate characterisation of the kinetics of reaction (4. 2a) is crucial to a quantitative understanding of polar O_3 depletion *via* atmospheric modelling studies. As a result, accurate determination of the rate coefficients describing ClO dimerisation has been the focus of many previous studies, including one in this laboratory.[3]

At high temperatures ($T > 298$ K) three additional 'bimolecular' channels of the ClO self-reaction are known to be in competition with the termolecular association channel (4. 2a):

(4. 2b)	$ClO + ClO$	$\rightarrow$	$Cl_2 + O_2$
(4. 2c)	$ClO + ClO$	$\rightarrow$	$ClOO + Cl$
(4. 2d)	$ClO + ClO$	$\rightarrow$	$OClO + Cl$

Under ambient conditions, the rates of these bimolecular channels are slow compared to the termolecular channel ($k_{4.2b+4.2c+4.2d} = 0.03k_{4.2a}$ at 298 K, 760 Torr).[4] Furthermore, these reaction channels also exhibit a positive temperature dependence and hence only become significant at high temperatures, precluding their significance in atmospheric

processes.[5] Studies of the ClO self-reaction can therefore be classed as low temperature, where the bimolecular channels can effectively be ignored, or high temperature, where both termolecular and bimolecular channels must be considered.

In addition to kinetic studies of the ClO self-reaction, investigations have also focused on the energetics of the dimerisation in an attempt to ascertain the thermal stability of the Cl_2O_2 dimer. There are three known isomers of Cl_2O_2 (ClOOCl, $ClClO_2$ and ClOClO) as established by matrix-isolation spectroscopy,[6, 7] however, ClOOCl is considered, from *ab initio* studies, to be the most stable. [8, 9] Furthermore, previous experimental work predicts that ClOOCl is the only major form of Cl_2O_2 produced in the ClO association reaction.[10-12]

4. 1 Previous Studies

4. 1. 1 Kinetics of the ClO Self-reaction

Porter and Wright[13] first proposed the possibility of ClO dimerisation during their development of the flash photolysis technique. Numerous experimental studies of the kinetics of the ClO association reaction followed, at ambient temperature[14-17] and as a function of temperature.[3, 5, 18-21]

The principal studies of ClO + ClO association carried out at reduced temperatures are those of Hayman *et al.*,[18] Sander *et al.*,[19] Trolier *et al.*,[20] Nickolaisen *et al.*,[5] Bloss *et al.*[21] and Boakes *et al.*,[3] the latter study being carried out in this laboratory.

Hayman *et al.* used molecular modulation to generate and monitor ClO radicals. All of the remaining reduced temperature studies used flash photolysis of Cl_2/C_2O or Cl_2/O_3 gas mixtures to generate ClO radicals. All of these low temperature investigations employed UV spectroscopy to monitor the ($A^2\Pi \leftarrow X^2\Pi$) vibronic absorption bands of ClO. Hayman *et al.*, Sander *et al.*, Trolier *et al.* and Nickolaisen *et al.* monitored a single wavelength corresponding to a ClO absorption peak. Bloss *et al.* used dual wavelength monitoring at a ClO absorption peak and at an adjacent trough to higher wavelengths. Calculating the difference between the absorption at the peak and at the

trough minimised interference from other absorbing species present in the system. Boakes *et al.* completely eliminated the effect that other absorbing species had on the recorded ClO absorbance by using broad band differential spectroscopy, employing the entire experimental wavelength region of the ClO vibronic structure, to monitor ClO.

Kinetic analysis of ClO absorbance *versus* time traces required accurate knowledge of ClO absorption cross-sections, σ(ClO). Hayman *et al.* took values for σ(ClO) from the literature.[22] However, subsequent discrepancies in the ClO absorption cross-sections used for this determination and hence the ClO concentrations inferred from absorption spectroscopy have raised questions as to the validity of the determination of the rate coefficients by Hayman *et al.* All other low temperature studies measured σ(ClO) directly over the temperature range investigated, although Sander *et al.* carried out kinetic experiments over a wider temperature range than the range used to measure σ(ClO), hence compromising their results at lowest temperatures, since extrapolation was necessary.

Results from these reduced temperature studies of the ClO self-reaction are summarised in Table 4. 1 below. The ClO association rate coefficient is defined by a pressure dependent third order rate coefficient, k_0 (the low pressure limit) and a limiting second order rate coefficient k_∞ (the high pressure limit), according to the expression derived by Troe[23] (as discussed in Section 2. 3. 2).

Reference	Technique	T / K	p / Torr	k_0(300 K) / 10^{-32} cm^6 molecule^{-2} s^{-1}	k_∞(300 K) / 10^{-12} cm^3 molecule^{-1} s^{-1}
Hayman *et al.*[18]	MM/UV	268-338	25-760	6.0 ± 0.36	
Sander *et al.*[19]	FP/UV	195-247	25-700	1.8 ± 0.5	6.0 ± 2.0
Trolier *et al.*[20]	FP/UV	200-263	25-600	1.64 ± 0.09	4.8 ± 0.5
Nickolaisen *et al.*[5]	FP/UV	260-390	50-700	2.00 ± 0.97	6 ± 2
Bloss *et al.*[21]	FP/UV	183-245	25-700	1.59 ± 0.60	1.36 ± 0.22
Boakes *et al.*[3]	FP/UV	206-298	25-760	2.78 ± 0.82	3.37 ± 1.67

Table 4. 1. Comparison of kinetic data from previous experimental studies of the termolecular channel, (4. 2a), of the ClO self-reaction. MM = Molecular modulation, FP = Flash photolysis, UV = Ultraviolet absorption spectroscopy. In all cases $F_c = 0.6$.[24]

4. 1. 2 Thermodynamics of the ClO Self-Reaction

At ambient or near ambient temperatures Basco and Hunt,[16] Cox and Hayman,[12] Nickolaisen *et al.*,[5] and most recently Plenge *et al.*[25] have reported the bond strength of the O-O bond in the ClOOCl dimer. Results of these studies are given in Table 4. 2 below.

Reference	$-\Delta_r H^\circ$ / kJ mol^{-1}
Basco and Hunt[16]	69 ± 3
Cox and Hayman.[12]	72.5 ± 3
Nickolaisen *et al.*[5]	81.6 ± 2.9
Plenge *et al.*[25]	72.39 ± 2.8

Table 4. 2 Results of previous studies of the bond strength of the ClO dimer at 298 K.

The value for $\Delta_r H^\circ$ reported by Basco and Hunt was estimated using known thermochemical data for chemically analogous radical and associated dimers. Cox and Hayman determined the equilibrium constant for ClO association over the temperature range 233-300 K and Nickolaisen *et al.* determined the same parameter over the temperature range 260-310 K. Both Cox and Hayman and Nickolaisen *et al.* then used van't Hoff plots to determine thermochemical data. In contrast to these two kinetic investigations, the study by Plenge *et al.* used photoionisation mass spectrometry to measure the strength of the ClO-OCl bond directly.

4. 2 This Work

This chapter presents results of a temperature dependence study of the ClO self-reaction. The first set of data presented is that of a high (near ambient) temperature study used to address some recent discrepancies in the literature concerning the thermodynamics of the ClO dimer. A second set of results were then taken over a lower temperature range using an alternative radical source. Due to the extensive data in the literature regarding the ClO self-reaction at low temperatures, this reaction was chosen as a test system to give confidence in subsequent results taken for different reactions using the same experimental set-up. Results from this second study therefore proved constructive in a subsequent study of the ClO + HO_2 reaction (Chapter 5).

4. 2. 1 High Temperature Study

4. 2. 1. 1 Radical Generation

For the high temperature study of ClO association, ClO radicals were generated using flash photolysis of $Br_2/Cl_2O/Cl_2/N_2$ gas mixtures. Gaseous Br_2 was introduced to the reaction cell by continuously bubbling a slow flow of N_2 (BOC, > 99.98%) through liquid bromine (Acros, > 99.8%). The bubbler was kept at 273 K to ensure that a known, constant, vapour pressure of Br_2 was introduced to the N_2 flow. Cl_2O was synthesised using the method of Hinshelwood and Pritchard[26] *via* the reaction of gaseous Cl_2 (BOC, 5% in N_2, purity > 99%) with solid dried yellow mercuric (II) oxide (Sigma Aldrich, > 99%), reaction (4. 5). Gaseous Cl_2O was introduced to the reaction vessel directly by continuously flowing gaseous Cl_2 through a trap containing the solid reactant interspersed with glass pieces to allow a flow of gas upstream of the gas mixing line. A known flow of Cl_2 was passed through the HgO trap and became diluted in a flow of N_2 before entering the reaction cell.

(4. 5) $2Cl_2\,(g) + 2HgO\,(s) \rightarrow HgCl_2.HgO\,(s) + Cl_2O\,(g)$

Photolysis of Br_2 resulted in Br atoms, reaction (4. 6), subsequent reaction of these atoms with Cl_2O was the primary source of ClO radicals in the gas system, reaction (4. 7).

(4. 6) $Br_2 + h\nu \rightarrow 2Br$

(4. 7) $Br + Cl_2O \rightarrow ClO + BrCl$

As a consequence of the in-line generation of Cl_2O, unless the conversion of Cl_2 to Cl_2O was 100% efficient there would be some residual Cl_2 in the reaction mixture (conversion was typically 70%). This residual Cl_2 could also undergo photolysis, reaction (4. 8), and provide additional ClO production *via* reactions (4. 9) and (4. 10).

(4. 8) $Cl_2 + h\nu \rightarrow 2Cl$

(4. 9) $Cl + Br_2 \rightarrow BrCl + Br$

(4. 10) $Cl + Cl_2O \rightarrow Cl_2 + ClO$

A further source of ClO was from direct Cl_2O photolysis:

(4. 11a) $Cl_2O + h\nu \rightarrow Cl + ClO$

In addition to this photochemistry it is possible that alternative Cl_2O photolysis channels exist:[27]

(4. 11a) $Cl_2O + h\nu \rightarrow Cl + ClO$ ($\lambda_{max} = 840$ nm)

(4. 11b) $Cl_2O + h\nu \rightarrow Cl_2 + O(^3P)$ ($\lambda_{max} = 710$ nm)

(4. 11c) $Cl_2O + h\nu \rightarrow 2Cl + O(^3P)$ ($\lambda_{max} = 292$ nm)

(4. 11d) $Cl_2O + h\nu \rightarrow Cl_2 + O(^1D)$ ($\lambda_{max} = 335$ nm)

The threshold wavelengths for reactions (4. 11a)-(4. 11d) indicate that all reaction channels are in principle accessible using broad band flashlamp photolysis. However, Bedjanian *et al.*[27] have shown that only channel (4. 11a) is active above wavelengths of 308 nm. Experiments for this dissertation have used a thermostatting fluid (Galden, HT110) in the reaction cell jacket that prevents short wavelength radiation ($\lambda < 280$ nm) reaching the reaction cell to ensure only channel (4. 11a) occurred. Further confirmation that only channel (4. 11a) took place in these experiments was achieved by adding O_2 to the system and looking for the production of O_3 *via* reaction (4. 12), by monitoring absorbance changes at and around 265 nm, where O_3 is known to absorb very strongly.

(4. 12) $O + O_2 + M \rightarrow O_3 + M$

No significant absorbance due to O_3 was observed above the experimental noise threshold, which corresponded to a concentration of O_3 of 2.5×10^{12} molecule cm^{-3}, < 1.5% of the maximum initial ClO concentration used.

4. 2. 1. 2 Quantification of ClO Radical Concentrations

Quantification of ClO radical concentrations using absorbance required the knowledge of the ClO absorption cross-section, σ(ClO). Differential spectroscopy was used to determine time-resolved ClO radical concentrations in the presence of other UV absorbing species (Cl_2O and Cl_2O_2), as described in detail in Chapter 3. Absorption cross-sections are available in the literature but since spectrally structured cross-sections, such as σ(ClO), depend critically upon both temperature and instrumental resolution, accurate determination of σ(ClO) under experimental conditions is imperative. This can be achieved either by convolving a literature cross-section to the experimental resolution used, by measuring σ(ClO) directly or by scaling measured ClO spectra to literature values. For these experiments each spectrum was calibrated according to an extensive study carried out in this laboratory by Boakes *et al.*,[3] under identical conditions using the same spectrometer. From this study the differential cross-section for the (12, 0) vibronic band, corresponding to a peak at 275.2 nm and trough at 276.4 nm, recorded at 0.8 nm full width half maximum (FWHM) spectral resolution, is given by (E4. 1).

(E4. 1) $$\sigma(\mathrm{ClO})_{\mathrm{d}} = 1.14\times10^{-17} - \left(2.52\times10^{-20}T\right)\ \mathrm{cm^2\ molecule^{-1}}$$

However, to vindicate the use of Boakes *et al.* absorption cross-sections, experiments were carried out to verify the calibration method. The instrument settings used for these experiments are given in Table 4. 3. A description of the calibration method is given below.

Spectrograph diffraction grating	600 grooves / mm
Entrance slit width	112 μm
Resolution	0.8 nm (FWHM)
Wavelength region	255-285 nm
CCD shift time	50 μs

Table 4. 3 Instrument settings used for experiments to determine ClO cross-sections.

The method developed by Boakes *et al.* for determining σ(ClO) in the presence of other absorbing species takes advantage of the simultaneous time and wavelength-resolved data recorded by the CCD. For the purpose of this calibration spectra were taken over the wavelength region 255-285 nm encompassing both the spectrally smooth and structured region. An example time averaged spectrum is shown in Figure 4. 1.

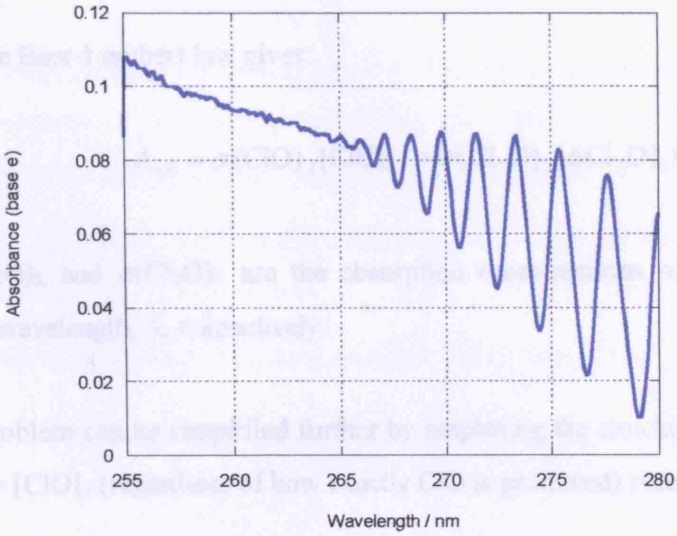

Figure 4. 1 Typical post-photolysis absorption spectrum recorded for a $Br_2/Cl_2/Cl_2O/N_2$ gas mixture.

Aside from ClO radicals, both the Cl_2O precursor and the Cl_2O_2 product are known to absorb between 200 and 300 nm. Therefore, in the continuum region of this spectrum (λ < 265 nm) the total absorbance, $A_{\lambda,t}$, recorded relative to pre-photolysis intensities contains contributions from any ClO and Cl_2O_2 produced and the *change* in absorbance of the precursor molecule Cl_2O. Thus, at any wavelength, λ, and at given time point, t, the total absorbance in this continuum region may be expressed as:

(E4. 2) $$A_{\lambda,t} = A(\mathrm{ClO})_{\lambda,t} + A(\mathrm{Cl_2O_2})_{\lambda,t} + A(\Delta\mathrm{Cl_2O})_{\lambda,t}$$

Here, $A(\Delta\mathrm{Cl_2O})_{\lambda,t}$ represents the change in Cl_2O absorbance relative to the pre-photolysis value.

If this absorbance is recorded at the time point immediately post-photolysis (hereafter referred to as t_0), the system is reduced to just two absorbers, ClO and Cl_2O since ClO is formed promptly (by design) and Cl_2O_2 will not yet have been produced. Hence at time t_0 the total post-photolysis absorbance in the spectral continuum can be written:

(E4. 3) $$A_{\lambda,0} = A(\mathrm{ClO})_{\lambda,0} + A(\Delta \mathrm{Cl_2O})_{\lambda,0}$$

Applying the Beer-Lambert law gives:

(E4. 4) $$A_{\lambda,0} = \sigma(\mathrm{ClO})_\lambda [\mathrm{ClO}]_0 l + \sigma(\mathrm{Cl_2O})_\lambda [\Delta \mathrm{Cl_2O}]_0 l$$

where $\sigma(\mathrm{ClO})_\lambda$ and $\sigma(\mathrm{Cl_2O})_\lambda$ are the absorption cross-sections of ClO and Cl_2O at continuum wavelength, λ, respectively.

At t_0 the problem can be simplified further by employing the stoichiometric relationship $-[\Delta \mathrm{Cl_2O}]_0 = [\mathrm{ClO}]_0$ (regardless of how exactly ClO is produced) resulting in:

(E4. 5) $$A_{\lambda,0} = [\mathrm{ClO}]_0 l \{\sigma(\mathrm{ClO})_\lambda - \sigma(\mathrm{Cl_2O})_\lambda\}$$

Consequently, the ClO concentration at t_0, $[\mathrm{ClO}]_0$ can be expressed in terms of the t_0 absorbance, $A_{\lambda,0}$, the continuum cross-sections of ClO and Cl_2O (both of which are well defined in the literature) and the optical path length, l:

(E4. 6) $$[\mathrm{ClO}]_0 = \frac{A_{\lambda,0}}{\{\sigma(\mathrm{ClO})_\lambda - \sigma(\mathrm{Cl_2O})_\lambda\} l}$$

At longer wavelengths, where ClO exhibits characteristic vibronic structure, the differential absorbance, A_{λ_d}, is solely due to ClO, since by definition other contributions to absorbance have been filtered out.

(E4. 7) $$A_{\lambda_d,t} = \sigma(\mathrm{ClO})_{\lambda_d} [\mathrm{ClO}]_t l$$

where $\sigma(\mathrm{ClO})_{\lambda_d}$ is now the *differential* ClO absorption cross-section.

Again at the initial post-photolysis time, t_0, and using the expression for $[ClO]_0$, (E4. 6), the differential absorbance immediately post-photolysis, denoted $A_{\lambda_d,0}$, can be expressed as:

(E4. 8) $$A_{\lambda_d,0} = \frac{\sigma(ClO)_{\lambda_d}}{\{\sigma(ClO)_\lambda - \sigma(Cl_2O)_\lambda\}} \times A_{\lambda,0}$$

This relationship between the immediate post-photolysis differential absorbance and the calibrating continuum wavelength absorbance can therefore be readily exploited to determine the ClO differential absorption cross-section, $\sigma(ClO)_{\lambda_d}$, provided that the cross-sections of ClO and Cl_2O at the calibrating wavelength are known. Equation (E4. 8) shows that determination of both $A_{\lambda_d,0}$ and $A_{\lambda,0}$ from experiments with differing initial ClO absorbances (*i.e.* differing $[ClO]_0$) will permit a plot of $A_{\lambda_d,0}$ *versus* $A_{\lambda,0}$ which should be linear with a gradient of $\frac{\sigma(ClO)_{\lambda_d}}{\{\sigma(ClO)_\lambda - \sigma(Cl_2O)_\lambda\}}$ and zero intercept.

Consistent with the work of Boakes *et al.* and Bloss *et al.*,[21] the chosen differential wavelengths were those of the (12, 0) band of the ($A^2\Pi \leftarrow X^2\Pi$) vibronic transition whose peak was at 275.2 nm and the corresponding trough at 276.4 nm. The chosen continuum wavelength was 257.5 nm.

$A_{\lambda_d,0}$ was determined by generating an uncalibrated time averaged spectrum and fitting this to each sequential spectrum for the same data set. This produced a time-resolved trace proportional to [ClO] which was fitted to a model of the ClO dimerisation kinetics (discussed in Section 4. 2. 1. 3) with albeit arbitrary kinetic parameters. This model simply accounted for the sliding average imparted on the data by the CCD and therefore allowed back extrapolation to the true t_0. Multiplying A_0 by A_{λ_d} from the time averaged spectrum used to generate the ClO A_{λ_d} temporal trace then resulted in the determination of $A_{\lambda_d,0}$. A time-resolved A_{λ_d} plot with accompanying fit and back extrapolation is shown in Figure 4. 2.

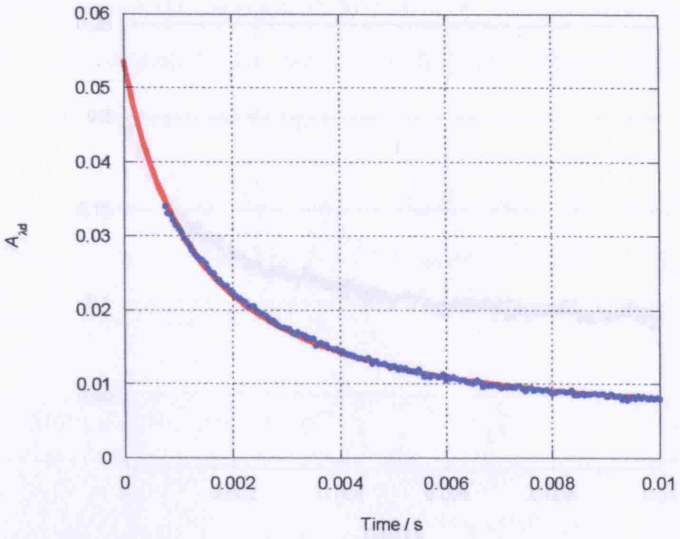

Figure 4. 2 Least squares fit of modelled A_{λ_d} (red line) to time-resolved data (blue points), back extrapolated to t_0.

Time-resolved absorbance traces at the chosen continuum wavelength were also generated and fitted as a function of time. In contrast to the differential case, the continuum trace contains contributions from ClO, Cl_2O and Cl_2O_2 and in this case, the relative [ClO] as a function of time, obtained from differential fitting, was used along with the relative $[Cl_2O_2]$ inferred from this to constrain the fit. In this case the continuum cross-sections of ClO, Cl_2O and Cl_2O_2 were allowed to optimise to fit the continuum temporal trace, although these (arbitrary) cross-sections were not used in any subsequent analysis. The purpose of the continuum trace fitting was solely to carry out the short back extrapolation of absorbance to obtain $A_{\lambda,0}$. An example time-resolved A_λ plot with this fit to determine $A_{\lambda,0}$ is given in Figure 4. 3.

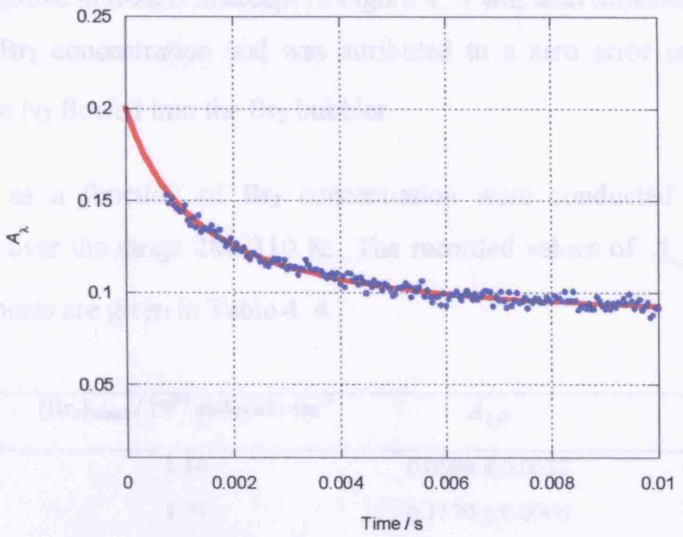

Figure 4. 3 Least squares fit of modelled A_λ (red line), in the spectral continuum, to time-resolved data (blue points), back extrapolated to t_0.

Variation of initial absorbances in both spectral regions, to facilitate use of equation (E4. 8), was achieved by varying the precursor bromine concentrations and consequently the initial ClO radical concentrations. Figure 4. 4 shows the variation in the initial differential absorbance for ClO as a function of precursor bromine concentration.

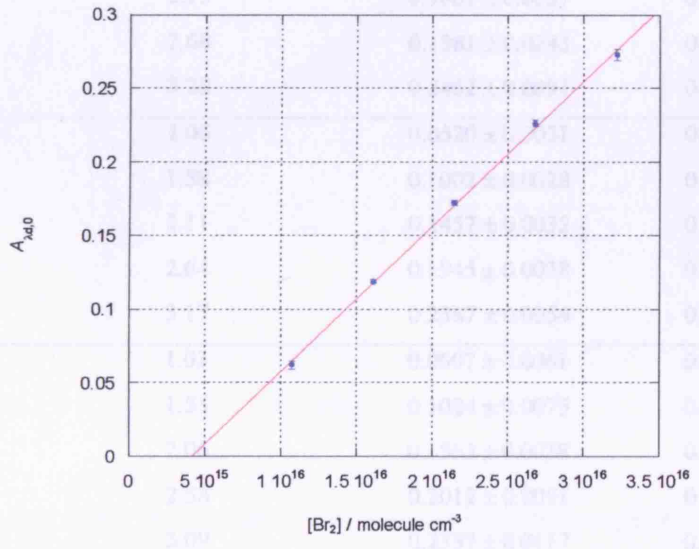

Figure 4. 4 $A_{\lambda_d,0}$ as a function of initial Br_2 concentration (blue points), with linear fit to data (red line).

The small negative non-zero intercept in Figure 4. 4 was also observed in the variation of A_λ with Br_2 concentration and was attributed to a zero error on the flow meter controlling the N_2 flowed into the Br_2 bubbler.

Experiments as a function of Br_2 concentration were conducted at five different temperatures over the range 280-310 K. The recorded values of $A_{\lambda_d,0}$ and $A_{\lambda,0}$ from these experiments are given in Table 4. 4.

T / K	$[Br_2]_{initial}$ / 10^{16} molecule cm^{-3}	$A_{\lambda,0}$	$A_{\lambda_d,0}$
280.0	1.14	0.0580 ± 0.0052	0.0644 ± 0.0018
	1.71	0.1170 ± 0.0066	0.1243 ± 0.0235
	2.28	0.1639 ± 0.0040	0.1890 ± 0.0038
	2.86	0.2206 ± 0.0054	0.2464 ± 0.0026
	3.43	0.2661 ± 0.0094	0.3051 ± 0.0046
288.0	1.11	0.0523 ± 0.0061	0.0641 ± 0.0009
	1.66	0.1114 ± 0.0105	0.1276 ± 0.0012
	2.22	0.1828 ± 0.0071	0.1890 ± 0.0034
	2.78	0.2009 ± 0.0113	0.2459 ± 0.0012
	3.33	0.2639± 0.0095	0.3008 ± 0.0057
298.0	1.07	0.0587 ± 0.0054	0.0624 ± 0.0026
	1.61	0.1117 ± 0.0156	0.1189 ± 0.0014
	2.15	0.1601 ± 0.0057	0.1724 ± 0.0019
	2.68	0.1981 ± 0.0243	0.2262 ± 0.0020
	3.22	0.2462 ± 0.0091	0.2728 ± 0.0037
303.0	1.06	0.0520 ± 0.0031	0.0539 ± 0.0011
	1.58	0.1002 ± 0.0028	0.1047 ± 0.0008
	2.11	0.1457 ± 0.0032	0.1508 ± 0.0015
	2.64	0.1945 ± 0.0038	0.1928 ± 0.0020
	3.17	0.2387 ± 0.0054	0.2333 ± 0.0062
310.0	1.03	0.0607 ± 0.0061	0.0558 ± 0.0025
	1.55	0.1024 ± 0.0075	0.1024 ± 0.0025
	2.06	0.1563 ± 0.0038	0.1450 ± 0.0011
	2.58	0.2012 ± 0.0091	0.1865 ± 0.0037
	3.09	0.2357 ± 0.0117	0.2258 ± 0.0016

Table 4. 4 Experimentally determined values of $A_{\lambda,0}$ and $A_{\lambda_d,0}$. Errors are 2σ, statistical only.

The resulting calibration plots of $A_{\lambda_d,0}$ *versus* $A_{\lambda,0}$, recorded at 298 K as well as plots for the other four experimental temperatures are given in Figures 4. 5 (a) and (b).

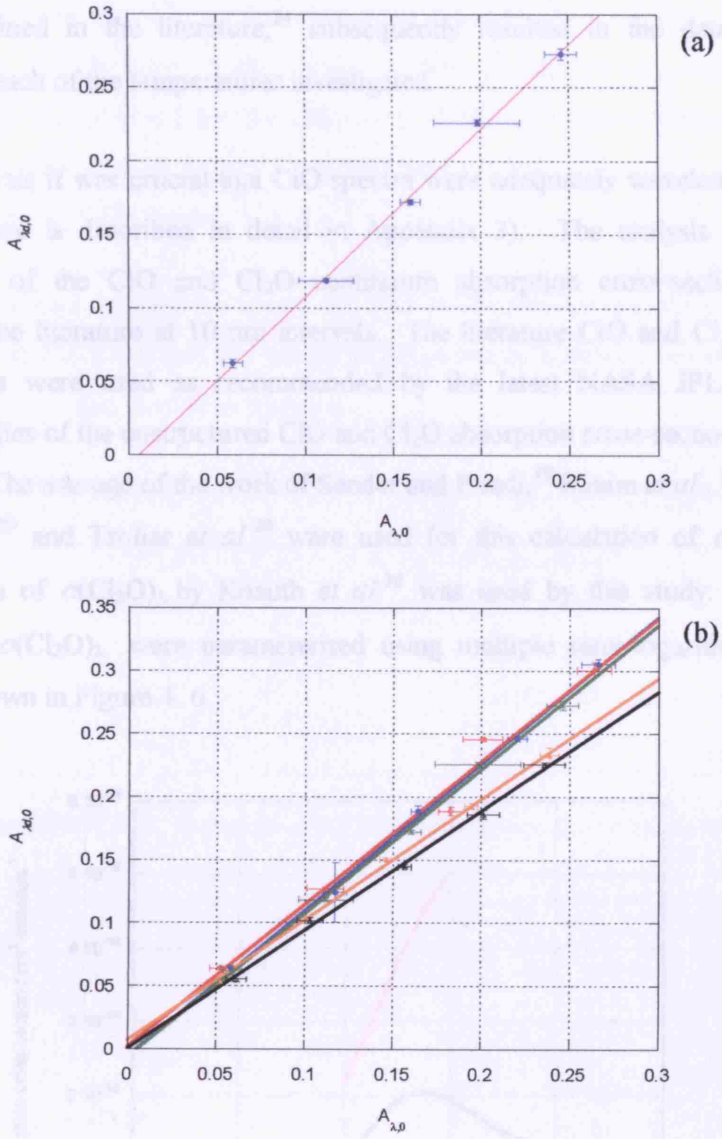

Figure 4. 5 Calibration plots to determine $\sigma(\mathrm{ClO})_{\lambda_d}$ using (E4. 8). (a) 298 K (b) 280 K (blue), 288 K (red), 298 K (green), 303 K (orange) and 310 K (black).

Calibration plots at all experimental temperatures showed excellent linearity and near zero intercepts, satisfying (E4. 8). The similarity in the gradients of the plots indicates that $\sigma(\mathrm{ClO})_{\lambda_d}$ has a weak temperature dependence over the range studied.

As discussed above, and shown explicitly in (E4. 8), the gradient of each of these linear plots is equivalent to $\frac{\sigma(\mathrm{ClO})_{\lambda_d}}{\{\sigma(\mathrm{ClO})_{\lambda} - \sigma(\mathrm{Cl_2O})_{\lambda}\}}$. Knowledge of the absorption cross-sections of ClO and Cl_2O at the continuum calibration wavelength of 257.5 nm, both of which are well defined in the literature,[24] subsequently resulted in the determination of $\sigma(\mathrm{ClO})_{\lambda_d}$ at each of the temperatures investigated.

For this analysis it was crucial that ClO spectra were adequately wavelength calibrated (this procedure is described in detail in Appendix 3). The analysis also required interpolation of the ClO and Cl_2O continuum absorption cross-sections, typically reported in the literature at 10 nm intervals. The literature ClO and Cl_2O absorption cross-sections were used as recommended by the latest NASA JPL evaluation.[24] Previous studies of the unstructured ClO and Cl_2O absorption cross-sections are in good agreement. The average of the work of Sander and Friedl,[19] Simon *et al.*, [28] Mandelman and Nicholls[29] and Trolier *et al.*[20] were used for this calculation of $\sigma(\mathrm{ClO})_{\lambda}$. The determination of $\sigma(\mathrm{Cl_2O})_{\lambda}$ by Knauth *et al.*[30] was used by this study. Each of the $\sigma(\mathrm{ClO})_{\lambda}$ and $\sigma(\mathrm{Cl_2O})_{\lambda}$ were parameterised using multiple semi-logarithmic Gaussian fitting, as shown in Figure 4. 6.

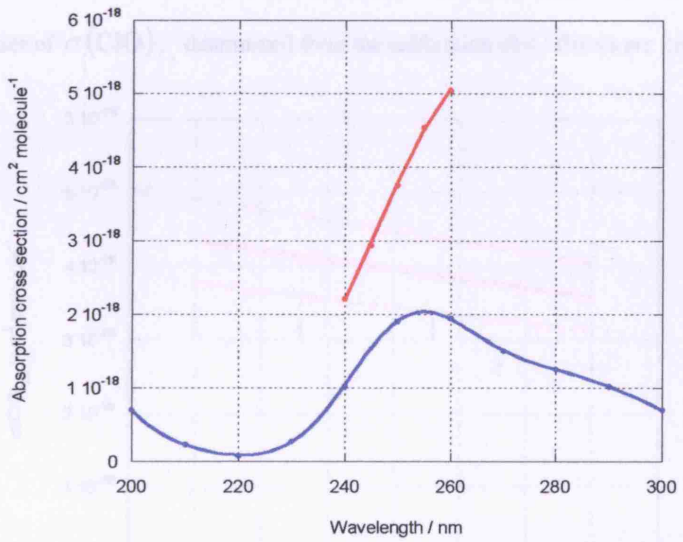

Figure 4. 6 Cl_2O (blue points) and ClO (red points) absorption cross-sections taken from the literature parameterised using semi-logarithmic Gaussians (blue and red lines respectively).

Since the temperature dependences of both of these continuum cross-sections are well characterised and shown to be negligible,[24] all cross-section calibrations carried out over the experimental temperature range, 280-310 K, used the 298 K values.

Boakes *et al.* report minor inconsistencies in the determined ClO differential absorption cross-sections as a function of the chosen continuum (calibrating) wavelength. The continuum wavelength used for the calibration of the ClO cross-sections in this study was 257.5 nm which lies in the middle of the range studied by Boakes *et al.* and is close to the mean value of this range.

An average of five determinations of the ClO differential cross-sections between the (12, 0) peak at 275.2 nm and the trough at 276.4 nm as a function of temperature are given in Table 4. 5 and plotted in Figure 4. 7.

T / K	$\sigma(\mathrm{ClO})_{\lambda_d}$ / × 10^{-18} cm^2 molecule^{-1}
280.0	3.24 ± 0.18
288.0	3.16 ± 0.51
298.0	3.20 ± 0.18
303.0	2.67 ± 0.13
310.0	2.64 ± 0.18

Table 4. 5 Values of $\sigma(\mathrm{ClO})_{\lambda_d}$ determined from the calibration plot. Errors are 2σ, statistical only.

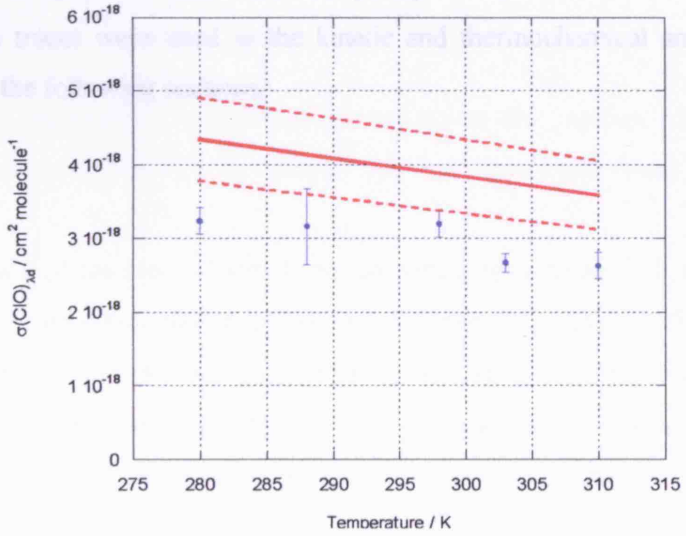

Figure 4. 7 $\sigma(\mathrm{ClO})_{\lambda_d}$ as a function of temperature. This study (blue points) where errors are 2σ, statistical only, and Boakes *et al.* (red line) with associated error (dashed red line).

Figure 4. 7 shows $\sigma(\mathrm{ClO})_{\lambda_d}$ to have a weak negative temperature dependence over the temperature range studied, described by:

(E4. 9) $$\sigma(\mathrm{ClO})_{\lambda_d} = (9.33 \pm 4.54) \times 10^{-18} - \left((2.14 \pm 1.54) \times 10^{-20} T\right)$$

where errors are 2σ, statistical only.

Since the study of $\sigma(\mathrm{ClO})_{\lambda_d}$ carried out by Boakes *et al.* was over a much more extensive temperature range than this one, the parameterisation given by (E4. 1) was used to calibrate ClO spectra for these experiments.

(E4. 1) represents $\sigma(\mathrm{ClO})_{\lambda_d}(T)$ for the single peak-trough at 275.2-276.4 nm respectively, corresponding to the (12, 0) peak. For each spectrum the entire structured wavelength region is readily calibrated such that:

(E4. 10) $$\sigma(\mathrm{ClO})_{\lambda} = A_{\lambda} \times \frac{\sigma(\mathrm{ClO})_{\lambda_d}}{A_{\lambda_d}}$$

Hence, a calibrated ClO cross-section was generated for every experimental spectrum at every experimental temperature and subsequently fitted to every time point in each kinetic run to generate time-resolved [ClO] *versus* time trace. Each of these experimental traces were used in the kinetic and thermochemical analyses, which are described in the following sections.

4. 2. 1. 3 Kinetic Analysis

Initial experiments were carried out to characterise the kinetics and thermochemistry of ClO dimerisation (4. 2a) as a function of temperature and at atmospheric pressure over the temperature range 280-310 K.

(4. 2a) $ClO + ClO + M \leftrightarrow Cl_2O_2 + M$

Since the differential cross-sections are a strong function of resolution these kinetic experiments were carried out at the same spectral settings as the experiments to determine σ(ClO).

Taking into account the incomplete conversion of Cl_2 to Cl_2O, typical pre-photolysis concentrations of precursor gases at 298 K are given below, in Table 4. 6.

Precursor gas	Pre-photolysis concentration / 10^{16} molecule cm^{-3}
Br_2	1-4
Cl_2	0.3-4
Cl_2O	0.4-5
N_2	Balance to 1 atmosphere

Table 4. 6 Typical experimental precursor gas concentrations at 298 K, 760 Torr.

Under these experimental conditions, photolysis of the gaseous mixture resulted in prompt formation of ClO radicals compared to their subsequent decay.

The application of the Beer-Lambert law, as described in Chapter 3, to post-photolysis data relative to pre-photolysis data resulted in some 1000 time-resolved spectra. The use of automated fitting routines to match each of these spectra to an appropriate differential cross-section, according to the Beer-Lambert law and also as described earlier, gave rise to temporally resolved ClO decay profiles, $[ClO]_t$.

The photolysis of $Br_2/Cl_2/Cl_2O/N_2$ gas mixtures has demonstrated the presence of the ClO self-reaction. Figure 4. 8 shows an example time-resolved trace taken at 298 K,

760 Torr. Post-photolysis temporal traces showed rapid formation of ClO radicals followed by subsequent decay to equilibrium attributed to the reversible ClO dimerisation.

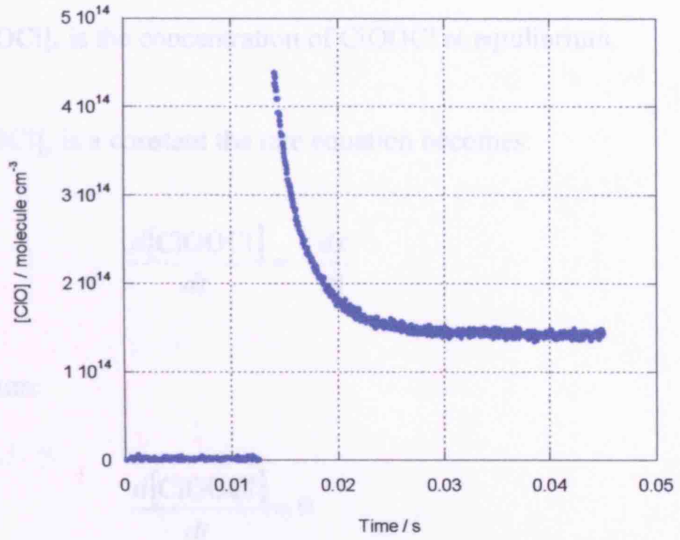

Figure 4. 8 Typical ClO concentration as a function of time trace, with photolysis initiated at time = 0.012 s.

Taking into account the reversible dimerisation of ClO at ambient temperature the temporal variation of ClO radicals and ClOOCl molecules can be described by equation (E4. 11).

(E4. 11) $$-\frac{1}{2}\frac{d[\mathrm{ClO}]}{dt}=\frac{d[\mathrm{ClOOCl}]}{dt}=k_{4.2a}[\mathrm{ClO}]^2-k_{-4.2a}[\mathrm{ClOOCl}]$$

The solution to this differential equation is complex but an exact solution can be evaluated by making the following substitution:

(E4. 12) $$[\mathrm{ClO}]=[\mathrm{ClO}]_e+2x$$

where $2x$ is the concentration of ClO radicals in excess of the equilibrium concentration of ClO, $[\mathrm{ClO}]_e$.

Using equation (E4. 12) and by stoichiometry,

(E4. 13) $$[\mathrm{ClOOCl}] = [\mathrm{ClOOCl}]_e - x$$

where $[\mathrm{ClOOCl}]_e$ is the concentration of ClOOCl at equilibrium.

Since $[\mathrm{ClOOCl}]_e$ is a constant the rate equation becomes:

(E4. 14) $$\frac{d[\mathrm{ClOOCl}]}{dt} = -\frac{dx}{dt}$$

At equilibrium:

(E4. 15) $$\frac{d[\mathrm{ClOOCl}]}{dt} = 0$$

Hence, from (E4. 11):

(E4. 16) $$k_{4.2a}[\mathrm{ClO}]_e^2 = k_{-4.2a}[\mathrm{ClOOCl}]_e$$

Thus combining (E4. 12)-(E4. 16) gives:

(E4. 17) $$-\frac{dx}{dt} = k_{4.2a}([\mathrm{ClO}]_e + 2x)^2 - k_{-4.2a}([\mathrm{ClOOCl}]_e - x)$$

$$= 4k_{4.2a}[\mathrm{ClO}]_e x + 4k_{4.2a}x^2 + k_{-4.2a}x$$

Rearranging:

$$\frac{dx}{x(4k_{4.2a}[\mathrm{ClO}]_e + 4k_{4.2a}x + k_{-4.2a})} = -dt$$

This is a differential equation of the form:

$$\frac{dx}{x(a+bx)} = -dt$$

where

$$a = 4k_{4.2a}[\mathrm{ClO}]_e + k_{-4.2a} \qquad \text{and} \qquad b = 4k_{4.2a}$$

Between limits of t and 0 (defined as immediately post-photolysis):

$$\int_{x_0}^{x_t} \frac{dx}{x(a+bx)} = -\int_0^t dt$$

Integrating gives:

$$-\frac{1}{a}\ln\left(\frac{a+bx_t}{x_t}\right) + \frac{1}{a}\ln\left(\frac{a+bx_0}{x_0}\right) = -t$$

$$\ln\left(\frac{a+bx_0}{x_0} \cdot \frac{x_t}{a+bx_t}\right) = -at$$

Thus,

(E4. 18) $$x_t = \frac{ax_0 \exp(-at)}{a + bx_0 - bx_0 \exp(-at)}$$

Consequently from (E4. 13):

(E4. 19) $$[\mathrm{ClO}]_t = [\mathrm{ClO}]_e + 2x_t$$

where $[\mathrm{ClO}]_t$ is the concentration of ClO at any time t after photolytic production.

$[\mathrm{ClO}]_t$ is readily parameterised using the variables a, b and x_0 resulting in a simulated ClO decay. These parameters were optimised by minimising the sum of residuals between experimental $[\mathrm{ClO}]_t$ and simulated $[\mathrm{ClO}]_t$ allowing three parameters, $[\mathrm{ClO}]_0$, $k_{4.2a}$ and $k_{-4.2a}$ to vary.

A typical fit of $[ClO]_t$ described by (E4. 19) to an experimental ClO decay trace is given in Figure 4. 9.

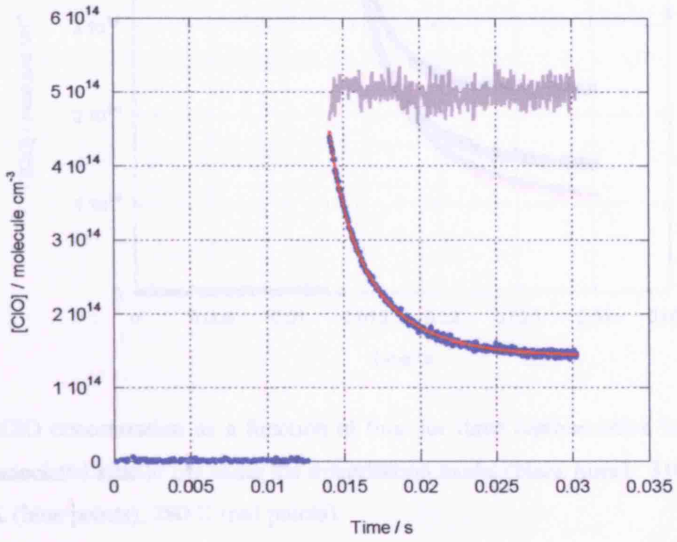

Figure 4. 9 Comparison of 298 K experimental ClO concentration (blue points) as a function of time and classical model fit (red line). The offset residual (grey line) is shown × 5, for clarity.

Determination of the forward and reverse rate coefficients permits the calculation of the equilibrium constant K_c.

(E4. 20) $$K_c = \frac{k_{4.2a}}{k_{-4.2a}}$$

For this initial study experiments were carried out at 13 temperatures over the range 280-310 K. The ClO concentration *versus* time traces for three representative traces recorded at different temperatures but otherwise under identical conditions, along with associated model fits, are given in Figure 4. 10.

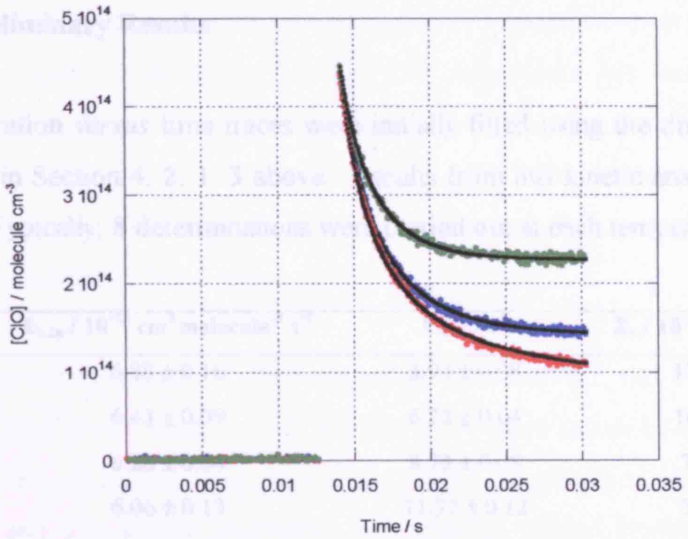

Figure 4. 10 ClO concentration as a function of time for three representative temperatures along with associated kinetic fits using the dimerisation model (black lines). 310 K (green points), 298 K (blue points), 280 K (red points).

Figure 4. 10 shows K_c has a strong temperature dependence permitting investigation of $\Delta_r H^\circ$ for ClO dimerisation as discussed in the following section.

4. 2. 1. 4 Preliminary Results

ClO concentration *versus* time traces were initially fitted using the dimerisation model as described in Section 4. 2. 1. 3 above. Results from this kinetic analysis are given in Table 4. 7. Typically, 8 determinations were carried out at each temperature.

T / K	$k_{4.2a}$ / 10^{-13} cm^3 molecule^{-1} s^{-1}	$k_{-4.2a}$ / s^{-1}	K_c / 10^{-14} cm^3 molecule^{-1}
280.0	6.88 ± 0.16	3.94 ± 0.08	17.46 ± 0.59
283.0	6.43 ± 0.09	6.22 ± 0.04	10.34 ± 0.14
285.5	6.28 ± 0.14	8.73 ± 0.08	7.19 ± 0.18
288.0	6.06 ± 0.13	11.72 ± 0.12	5.17 ± 0.16
290.5	5.82 ± 0.07	16.12 ± 0.15	3.61 ± 0.04
293.0	5.72 ± 0.17	21.14 ± 0.13	2.70 ± 0.09
295.5	5.37 ± 0.05	27.54 ± 0.09	1.95 ± 0.02
298.0	4.92 ± 0.04	35.20 ± 0.20	1.40 ± 0.01
300.5	4.82 ± 0.10	45.15 ± 1.42	1.07 ± 0.03
303.0	4.74 ± 0.10	55.73 ± 1.13	0.85 ± 0.03
305.5	4.23 ± 0.09	68.76 ± 0.85	0.62 ± 0.01
308.0	4.09 ± 0.15	83.04 ± 0.76	0.49 ± 0.02
310.0	3.88 ± 0.07	99.89 ± 2.05	0.39 ± 0.01

Table 4. 7 Average values of $k_{4.2a}$, $k_{-4.2a}$ and K_c, as a function of temperature, determined by fitting experimental decay traces to the dimerisation model described in Section 4. 2. 1. 3. Errors are 2σ, statistical only, and have been divided by $n^{1/2}$ to account for non-equivalence of sample sizes, where n is the number of determinations.

4. 2. 1. 5 Refined Analysis and Results

As previously discussed, at high temperatures (T = 280-310 K in this work) the termolecular ClO association channel, although still dominant, has competition from the bimolecular channels of the ClO self-reaction. As a result the use of a dimerisation only model to determine the kinetics of ClO association introduces a small distortion to observed kinetics, which is greatest at the highest temperature used. The degree to which the kinetics are affected by the bimolecular channels was assessed therefore in two ways, both resulting in correction factors which were subsequently used to amend data calculated using the 'dimerisation only' model. In the first instance a kinetic model

using numerical integration that included both the ClO dimerisation and the bimolecular channels was used to generate an artificial ClO decay trace with associated (known) kinetic parameters, k_{true}. This trace was then analysed as an experimental trace in the 'dimerisation only' model and the returned rate coefficients, termed k_{false}, compared to the initial input parameters to give a correction factor, f_1. This procedure was typically carried out for 2 representative traces at each temperature.

An analogous second test of this correction was carried out by analysing real experimental ClO decay traces, which had initially yielded values of k from analysis in the dimerisation only model, now termed k_{false}, in the full numerical model including the dimerisation and bimolecular channels. This analysis yielded kinetic parameters k_{true} and the values from the 'dimerisation only' and full models were compared to give a correction value, f_2. In both cases the values of $k_{4.2a}$ and $k_{-4.2a}$ initially recorded using the 'dimerisation only' model were corrected according to:

(E2. 21) $$f_1 = f_2 = \frac{k_{false}}{k_{true}}$$

The resulting correction factors, f_1 and f_2, all fell within the range 0.96-1.10 (*i.e.* represented a small correction of the kinetic parameters) and showed excellent agreement at high temperatures, as shown in Figure 4. 11. Deviation between these correction factors at low temperatures in the $k_{-4.2a}$ case highlights the insensitivity of the models to the reverse rate constant at low temperatures, as discussed below.

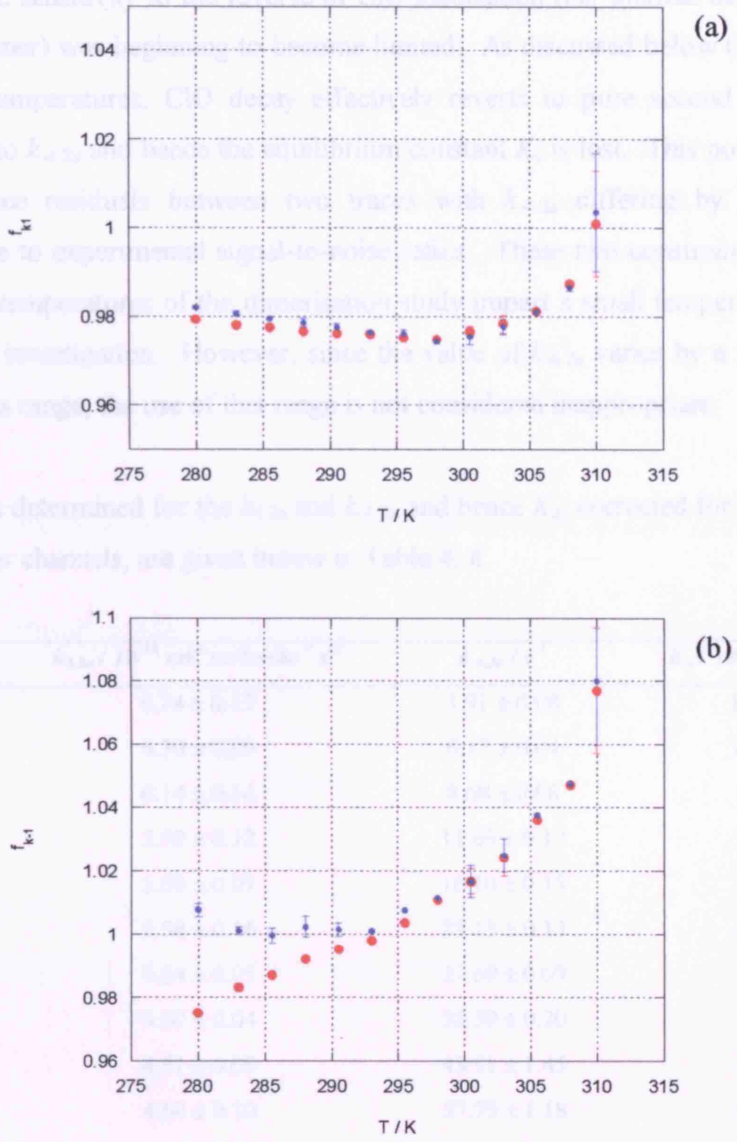

Figure 4. 11 Correction factors as a function of temperature for $k_{4.2a}$, plot (a) and $k_{-4.2a}$, plot (b) determined using fitting method 1 (blue points) and method 2 (red points).

The values of f_1 and f_2 at the upper limit of temperature studied in this work (approximately 1.08 for $k_{-4.2a}$) also effectively determined the maximum temperature at which ClO dimerisation was investigated. Arbitrarily this temperature (310 K) was set such that no more than a 10% deviation between the 'dimerisation only' and the full ClO kinetic model existed. This limited possible uncertainties in the ClO bimolecular rate coefficients affecting kinetic parameters for the dimerisation.

Similarly, the low temperature limit of the dimerisation study (280 K) was taken at a point where sensitivity to the reverse of ClO association (*i.e.* thermal decomposition of the ClO dimer) was beginning to become limited. As discussed below (Section 4. 2. 2) at lower temperatures, ClO decay effectively reverts to pure second order, and all sensitivity to $k_{-4.2a}$ and hence the equilibrium constant K_c is lost. This point, 280 K, was chosen since residuals between two traces with $k_{-4.2a}$ differing by 25 % became comparable to experimental signal-to-noise ratios. These two constraints on the upper and lower temperatures of the dimerisation study impart a small temperature range (30 K) on this investigation. However, since the value of $k_{-4.2a}$ varies by a factor of nearly 50 over this range, the use of this range is not considered inappropriate.

The results determined for the $k_{4.2a}$ and $k_{-4.2a}$ and hence K_c, corrected for the existence of bimolecular channels, are given below in Table 4. 8.

T / K	$k_{4.2a}$ / 10^{-13} cm^3 molecule^{-1} s^{-1}	$k_{-4.2a}$ / s^{-1}	K_c / 10^{-14} cm^3 molecule^{-1}
280.0	6.74 ± 0.15	3.91 ± 0.08	17.27 ± 0.58
283.0	6.30 ± 0.09	6.17 ± 0.04	10.21 ± 0.14
285.5	6.14 ± 0.14	8.68 ± 0.08	7.08 ± 0.18
288.0	5.92 ± 0.12	11.69 ± 0.12	5.07 ± 0.15
290.5	5.69 ± 0.07	16.10 ± 0.15	3.53 ± 0.04
293.0	5.58 ± 0.16	21.13 ± 0.13	2.64 ± 0.08
295.5	5.24 ± 0.05	27.69 ± 0.09	1.89 ± 0.02
298.0	4.80 ± 0.04	35.59 ± 0.20	1.34 ± 0.01
300.5	4.71 ± 0.09	45.91 ± 1.45	1.03 ± 0.03
303.0	4.64 ± 0.10	57.79 ± 1.18	0.80 ± 0.03
305.5	4.15 ± 0.08	71.31 ± 0.88	0.58 ± 0.01
308.0	4.04 ± 0.14	86.98 ± 0.79	0.46 ± 0.02
310.0	3.89 ± 0.07	107.74 ± 2.21	0.36 ± 0.01

Table 4. 8 Values of $k_{4.2a}$, $k_{-4.2a}$ and K_c calibrated to account for the bimolecular channels of the ClO self-reaction. Errors are 2σ, statistical only.

4. 2. 1. 6 Thermochemical Analysis

As discussed above, this high temperature study (T = 280-310 K) of the ClO self-reaction provides sufficient sensitivity to the forward and reverse rate coefficients to determine the equilibrium constant K_c. Second Law analysis can be used to investigate the energetics of the dimerisation in the following way. Firstly K_c, in reciprocal concentration units, must be converted to the (strictly) dimensionless K_p using the following relationship:

(E4. 22) $$K_p = K_c(RT)^{\Delta n}$$

where Δn is the mole change in the reaction, which for the ClO dimerisation is –1.

K_p is then directly related to the standard Gibbs free energy change for the reaction, according to:

(E4. 23) $$\Delta_r G^\circ = -RT \ln K_p$$

$\Delta_r G^\circ$ is itself related to the standard reaction enthalpy, $\Delta_r H^\circ$, and the standard reaction entropy, $\Delta_r S^\circ$ over a limited temperature range *via*:

(E4. 24) $$\Delta_r G^\circ = \Delta_r H^\circ - T\Delta_r S^\circ$$

Combination of the two relationships results in the van't Hoff equation:

(E4. 25) $$\ln K_p = -\frac{\Delta_r H^\circ}{R} \cdot \frac{1}{T} + \frac{\Delta_r S^\circ}{R}$$

Consequently, a graph of ln K_p *versus* reciprocal temperature should be linear with gradient $-\frac{\Delta_r H^\circ}{R}$ and intercept $\frac{\Delta_r S^\circ}{R}$.

The results of ln K_p as a function of temperature are given in Table 4. 9 and plotted in van't Hoff form in Figure 4. 12 below.

T / K	ln K_p / atm^{-1}
280.0	15.32 ± 0.02
283.0	14.79 ± 0.01
285.5	14.41 ± 0.02
288.0	14.07 ± 0.02
290.5	13.70 ± 0.01
293.0	13.40 ± 0.02
295.5	13.06 ± 0.01
298.0	12.713 ± 0.004
300.5	12.43 ± 0.02
303.0	12.18 ± 0.02
305.5	11.84 ± 0.01
308.0	11.61 ± 0.03
310.0	11.36 ± 0.02

Table 4. 9 Determined values of ln K_p as a function of temperature. Errors are 2σ, statistical only.

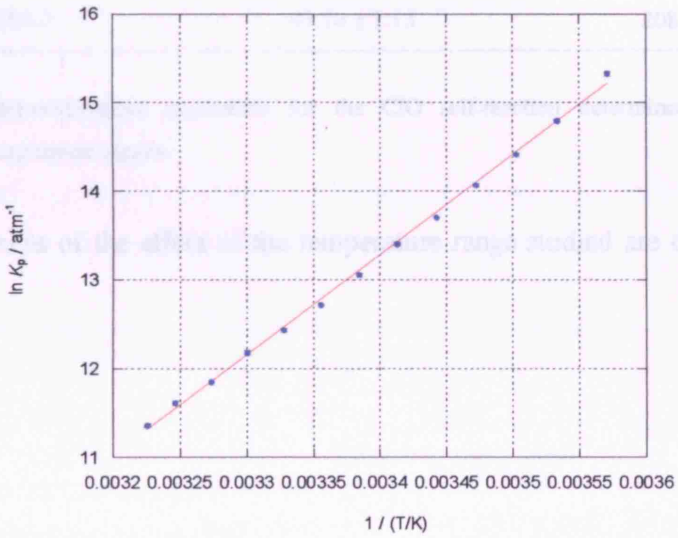

Figure 4. 12 Plot of ln K_p *versus* $1/T$ (blue points). The gradient of the linear parameterisation of this plot (red line) yields $\Delta_r H^\circ$. Errors are 2σ, statistical only.

An unweighted linear parameterisation of the data shown in Figure 4. 12 results in a value of $\Delta_r H° = -(93.74 \pm 1.13)$ kJ mol^{-1} and $\Delta_r S° = -(208.37 \pm 3.82)$ J K^{-1} mol^{-1}.

Although on first inspection this parameterisation appears perfectly linear, further detailed investigation indicated otherwise. Reanalysis of the thermochemical data over successively smaller high temperature ranges resulted in significant deviation of the calculated parameters from the values calculated if the entire data set was used. This phenomenon is illustrated by the data in Table 4. 10.

T range / K	$-\Delta_r H°$ / kJ mol^{-1}	$-\Delta_r S°$ / J K^{-1} mol^{-1}
310.0-305.5	85.41 ± 7.96	180.98 ± 25.89
310.0-303.0	89.58 ± 4.05	194.46 ± 13.20
310.0-300.5	87.50 ± 2.53	187.76 ± 8.30
310.0-298.0	86.40 ± 1.74	184.14 ± 5.72
310.0-295.5	87.79 ± 1.43	188.34 ± 4.74
310.0-293.0	89.30 ± 1.35	193.64 ± 4.48
310.0-290.5	89.68 ± 1.05	194.88 ± 3.51
310.0-288.0	90.64 ± 0.99	198.04 ± 3.30
310.0-285.5	91.32 ± 0.88	200.28 ± 2.97
310.0-283.0	92.11 ± 0.85	202.91 ± 2.87
310.0-280.0	93.74 ± 1.13	208.37 ± 3.82

Table 4. 10 Thermochemical parameters for the ClO self-reaction determined over increasing temperature ranges.

The consequences of the effect of the temperature range studied are discussed later in Section 4. 3.

4. 2. 2 Low Temperature Study

A second set of experiments was performed in order to study the kinetics of the ClO self-reaction at low temperatures. The results of this study were to be utilised in a subsequent study of the ClO + HO_2 reaction, described in detail in Chapter 5.

4. 2. 2. 1 Radical Generation

In order that the experimental complexity of the subsequent ClO + HO_2 system was not unnecessarily enhanced, the production of ClO radicals for this low temperature study had to be as 'clean' as possible. Consequently, for this study, Br_2 was not used to produce ClO and the major source of ClO radicals became Cl_2O in an otherwise identical system.

(4. 11a) $Cl_2O + h\nu \rightarrow Cl + ClO$

(4. 10) $Cl + Cl_2O \rightarrow Cl_2 + ClO$

Once again, incomplete conversion of Cl_2 to Cl_2O resulted in residual Cl_2 which was itself photolysed to give Cl atoms which subsequently formed ClO.

4. 2. 2. 2 Kinetic Analysis

Taking into account this incomplete conversion of Cl_2 to Cl_2O typical pre-photolysis concentrations of precursor gases are given below in Table 4. 11.

Precursor gas	Pre-photolysis concentration / 10^{16} molecule cm^{-3}
Cl_2	0.3-4
Cl_2O	0.4-5
N_2	Balance to 1 atmosphere

Table 4. 11 Typical precursor gas concentrations used in the $Cl_2/Cl_2O/N_2$ system for the study of the ClO self-reaction.

At lower temperatures precursor gas flow rates and subsequent radical concentrations were determined by applying appropriate thermal expansion/contraction factors given by the perfect gas law to these values at 298 K. This is appropriate since none of the chemical sources of ClO, *e.g.* Cl + Cl_2O, exhibit strong temperature dependencies.[24]

ClO absorption cross-sections were once again characterised using the parameterisation of Boakes *et al.*, and calibrated cross-sections were fitted to sequential time-resolved spectra to obtain ClO temporal profiles.

The photolysis of $Cl_2/Cl_2O/N_2$ gas mixtures once again demonstrated the presence of the ClO self-reaction. Figure 4. 13 shows an example time-resolved trace taken at 250 K, 760 Torr.

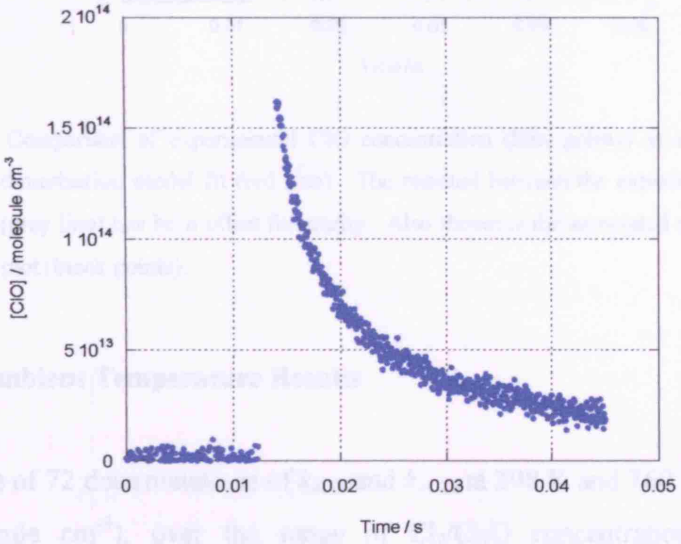

Figure 4. 13 Typical ClO concentration as a function of time trace recorded at 250 K, 760 Torr.

In this low temperature study, the use of Cl_2/Cl_2O precursor gas mixtures gave typically lower initial radical concentrations than the experiments employing Br_2.

The kinetic model described in Section 4. 2. 1. 3 was once again fitted to the ClO concentration *versus* time decay traces. In this case, it was appropriate to use this dimerisation only model since, at low temperatures the contribution of the bimolecular channels to the observed decay becomes negligible. Fits of the dimerisation model to

the observed experimental decays were excellent, but the $k_{-4.23}$ parameter was set to an arbitrarily small value. A typical ClO decay trace along with associated model fit is given in Figure 4. 14.

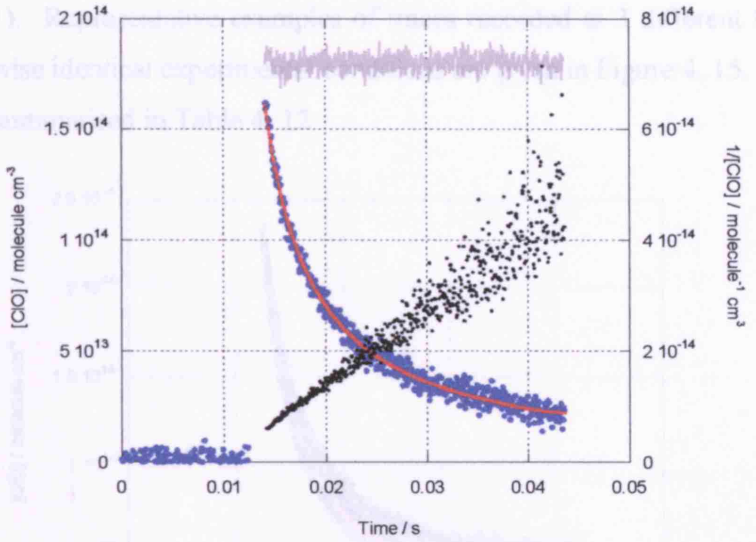

Figure 4. 14 Comparison of experimental ClO concentration (blue points) as a function of time and dimerisation model fit (red line). The residual between the experimental data and model (grey line) has been offset for clarity. Also shown is the associated second order reciprocal plot (black points).

4. 2. 2. 3 Ambient Temperature Results

The average of 72 determinations of $k_{4.2a}$ and $k_{-4.2a}$ at 298 K and 760 Torr ([M] = 2.46 × 10^{19} molecule cm^{-3}), over the range of Cl_2/Cl_2O concentrations consistent with maintaining rapid radical generation were $k_{4.2a} = (4.66 \pm 1.39) \times 10^{-13}$ cm^3 $molecule^{-1}$ s^{-1} and $k_{-4.2a} = (42.94 \pm 6.55)$ s^{-1} where errors are 2σ, statistical only. These results are in good agreement with those reported in the detailed ClO dimerisation study (using Br_2 as a precursor) discussed above, with previous published studies and with a previous study carried out by Boakes[31] in this laboratory that found $k_{4.2a} = (4.92 \pm 0.66) \times 10^{-13}$ cm^3 $molecule^{-1}$ s^{-1} and $k_{-4.2a} = (31.47 \pm 5.00)$ s^{-1}. No systematic variation of $k_{4.2a}$ and $k_{-4.2a}$ on initial reactant concentration was observed.

4. 2. 2. 4 Temperature Dependence

Low temperature experiments were carried out over the temperature range 250-300.3 K and traces analysed using ClO cross-sections calibrated for the appropriate temperature using (E4. 1). Representative examples of traces recorded at 3 different temperatures under otherwise identical experimental conditions are given in Figure 4. 15.
Results are summarised in Table 4. 12.

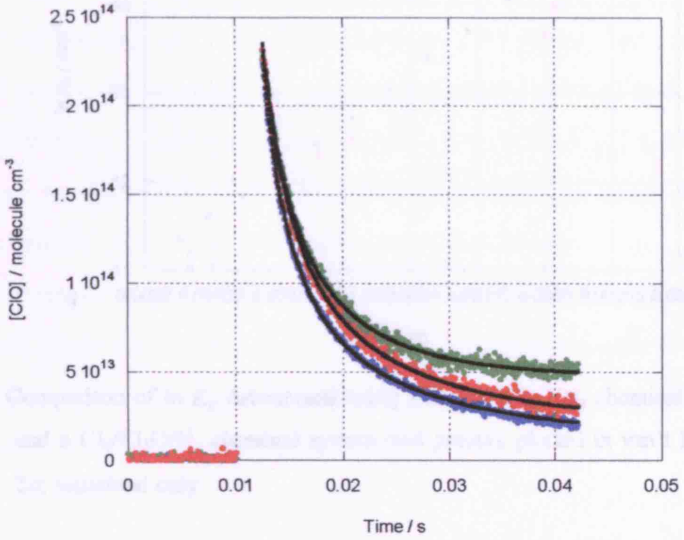

Figure 4. 15 Typical ClO concentrations as a function of time recorded at 3 different experimental temperatures, 250 K (blue points), 270 K (red points) and 285 K (green points) with associated dimerisation model fits (black lines).

T / K	$k_{4.2a}$ / 10^{-13} cm^3 molecule^{-1} s^{-1}	$k_{-4.2a}$ / s^{-1}	N° of Determinations
300.3	4.89 ± 0.29	53.91 ± 1.94	8
298.0	4.66 ± 0.16	42.94 ± 0.78	72
285.4	5.07 ± 0.14	14.38 ± 0.75	16
277.8	5.68 ± 0.12	N/A	30
270.0	6.14 ± 0.19	N/A	10
260.0	6.70 ± 0.20	N/A	8
250.0	8.01 ± 0.35	N/A	50

Table 4. 12 Determinations of $k_{4.2a}$and $k_{-4.2a}$ using classical analysis. Errors are 2σ, statistical only, and have been divided by $n^{1/2}$ to account for non-equivalence of sample sizes.

Over the common temperature range with this low temperature study, the forward and reverse rate coefficients give equilibrium constants in agreement with the thermochemical study discussed in Section (4. 2. 1. 6) above, as shown in Figure 4. 16.

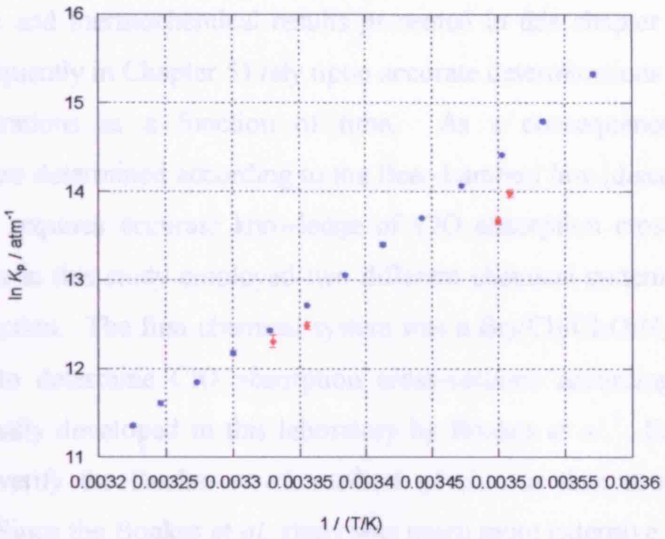

Figure 4. 16 Comparison of ln K_p determined using a $Br_2/Cl_2/Cl_2O/N_2$ chemical system (blue points) and a $Cl_2/Cl_2O/N_2$ chemical system (red points), plotted in van't Hoff form. Errors are 2σ, statistical only.

Furthermore, results for $k_{4.2a}$ compare extremely well to a previous study from this laboratory, plotted in Arrhenius form in Figure 4. 17.

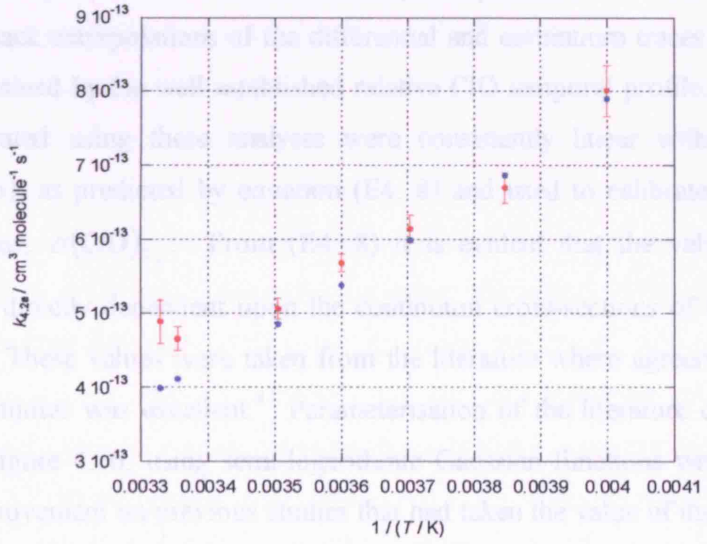

Figure 4. 17 Comparison of $k_{4.2a}$ as a function of temperature as determined by this study (red points) compared to that of Boakes[3] (blue points). Errors are 2σ, statistical only.

4. 3 Discussion

4. 3. 1 Use of ClO Differential Cross-sections and Spectral Fitting

Both the kinetic and thermochemical results presented in this chapter (and the results presented subsequently in Chapter 5) rely upon accurate determinations of absolute ClO radical concentrations as a function of time. As a consequence, since radical concentrations are determined according to the Beer-Lambert law (discussed in detail in Chapter 2) this requires accurate knowledge of ClO absorption cross-sections. The work carried out in this study employed two different chemical systems to characterise the ClO self-reaction. The first chemical system was a $Br_2/Cl_2/Cl_2O/N_2$ gas system and this was used to determine ClO absorption cross-sections according to an analysis technique originally developed in this laboratory by Boakes *et al.*[3] Experiments were carried out to verify the Boakes *et al.* method which was then used in subsequent investigations. Since the Boakes *et al.* study was much more extensive than this one the ClO absorption cross-sections determined in this study were normalised to the parameters determined by Boakes *et al.*

The method developed by Boakes *et al.* for determining σ(ClO) and subsequently used in this work offers advantages over previous single or dual wavelength methods. Simultaneous recording of spectral structure as well as spectral continuum using the CCD detector precludes the need for multiple experiments at different wavelengths. The short back extrapolations of the differential and continuum traces were robust and were constrained by the well established relative ClO temporal profile. The calibration plots generated using these analyses were consistently linear with zero intercepts (Figure 4. 5), as predicted by equation (E4. 8) and used to calibrate ClO differential cross-sections, $\sigma(\mathrm{ClO})_{\lambda_d}$. From (E4. 8) it is evident that the value of $\sigma(\mathrm{ClO})_{\lambda_d}$ obtained is directly dependent upon the continuum cross-sections of ClO and Cl_2O at 257.5 nm. These values were taken from the literature where agreement between the numerous studies was excellent.[4] Parameterisation of the literature cross-sections, as shown in Figure 4. 6, using semi-logarithmic Gaussian functions was successful and was an improvement on previous studies that had taken the value of the cross-section to be a linear interpolation between reported values.[21] The differential cross-sections used

in this study will, however, potentially contain systematic errors resulting from possible errors in the continua cross-sections used at the calibrating wavelength, estimated by NASA to be 10% on each.[4] Consequently, since from (E4. 8) the difference between the continuum cross-sections is used, the final differential ClO absorption cross-section will contain a possible systematic error of approximately 14%.

The ClO differential absorption cross-sections reported for this study are for the (12, 0) band at 275.2 nm and the associated trough to higher wavelength, consistent with the work of Boakes *et al.* and Bloss *et al.*[21], degraded to account for lower resolution in this study. Temperature dependent values of σ(ClO) obtained for this study lie within but close to the lower limit of error for the parameterisation, over a broad temperature range, reported by Boakes *et al.* (Figure 4. 7), although individual points near 298 K are consistent (Section 4. 2. 2. 3). Both this study and Boakes *et al.* report a weak negative temperature dependence compared to the study of Bloss *et al.* reporting a quadratic temperature dependence, with a near zero temperature dependence over the temperature range used in this study.

The differential fitting routine used in this study to fit ClO absorption cross-sections to sequential absorbance spectra (as described in Chapter 3, and shown in Figure 3. 6) ensured that ClO radical concentrations were determined unequivocally. This analysis technique offers considerable advantages over methods used in previous studies. Previous investigations have typically used single wavelength monitoring, at a chosen vibronic peak of the ClO absorption spectrum,[5, 19, 20] or dual wavelength monitoring at a single peak and the adjacent trough.[21] In all of these previous cases monitoring of experimental absorbances will have recorded a composite time-resolved absorption signal at the chosen wavelength(s). This signal will contain contributions from all UV absorbing species present in the gas mixture, which must in principle be accounted for in the analysis procedure, inevitably increasing the chance of error on the result. Unforeseen errors may also occur when measuring absorbance at a single peak. This kind of measurement relies on extremely well defined wavelength calibration. During this study, even though routine wavelength calibrations were carried out, using well known peaks from a mercury lamp, small (< 0.5 nm) shifts in wavelength were often necessary to optimise the fit of a ClO reference absorption cross-section to the

experimental spectrum. These shifts could be attributed to small movements in the wavelength calibration of the spectrometer over the course of the experiments. It is possible that this effect is unique to the apparatus used for this study, but if similar shifting were to occur in single or dual wavelength monitoring not only would it be very difficult to recognise and adjust for, but it could profoundly affect the perceived σ(ClO), and consequently kinetic results determined from this.

4. 3. 2 Kinetics of the ClO Self-Reaction

The kinetics of the ClO self-reaction were studied using two separate chemical systems. The first, $Br_2/Cl_2/Cl_2O/N_2$ gas system, was used for a high temperature study (T = 280-310 K) where the kinetic parameters determined were ultimately used for a thermochemical study of the Cl_2O_2 dimer, the results of which are discussed in the following section. The second, $Cl_2/Cl_2O/N_2$ gas system, was employed in a low temperature study (T = 250-300.3 K) in an attempt to assess how valid the use of such a chemical system would be in subsequent investigations of the ClO + HO_2 reaction (described in Chapter 5). Regardless of the source of ClO radicals the kinetic parameters for the self-reaction should, of course, be comparable.

As discussed previously, the association of ClO and subsequent dissociation of the Cl_2O_2 dimer requires a third body, M, and are therefore both dependent upon pressure. In principle the observed bimolecular association rate constant and unimolecular dissociation rate constant may be converted to termolecular and bimolecular rate constants, respectively, through division by [M]. The results of this study, carried out at ambient pressure, lie within a so called 'fall-off' region (discussed in Chapter 2 and shown in Figure 2. 3) where the kinetics of ClO association are between third and second order. The kinetics of this study may therefore be described adequately using the Lindemann mechanism as described in Section 2. 3. 2. A full pressure dependence study of ClO association has been carried out in this laboratory in the extensive study by Boakes.[31] This study subsequently used the Troe parameterisaiton of kinetic parameters as a function of pressure (described in Section 2. 3. 2) to obtain the kinetic parameters k_0 and k_∞. The forward and reverse rate constants reproduced from this parameterisation,

along with the current NASA recommendation[4] for $k_{4.2a}$ and $k_{-4.2a}$ are compared to the data generated in this study in Figure 4. 18 (a) and (b) below.

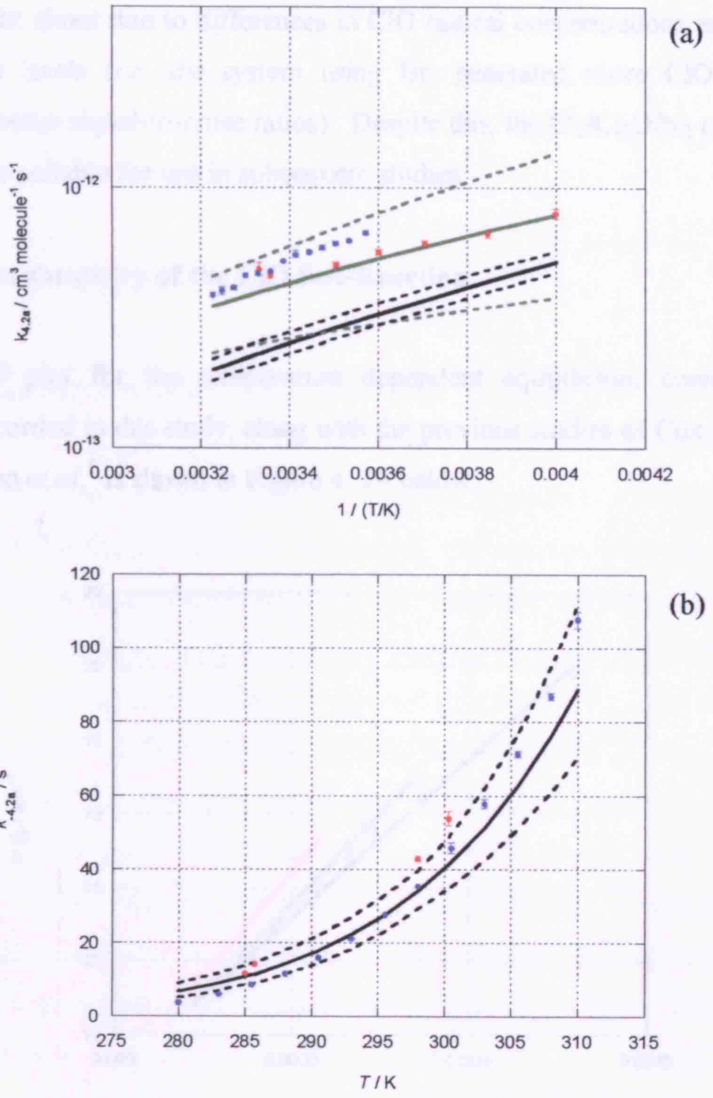

Figure 4. 18 (a) $k_{4.2a}$ plotted in Arrhenius form. Plotted are the results for the two different chemical systems used in this study, $Br_2/Cl_2/Cl_2O/N_2$ (blue points), $Cl_2/Cl_2O/N_2$ (red points) with errors of 2σ, statistical only. Also plotted is the parameterisation of the forward rate constant by Boakes *et al.* (green line) and associated error (green dashed line) and the NASA recommendation[4] (black line) with error limits (black dashed line).

(b) $k_{-4.2a}$ as a function of temperature determined in the two different chemical systems of this work, $Br_2/Cl_2/Cl_2O/N_2$ (blue points), $Cl_2/Cl_2O/N_2$ (red points) where errors are 2σ, statistical only, and the current NASA recommendation[4] (black line) with associated error limits (black dashed line).

Results from the two different chemical systems employed in this study compare well to each other and to the parameterisation of Boakes *et al.* Any small discrepancies between the two chemical systems used may indicate differences in sensitivity to the kinetics brought about due to differences in ClO radical concentrations and subsequent signal-to-noise levels (*i.e.* the system using Br_2 generated more ClO radicals and therefore had better signal-to-noise ratios). Despite this, the $Cl_2/Cl_2O/N_2$ produced good results and was suitable for use in subsequent studies.

4. 3. 3. Thermochemistry of the ClO Self-Reaction

A van't Hoff plot for the temperature dependent equilibrium constant for ClO association recorded in this study, along with the previous studies of Cox and Hayman[12] and Nickolaisen *et al.*[5] is shown in Figure 4. 19 below.

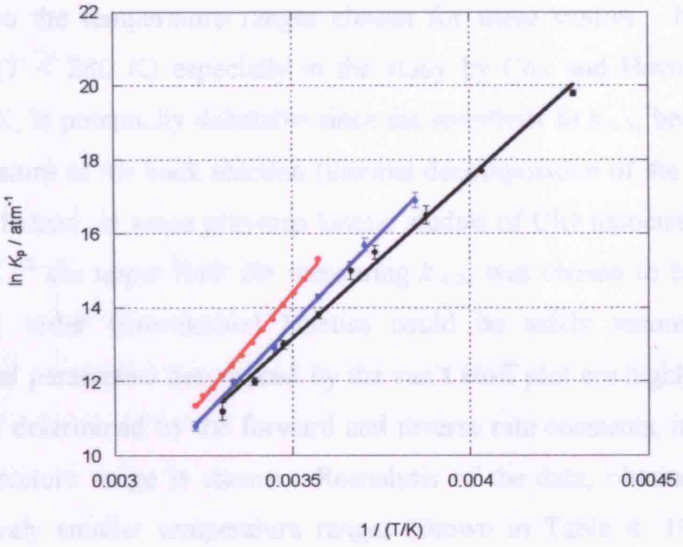

Figure 4. 19 ln K_p determined in this work (red points) with van't Hoff parameterisation (red line) compared to the studies of Cox and Hayman[12] (black points and line) and Nickolasien *et al.*[5] (blue points and line).

In comparison, results from this study are in broad agreement with those of previous studies. Differences in the gradients of the plots are however present, clearly evident when comparing the thermochemical parameters determined from the gradient and intercept of the plots, as given in Table 4. 13.

Reference	$-\Delta_r H^\circ$ / kJ mol^{-1}	$-\Delta_r S^\circ$ / J K^{-1} mol^{-1}
This work	93.74 ± 1.13	208.37 ± 3.82
Cox and Hayman.[12]	72.5 ± 3	144.0 ± 16.6
Nickolaisen *et al.*[5]	81.6 ± 2.9	173.2 ± 10.0
Plenge *et al.*[25]	72.39 ± 2.8	
NASA recommendation[4]	74.5 ± 12.6	150.6

Table 4. 13 Comparison of current thermochemical data for the ClO dimerisation available in the literature to that determined in this work.

The thermochemical parameters reported by this work are the largest (magnitude) recorded to date, with $\Delta_r H^\circ$ over 10 kJ mol^{-1} more negative than that of Nickolaisen *et al.* and some 20 kJ mol^{-1} more negative than Cox and Hayman and Plenge *et al.* Careful consideration of the results reported by Cox and Hayman and Nickolaisen *et al.* raise questions as to the temperature ranges chosen for these studies. Inclusion of low temperatures (T < 280 K) especially in the study by Cox and Hayman, which went down to 233 K, is potentially debatable since the sensitivity to $k_{-4.2a}$ becomes negligible at low temperature as the back reaction (thermal decomposition of the dimer) becomes insignificant. Indeed, in some previous kinetic studies of ClO association, such as that of Bloss *et al.*,[21] the upper limit for measuring $k_{-4.2a}$ was chosen to be 245 K, below which second order (irreversible) kinetics could be safely assumed. Since the thermochemical parameters determined by the van't Hoff plot are highly sensitive to the gradient, itself determined by the forward and reverse rate constants, it is crucial that a suitable temperature range is chosen. Reanalysis of the data, obtained in this study, over successively smaller temperature ranges (shown in Table 4. 10) highlights the sensitivity of the thermochemical parameters to the van't Hoff plot gradient. This analysis showed the value of $\Delta_r H^\circ$ determined to vary over some 10 kJ mol^{-1} depending on the chosen temperature range. This effect is further stressed on close inspection of the Cox and Hayman data, reanalysis of which, excluding the four lowest temperature points results in a decrease in both $\Delta_r H^\circ$ and $\Delta_r S^\circ$, giving values of $\Delta_r H^\circ$ = -(86.12 ± 3.62) kJ mol^{-1} and $\Delta_r S^\circ$ = -(191.57 ± 12.61) J K^{-1} mol^{-1}.

The variation in thermochemical parameters gained from the plots of this work and that of Cox and Hayman depending on the temperature range used may also indicate a degree of curvature in these plots. This could be accounted for by a temperature dependent systematic error in the data. Alternatively, curvature in these plots may indicate that ClO association occurs *via* more than one channel in competition with another, over the small temperature range investigated, and hence takes place through more than one isomer of the Cl_2O_2 dimer. Indeed, recent *ab initio* studies do predict that ClO association proceeds resulting in both ClOOCl (widely accepted to be the only stable form of the Cl_2O_2 dimer) and the asymmetrical ClOClO.[32] If the ClOClO dimer did form in the atmosphere the effect would be to offset the odd-oxygen destroying efficiency of the ClO self-reaction through likely photolysis to Cl + OClO, and subsequent OClO photolysis to O + ClO. The existence of a secondary ClO association channel, with different related thermochemical parameters, might also account for a change in gradient of the van't Hoff plot.

The direct measurement of $\Delta_r H^o$ by Plenge *et al.*,[25] using photoionisation mass spectrometry, assumed that even though the gas mixture was shown to be composed only (83 ± 2)% of the ClOOCl isomer, upon ionisation of low temperature mixtures, ClO^+ fragmentation was 100% from ClOOCl. Thermal corrections that relied on data in the literature were also applied to their final result to give $\Delta_r H^o$ at 298 K, with associated uncertainties. Interestingly, the extensive study of Plenge *et al.* appears to confirm the lower K_c values of Cox and Hayman,[12] but are not in accord with analysis of *in situ* high altitude aircraft measurements of ClO abundances.[33] However, care should be taken using field observational data to extract kinetic and thermochemical parameters for isolated reactions. Given the uncertainty in the all the reported data and the importance of the stability of the Cl_2O_2 dimer in polar O_3 chemistry, further studies of these parameters are surely warranted.

4. 4 References

1. L. Molina and M. Molina, *J. Phys. Chem.*, **1987**, 91, 433.
2. WMO, *Scientific Assessment of Ozone Depletion: 2002*, World Meteorological Association, Geneva, **2002**.
3. G. Boakes and D.M. Rowley, *Phys. Chem. Chem. Phys.*, **2005**, 7, 24, 4102.
4. S.P. Sander, R.R. Friedl, D.M. Golden, M.J. Kurylo, R.E. Huie, V.L. Orkin, G.K. Moortgat, A.R. Ravishankara, C.E. Kolb, and M.J. Molina, *Chemical Kinetics and Photochemical Data for Use in Atmospheric Studies*, JPL Publication 02-25, Jet Propulsion Laboratory, Pasadena, CA, **2002**.
5. S. Nickolaisen, R. Friedl, and S. Sander, *J. Phys. Chem.*, **1994**, 98, 155.
6. M.M. Rochkind and G.C. Pimentel, *J. Chem. Phys.*, **1967**, 46, 4481.
7. W.G. Alcock and G.C. Pimentel, *J. Chem. Phys.*, **1968**, 48, 2373.
8. M. McGrath, K. Clemitshaw, F. Rowland, and W. Hehre, *J. Phys. Chem.*, **1990**, 94, 6126.
9. J. Stanton, C. Rittby, R. Bartlett, and D. Toohey, *J. Phys. Chem.*, **1991**, 95, 2107.
10. M. Birk, R. Friedl, E. Cohen, H. Pickett, and S. Sander, *J. Chem. Phys.*, **1989**, 91, 6588.
11. W. DeMore and E. Tschuikow-Roux, *J. Phys. Chem.*, **1990**, 94, 5856.
12. R. Cox and G. Hayman, *Nature*, **1988**, 322, 28, 796.
13. G. Porter and F. Wright, *Discuss. Faraday Soc.*, **1953**, 14, 23.
14. H. Johnston, E. Morris Jr, and J. Van den Bogaerde, *J. Am. Chem. Soc.*, **1969**, 91, 7712.
15. R. Cox, R. Derwent, A. Eggleton, and J. Reid, *J. Chem. Soc. Faraday Trans. I*, **1979**, 75, 1648.
16. N. Basco and J. Hunt, *Int. J. Chem. Kinet.*, **1979**, 61, 649.
17. T. Ellerman, K. Johnsson, A. Lund, and P. Pagsberg, *Acta. Chem. Scand.*, **1995**, 49, 25.
18. G. Hayman, J. Davies, and R. Cox, *Geophys. Res. Lett.*, **1986**, 13, 1347.
19. S. Sander, R. Friedl, and Y. Yung, *Science*, **1989**, 145, 1095.
20. M. Trolier, R. Mauldin, and A. Ravishankara, *J. Phys. Chem.*, **1990**, 94, 4896.
21. W. Bloss, S. Nickolaisen, R. Salawitch, R. Friedl, and S. Sander, *J. Phys. Chem. A*, **2001**, 105, 11226.

22. M. Clyne and J. Coxon, *Proc. Roy. Soc.*, **1968**, 303, 207.

23. J. Troe, *J. Chem. Phys.*, **1977**, 66, 4745.

24. W.B. DeMore, S.P. Sander, D.M. Golden, R.F. Hampson, M.J. Kurylo, C.J. Howard, A.R. Ravishankara, C.E. Kolb, and M.J. Molina, *Chemical Kinetics and Photochemical Data for Use in Stratospheric Modelling*, JPL Publication 02-25, Jet Propulsion Laboratory, Pasadena, CA, **1997**.

25. J. Plenge, S. Kuhl, B. Vogel, R. Muller, F. Stroh, M. von Hobe, R. Flesch, and E. Ruhl, *J. Phys. Chem.*, **2005**, 109, 6730.

26. C.N. Hinshelwood and C.R. Pritchard, *J. C. S.*, **1923**, 123, 2730.

27. Y. Bedjanian, G. Laverdet, and G. LeBras, *J. Phys. Chem.*, **1998**, 102, 953.

28. F. Simon, W. Schneider, G. Moortgat, and J. Burrows, *J. Photochem. and Photobio. A: Chem.*, **1990**, 55, 1.

29. M. Mandelman and R. Nicholls, *J. Quantum Spec. and Rad. Trans.*, **1977**, 17, 483.

30. H. Knauth, H. Alberti, and H. Clausen, *J. Phys. Chem.*, **1979**, 83, 1604.

31. G. Boakes, *PhD Thesis*, University of London, **2003**.

32. R.S. Zhu and M.C. Lin, **2003**, 118, 9, 4094.

33. L. Avallone and D. Toohey, *J. Geophys. Res.*, **2001**, 106, 10, 411.

Chapter 5
The ClO + HO_2 Reaction

The most recent assessment of stratospheric O_3 depletion by the World Meteorological Organisation[1] indicates that atmospheric models are still unable to predict atmospheric O_3 abundances accurately. In the lower stratosphere (altitude 15-21 km), model calculations underestimate observed trends by at least a factor of 2. Discrepancies between the observed and modelled trends arise due to uncertainties in model dynamics and/or knowledge of atmospheric chemistry. An increased understanding of the kinetics of reactions shown to have atmospheric significance is therefore of importance in understanding the atmospheric O_3 budget.

Whilst it is traditional and convenient to group atmospheric trace species into chemical families, such as ClO_x, NO_x, HO_x and to study reactions within such families (as shown in Chapters 4 and 6), it is now well recognised that many significant atmospheric cycles incorporate reactions that couple different chemical families together. Studying the interactions between radical families requires more complicated chemical schemes in the laboratory and hence proves a much greater experimental challenge. As a result, despite their considerable atmospheric significance, mixed radical cross-reactions are much less well characterised than their self-reaction counterparts.

Field measurements of inter-related reactive species in the stratosphere aim to determine relative amounts of such species. Using field measurements and taking into account the current understanding of reaction kinetics and dynamics, the reactions that have been highlighted to be the most important at mid-latitudes in the lower stratosphere are ClO + HO_2, BrO + HO_2 and ClO + BrO.[2, 3] Indeed, using measurements from the recent SPADE (Stratospheric Photochemistry, Aerosols and Dynamics Expedition) campaign, the ClO + HO_2 reaction and subsequent photochemistry is predicted to account for up to 30% of the total halogen mediated O_3 loss at these altitudes and latitudes.[4]

Despite the highlighted atmospheric significance of the ClO + HO_2 reaction, the current kinetic and mechanistic database for this reaction shows severe discrepancies. To date there have been only three published temperature dependence studies, all of which are

conflicting, especially at temperatures relevant to the stratosphere. These studies are discussed in detail in Section 5. 2.

5. 1 Reaction Channels

The possible exothermic bimolecular reaction channels for the ClO + HO_2 reaction are:

(5. 1a) $ClO + HO_2 \rightarrow HOCl + O_2$ $\Delta_r H_{298}^5 = -180$ kJ mol^{-1}

(5. 1b) $ClO + HO_2 \rightarrow HCl + O_3$ $\Delta_r H_{298}^5 = -50$ kJ mol^{-1}

(5. 1c) $ClO + HO_2 \rightarrow HClO + O_2$

Considering the reaction enthalpies above, channel (5. 1a) is expected to be the dominant pathway for the ClO + HO_2 reaction and this has been supported by experimental observations.[6-9] The rate of this process and the subsequent fate of HOCl are consequently of profound atmospheric significance. As discussed below however, the possibility of this reaction branching to other channels also has potential importance when considering the effect this reaction has upon stratospheric O_3 levels.

It has also been suggested that a termolecular association channel to form an $HClO_3$ species may exist:[6, 10-17]

(5. 1d) $ClO + HO_2 + M \rightarrow HOOOCl + M$

(5. 1e) $ClO + HO_2 + M \rightarrow HOOClO + M$

5. 2 The ClO + HO_2 Reaction in the Atmosphere

The principal product of the ClO + HO_2 reaction, HOCl, is likely to photolyse rapidly in sunlight with a typical lifetime against photodissociation in the stratosphere of around 2×10^3 s.[18] The effect that HOCl formation has is therefore dependent on the photolysis products.

The major photolytic products of HOCl are OH and Cl:[19]

(5. 2a) $HOCl + h\nu \rightarrow OH + Cl \quad (\lambda < 503\ nm)$

In the stratosphere, both OH and Cl could reform HO_2 and ClO respectively through the subsequent reaction with O_3, thereby completing a catalytic O_3 loss cycle:[20, 21]

(5. 1a) $ClO + HO_2 \rightarrow HOCl + O_2$

(5. 2a) $HOCl + h\nu \rightarrow OH + Cl$

(5. 3) $Cl + O_3 \rightarrow ClO + O_2$

(5. 4) $OH + O_3 \rightarrow HO_2 + O_2$

Net: $2O_3 \rightarrow 3O_2$

Under conditions in which reaction (5. 2a) is rapid, and given the excess of O_3 in the stratosphere, reaction (5. 1a) will be the rate determining step for this cycle.

An alternative channel for HOCl photolysis is H atom formation *via* channel (5. 2b).[10] In the atmosphere, however, this channel would have no net effect on O_3 depletion since the H atoms would react rapidly with excess O_2 forming HO_2 and hence process (5. 2b) is simply the reverse of the original ClO + HO_2 reaction.

(5. 2b) $HOCl + h\nu \rightarrow ClO + H \quad (\lambda < 301\ nm)$

A third potential channel for HOCl photolysis has been suggested forming HCl:[10]

(5. 2c) $HOCl + h\nu \rightarrow HCl + O \quad (\lambda < 508\ nm)$

In the stratosphere, the existence of channel (5. 2c) would result in a decrease in perceived O_3 loss by increasing the fraction of Cl held inactive with respect to O_3 loss in reservoir form (the Cl reservoir, HCl, does not take part in odd oxygen destruction

cycles). Furthermore, an oxygen atom is formed in channel (5. 2c) mitigating odd-oxygen loss. The occurrence of this bond forming channel does however, seem somewhat unlikely.

Whilst it is difficult to envisage HCl formation from HOCl photolysis, formation of HCl in channel (5. 1b) of the ClO + HO_2 reaction has been suggested[22] and is likely to diminish O_3 loss by reaction with Cl atoms and produce an O_3 molecule. Indeed, given the catalytic nature of O_3 destruction through the ClO + HO_2 reaction producing HOCl and in turn OH + Cl, even a small (1%) branching ratio to HCl in reaction (5. 1b) could have a disproportionately large effect since the chain length of the O_3 loss cycle is reduced. As an illustration of this, consider the O_3 loss cycle reactions (5. 1a), (5. 2a), (5. 3)-(5. 4). For each cycle, if ClO + HO_2 reacts only to give HOCl and O_2 then the number of O_3 molecules lost *per* cycle is 2 and the total potential number of O_3 lost is essentially infinite. If however some of the ClO + HO_2 reaction branched to give HCl and O_3 the loss *per* cycle is successively reduced. Thus, the number of O_3 molecules destroyed overall by this cycle is effectively a converging geometric series, as shown in Figure 5. 1, and the sum of O_3 molecules destroyed by multiple cycles through this reaction sequence may be calculated.

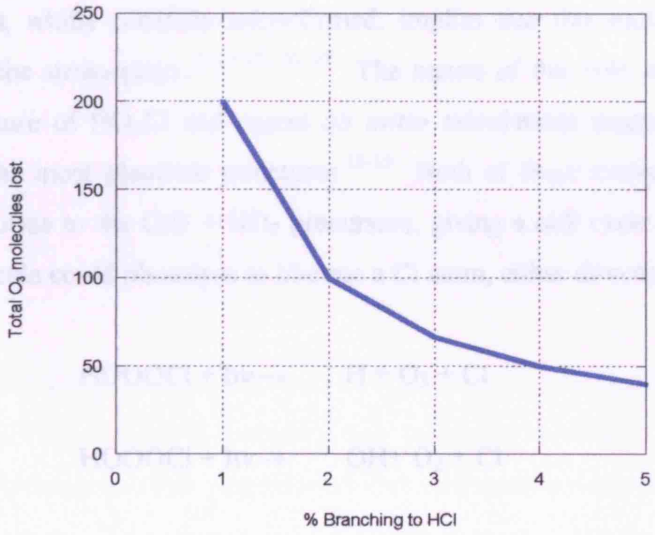

Figure 5. 1 Maximum number of O_3 molecules destroyed *per* kinetic chain length as a function of percentage branching to the HCl forming channel (5. 1b).

Whilst such a simplistic calculation as presented in Figure 5. 1 gives an unrealistic assessment of the total O_3 loss through the ClO + HO_2 reaction, it is interesting to note that the maximum possible change in O_3 is profoundly reduced by even a small branching ratio to HCl. This is also confirmed by modelling studies which indeed show that even if HCl formation accounted for only a few percent of the ClO + HO_2 cycle then the perturbation to the Cl_y/HCl (where Cl_y is the total inorganic chlorine) partitioning could be significant.[2, 23-25] As a result, the predicted O_3 loss due to Cl would be less significant and the overall O_3 loss would be reduced due to HCl formation being accompanied by O_3 formation.

If HClO is formed as a product of the ClO + HO_2 reaction then all subsequent stratospheric routes will lead to HCl formation and consequent mitigation of O_3 loss:[6]

(5. 5) $HClO + O_2 \rightarrow HCl + O_3$

(5. 6) $HClO + O_3 \rightarrow HCl + O_2$

(5. 7) $HClO + h\nu \rightarrow HCl + O$

The suggestion that a HO_3Cl species might be formed and stabilised following the ClO + HO_2 reaction, whilst currently unconfirmed, implies that this molecule could also have a role in the stratosphere.[7, 10-17, 26, 27] The nature of this role will be dependent upon the structure of HO_3Cl and recent *ab initio* calculations suggest HOOOCl and HOOClO are the most plausible structures.[13-15] Both of these molecules could most obviously photolyse to the ClO + HO_2 precursors, giving a null cycle. In addition, the HOOOCl molecule could photolyse to liberate a Cl atom, either directly:

(5. 8a) $HOOOCl + h\nu \rightarrow H + O_3 + Cl$

(5. 8b) $HOOOCl + h\nu \rightarrow OH + O_2 + Cl$

or *via* production of unstable ClOO:

(5. 8c) $HOOOCl + h\nu \rightarrow OH + ClOO$

(5. 9) $ClOO + M \rightarrow O_2 + Cl + M$

In terms of O_3 loss this latter case would effectively be the same as HOCl formation and subsequent photolysis, the efficiency of which would depend on the photostability of the HO_3Cl molecule. By contrast HOOClO could photolyse to OH + OClO. Subsequent photolysis of OClO generates an O atom thereby mitigating odd-oxygen destruction. As discussed below however, no solid evidence for an association channel of ClO + HO_2 has yet been presented, although discrepancies observed in this work compared with previous studies could potentially arise from transient radical association.

5. 3 Previous Studies

Reimann and Kaufmann[28] first published ambient temperature kinetic data for the ClO + HO_2 reaction in 1978. The study was carried out using the discharge flow technique, results from which are summarised along with those from other studies in Table 5. 1. The source for HO_2 radicals in these initial experiments was reaction (5. 10):

(5. 10) $\quad H + O_2 + M \rightarrow HO_2 + M$

where H atoms were formed by passing H_2 through a microwave discharge. ClO was formed through the reaction of excess O_3 with Cl generated by microwave discharge of Cl_2 in excess He:

(5. 3) $\quad Cl + O_3 \rightarrow ClO + O_2$

Pseudo-first order loss of HO_2 in the presence of excess ClO was indirectly monitored by converting HO_2 stoichiometrically to OH *via* titration with excess NO. OH concentrations were measured using laser induced fluorescence.

Subsequent to this initial study Stimpfle *et al.*[10] were able to carry out direct detection of both ClO and HO_2 radicals by coupling laser magnetic resonance detection with the discharge flow technique. This was also the first temperature dependence study of the ClO + HO_2 reaction. Two sources of ClO were used by Stimpfle *et al.*, Cl + O_3, reaction (5. 3), and Cl + Cl_2O, reaction (5. 11) where in both cases Cl atoms were formed using a microwave discharge.

(5. 11) $\quad Cl + Cl_2O \rightarrow ClO + Cl_2$

Analogous to the previous study, the source of HO_2 was the H + O_2 + M reaction, (5. 10). All measurements were made under pseudo-first order conditions with ClO in excess. Stimpfle *et al.* recorded $k_{5.1}$ at five temperatures over the range 235-393 K. A non-linear temperature dependence was reported at temperatures below 298 K. One proposed explanation by Stimpfle *et al.* for the observed temperature dependence was that the ClO + HO_2 reaction may occur *via* two different mechanisms involving short lived HO_3Cl intermediates:

(5. 1d) $ClO + HO_2 \leftrightarrow HOOClO \rightarrow HOCl + O_2$

(5. 1e) $ClO + HO_2 \leftrightarrow HOOOCl \rightarrow HCl + O_3$

Since neither the Reimann and Kaufmann nor the Stimpfle *et al.* studies of the ClO + HO_2 reaction had the ability to offer identification of species other than the reacting radicals no further speculation into possible reaction mechanisms was possible at this time. Stimpfle *et al.* did however use bond additivity rules to estimate the bond dissociation energies for each of the HO_3Cl intermediate species and on this basis speculated that channel (5. 1d) would be favoured. Stimpfle *et al.* found the ClO + HO_2 rate coefficient to be *ca.* 60% faster that that determined by Reimann and Kaufmann. The origin of this discrepancy was, and remains, unknown.

A subsequent 298 K study of the ClO + HO_2 reaction by Leck *et al.*[6] used discharge flow coupled with mass spectrometry and hence did permit the identification of products. These authors found that HOCl was the major product of the ClO + HO_2 reaction and indeed measured the rate coefficient for this reaction using detection of HOCl. The technique also permitted the direct detection of ClO radicals as well as many other precursor, reactant and product species. In a similar fashion to Reimann and Kaufmann, HO_2 concentrations were determined indirectly, in the absence of ClO, *via* reaction of HO_2 with excess NO to form OH. As with previous work ClO radicals were generated using the reaction of Cl with O_3, reaction (5. 3). In this work, however, HO_2 was formed in one of two chemical schemes, H + O_2 + M, reaction (5. 10), or Cl + H_2O_2:

(5. 12) $Cl + H_2O_2 \rightarrow HCl + HO_2$

Kinetic results from both sources of HO_2 were in good agreement with one another, and at 298 K results compare well to those of Reimann and Kaufmann

Leck *et al.* also carried out experiments to determine the branching of the ClO + HO_2 reaction to give different products. Ion current signals due to HCl^+ proved difficult to detect due to background interference from other chlorine containing compounds, so Leck *et al.* attempted to look for signals due to O_3 in order to place limits on the branching to the reaction channel (5. 1b). $HOCl^+$ was also monitored directly in order to quantify this channel branching. For these experiments the source of HO_2 used was either reaction (5. 10) or reaction (5. 12) and the source of ClO was amended to either Cl + Cl_2O, reaction (5. 11) or reaction (5. 13).

(5. 13) $\quad Cl + OClO \rightarrow ClO + ClO$

Through monitoring both the O_3^+ (*m/e* = 48) and the $HOCl^+$ (*m/e* = 52) ion currents Leck *et al.* placed an upper limit of 2% on the reaction channel (5. 1b) leading to HCl + O_3 formation at 298 K.

Burrows and Cox[7] studied the ClO + HO_2 reaction at 298 K using modulated photolysis coupled with UV spectroscopy. Photolysis of $Cl_2/Cl_2O/H_2/O_2/N_2$ mixtures was used with the H_2 + Cl reaction and subsequent combination of H + O_2, reaction (5. 10), used as a source of HO_2 and the Cl + Cl_2O reaction (5. 11) and Cl_2O photolysis as the source of ClO.

(5. 14a) $\quad Cl_2O + h\nu \rightarrow Cl + ClO$

ClO and HO_2 were produced at approximately the same rates and observing the phase lag of radical concentrations behind the modulated photolysis light source was used to extract kinetic parameters. The 298 K results of Burrows and Cox were in good agreement with the previous study by Leck *et al.* Burrows and Cox were also able to place an upper limit on the rate of HCl formation by using chemiluminescence to observe O_3 production, resulting in an upper limit of branching to HCl of 0.3% at 298 K.

Leu[8] carried out a study of the product distribution of the ClO + HO_2 reaction using discharge flow coupled with mass spectrometry. HOCl was observed and used to place limits on branching to the HCl channel ($k_{5.1b}/k_{5.1}$) of < 0.015 at 298 K and < 0.03 at 248 K. No significant O_3 production was observed.

The formation of a radical association complex, HO_3Cl, might be expected to be accompanied by an observed pressure dependence. A review of the kinetic studies to this point shows that at 298 K, the low pressure studies of Reimann and Kaufmann, Stimpfle *et al.*, Leck *et al.* and Leu are consistent with the higher pressure study of Burrows and Cox indicating no pressure dependence, although the uncertainties in the Burrows and Cox study are large and therefore a dependence could not be ruled out. Cattell and Cox[26] investigated the pressure dependence of the ClO + HO_2 reaction at 298 K using molecular modulation coupled with UV absorption spectroscopy. Cattell and Cox saw no clear indication of a pressure dependence. However, Cattell and Cox did recognise that due to a possible change in mechanism at low temperatures, indicated by the strong negative non-Arrhenius temperature dependence observed by Stimpfle *et al.*, the pressure dependence should be investigated at temperatures < 250 K. To date this recommendation has not been followed up.

The first theoretical study to address the mechanism of the ClO + HO_2 reaction was carried out by Mozurkewich.[27] Using RRKM theory, the study could not reproduce the negative temperature dependence observed by Stimpfle *et al.* Calculations indicated large barriers to radical cyclisation suggesting the reaction is likely to proceed *via* an H-bonded intermediate on the triplet surface.

Toohey and Anderson[11] also tackled the problem of the ClO + HO_2 reaction mechanism using *ab initio* calculations. This study calculated the saddle-point geometry and energy for hydrogen abstraction from HO_2 by ClO, as well as a number of other species. Results suggested that more than one mechanism may be present depending on the temperature. At high temperatures calculations suggested that the mechanism was primarily direct H atom abstraction. At low temperatures elimination to form a stable intermediate was shown to dominate.

Buttar and Hirst[12] performed MP2. (Møller-Plesset second order perturbation theory) level theory on both the singlet and triplet surface. They predicted a 1,2-H shift from HOOOCl → HOCl + O_2 on the singlet surface and direct H-abstraction if the reaction proceeds on the triplet surface.

The most detailed experimental investigation of product formation of the ClO + HO_2 reaction has been carried out by Finkbeiner *et al.*[9] Matrix isolation coupled with FTIR was employed over the temperature range 210-300 K. $Cl_2/Cl_2O/H_2/O_2$ gas mixtures were used for radical generation and HOCl, O_3, OClO, H_2O_2, HCl and Cl_2O were all measured within the matrix. At all experimental temperatures, HOCl was observed as the major product, using the absorbance of the band at 1235 cm^{-1}. This agrees with previous studies and the assumption that channel (5. 1a), leading to HOCl formation, is the dominant pathway. HCl and O_3 were both detected, but since HCl had other sources in this gas system (Cl + H_2) that could not be quantified easily, only O_3 could be used to quantify the extent that the HCl forming channel, (5. 1b), contributed to the product branching. As with HOCl, O_3 was observed at all temperatures. However, like HCl, O_3 had an additional source other than channel (5. 1b). This was from OClO photolysis following its generation in the ClO self-reaction. As a result, qualification of the source of O_3 relied on accurate kinetic and mechanistic characterisation of the ClO self-reaction. Finkbeiner *et al.* relied on kinetic data for the ClO self-reaction from Nickolaisen *et al.*[13] In contrast with previous studies, in which O_3 production was not observed, results from this study show that branching to HCl ranges from < 1% at 300 K to (5 ± 2)% at 210 K. A full assessment of all other possible sources of O_3 within the chemical system used was carried out in a justification of their observations and no other direct sources, other than those that had been calibrated for, were thought to be possible. In comparison with the previous studies of product distribution by Leck *et al.* and Leu, the main experimental difference between Finkbeiner *et al.* and Leck *et al.* and Leu is that the Leck *et al.* and Leu experiments were carried out at low pressure (< 6 Torr) whereas the study of Finkbeiner *et al.* was at high pressure (700 Torr). Furthermore, 298 K results of Finkbeiner *et al.* and Burrows and Cox, also carried out at ambient pressure, compare well. These comparisons might imply that the HCl + O_3 forming channel is not only temperature but also pressure dependent.

Francisco and Sander[16] carried out calculations at the MP4 level of theory on the singlet surface to determine the relative energies of the HO_3Cl isomers. HOOOCl was found to be the most stable, followed by HOOClO and of the four possible structures (those at potential energy minima) of HO_3Cl it was speculated that only HOOOCl and HOOClO could be formed as nascent products of the ClO + HO_2 reaction.

Nickolaisen *et al.*[13] have carried out the most extensive temperature dependence study of the kinetics of the ClO + HO_2 reaction to date, using flash photolysis coupled with UV absorption spectroscopy. The study was carried out over the temperature range 203-364 K and over the pressure range 50-700 Torr at 298 K. Two chemical schemes were used for the photolytic generation of radicals, to minimise the effects of possible systematic errors caused by secondary reactions. One source was photolysis of a $F_2/H_2/O_2/Cl_2O$ mixture:

(5. 15) $F_2 + h\nu \rightarrow 2F$

(5. 16) $F + H_2 \rightarrow HF + H$

(5. 10) $H + O_2 + M \rightarrow HO_2 + M$

(5. 14a) $Cl_2O + h\nu\ (\lambda > 220\ nm) \rightarrow ClO + Cl$

(5. 14b) $Cl_2O + h\nu\ (\lambda > 220\ nm) \rightarrow O + Cl_2$

(5. 11) $Cl + Cl_2O \rightarrow ClO + Cl_2$

The second radical source was photolysis of a $Cl_2/Cl_2O/CH_3OH/O_2$ mixture:

(5. 15) $Cl_2 + h\nu\ (\lambda > 300\ nm) \rightarrow 2Cl$

(5. 14a) $Cl_2O + h\nu\ (\lambda > 300\ nm) \rightarrow ClO + Cl$

(5. 11) $Cl + Cl_2O \rightarrow ClO + Cl_2$

(5. 16) $Cl + CH_3OH \rightarrow CH_2OH + HCl$

(5. 17) $CH_2OH + O_2 \rightarrow HO_2 + CH_2O$

The experimental study by Nickolaisen *et al.* monitored both radical absorbances directly. The change in HO_2 absorbance was monitored at 210 nm assuming that all other species that absorb in this region do not change significantly over the experimental timescale. The change in ClO absorbance was monitored *via* the differential vibronic peak (12, 0) at 275.2-276.4 nm. With the CH_3OH system aerosol formation was observed at low temperature and high CH_3OH concentrations. The behaviour could not be well characterised as a function of temperature and CH_3OH concentration, and as a result conditions were limited to below 235 K. Pseudo-first order conditions were used with HO_2 in excess. For each of the two chemical schemes used, different parameters were optimised within the kinetic models. For the F_2 system four parameters were varied: the fractional dissociations of F_2 and Cl_2O and the rate coefficients for the ClO + HO_2 and HO_2 + HO_2 reactions. The rate coefficient of the HO_2 self-reaction was varied to fit the HO_2 decay and found to be within the limits of the NASA recommended value. For the CH_3OH system four parameters were also varied to optimise the model fit to the experimental decays. These were the initial Cl atom concentration, and the rate coefficients for the ClO + HO_2, HO_2 + HO_2 and Cl + Cl_2O reactions, the latter of which fell within 25% of the recommended values. The rate coefficient for the ClO + HO_2 reaction was determined over the stated temperature range. The results of the two chemical systems were found to lie within 2σ of one another. The temperature dependence of the ClO + HO_2 reaction was found to be linear, in contrast to that reported by Stimpfle *et al.*, and negative. At 298 K no significant pressure dependence was observed although it could not be ruled out since the lowest pressure that the experiments were carried out at was 50 Torr. There may be a pressure effect at low pressure (< 50 Torr) that reaches a high pressure limit before/at 50 Torr. Interestingly preliminary unpublished results for a low pressure study from the same laboratory show a near-zero temperature dependence over the range 233-380 K and the 298 K rate coefficient is a factor of 2 smaller than this higher pressure study.[29]

Nickolaisen *et al.* also carried out an *ab initio* study of the structures and energetics of intermediates and transition states in the ClO + HO_2 reaction in an attempt to account for the observed temperature and pressure behaviour of the kinetics. These authors calculated energies of intermediates and transition states on both singlet and triplet potential energy surfaces. On the triplet surface the reaction was found to proceed

primarily through a ClOHOO transition state. On the singlet surface however, HOOOCl stabilised due to collisions was shown to possess large barriers toward decomposition into HCl and HOCl.

Knight *et al.*[30] have carried out the only other temperature dependence study of the ClO + HO_2 reaction at low pressure, using discharge flow coupled with mass spectrometry. Three different sources of both radicals were used in combination, resulting in nine possible combinations of radical precursors, seven of which are used in the final analysis. HO_2 sources were CH_3OH, (5. 16)-(5. 17), H_2O_2, (5. 18) and HCHO, (5. 19)-(5. 20).

(5. 18) $F + H_2O_2 \rightarrow HO_2 + HF$

(5. 19) $HCHO + Cl \rightarrow HCO + HCl$

(5. 20) $HCO + O_2 \rightarrow HO_2 + CO$

ClO was formed in excess *via* Cl reaction with either O_3, Cl_2O or OClO in reactions (5. 3), (5. 11) and (5. 13) respectively. The HO_2 decay was monitored by the HO_2^+ parent ion (*m/e* = 33) and ClO by the parent ion ClO^+ (*m/e* = 51) with relative corrections for $^{13}CH_3OH$ and ^{17}OO. To ensure pseudo-first order conditions had been adopted both HO_2 and ClO initial radical concentrations were determined *via* titration with excess NO, measuring NO_2 product signal. Experiments were carried out over the temperature range 203-333 K and the pressure range 1.1-1.7 Torr. Rate coefficients were reported to be significantly smaller than previously determined over the range 215-298 K. Furthermore, in contrast to Stimpfle *et al.* and Nickolaisen *et al.*, the temperature dependence reported by Knight *et al.* was weakly positive.

Knight *et al.* also looked at product formation. O_3 was not detected at any temperature and an upper limit of 1% was placed upon its formation and consequently on channel (5. 1b). $HClO_3^+$ isomers were looked for at *m/e* = 83 and *m/e* = 86 but signals were not observed at these mass to charge ratios.

Kaltsoyannis and Rowley[14] carried out an extensive theoretical study of the potential energy surfaces of the ClO + HO_2 reaction in 2002. Kaltsoyannis and Rowley conclude that reaction along the triplet surface to form HOCl is most favourable due to a small negative activation barrier to products. They go on to predict a theoretical negative temperature dependence that is slightly greater than that observed experimentally. On the singlet surface, in agreement with Nickolaisen *et al.*, HOOOCl had a stable energetic minimum with high exit barriers to products. As a result, if HOOOCl is formed it is likely to be thermally stable. Formation of HCl is thought to be unlikely, which mirrors the paucity of experimental observations.

Xu *et al.*[15] have completed the most recent theoretical study of the ClO + HO_2 reaction. In agreement with previous studies reaction *via* the triplet surface to form HOCl is thought to dominate. A strong negative temperature dependence is also predicted.

Reference	Technique	T / K	p / Torr	$k_{5.1}$ / 10^{-12} cm^3 molecule^{-1} s^{-1}	$\frac{k_{5.1b}}{k_{5.1}} \times 100$
Reimann and Kaufmann[28]	DF/LIF	298	2-3	3.8 ± 0.1	
Stimpfle *et al.*[10]	DF/LMR	235-393	0.8-3.4	6.3	
Leck *et al.*[6]	DF/MS	298	2-6	4.5 ± 0.9	≤ 2
Burrows and Cox[7]	MM/UV	300	760	[a] 5.4^{+4}_{-2}	≤ 0.3
Leu[8]	DF/MS	228, 298			≤ 1.5
Cattell and Cox[26]	MM/UV	308	50-760	[b] 6.2 ± 1.5	
Finkbeiner *et al.*[9]	MI/FTIR	210-300	700		≤ 5
Nickolaisen *et al.*[13]	FP/UV	203-364	50-700	$8.09^{+1.81}_{-1.47}$	
Knight *et al.*[30]	DF/MS	215-298	1.1-1.7	7.1 ± 1.8	≤ 1

[a] 300 K, [b] 308 K

Table 5. 1 298 K Results of previous experimental studies of the ClO + HO_2 reaction kinetics and branching ratio. DF = Discharge flow, LIF = Laser induced fluorescence, LMR = Laser magnetic resonance, MS = Mass spectrometry, MM = Molecular modulation, UV = Ultraviolet spectroscopy, MI = Matrix isolation, FTIR = Fourier transform infrared spectroscopy.

Reference	T / K	p / Torr	A / cm^3 molecule^{-1} s^{-1}	($-E_a/R$) / K
Stimpfle *et al.*[10]	235-393	0.8-3.4	Data too complex to extract	
Nickolaisen *et al*[13].	203-364	700	2.84×10^{-12}	312 ± 60
Knight *et al.*[30]	215-298	1.1-1.7	$(7.1 \pm 0.4) \times 10^{-12}$	-16 ± 17
NASA Recommedation[31]	200-300		4.80×10^{-13}	700

Table 5. 2 Results of previous experimental studies of and the current NASA recommendation for the temperature dependence of the ClO + HO_2 reaction, where $k_{5.1}(T) = A\exp\left(\frac{-E_a}{RT}\right)$.

5. 4 This Work

This study of the ClO + HO_2 reaction has attempted to use a number of different analysis techniques in order to determine the HO_2 radical concentration, which cannot be directly measured with this experimental set-up, as discussed below. As a consequence a test study of the (reversible) ClO self-reaction was first carried out and forward and reverse rate constants determined, the results of which were then used in determination of the rate coefficient of the ClO + HO_2 cross-reaction, $k_{5.1}$. The results of the ClO self-reaction study are presented in Chapter 4 along with an explanation as to how ClO radicals were monitored. For both ClO self-reaction and the ClO + HO_2 cross-reaction ClO radicals were monitored in an identical way.

5. 4. 1 Radical Generation

For the study of the ClO + HO_2 cross-reaction radicals were generated in the following way. Chlorine atoms and ClO radicals were formed as in the chemical system used to study the ClO self-reaction, *i.e.* through photolysis of both Cl_2O and residual Cl_2:

(5. 14a) $Cl_2O + h\nu \rightarrow Cl + ClO$

(5. 15) $Cl_2 + h\nu \rightarrow 2Cl$

(5. 11) $Cl + Cl_2O \rightarrow Cl_2 + ClO$

The addition of CH_3OH (Ridel-de-Haën, 99.9%, spectrophotometric grade) to this chemical system was used to establish a competition for the Cl atoms between reaction with Cl_2O and CH_3OH:

(5. 16) $\quad Cl + CH_3OH \rightarrow CH_2OH + HCl$

In the presence of excess O_2 (BOC, 99.99 %), HO_2 radicals are formed:

(5. 17) $\quad CH_2OH + O_2 \rightarrow HO_2 + CH_2O$

Numerical modelling confirms that under all experimental conditions used, flash photolysis of precursor gas mixtures resulted in rapid ClO and HO_2 formation compared to their subsequent decay.

Experiments were carried out using the same spectral settings as the ClO self-reaction system, listed in Table 5. 3. ClO radical concentrations were monitored as a function of time using differential spectroscopy as described in Section 3. 5. 1. HO_2 radical concentrations could not, however, be measured in this way. The analysis techniques developed in order to determine the HO_2 radical concentrations are discussed in later sections.

Initial experiments were carried out to test the sensitivity of the reacting system to the precursor gases and ensure that the system behaved in a way that could be rationalised. Flash photolysis of $Cl_2/Cl_2O/N_2$ gas mixtures has shown that in the absence of other reagents ClO radicals self react. Upon the addition of excess O_2 to the $Cl_2/Cl_2O/N_2$ system, adjusting the flow of N_2 to maintain a constant number density, no significant change to the initial ClO radical concentration, $[ClO]_0$ was observed. Furthermore, the ClO dimerisation (reaction (4. 2a)) kinetics ($k_{4.2a}$ and $k_{-4.2a}$) for both systems were in excellent agreement with previous work. When CH_3OH was added to $Cl_2/Cl_2O/N_2$ mixtures, again maintaining constant number densities, a small reduction in $[ClO]_0$ was observed since CH_3OH now competes for Cl atoms, but no kinetic deviations occur since in the absence of O_2, HO_2 may not be formed. Slight deviations in $[ClO]_0$ were also observed due to fluctuations in precursor Cl_2 flows, inevitable since this flow is

controlled by a needle valve rather than a mass flow controller. When however, both O_2 and CH_3OH were added to the system both a significant reduction in $[ClO]_0$ and a distinct change in kinetic signature, such that traces no longer fitted to the ClO dimerisation model, were observed. The observed reduction in $[ClO]_0$ was attributed to CH_3OH competing with Cl_2O for Cl atoms in a reaction that did not result in ClO production. The change in kinetic signature was attributed to the formation of HO_2 and the reaction between ClO and HO_2 radicals now, additionally, taking place within the system. Example traces for all of these precursor gas combinations are shown in Figure 5. 2 and the kinetics of these decays are given in Table 5. 3.

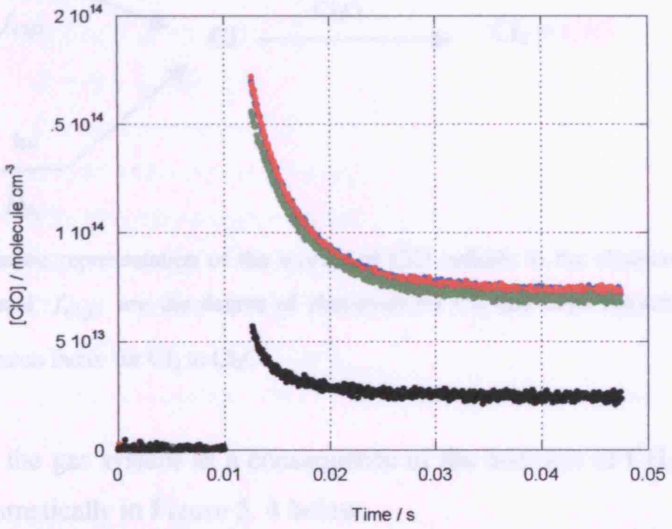

Figure 5. 2 ClO radical concentrations as a function of time recorded using different precursor gas systems, $Cl_2/Cl_2O/N_2$ (blue), $Cl_2/Cl_2O/O_2/N_2$ (red), $Cl_2/Cl_2O/CH_3OH/N_2$ (green), $Cl_2/Cl_2O/CH_3OH/O_2/N_2$ (black).

Gas system	Precursor gases			$[ClO]_0 \times 10^{14}$	$k_{4.2a}$ / 10^{-13} cm^3 molecule^{-1} s^{-1}	$k_{-4.2a}$ / s^{-1}
	$[Cl_2]$ $\times 10^{16}$	$[O_2]$ $\times 10^{18}$	$[CH_3OH]$ $\times 10^{16}$			
Cl_2/Cl_2O	4.17	0	0	1.99 ± 0.30	4.66 ± 0.04	43.31 ± 0.34
$Cl_2/Cl_2O/O_2$	4.21	1.99	0	1.85 ± 0.01	4.59 ± 0.18	43.03 ± 0.54
$Cl_2/Cl_2O/CH_3OH$	4.61	0	9.36	1.69 ± 0.01	4.48 ± 0.12	42.74 ± 0.60
$Cl_2/Cl_2O/CH_3OH/O_2$	4.43	1.99	9.36	0.69 ± 0.02	No longer fits dimerisation model	

Table 5. 3 ClO dimerisation kinetics determined using different precursor gas systems. All concentrations have units of molecule cm^{-3}. Kinetics are an average of 2 determinations, errors are 2σ, statistical only.

Since the addition of O_2 alone to the $Cl_2/Cl_2O/N_2$ system had no effect O_2 was left in for subsequent ClO self-reaction experiments, carried out in between ClO + HO_2 experiments.

The observed behaviour of the photolysed gas mixtures can be rationalised by the following schematic diagrams. In the absence of methanol, the sources of ClO, both direct and from reaction of Cl with Cl_2O can be represented as:

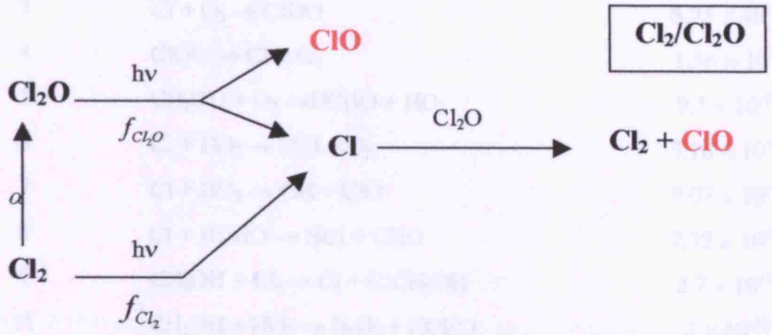

Figure 5. 3 Schematic representation of the sources of ClO radicals in the absence of CH_3OH where f_{Cl_2} and f_{Cl_2O} are the degree of photolysis for Cl_2 and Cl_2O respectively and α is the conversion factor for Cl_2 to Cl_2O.

The changes to the gas system as a consequence of the addition of CH_3OH and O_2 can be seen diagrammatically in Figure 5. 4 below:

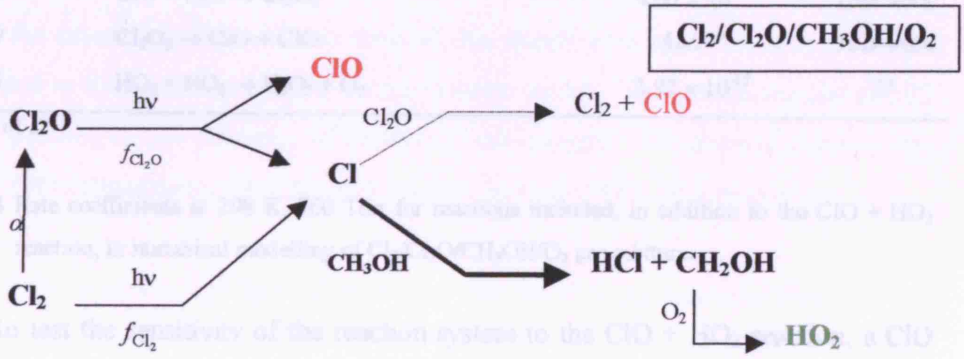

Figure 5. 4 Schematic representation of the sources of ClO radicals in the presence of CH_3OH leading to the formation of both ClO and HO_2 radicals.

Since the kinetic signature exhibited in the presence of methanol and oxygen no longer fits the simple ClO scheme, a model was developed to simulate ClO decay in this new gas system. The comprehensive set of reactions used, in addition to reaction (5. 1), to describe the ClO + HO_2 chemical system is given in Table 5. 4.

Reaction number	Reaction	k / $cm^3 molecule^{-1} s^{-1}$	Reference
1	$Cl + CH_3OH \rightarrow HCl + CH_2OH$	5.4×10^{-11}	31
2	$Cl + Cl_2O \rightarrow Cl_2 + ClO$	9.6×10^{-11}	31
3	$Cl + O_2 \rightarrow ClOO$	6.75×10^{-14}	31
4	$ClOO \rightarrow Cl + O_2$	1.56×10^{7}[a]	31
5	$CH_2OH + O_2 \rightarrow HCHO + HO_2$	9.1×10^{-12}	31
6	$Cl + HO_2 \rightarrow HCl + O_2$	3.18×10^{-11}	31
7	$Cl + HO_2 \rightarrow OH + ClO$	9.07×10^{-12}	31
8	$Cl + HCHO \rightarrow HCl + CHO$	7.32×10^{-11}	31
9	$CH_2OH + Cl_2 \rightarrow Cl + ClCH_2OH$	2.7×10^{-11}	32
11	$CH_2OH + HO_2 \rightarrow H_2O_2 + HCHO$	2×10^{-11}	33
12	$CH_2OH + CH_2OH \rightarrow HOCH_2CH_2OH$	8.63×10^{-11}	34
13	$CH_2OH + CH_2OH \rightarrow CH_3OH + HCHO$	8×10^{-12}	33
14	$OH + CH_3OH \rightarrow H_2O + CH_2OH$	8.79×10^{-13}	34
15	$OH + Cl_2O \rightarrow HOCl + ClO$	6.96×10^{-12}	35
16	$OH + Cl_2 \rightarrow HOCl + Cl$	6.83×10^{-14}	31
17	$HCO + O_2 \rightarrow CO + HO_2$	5.6×10^{-12}	31
18	$HCO + O_2 \rightarrow HC(O)O_2$	1.16×10^{-11}	36
18	$ClO + ClO \rightarrow Cl_2O_2$	4.66×10^{-13}	This work
19	$Cl_2O_2 \rightarrow ClO + ClO$	42.94[a]	This work
20	$HO_2 + HO_2 \rightarrow H_2O_2 + O_2$	3.92×10^{-12}	37

[a] Units of s^{-1}

Table 5. 4 Rate coefficients at 298 K, 760 Torr for reactions included, in addition to the ClO + HO_2 reaction, in numerical modelling of $Cl_2/Cl_2O/CH_3OH/O_2$ gas mixture.

In order to test the sensitivity of the reaction system to the ClO + HO_2 reaction, a ClO temporal trace was simulated with typical $[ClO]_0$ as observed in experiments and using literature values of rate coefficients as given above. This trace was then re-analysed using a model in which the rate coefficients for each of the reactions were successively perturbed by halving and doubling. The returned value for $k_{5.1}$ was then used to

calculate a percentage change in this parameter from the original value, as shown in Figure 5. 5.

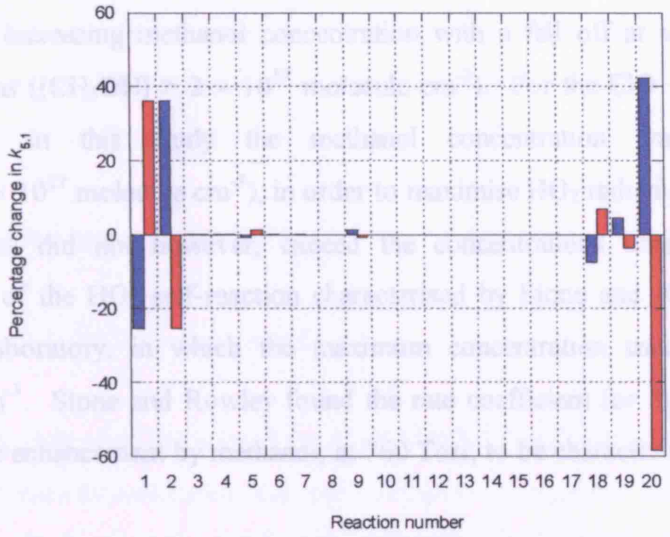

Figure 5. 5 Percentage change in $k_{5.1}$ as a result of a perturbation in rate constants for reactions 1-20. Reaction numbers refer to the reactions listed in Table 5. 4.

Figure 5. 5 shows that many of the secondary reactions in the model have a small effect on the determination of $k_{5.1}$. The complexity of the scheme could therefore be reduced by disregarding any reactions whose rate coefficient change resulted in a less than 0.1% change in the returned $k_{5.1}$. As a result, since the remaining reactions were relatively slow, or involved the CH_2OH intermediate, which reacted rapidly and exclusively with O_2 under the experimental conditions adopted, the steady state approximation could be implemented in the construction of a simpler kinetic model. This model simulated ClO temporal profiles in the presence of methanol and oxygen, with the inclusion of the reversible ClO dimerisation, the HO_2 self-reaction and the ClO + HO_2 reaction.

The sensitivity analysis highlights that two of the most important reactions for this reacting system are the self-reactions of ClO and HO_2 respectively. Extensive studies of both of these reactions have been carried out in this laboratory and elsewhere. The preliminary study of the ClO self-reaction (discussed in Chapter 4) provides a direct measurement of the forward and reverse rate coefficients of ClO dimerisation, $k_{4.2a}$ and $k_{-4.2a}$ respectively, in these ClO + HO_2 experiments. Previous studies of the HO_2 self-reaction indicate that the rate is enhanced in the presence of polar molecules including

CH_3OH, as well as water and ammonia.[38] Polar molecules can form hydrogen-bonded complexes with HO_2 which act as a chaperone to the formation of reaction intermediates. Studies show that linear enhancement of the HO_2 self-reaction rate occurs with increasing methanol concentration with a fall off at very high methanol concentrations ($[CH_3OH] > 2 \times 10^{17}$ molecule cm^{-3}). For the ClO + HO_2 experiments carried out in this study the methanol concentration was relatively high (5×10^{15}-1×10^{17} molecule cm^{-3}), in order to maximise HO_2 radical production. These concentrations did not however, exceed the concentrations used in the methanol dependence of the HO_2 self-reaction characterised by Stone and Rowley[37] in a study from this laboratory, in which the maximum concentration used was 4.4×10^{17} molecule cm^{-3}. Stone and Rowley found the rate coefficient for the HO_2 self-reaction including the enhancement by methanol, at 760 Torr, to be characterised by (E5. 1).

(E5. 1)

$$k_{HO_2+HO_2} = \left\{(1.8 \pm 0.8) \times 10^{-14} \exp\left(\frac{1500 \pm 120}{T/K}\right)\right\} \times \left\{1 + (0.56 \pm 1.00) \times 10^{-21} [CH_3OH] \exp\left(\frac{2550 \pm 500}{T/K}\right)\right\}$$

where $[CH_3OH]$ is in molecule cm^{-3}.

The propagation of uncertainties in important side reactions into the uncertainty in the final reported kinetics of the ClO + HO_2 reaction are discussed in Section 5. 7 below.

5. 4. 2 Determining HO_2 Radical Concentrations

Unlike ClO radicals, the concentration of HO_2 radicals could not be determined directly in these experiments. This was because, throughout the UV spectral region, the absorption cross-section of HO_2, $\sigma(HO_2)$, does not exhibit structure and hence differential spectroscopy could not be employed. Furthermore, over the entire experimental wavelength region the HO_2 absorbance is masked by all other absorbing species present (ClO, Cl_2O, Cl_2O_2). Indeed, even if these additional absorbers were not present $\sigma(HO_2)$ maximises around 210 nm, a wavelength at which signal-to-noise is compromised and that is well out of the experimental wavelength region adopted to

maximise ClO absorption. Despite this inability to determine HO_2 concentration directly it was vital for the kinetic analysis for the initial HO_2 concentration, $[HO_2]_0$, to be known. Three separate methods for determining this parameter were developed. The principles and validity of each of these methods are discussed in turn in the following sections. One representative data set, recorded at 298 K and 760 Torr, has been analysed using all three methods.

5. 5 Methods for determining $[HO_2]_0$

5. 5. 1 Method 1: Difference Analysis

Numerical modelling of the photolysed $Cl_2/Cl_2O/O_2/CH_3OH$ gas system has shown that under experimental conditions the only effective competing chemistry with Cl_2O reacting with Cl atoms is the reaction of methanol with Cl atoms. Taking into account all known chemistry the reaction of Cl with CH_3OH is expected therefore to lead to a reduction in $[ClO]_0$ and, under all experimental conditions, the prompt formation of HO_2. Thus, quantification of the reduction in $[ClO]_0$ upon the addition of CH_3OH in successive experiments can be directly related, using stoichiometric arguments, to $[HO_2]_0$, as indicated in Figure 5. 6.

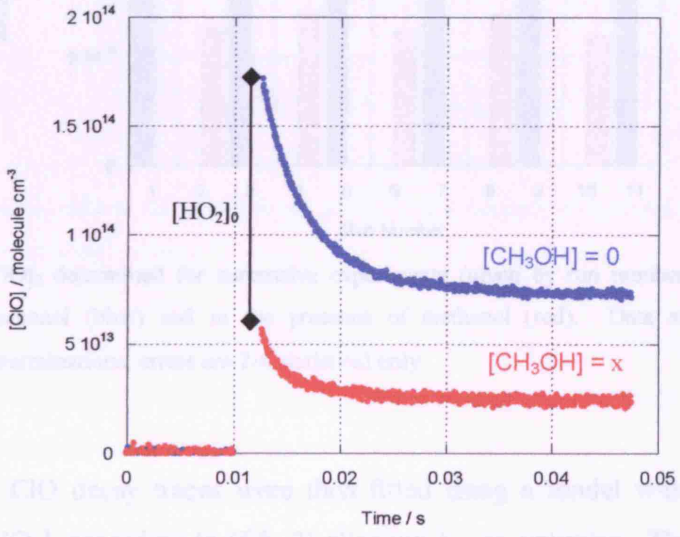

Figure 5. 6 ClO radical concentration as a function of time for a typical $Cl_2/Cl_2O/N_2$ gas mixture (blue) and that of a subsequent $Cl_2/Cl_2O/O_2/CH_3OH/N_2$ gas mixture (red).

A series of experiments carried out as a function of CH_3OH concentration, where $[CH_3OH]$ was alternately varied between a given concentration, $[CH_3OH] = x$, and zero concentration, $[CH_3OH] = 0$, led to the determination of the initial HO_2 concentration for each data set according to:

(E5. 2) $$[HO_2]_{0,[CH_3OH]=x} = [ClO]_{0,[CH_3OH]=0} - [ClO]_{0,[CH_3OH]=x}$$

The slow drift in $[ClO]_0$ observed between experiments carried out in the absence of methanol, under otherwise identical conditions (see Figure 5. 8 runs 1, 3, 5, 7, 9, 11) was accounted for by taking the $[ClO]_{0,[CH_3OH]=0}$ to be the average $[ClO]_0$ recorded for the neighbouring data sets of the $[ClO]_{0,[CH_3OH]=x}$ data. For example, from Figure 5. 7 the $[ClO]_{0,[CH_3OH]=0}$ for data set 2 was taken to be the average of that recorded in data sets 1 and 3.

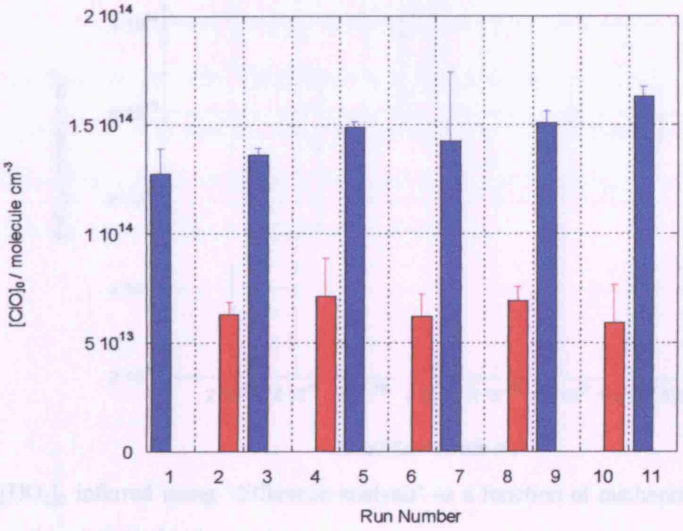

Figure 5. 7 $[ClO]_0$ determined for successive experiments (given by run number) in the absence of methanol (blue) and in the presence of methanol (red). Data are an average of 2 determinations, errors are 2σ, statistical only.

Experimental ClO decay traces were then fitted using a model with fixed values of $[ClO]_0$ and $[HO_2]_0$ according to (E5. 2) allowing $k_{5.1}$ to optimise. The $[HO_2]_0$ inferred using this method, as a function of initial methanol concentration, along with determined $[ClO]_0$ and $k_{5.1}$ are given in Table 5. 5.

Initial $[CH_3OH]$ / 10^{16} molecule cm^{-3}	$[ClO]_0$ / 10^{13} molecule cm^{-3}	$[HO_2]_0$ / 10^{13} molecule cm^{-3}	$k_{5.1}$ / 10^{-12} cm^3 $molecule^{-1}$ s^{-1}
2.06	10.10 ± 0.95	3.56 ± 0.95	2.82 ± 4.18
4.62	7.13 ± 1.77	7.17 ± 1.77	2.14 ± 0.34
7.14	5.92 ± 1.79	9.78 ± 1.79	2.03 ± 0.97
9.76	6.31 ± 0.60	6.89 ± 0.60	2.54 ± 0.23
12.3	6.23 ± 1.00	7.87 ± 1.00	2.34 ± 1.43
15.0	6.96 ± 6.51	7.93 ± 6.51	2.98 ± 0.98

Table 5. 5 $[HO_2]_0$ inferred determined using difference analysis along with $k_{5.1}$ determined at 298 K and 760 Torr for a number of experiments at different initial methanol concentrations. Results are an average of 2 determinations, errors are 2σ, statistical only.

The inferred $[HO_2]_0$ as a function of $[CH_3OH]$ is given in Figure 5. 8.

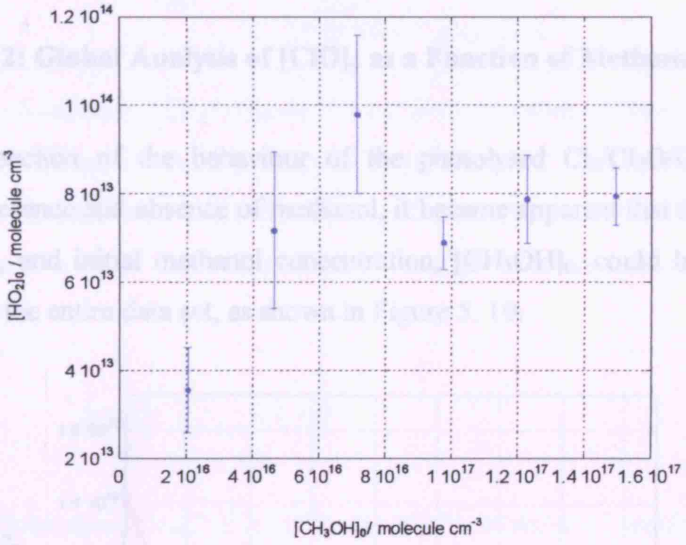

Figure 5. 8 $[HO_2]_0$ inferred using 'difference analysis' as a function of methanol concentration. Errors are 2σ, statistical only.

In all cases the returned rate coefficient at the lowest methanol concentration (2.06×10^{16} molecule cm^{-3}) were omitted, since as discussed in Section 5. 5. 2 at this concentration there is no sensitivity to the cross-reaction. The average of the remaining 10 determinations at 298 K, 760 Torr gave $k_{5.1} = (2.41 \pm 0.98) \times 10^{-12}$ cm^3 $molecule^{-1}$ s^{-1}, where errors are 2σ, statistical only. Results showed no significant variation of $k_{5.1}$ with CH_3OH concentration, as shown in Figure 5. 9.

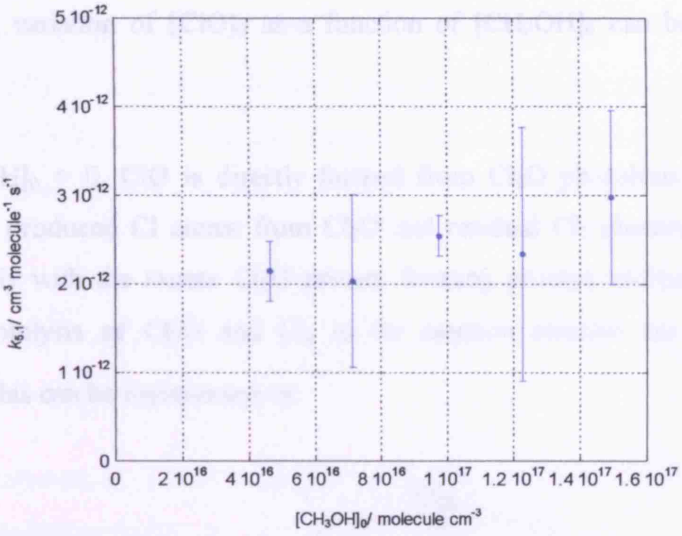

Figure 5. 9 $k_{5.1}$, as a function of initial methanol concentration, $[CH_3OH]_0$, determined using $[HO_2]_0$ inferred using 'difference analysis'. Errors are 2σ, statistical only.

5. 5. 2 Method 2: Global Analysis of $[ClO]_0$ as a Function of Methanol

On further inspection of the behaviour of the photolysed $Cl_2/Cl_2O/O_2N_2$ chemical system in the presence and absence of methanol, it became apparent that the relationship between $[ClO]_0$, and initial methanol concentration, $[CH_3OH]_0$, could be exploited to infer $[HO_2]_0$ for the entire data set, as shown in Figure 5. 10.

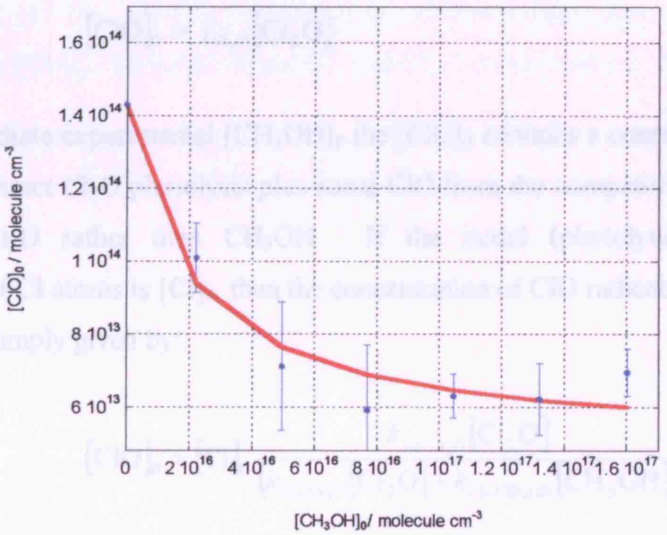

Figure 5.10 Initial ClO concentration, $[ClO]_0$, *versus* initial CH_3OH concentration, $[CH_3OH]_0$. The fit through this data (red line) can be used to infer initial HO_2 concentration for each experiment, $[HO_2]_0$. Errors are 2σ, statistical only.

The observed variation of $[ClO]_0$ as a function of $[CH_3OH]_0$ can be rationalised as follows:

(i) At $[CH_3OH]_0 = 0$, ClO is directly formed from Cl_2O photolysis. Moreover, all photolytically produced Cl atoms from Cl_2O and residual Cl_2 photolysis react rapidly and exclusively with the excess Cl_2O present forming prompt additional ClO. If the fractional photolysis of Cl_2O and Cl_2 in the reaction mixture are f_{Cl_2O} and f_{Cl_2} respectively, this can be represented as:

$$\text{(E5. 3)} \qquad [ClO]_0 = \underbrace{f_{Cl_2O}[Cl_2O]}_{\text{Direct ClO}} + \overbrace{\underbrace{f_{Cl_2O}[Cl_2O]}_{\text{Cl from } Cl_2O \text{ photolysis}} + \underbrace{2f_{Cl_2}[Cl_2]}_{\text{Cl from } Cl_2 \text{ photolysis}}}^{[Cl]_0}$$

(ii) By contrast, at notional $[CH_3OH]_0 \rightarrow \infty$ (*i.e.* the asymptote of the observed $[ClO]_0$ *versus* $[CH_3OH]_0$ dependence) all photolytically produced Cl atoms must react rapidly and exclusively with CH_3OH (followed by $CH_2OH + O_2$), leading to HO_2 formation. Consequently, $[ClO]_0$ under these (hypothetical) conditions arises solely from the direct photolysis of Cl_2O:

$$\text{(E5. 4)} \qquad [ClO]_0 = f_{Cl_2O}[Cl_2O]$$

(iii) At intermediate experimental $[CH_3OH]_0$ the $[ClO]_0$ contains a contribution from (ii) *i.e.* ClO from direct Cl_2O photolysis plus some ClO from the competitive reaction of Cl atoms with Cl_2O rather than CH_3OH. If the initial (photolytically produced) concentration of Cl atoms is $[Cl]_0$, then the concentration of ClO radicals produced from these atoms is simply given by:

$$\text{(E5. 5)} \qquad [ClO]_0 = [Cl]_0 \frac{k_{Cl+Cl_2O}[Cl_2O]}{\left(k_{Cl+Cl_2O}[Cl_2O] + k_{Cl+CH_3OH}[CH_3OH]\right)}$$

Taking k_{Cl+Cl_2O} and k_{Cl+CH_3OH} from the literature (both are well defined), and using the known $[CH_3OH]_0$ from calibrated flow rates in the experiments hence allows the representation of $[ClO]_0$ from this data set as a function of methanol concentration. The functional form of the dependence of $[ClO]_0$ *versus* $[CH_3OH]_0$ is given by equation (E5. 6).

$$[ClO]_0 = A + \frac{B}{1 + C[CH_3OH]_0} \quad \text{(E5. 6)}$$

where the parameters A, B and C are defined in terms of precursor concentrations and fractional photolysis as follows:

$$A = f_{Cl_2O}[Cl_2O]_0 \quad \text{(E5. 7)}$$

$$B = [Cl]_0 = 2f_{Cl_2}[Cl_2]_0 + f_{Cl_2O}[Cl_2O]_0 \quad \text{(E5. 8)}$$

$$C = \frac{k_{Cl+CH_3OH}}{k_{Cl+Cl_2O}[Cl_2O]_0} \quad \text{(E5. 9)}$$

Furthermore, since the total Cl_2 concentration in the gas mixture, assuming zero conversion to Cl_2O (*i.e.* the Cl_2 concentration calculated from known flow rates), is known, denoted $[Cl_2]_{0,f}$, the initial *actual* Cl_2 and Cl_2O concentrations are linked by:

$$[Cl_2]_{0,f} = [Cl_2]_0 + 2[Cl_2O]_0 \quad \text{(E5. 10)}$$

where the $2[Cl_2O]_0$ takes into account the 2:1 stoichiometry of Cl_2 to Cl_2O conversion.

Fitting (E5. 6) to the observed variation of $[ClO]_0$ as a function of methanol, shown in Figure 5. 11, and determining parameters A, B and C therefore allows the sources of ClO to be quantified and hence $[HO_2]_0$ to be inferred. In the case of HO_2, no direct photolytic source is present and it can be shown using simple competition arguments that the $[HO_2]_0$ is given by (E5. 11).

$$(E5.\ 11) \qquad [HO_2]_0 = [Cl]_0 \frac{k_{Cl+CH_3OH}[CH_3OH]_0}{k_{Cl+CH_3OH}[CH_3OH]_0 + k_{Cl+Cl_2O}[Cl_2O]_0}$$

Using this $[HO_2]_0$ and fitting the entire data set to determine $k_{5.1}$ returns the parameters given in Table 5. 6.

Initial $[CH_3OH]$ / 10^{16} molecule cm^{-3}	$[ClO]_0$ / 10^{13} molecule cm^{-3}	$[HO_2]_0$ / 10^{13} molecule cm^{-3}	$k_{5.1}$ / 10^{-12} cm^3 $molecule^{-1}$ s^{-1}
2.06	10.10 ± 0.95	4.96	2.41 ± 1.00
4.62	7.13 ± 1.77	6.70	2.24 ± 0.07
7.14	5.92 ± 1.79	7.46	2.85 ± 0.74
9.76	6.31 ± 0.60	7.89	2.75 ± 0.30
12.3	6.23 ± 1.00	8.15	2.26 ± 1.18
15.0	6.96 ± 6.51	8.34	1.39 ± 0.90

Table 5. 6 $[HO_2]_0$ inferred determined using method 2 ('global analysis' of $[ClO]_0$) along with $k_{5.1}$ determined at 298 K, 760 Torr for a number of experiments at different initial methanol concentrations. Results are an average of 2 determinations, errors are 2σ, statistical only.

The average of 10 determinations taken at the higher methanol concentrations gives a value for $k_{5.1}$ of $k_{5.1} = (2.50 \pm 0.79) \times 10^{-12}$ cm^3 $molecule^{-1}s^{-1}$. Errors are 2σ, statistical only. Figure 5. 11 shows no systematic variation of $k_{5.1}$ with $[CH_3OH]_0$, except at the highest $[CH_3OH]_0$ used in these experiments.

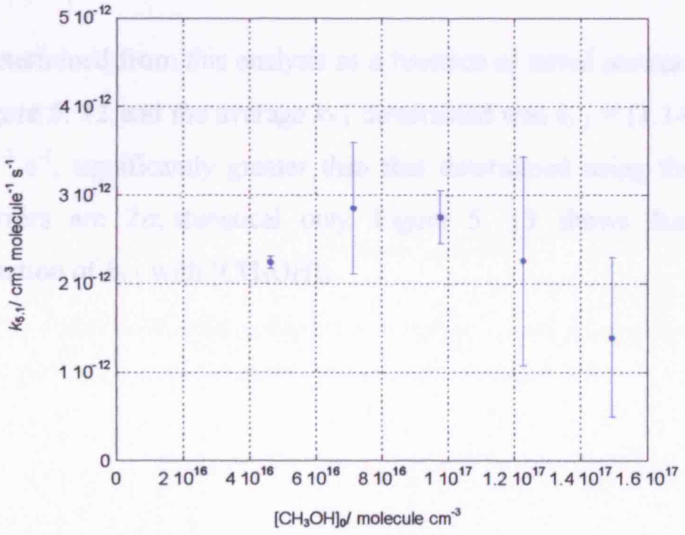

Figure 5. 11 $k_{5.1}$as a function of initial methanol concentration, determined using $[HO_2]_0$ inferred using method 2. Errors are 2σ, statistical only.

5. 5. 3 Method 3: Numerical Modelling

A further determination of $k_{5.1}$ from analysis of ClO decay traces, recorded in the presence of methanol, was possible by allowing $[HO_2]_0$ to undergo optimisation within the numerical model in addition to $k_{5.1}$ and $[ClO]_0$. Initial results from this analysis returned $[HO_2]_0$ values that were much smaller than previously predicted using methods 1 and 2 (which themselves were in good agreement), $[ClO]_0$ was in good agreement (unsurprisingly as all analyses used measured ClO concentrations as a function of time) and $k_{5.1}$ in this third analysis was consequently greater than given by the other methods. The results of this method of analysis are given in Table 5. 7.

Initial $[CH_3OH]$ / 10^{16} molecule cm^{-3}	$[ClO]_0$ / 10^{13} molecule cm^{-3}	$[HO_2]_0$ / 10^{13} molecule cm^{-3}	$k_{5.1}$ / 10^{-12} cm^3 $molecule^{-1}$ s^{-1}
2.06	16.67 ± 0.11	8.82 ± 1.15	32.12 ± 0.04
4.62	7.13 ± 0.88	2.64 ± 0.15	10.67 ± 0.57
7.14	5.92 ± 0.89	2.52 ± 0.58	12.16 ± 2.29
9.76	6.16 ± 0.09	2.59 ± 0.06	11.48 ± 0.80
12.3	4.40 ± 2.09	1.79 ± 0.48	12.37 ± 6.41
15.0	6.96 ± 0.33	3.32 ± 0.40	10.26 ± 0.47

Table 5. 7 Optimised values of $[HO_2]_0$ along with $k_{5.1}$ determined using method 3 ('numerical modelling') at 298 K, 760 Torr for a number of experiments at different initial methanol concentrations. Results are an average of 2 determinations, errors are 2σ, statistical only.

The $[HO_2]_0$ determined from this analysis as a function of initial methanol concentration is given in Figure 5. 12 and the average $k_{5.1}$ determined was $k_{5.1} = (1.14 \pm 0.29) \times 10^{-11}$ cm^3 $molecule^{-1}$ s^{-1}, significantly greater than that determined using the preceding two methods. Errors are 2σ, statistical only. Figure 5. 13 shows that there was no systematic variation of $k_{5.1}$ with $[CH_3OH]_0$.

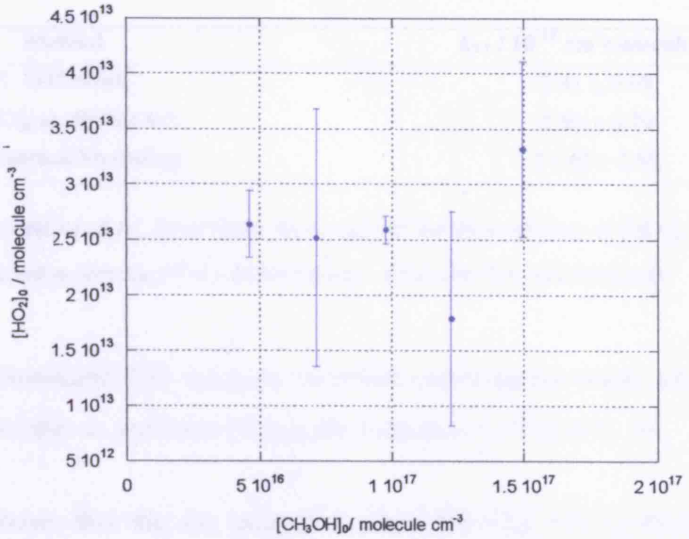

Figure 5. 12 Optimised $[HO_2]_0$ as a function of methanol concentration. The predicted $[HO_2]_0$ at the lowest methanol concentration has been omitted for clarity. Errors are 2σ, statistical only.

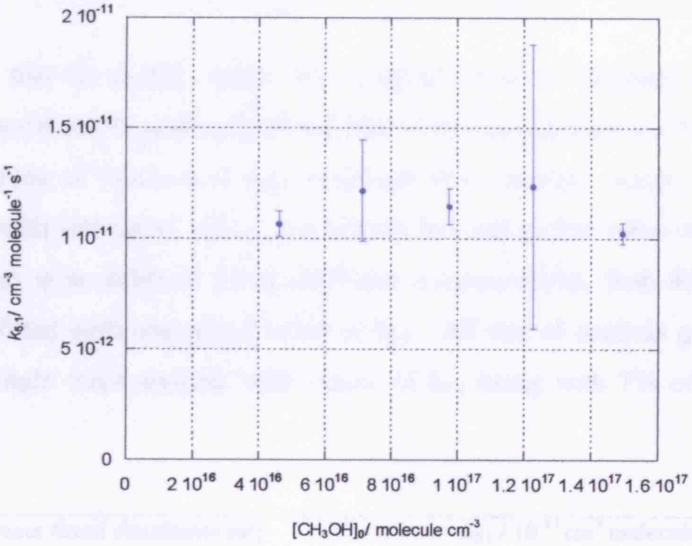

Figure 5. 13 $k_{5.1}$, as a function of initial methanol concentration, determined using optimisation of $[ClO]_0$ and $[HO_2]_0$ in a numerical model. Errors are 2σ, statistical only.

The returned kinetic parameters for all three methods are summarised in Table 5. 8.

Method	$k_{5.1}$ / 10^{-12} $cm^3 molecule^{-1} s^{-1}$
1. Difference	2.41 ± 0.98
2. $[ClO]_0$ as $f([CH_3OH])$	2.50 ± 0.79
3. Numerical Modelling	11.40 ± 2.88

Table 5. 8 Average values of $k_{5.1}$ determined using each of the three sources of $[HO_2]_0$ discussed above. Results are an average of 10 determinations. Errors are 2σ, statistical only.

Typical fits of simulated ClO decay to observed experimental decay using each of the three methods to infer or optimise $[HO_2]_0$ are compared in Figure 5. 14.

Figure 5. 14 shows that the fits generated when allowing $[HO_2]_0$ to optimise in the model (method 3) were somewhat better than when $[HO_2]_0$ was inferred from the other two methods. This was indicated by the residual from the least squares fitting routine, which can be thought of, as a 'goodness of fit' parameter. Typically this parameter was some 25% smaller when allowing $[HO_2]_0$ to optimise as opposed to stipulating it.

This effect on this fit quality might be expected since in allowing $[HO_2]_0$ to be optimised the model is less well constrained than when this parameter is fixed. Thus, to reduce the degrees of freedom it was proposed than multiple traces may be fitted simultaneously with individual $[ClO]_0$ and $[HO_2]_0$ but one global value of $k_{5.1}$. In turn two random files with different initial methanol concentrations, then three files were simultaneously fitted with one global value of $k_{5.1}$. All sets of analysis gave consistent results to the single trace analysis with values of $k_{5.1}$ being with 7% of one another, Table 5. 9.

Number of traces fitted simultaneously	$k_{5.1}$ / 10^{-11} cm^3 $molecule^{-1} s^{-1}$
1	1.14 ± 0.29
2	1.19 ± 0.18
3	1.22 ± 0.09

Table 5. 9 $k_{5.1}$ determined by fitting a different number of ClO decay traces simultaneously with one global value of $k_{5.1}$. Errors are 2σ, statistical only.

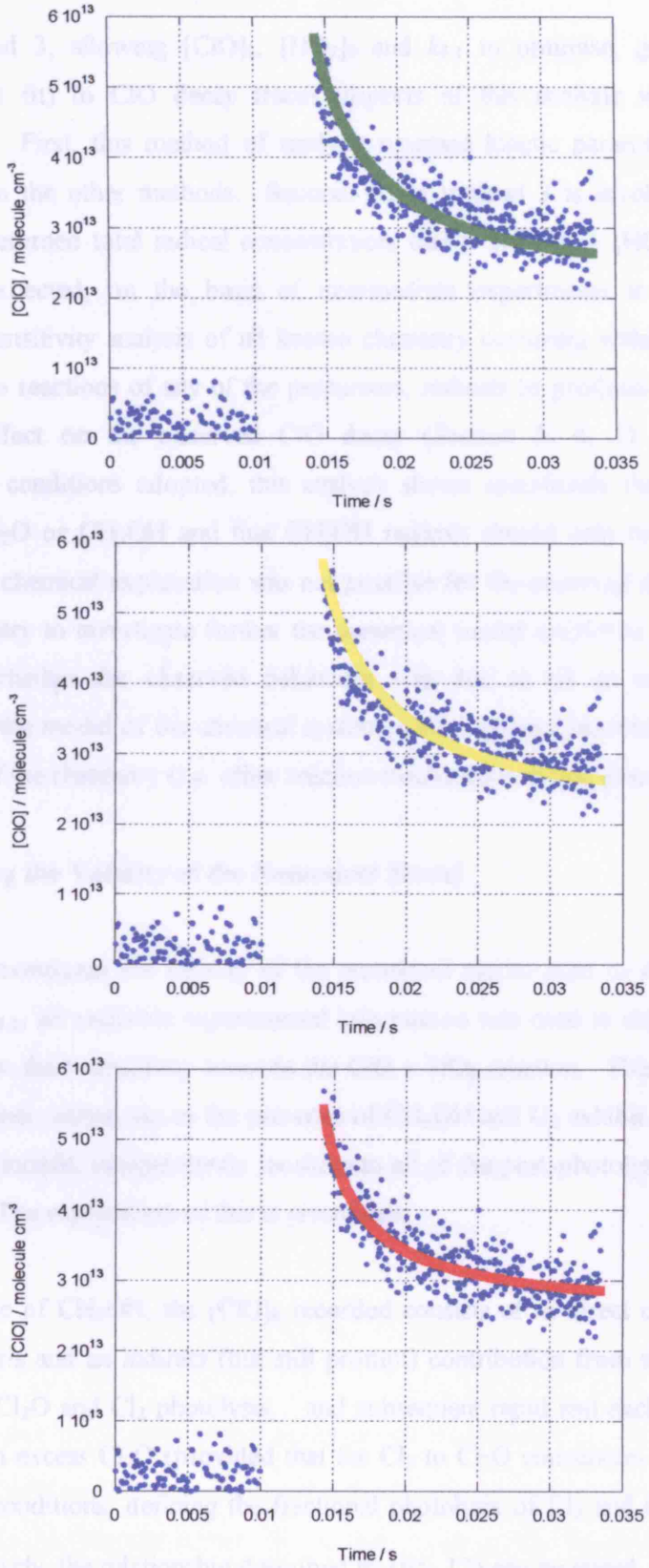

Figure 5. 14 Typical model fits to experimental ClO radical concentrations as a function of time (blue) for the three different sources of $[HO_2]_0$. Method 1 = green, Method 2 = yellow and Method 3 = red. See text for details.

Whilst method 3, allowing $[ClO]_0$, $[HO_2]_0$ and $k_{5.1}$ to optimise, gave the smallest residual (best fit) to ClO decay traces, aspects of this analysis warranted further investigation. First, this method of analysis returned kinetic parameters significantly different from the other methods. Second, when method 3 is invoked to determine $[HO_2]_0$, the returned total radical concentration, that is $\{[ClO]_0 + [HO_2]_0\}$, is less than chemically expected, on the basis of intermediate experiments in the absence of methanol. Sensitivity analysis of all known chemistry occurring within the system has shown that no reactions of any of the precursors, radicals or products should have any significant effect on the observed ClO decay (Section 5. 4. 1). Indeed, under experimental conditions adopted, this analysis shows specifically that Cl atoms only react with Cl_2O or CH_3OH and that CH_2OH radicals should only react with (excess) oxygen. If a chemical explanation was not possible for the observed discrepancies then it was necessary to investigate further the numerical model employed. It was essential to address whether the observed behaviour was due to (i) an inadequacy in the sensitivity of the model of the chemical system or (ii) a general inadequacy in the model description of the chemistry (*i.e.* other reaction mechanisms taking place).

5. 5. 4 Testing the Validity of the Numerical Model

In order to investigate the validity of the numerical model used to determine $[ClO]_0$, $[HO_2]_0$ and $k_{5.1}$, all available experimental information was used to simulate ClO decay traces and test their sensitivity towards the ClO + HO_2 reaction. This analysis showed that experiments carried out in the presence of CH_3OH and O_2 exhibit ClO decay traces that are, in principle, independently sensitive to all of the post-photolysis conditions and the rate $k_{5.1}$. The explanation of this is given here.

In the absence of CH_3OH, the $[ClO]_0$ recorded consists of a direct contribution from Cl_2O photolysis and an indirect (but still prompt) contribution from the reaction of Cl atoms, from Cl_2O and Cl_2 photolysis, and subsequent rapid and exclusive reaction of Cl atoms with excess Cl_2O (provided that the Cl_2 to Cl_2O conversion was *ca.* > 10%). Given these conditions, defining the fractional photolysis of Cl_2 and Cl_2O as f_{Cl_2} and f_{Cl_2O} respectively, the relationship described by (E5. 12) can be stated.

(E5. 12) $$[ClO]_{0,[CH_3OH]=0} = 2f_{Cl_2}[Cl_2] + 2f_{Cl_2O}[Cl_2O]$$

where $[Cl_2]$ and $[Cl_2O]$ in the gas mixture are determined by the total flow of Cl_2 gas introduced to the system and the extent of conversion of Cl_2 to Cl_2O. If we define this extent of conversion as α, and taking into account the Cl_2:Cl_2O stoichiometry of 2:1 in the reaction of Cl_2 with HgO, then we can write:

(E5. 13) $$[Cl_2]_{cell} = (1-\alpha)[Cl_2]_{0,f}$$

(E5. 14) $$[Cl_2O] = \frac{(\alpha[Cl_2]_{0,f})}{2}$$

where $[Cl_2]_{0,f}$ is the Cl_2 concentration introduced to the gas mixture calculated from known experimental flow rates (*i.e.* the concentration of Cl_2 that would be present if the Cl_2 to Cl_2O conversion was zero) of all components and $[Cl_2]_{cell}$ is the actual residual Cl_2 concentration expected after the Cl_2 has passed through the mercuric oxide. Combining these expressions gives:

(E5. 15) $$[ClO]_{0,[CH_3OH]=0} = 2f_{Cl_2}(1-\alpha)[Cl_2]_{0,f} + f_{Cl_2O}\alpha$$

$$= \{2f_{Cl_2}(1-\alpha) + f_{Cl_2O}\alpha\}[Cl_2]_{0,f}$$

Consequently, measurement of $[ClO]_0$ in the absence of CH_3OH, and calculation of $[Cl_2]_{0,f}$ from experimental flow rates enables the determination of the quantity, Q:

(E5. 16) $$Q = \{2f_{Cl_2}(1-\alpha) + f_{Cl_2O}\alpha\}$$

Since Q contains three interrelated experimental parameters, α, f_{Cl_2} and f_{Cl_2O}, its determination will reduce the number of unknown parameters to any two of the three. The adjustable parameters in the fitting then become the fractional Cl_2 to Cl_2O conversion, α, the fraction of Cl_2 photolysed, f_{Cl_2}, and the rate coefficient $k_{5.1}$. The numerical model was thus used to generate sample ClO decay traces using notional

values of the three adjustable parameters. These traces were then refitted to an identical model allowing all three parameters to vary. It was found that, in this second model, if the adjustable parameters were initially set close to the known input values for that trace (typically within 20%) then optimisation, by varying all three parameters, did indeed result in the input parameters being returned. If however, the parameters in the second model were initially set further away from the known input parameters, optimisation resulted in convergence to the simulated ClO decay but the three returned parameters did not match the three input parameters. Comparison of the fitted residuals from the two scenarios revealed that, in the case where the parameters were started at values furthest away from the input parameters, a significantly higher residual was returned (*i.e.* they gave a poorer fit) than the case where the parameters were started closer to their input values and the returned values were equal to the input values (in which case the residual should in theory be zero). The residuals were also inspected by fitting a model in which one of the three parameters was perturbed from its known input value, and the other two parameters varied in order to optimise the fit. In this case, the fits could never compensate for any one of the input parameters not being equal to its known value in the forward model. This analysis confirmed that a unique set of the three parameters did produce a global minimum fit to the ClO decay trace. This effect was further confirmed on returning to the full FACSIMILE model that incorporated all known secondary chemistry.

This sensitivity analysis demonstrated that whilst, in principle, the ClO trace had a unique global minimum best fit, with a unique set of all three adjustable parameters describing the ClO and HO_2 chemistry, *a priori* knowledge of the parameters was required in order to find this best fit. Consequently this method was rendered unusable for the analysis of individual experimental traces. As a result, methods in which the three parameter fit could be reasonably constrained were investigated, initially using idealised fitting to simulated ClO traces.

Of the three parameters, it would not be reasonable to apply any constraint to value that $k_{5.1}$ could take (other than it being nonzero and less than the gas kinetic collision limit). However, the conversion fraction, α, by definition must be constrained between the values zero and 1. The third parameter, the fraction of Cl_2 photolysed, f_{Cl_2}, could also

be constrained by independent measurements. Cl_2 is routinely used as a source of Cl atoms in the generation of peroxy radicals by H atom abstraction in reactions (5. 15)-(5.17).

(5. 15) $Cl_2 + h\nu \rightarrow 2Cl$

(5. 16) $Cl + CH_3OH \rightarrow CH_2OH + HCl$

(5. 17) $CH_2OH + O_2 \rightarrow HO_2 + CH_2O$

A set of separate experiments, carried out in this laboratory, on the HO_2 self-reaction on the same apparatus, was used to give an indication of the chlorine photolysis fraction. From 47 measurements of the initial HO_2 yield at 298 K and 760 Torr, f_{Cl_2} was found to be $(1.062 \pm 0.286) \times 10^{-3}$, where the statistical error was 2σ. This value of f_{Cl_2}, with $\pm$ 2 standard deviation limits, was therefore used to constrain the returned value of f_{Cl_2} when fitting the three parameters to simulated ClO traces over a matrix of starting conditions. The assumption that the value of f_{Cl_2} was not perturbed in the presence of Cl_2O was valid since the flashlamp output is maximum in a spectral region ($\lambda > 300$ nm) where Cl_2 and Cl_2O absorption cross-sections show no significant spectral overlap.

This fitting routine, where f_{Cl_2} was only permitted to optimised within set limits, did not constrain the model significantly and a similar outcome to the previous method, where *a priori* knowledge of the starting parameters was required, occurred. If however, f_{Cl_2} was fixed at the pre-determined value of 1.062×10^{-3} and only the parameters $k_{5.1}$ and α were allowed to vary during the optimisation, then the global minimum could be found. Indeed the global minimum (within a small percentage) was routinely found in this case without prior knowledge of the starting parameters. Furthermore, if the fixed value of f_{Cl_2} was perturbed to either the upper or lower error limit (*ca.* 13%) the returned value of $k_{5.1}$ remained at the set value (within < 1%) and only α changed in order to compensate for the perturbation in the fit.

Further investigation into the sensitivity of the model was carried out by looking at the effects of an incorrect determination of $[ClO]_{0,[CH_3OH]=0}$ and/or $[Cl_2]$. In the numerical model this would manifest itself as an erroneous calculation of the parameter Q. Indeed, since f_{Cl_2}, f_{Cl_2O} and α are also related by this factor Q any discrepancies in their determinations would also manifest as an incorrect value of Q. The real effect that an incorrect value of Q has on the model was investigated by simply fitting a simulated trace, with a known Q, using a numerical model that had a perturbed value of Q, optimising the parameters $k_{5.1}$ and α. Again a number of starting parameters were used for the model to check the reliance on *a priori* knowledge. Resulting optimisations showed that provided Q was within 30% of its actual value then no significant perturbation of the returned value of $k_{5.1}$ occurred. Minimisation in the model was again maintained *via* an alteration in α in order to compensate for the change in Q.

One further verification of this model was to examine the effect of an incorrect ClO absorption cross-section on the observed parameters. If σ(ClO) were for example, 10% too low, then the observed effect (according to the Beer-Lambert law) on $[ClO]_0$ would be a 10% increase. This would have a corresponding effect on the $[HO_2]_0$ inferred from $[ClO]_{0,[CH_3OH]=0}$ and $[ClO]_{0,[CH_3OH]=x}$. If both $[ClO]_0$ and $[HO_2]_0$ were determined wrongly then this could have a profound effect on $k_{5.1}$. Does an incorrect determination of σ(ClO) however, have an effect upon the observed *relationship* between $[ClO]_{0,[CH_3OH]=0}$ and $[ClO]_{0,[CH_3OH]=x}$ and hence affect our determination of $[HO_2]_0$? To address this question, traces were once again simulated with and without CH_3OH with a known σ(ClO) and then fitted to analogous traces in a model with the same σ(ClO) decreased by 10%. The observed effect was a *ca.* 25% increase in inferred $[HO_2]_0$ and consequently an underestimation of $k_{5.1}$. The process was repeated with a 50% perturbation on σ(ClO) resulting in a similar, but larger effect. An incorrect σ(ClO) could not therefore account for the observed behaviour.

In summary, controlled perturbation of the numerical model, using idealised traces, could not simulate observed experimental behaviour wherein $\{[ClO]_0 + [HO_2]_0\}$ was smaller than that implied from $[ClO]_0$ in the absence of methanol. The model should therefore have been able to fit the experimental decay, using known chemistry.

5. 6 Further explanations

5. 6. 1 Change in Mechanism

If the numerical model used is a true representation of the chemistry taking place within the ClO + HO_2 chemical system then it is necessary to provide an explanation as to why $\{[ClO]_0 + [HO_2]_0\}$ in the presence of methanol is much less than $[ClO]_0$ in the absence of methanol. One explanation is the possible existence of a pre-equilibrium between ClO, HO_2 and an $[ClO.HO_2]^*$ adduct intermediate.

(5. 1) $\quad ClO + HO_2 \leftrightarrow [ClO.HO_2]^* \rightarrow$ Products

If this pre-equilibrium is rapid compared to subsequent chemistry then the observed rate r_{obs}, will be dependent upon the rate coefficient $k_{5.1}$ and the equilibrium concentration of the intermediate $[ClO.HO_2]^*_{eq}$, which is itself dependent upon the pre-equilibrium concentrations of ClO and HO_2:

(E5. 17) $$r_{obs} = k_{5.1}[ClO.HO_2]^*_{eq}$$

(E5. 18) $$[ClO.HO_2]^*_{eq} = K_{eq}[ClO]_{eq}[HO_2]_{eq}$$

Combination of (E5. 17) and (E5. 18) therefore gives:

(E5. 19) $$r_{obs} = k_{5.1}K_{eq}[ClO]_{eq}[HO_2]_{eq}$$

In this case the observed rate is dependent upon the pre-equilibrium concentration of HO_2, $[HO_2]_{eq}$, as opposed to the genuine initial concentration of HO_2 $[HO_2]_0$, as the model suggests.

The occurrence of such a pre-equilibrium would certainly reduce the available 'free' HO_2 and could potentially have led to a model optimising $[HO_2]_0$, returning an erroneously small value for this parameter. The existence of complexes involving the

HO_2 radical is well established. HO_2 is known to complex to methanol, which is responsible for rate enhancements in the HO_2 self-reaction.[37] Similar complexation of HO_2 with small polar molecules, such as H_2O and NH_3 has also been reported,[39, 40] again showing a catalytic effect on the HO_2 self-reaction. More recently, the existence of a HO_2.NO complex in the reaction of OH with NO_2 has been proposed.[41-43] No example for the complexation of HO_2 with any other (reactive) free radical has however been reported. Existence of such a HO_2.ClO pre-equilibrium therefore remains a possibility, which could affect the stoichiometry arguments involved in deducing $[HO_2]_0$ (and which could also affect all previous studies of the ClO + HO_2 reaction). Alternatively, the model could have failed due to a simple lack of sensitivity, and methods to improve the sensitivity through simultaneous analysis of multiple decay traces were designed, as discussed below, following the observation of unusual heterogeneous behaviour in the reaction vessel.

5. 7 Problems with the Gaseous Methanol Concentration

Whilst in principle, single back-to-back experiments carried out in the absence, presence and absence of methanol should provide good constraint on the total radical budget, by monitoring ClO alone, as shown in Figure 5. 15(a), it was clear that the model could not locate the global fit including the ClO + HO_2 reaction. Furthermore, in some experiments, carried out at low Cl_2 to Cl_2O conversion (and therefore low initial ClO radical concentration), a degree of unreliability in the experimental procedure was observed. In such experiments, it was found that after flowing methanol vapour in the cell and then reverting to an experiment in the absence of methanol, the initial ClO radical concentration did not return to its pre-methanol level. This is shown in Figure 5. 15(b), which shows ClO traces recorded in three successive experiments.

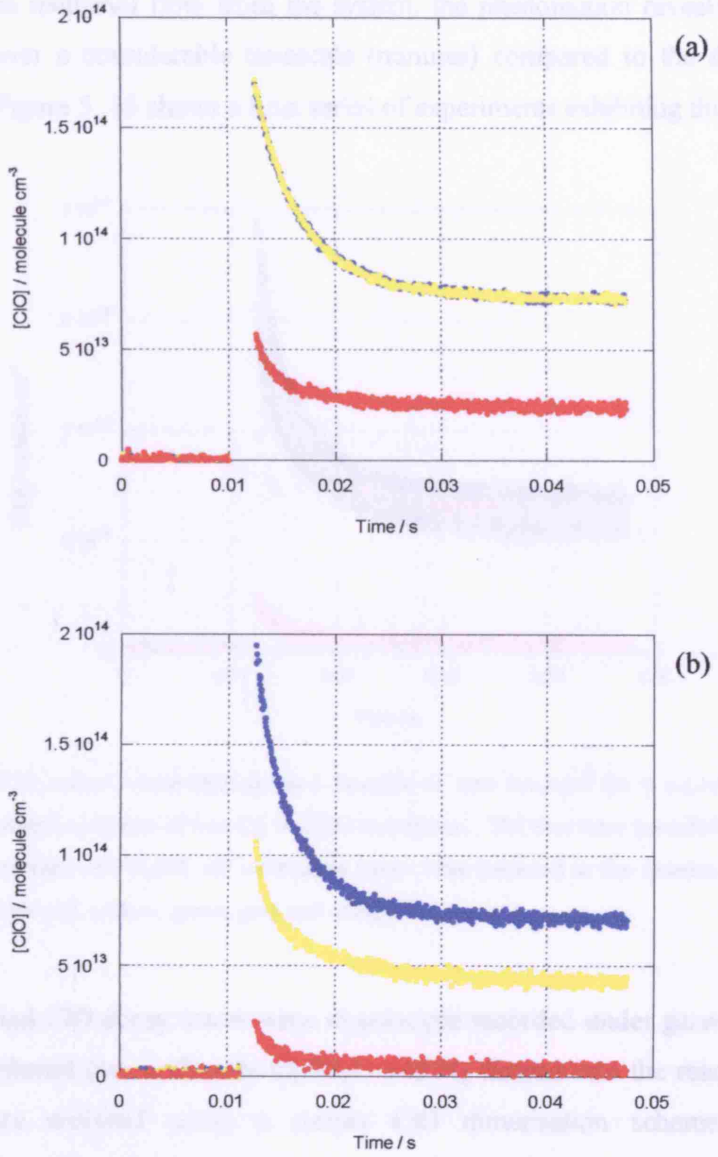

Figure 5. 15 ClO radical concentrations as a function of time for three successive experiments. (a) recorded with high Cl_2 to Cl_2O conversion (b) recorded at low Cl_2 to Cl_2O conversion. In both cases traces represent experiments recorded in the absence of CH_3OH (blue), in the presence of CH_3OH (red) and once again in the absence of CH_3OH (yellow).

On further inspection, if additional experiments were carried out subsequent to the removal of the methanol flow from the system, the phenomenon revealed a temporal dependence over a considerable timescale (minutes) compared to the duration of an experiment. Figure 5. 16 shows a time series of experiments exhibiting this effect.

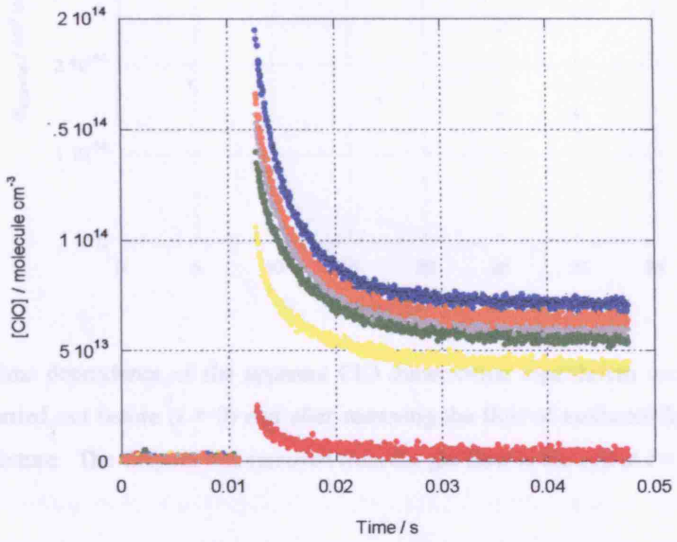

Figure 5. 16 ClO radical concentrations as a function of time recorded for 6 successive experiments under conditions of low Cl_2 to Cl_2O conversion. The first trace recorded (blue) was in the presence of CH_3OH, all subsequent traces were recorded in the absence of CH_3OH in the order red, yellow, green, grey and orange.

These individual ClO decay traces were in principle recorded under gaseous conditions devoid of methanol (*i.e.* with only Cl_2/Cl_2O and N_2 flowed into the reaction cell) and were therefore analysed using a simple ClO dimerisation scheme. The ClO dimerisation model could indeed be fitted to the observed traces, albeit with high residuals. However, the returned values for the ClO dimerisation equilibrium constant showed enhancement in the initial experiments carried out after stopping the methanol flow, with this value gradually, in successive experiments, reverting to the 'true' value recorded before methanol had been admitted to the system. The long term time dependence of the apparent equilibrium constant recorded in these experiments showed an exponential reversion to the 'pre-methanol' value, as shown in Figure 5. 17 below.

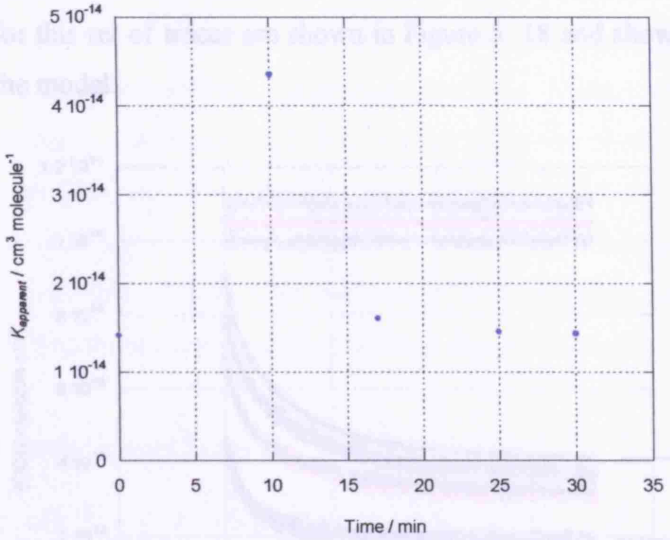

Figure 5. 17 Time dependence of the apparent ClO dimerisation equilibrium constant in experiments carried out before (t = 0) and after removing the flow of methanol from the precursor gas mixture. The CH_3OH was removed from the gas flow to the cell at t = 7 minutes.

Given that the gas phase composition, governed by the precursor flow rates, remained unchanged throughout these experiments, it was proposed that this behaviour resulted from the adsorption of gaseous methanol onto the walls of the gas mixing line and reaction vessel during the experiments carried out with methanol, and then desorbed into the reaction mixture in successive experiments. This effect was only observed at low initial ClO radical concentrations in the presence of methanol, which indicates low Cl_2 to Cl_2O conversions in the HgO column. Such conditions of low initial ClO would of course, be most sensitive to small perturbation in ClO and furthermore, in this case, since Cl_2 was relatively high, more Cl atoms would be present directly after photolysis for such a competition to operate even with a small gaseous methanol concentration.

A numerical model describing the chemistry for a series of experiments with different gas phase methanol (and therefore HO_2) concentrations was set up to investigate whether the observed behaviour, under these specific conditions, could be attributed to a gradual change in gas phase methanol concentrations between experiments. This model was used to fit to four ClO decay traces recorded under such experimental conditions, with a single global value for the ClO + HO_2 rate coefficient, consistent kinetic parameters for the ClO dimerisation (recorded prior to methanol had been added) but

with a different initial HO_2 radical concentration for each individual trace. The resulting fits for this set of traces are shown in Figure 5. 18 and show a strikingly good adherence to the model.

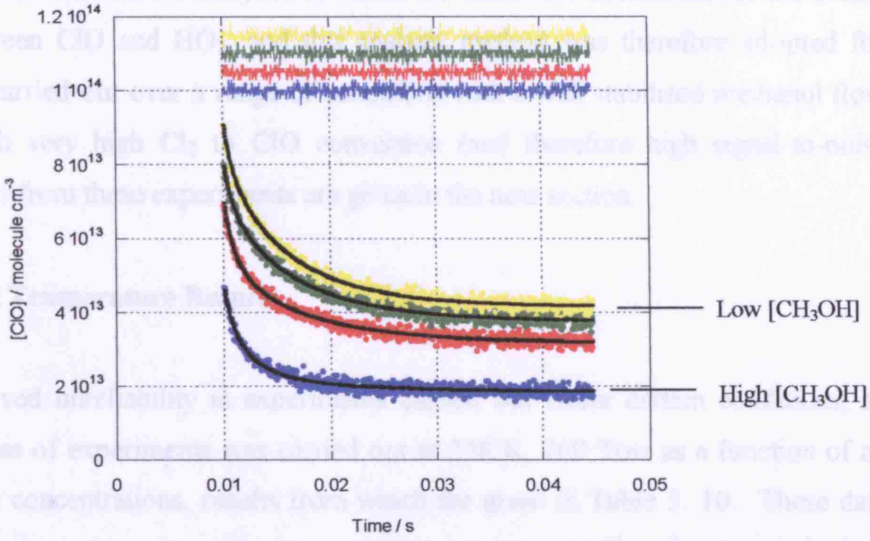

Figure 5. 18 Simultaneous fit of numerical model (black lines) to four experimental ClO decays recorded under conditions of successively lower CH_3OH concentrations (blue = high [CH_3OH], yellow = low [CH_3OH]). The residuals between the experimental decays and the simulated decays are plotted in corresponding colours to the experimental decays, offset for clarity.

Furthermore, the optimised initial HO_2 radical concentration as a function of experiment number (or time, in minutes) showed a gradual fall with successive experiments, during this 'post methanol' period.

The observation of this experimental complication, under conditions of low Cl_2 to Cl_2O conversion and in experiments carried out immediately after removing methanol from the gas mixture supplied to the reaction cell did provide an indication that the further constraint of the numerical model was possible. Using multiple traces with differing initial HO_2 concentrations the location of the global minimum value for the fitting determining the cross-reaction rate coefficient could be found. This promising method for obtaining a value for the ClO + HO_2 cross-reaction rate coefficient was not pursued further however, as (a) no control could be afforded over the methanol concentrations supplied in the gas phase in this way and (b) the simultaneous analysis of traces with intrinsically different HO_2 concentrations equally weights traces with a large and a small reactive flux through the ClO + HO_2 cross-reaction. However, this method did

illustrate the need to carry out experiments with a high Cl_2 to Cl_2O conversion, such that initial ClO concentrations were high, and the concentration of Cl atoms available for competition was therefore limited. Under such conditions, it was found that both single and multiple traces could be analysed to return the same rate coefficient for the cross-reaction between ClO and HO_2, and this analysis method was therefore adopted for experiments carried out over a range of conditions with a well stabilised methanol flow and only with very high Cl_2 to ClO conversion (and therefore high signal-to-noise ratio). Results from these experiments are given in the next section.

5. 8 Ambient Temperature Results

Having observed unreliability in experiments carried out under certain conditions, an extensive series of experiments was carried out at 298 K, 760 Torr as a function of all precursor gas concentrations, results from which are given in Table 5. 10. These data result in an average determination of $k_{5.1} = (1.12 \pm 0.39) \times 10^{-11}$ cm^3 molecule^{-1} s^{-1}, at 298 K and 760 Torr. Errors are 2σ, statistical only.

Most importantly, returned values of $k_{5.1}$ showed no systematic variation with any of the precursor concentrations of O_2, CH_3OH and Cl_2, as shown in Figure 5. 19 (a)–(c).

$[CH_3OH]_0$ / 10^{16} molecule cm^{-3}	$[ClO]_0$ / 10^{13} molecule cm^{-3}	$[HO_2]_0$ / 10^{13} molecule cm^{-3}	$k_{5,1}$ / 10^{-11} cm^3 $molecule^{-1}$ s^{-1}
9.76	6.09	2.63	1.18
9.76	6.22	2.54	1.12
4.62	7.76	2.75	1.09
4.62	6.51	2.53	1.05
12.28	5.88	2.13	1.01
12.28	2.91	1.45	1.46
14.95	7.19	3.60	1.04
14.95	6.73	3.04	1.01
7.14	6.55	2.93	1.30
7.14	5.28	2.11	1.14
10.76	5.84	3.01	0.98
10.76	5.94	3.03	1.01
9.75	2.43	2.38	1.42
9.75	2.44	2.29	1.57
9.75	2.29	2.37	1.32
9.75	2.51	2.48	1.38
3.60	2.99	3.08	0.95
3.60	2.86	2.79	1.19
9.36	6.79	3.83	1.07
9.36	6.98	3.95	1.03
6.40	7.76	3.68	1.05
6.40	8.23	4.24	1.19
8.37	6.99	3.91	0.91
8.37	6.97	3.93	0.94
4.43	9.05	3.35	1.18
4.43	8.73	3.38	1.14
7.38	5.52	3.32	1.04
7.38	5.42	3.14	1.10
5.42	6.21	3.17	0.99
5.42	6.40	3.48	1.04
5.42	6.74	3.74	1.02
8.59	13.68	4.83	1.45
8.59	12.91	4.20	1.28
8.59	15.17	5.90	1.78
8.59	7.24	5.41	1.01
8.59	7.22	5.20	0.96
4.97	8.79	4.75	1.06
4.97	8.31	4.69	1.03
7.68	6.91	5.89	0.98
7.68	6.75	5.90	0.96
4.07	9.60	6.24	0.92
4.07	8.89	6.28	0.87
5.87	7.78	7.18	0.82
5.87	8.08	7.7	1.06

Table 5. 10 Experimentally determined values of $[ClO]_0$, $[HO_2]_0$ and $k_{5,1}$ recorded at 298 K at a number of different initial methanol concentrations $[CH_3OH]_0$.

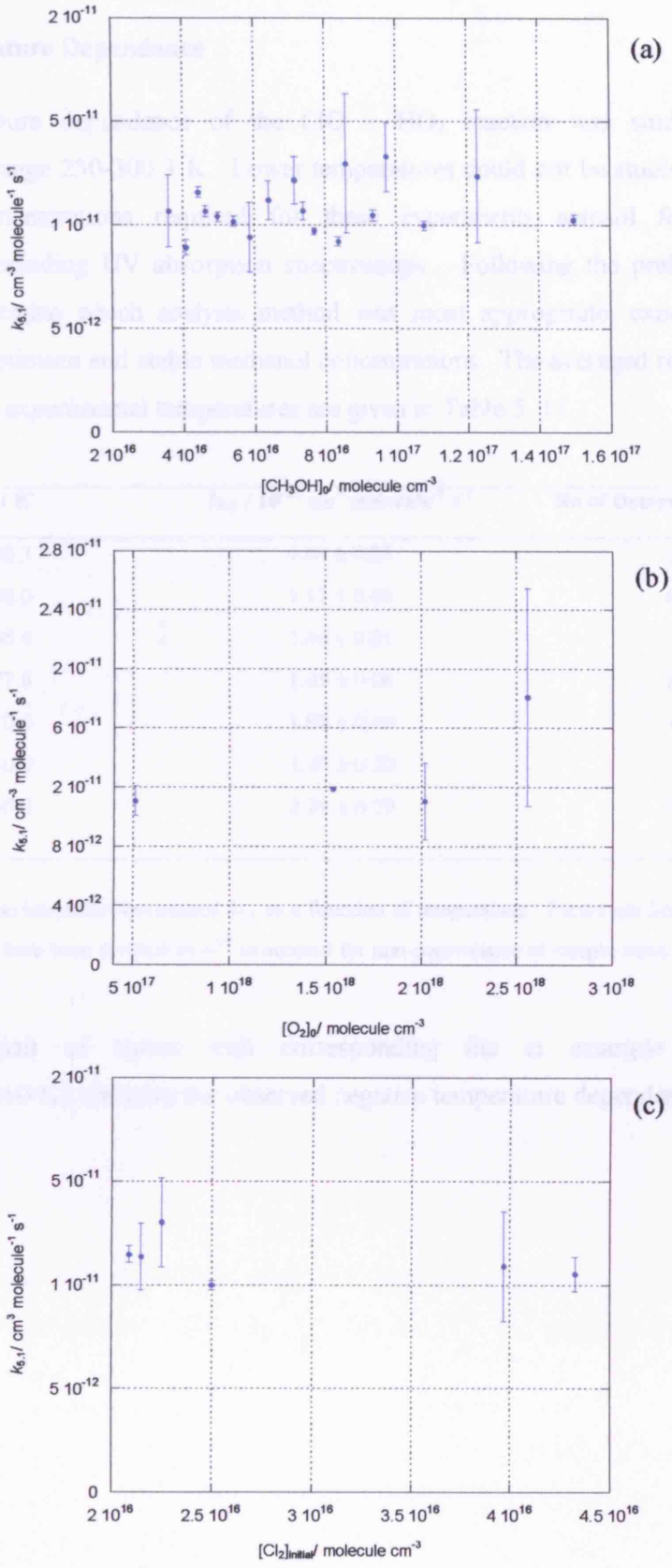

Figure 5. 19 Experimentally determined $k_{5.1}$ as a function of precursor gas concentrations, (a) Methanol, (b) oxygen and (c) chlorine.

5. 9 Temperature Dependence

The temperature dependence of the ClO + HO_2 reaction was studied over the temperature range 250-300.3 K. Lower temperatures could not be studied since at the methanol concentrations required for these experiments aerosol formation was observed, precluding UV absorption spectroscopy. Following the preliminary study used to determine which analysis method was most appropriate, experiments were repeated at optimum and stable methanol concentrations. The averaged results obtained at each of the experimental temperatures are given in Table 5. 11.

T / K	$k_{5.1}$ / 10^{-11} cm^3 molecule^{-1} s^{-1}	No of Determinations (n)
300.3	1.01 ± 0.23	6
298.0	1.12 ± 0.06	44
285.4	1.46 ± 0.21	5
277.8	1.45 ± 0.08	17
270.0	1.88 ± 0.49	6
260.0	1.49 ± 0.20	9
250.0	2.29 ± 0.29	9

Table 5. 11 Experimentally determined $k_{5.1}$ as a function of temperature. Errors are 2σ, statistical only, and have been divided by $n^{1/2}$ to account for non-equivalence of sample sizes.

A typical pair of traces with corresponding fits at example temperatures (298 K and 260 K), showing the observed negative temperature dependence, is given in Figure 5. 20.

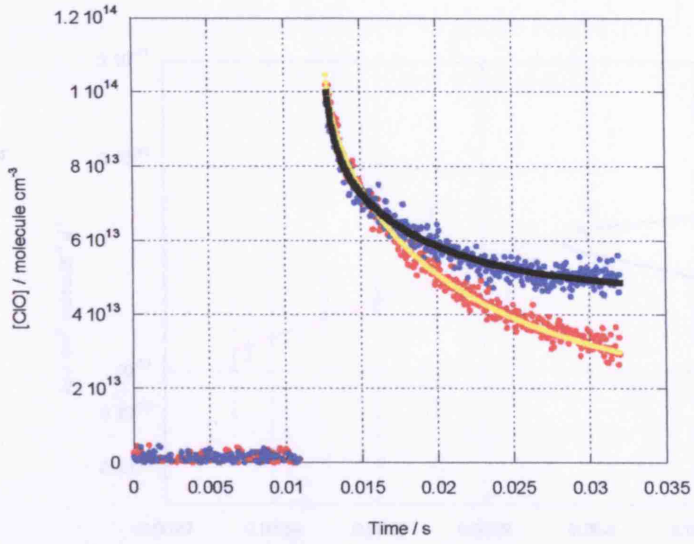

Figure 5. 20 ClO radical concentrations as a function of time recorded at 298 K (blue) and 260 K (red) along with associated model fits (black and yellow respectively).

The temperature dependent rate coefficients are described by Arrhenius behaviour according to:

(E5. 20) $$k_{5.1}(T) = (7.56 \pm 6.18) \times 10^{-13} \exp\left(\frac{819 \pm 220}{T}\right)$$

If the fit to the temperature dependent data is weighted to account for the different errors on the data points the Arrhenius expression becomes:

(E5. 21) $$k_{5.1}(T) = (6.44 \pm 3.77) \times 10^{-13} \exp\left(\frac{856 \pm 165}{T}\right)$$

The temperature dependent data along with both the un-weighted and the weighted Arrhenius parameterisations, given by (E5. 20) and (E5. 21) respectively are plotted in Figure 5. 21 below.

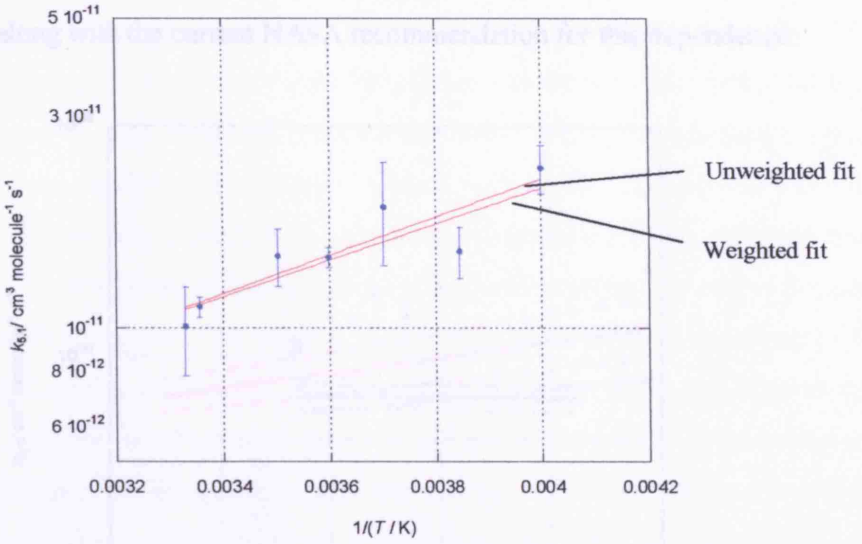

Figure 5.21 Experimentally determined $k_{5,1}$ (blue points) plotted in Arrhenius form along with Arrhenius fits (E5. 20) and (E5. 21) the latter of which has been weighted to account for different sized error bars. Errors are 2σ, statistical only, and have been divided by $n^{1/2}$ to account for non-equivalence of sample sizes.

5. 10 Discussion

The results presented in this work represent the first extensive study of the ClO + HO_2 reaction using broad band UV absorption spectroscopy to monitor radicals.

5. 10. 1 Kinetics of the ClO + HO_2 Reaction

Due to experimental limitations precluding HO_2 monitoring, preliminary experiments were conducted in order to characterise the initial concentration of HO_2 radicals in the $Cl_2/Cl_2O/CH_3OH/N_2$ gas system. Three techniques were developed for inferring $[HO_2]_0$, but after extensive investigations into the reliability of each of the techniques discussed above, only one method was considered viable. Following this initial study, the kinetics of the ClO + HO_2 reaction were however studied successfully over the temperature range 250-300.3 K. Results of this study have been plotted in Arrhenius form in Figure 5. 22 below. Also plotted in Figure 5. 22 are the Arrhenius

parameterisations of the two most recent temperature dependence studies of the ClO + HO_2 reaction along with the current NASA recommendation for this dependence.

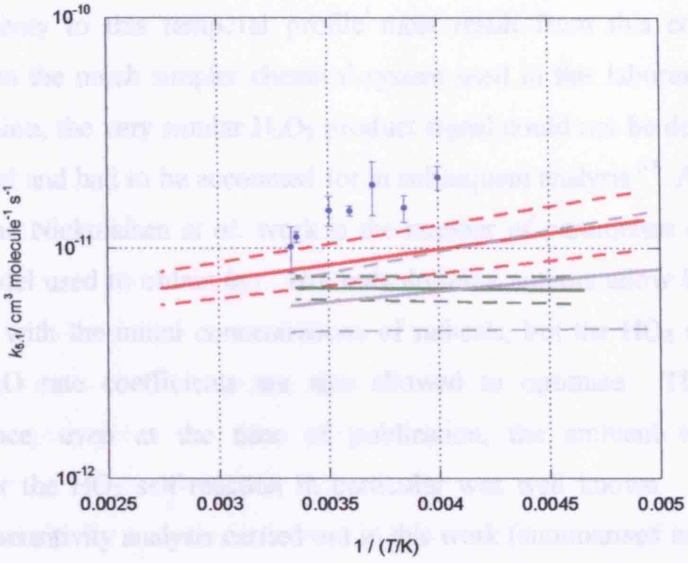

Figure 5. 22 Temperature dependent $k_{5.1}$ values determined in this study (blue points and error bars) plotted in Arrhenius form compared to the Arrhenius parameterisations determined by the previous studies of Nickolaisen *et al.*[13] (red), Knight *et al.*[30] (green) and the current NASA recommendation[31] (grey), along with their associated regions of error (given by the dotted lines of the same colour).

This study reports values of $k_{5.1}$ which are somewhat greater than those of previous studies and which lie close to the upper error limit reported by Nickolaisen *et al.*[13] Results from this work show a negative temperature dependence to $k_{5.1}$ in broad agreement with Nickolaisen *et al.* but in contrast to the dependence predicted by Knight *et al.* which shows $k_{5.1}$ to be independent of temperature.

The reasons for this discrepancy are not clear. Nickolaisen *et al.*, as discussed above, use a very similar experimental set-up to that used in this work, albeit with dual wavelength monitoring, rather than broad band spectroscopy, to monitor ClO. Nickolaisen *et al.* also monitor HO_2 absorbance at 210 nm, which was not possible in this work due to the large number of potential absorbing species at this wavelength coupled with the reduced signal-to-noise ratio near 210 nm. In analysing the 'HO_2' signal in their experiments, it is evident that the 210 nm trace is in fact contributed to by

up to five chemical species (Cl_2O_2, H_2O_2, HOCl, F_2 and Cl_2O) in addition to HO_2, all of which have a temporal dependence which may or may not correlate to the ClO + HO_2 reaction. Nickolaisen *et al.* do report that HO_2 dominates the 210 nm signal, but some loss of sensitivity to this temporal profile must result from this composite signal. Indeed, even in the much simpler chemical system used in this laboratory to study the HO_2 self-reaction, the very similar H_2O_2 product signal could not be deconvolved from the H_2O_2 signal and had to be accounted for in subsequent analysis.[37] Another potential criticism of the Nickolaisen *et al.* work is the number of parameters optimised in the numerical model used to obtain $k_{5.1}$. Not only do these authors allow $k_{5.1}$ to vary in the model, along with the initial concentrations of radicals, but the HO_2 self-reaction and the Cl + Cl_2O rate coefficients are also allowed to optimise. This is somewhat surprising since, even at the time of publication, the ambient temperature rate coefficient for the HO_2 self-reaction in particular was well known. Furthermore, as shown in the sensitivity analysis carried out in this work (summarised in Figure 5. 5) the value of the rate coefficient for the HO_2 self-reaction used in the model has a profound effect on the returned value of $k_{5.1}$. Allowing both the HO_2 + HO_2 and the ClO + HO_2 rate coefficients to vary could therefore return an erroneous pair of values. Nickolaisen *et al.* do use two different chemical schemes to generate the HO_2 radicals, namely F + H_2O_2 and Cl + CH_3OH + O_2 (as used in this work). Results from these two chemical systems used by Nickolaisen *et al.* systematically differ (the Cl + CH_3OH + O_2 system returns lower values of $k_{5.1}$) and an average value is reported.

The results reported in this work and in that of Knight *et al.*[30] differ significantly. As discussed above, Knight *et al.* use a discharge flow system to study this cross-reaction, and therefore operate at much lower pressures than in this work and that of Nickolaisen *et al.* Since in discharge flow the radicals are prepared separately, several different chemical systems can be (and indeed were) used to study the cross-reaction. Knight *et al.* report that these systems yield equivalent results, although they omitted results obtained using O_3 as a radical precursor in their final expression describing the temperature dependence of $k_{5.1}$.

As discussed above, all previous studies of the ClO + HO_2 reaction seem to indicate that the reaction is bimolecular, with the principal product HOCl. However, the possibility of a reaction channel forming a stabilised HO_3Cl adduct has been raised, initially by

Nickolaisen *et al.*, and some evidence for potential pre-equilibrium formation between the two radicals was observed in this work. The existence of a termolecular channel to the ClO + HO_2 reaction could imply that this reaction is pressure dependent and could therefore potentially explain some of the discrepancies between the high pressure flash photolysis and discharge flow results. Furthermore, the existence of HO_3Cl, most likely as HOOOCl, has been suggested by *ab initio* studies, most of which show a significant energy barrier to subsequent fragmentation.[14, 15] Nickolaisen *et al.* did investigate the pressure dependence of the ClO + HO_2 reaction, and found no significant effects at 298 K. Some exploratory experiments were also performed in this work to try to investigate the pressure dependence. Unfortunately, however, these results were inconclusive due in part to problems with the low and unstable conversion of Cl_2 to Cl_2O, essential for this work, presumably due to the different residence times of the Cl_2 in the HgO trap, and are not reported in this thesis.

It is interesting to note that other unpublished results[29] from a low pressure (discharge flow) study of the ClO + HO_2 reaction carried out in the same laboratory as the Nickolaisen *et al.* work, report $k_{5.1}$ to be significantly lower than all previous studies. Again, this raises the possibility of a pressure dependent channel to the reaction, but until these data are published, this remains unresolved.

Experiments carried out under conditions of low Cl_2 to Cl_2O conversion, as discussed above, indicated that methanol adsorption onto the reaction vessel wall may have occurred followed by desorption back into the vessel over a period of minutes. As a result the methanol concentration within the reaction cell at any given time throughout the course of an experiment could not be relied upon. For this study this issue was hopefully resolved due to awareness of the effect and the fact that the exact methanol concentration only needed to be known when calculating the rate coefficient for the HO_2 self-reaction, under experimental conditions. Furthermore, the calibration of this rate coefficient due to enhancement by methanol was achieved using a parameterisation developed in this laboratory using the same apparatus as this study, operated under similar conditions. As a result, it could be assumed that any anomalous methanol effect would be the same for both experiments. Of course, any problems of methanol adsorption and desorption which were encountered in this work may also have been

present in other, previous studies of the ClO + HO_2 reaction which also used methanol as a precursor to HO_2 radicals, in similar experimental set-ups.

5. 10. 2 Further Work

This study could be further enhanced and extended in two principal ways. First, if HO_2 radicals could be successfully monitored in the cross-reaction with ClO, the numerical fitting would be far more constrained (although no additional parameters ought to be optimised in doing this). Alternatively, reliable knowledge of $[HO_2]_0$, ideally through direct measurement, would help in the analysis of ClO traces, as has been discussed extensively above. Such improvements might be achieved by adding another diagnostic to probe the reacting gas mixture. In recent years, for example, infrared detection of HO_2 radicals has been developed and successfully applied in kinetics studies.[44] Infrared detection of peroxy radicals has the advantage that the IR spectra of such species are often structured, allowing unequivocal detection to be achieved far easier than in the UV, where peroxy radical spectra are usually broad and structureless. Thus, adding an IR detection system to the experiment, coupled with the broad band UV absorption system made possible using the CCD, would certainly render the technique far more powerful for studies of such complex systems. The second way in which these studies might be improved is by using multiple chemical systems to generate the free radicals in separate experiments, such as has been reported by Knight *et al.* As discussed above, the need for a premixed reactant precursor gas mixture, and the need to minimise secondary chemistry in flash photolysis offers less flexibility in how radicals are prepared (compared to, for example, discharge flow) and the number of potential chemical systems is consequently limited. However, as the problems encountered with methanol demonstrate, such issues can arise with some precursor species and are best eliminated by addressing the same reaction with different chemistry.

5. 10. 3 Summary

After considerable development of the numerical analysis method, this study has successfully reported rate coefficients for the ClO + HO_2 reaction over a range of temperatures. These results confirm that the reaction is fast and with a weak negative temperature dependence. Evidently, these results therefore support the existence of a stratospheric O_3 loss cycle containing the ClO + HO_2 reaction, and if as results suggest, the main product is HOCl, which photolyses rapidly in sunlight, these results imply that the ClO + HO_2 cycle is more efficient than previously thought. Of course, in regions of the stratosphere and at times where HOCl is less rapidly photodissociated, the enhanced rapidity of the ClO + HO_2 reaction alters the partitioning of Cl_y towards the HOCl temporary reservoir, thereby reducing the free ClO available to participate in other O_3 loss cycles such as those involving ClO + BrO. In this case, a more rapid ClO + HO_2 reaction could potentially diminish O_3 loss. Similar arguments may be advanced concerning the effects of the increased ClO + HO_2 rate coefficient reported here on the HO_x partitioning and therefore O_3 loss. Clearly, atmospheric model studies are required to investigate the effects of such changes in the kinetics.

This work has also reported some evidence for the possible association, in a pre-equilibrium, of ClO and HO_2 radicals. If such association were to take place, then the possibility of a stabilised HO_3Cl adduct could exist, which might cause the ClO + HO_2 reaction to be pressure dependent. Clearly further detailed investigations of this are required. If HO_3Cl were to form in the stratosphere, the chemical and photochemical properties of this species would of course need to be investigated.

Finally, the considerable spread of data reported for the ClO + HO_2 reaction reflects the immense difficulty of studying mixed radical-radical reactions in the gas phase. The unequivocal monitoring of ClO, afforded by the broad band CCD technique used here, allows 'pure' ClO temporal traces to be obtained, which clearly show the difference between a dimerisation only and more complex chemistry. Further work to enhance the system for the monitoring of HO_2, would resolve any remaining uncertainties in this and other key atmospheric reactions.

5. 11 References

1. WMO, *Scientific Assessment of Ozone Depletion: 2002*, World Meteorological Association, Geneva, **2002**.
2. M. McElroy and R.J. Salawitch, *Science*, **1989**, 243, 763.
3. D.J. Lary, *J. Geophys. Res.*, **1997**, 102, 21515 .
4. P.O. Wennberg, R.C. Cohen, R.M. Stimpfle, J.P. Koplow, J.G. Anderson, R.J. Salawitch, D.W. Fahey, E.L. Woodbridge, E.R. Keim, R.S. Gao, C.R. Webster, R.D. May, D.W. Toohey, L.M. Avallone, M.H. Proffitt, M. Loewenstein, J.R. Podolske, K.R. Chan, and S.C. Wofsy, *Science*, **1994**, 266, 5184, 398.
5. J.D. Cox, D.D. Wagman, and V.A. Medvedev, *CODATA. Key Values for Thermodynamics*, **1989**, New York: Hemisphere Publishing.
6. T.J. Leck, Cook, J. E. L. and Birks, J. W., *J. Chem. Phys.*, **1980**, 72, 4, 2364.
7. J.P. Burrows and R.A. Cox, *J. Chem. Soc. -Faraday Trans. I*, **1981**, 77, 2465.
8. M.T. Leu, *Geophys. Res. Lett.*, **1980**, 7, 173.
9. M. Finkbeiner, J.N. Crowley, O. Horie, R. Muller, and G.K. Moortgat, *J. Phys. Chem.*, **1995**, 99, 44, 16264.
10. R.M. Stimpfle, Perry, R. A. and Howard, C. J., *J. Chem. Phys.*, **1979**, 71, 12, 5183.
11. D.W. Toohey and J.G. Anderson, *J. Phys. Chem.*, **1989**, 93, 1049.
12. D. Buttar and D.M. Hirst, *J. Chem. Soc.-Faraday Trans.*, **1994**, 90, 13, 1811.
13. S.L. Nickolaisen, C.M. Roehl, L.K. Blakeley, R.R. Friedl, J.S. Francisco, R. Liu, and S.P. Sander, *J. Phys. Chem.*, **2000**, 104, 308.
14. N. Kaltsoyannis and D.M. Rowley, *Phys. Chem. Chem. Phys.*, **2002**, 4, 3, 419.
15. Z.F. Xu, R.S. Zhu, and M.C. Lin, *J. Phys. Chem. A*, **2003**, 107, 19, 3841.
16. J. Francisco and S. Sander, *J. Phys. Chem.*, **1996**, 100, 573.
17. M. Grela and A. Colussi, *J. Phys. Chem.*, **1996**, 100, 10150.
18. L.T. Molina and M.J. Molina, *J. Phys. Chem.*, **1978**, 82, 2410.
19. R. Vogt and R.N. Schindler, *J. Photochem. Photobiol. A-Chem.*, **1992**, 66, 2, 133.
20. S. Solomon, R.R. Garcia, F.S. Rowland, and D.J. Wuebbles, *Nature*, **1986**, 321, 755.
21. P.J. Crutzen and F. Arnold, *Nature*, **1986**, 324, 651.
22. P. Crutzen, I. Isaksen, and J. McAfee, *J. Geophys. Res.*, **1978**, 83, 345.

23. M. Natarajan and L.B. Callis, *J. Geosphys. Res.*, **1991**, 96, 9361.
24. S. Chandra, C.H. Jackman, A.R. Douglas, E.L. Fleming, and D.B. Considine, *Geophys. Res. Lett.*, **1993**, 20, 351.
25. R. Toumi and S. Bekki, *Geophys. Res. Lett.*, **1993**, 20, 2447.
26. F.C. Cattell and R.A. Cox, *J. Chem. Soc. -Faraday Trans. Ii*, **1986**, 82, 1413.
27. M. Mozurkewich, *J. Phys. Chem.*, **1986**, 90, 2216.
28. B. Reimann and F. Kaufman, *J. Chem. Phys. Letts.*, **1978**, 69, 6, 2925.
29. S.P. Sander, *Private communication*, **2002**.
30. G.P. Knight, T. Beiderhase, F. Helleis, G.K. Moortgat, and J.N. Crowley, *J. Phys. Chem. A*, **2000**, 104, 8, 1674.
31. S.P. Sander, R.R. Friedl, D.M. Golden, M.J. Kurylo, R.E. Huie, V.L. Orkin, G.K. Moortgat, A.R. Ravishankara, C.E. Kolb, and M.J. Molina, *Chemical Kinetics and Photochemical Data for Use in Atmospheric Studies*, JPL Publication 02-25, Jet Propulsion Laboratory, Pasadena, CA, **2002**.
32. G. Tyndall, T. Wallington, M. Hurley, and W. Schneider, *J. Phys. Chem.*, **1993**, 97, 1576 .
33. W. Tsang, *J. Phys. Chem. Ref. Data*, **1987**, 16, 471.
34. P. Pagsberg, J. Munk, A. Sillesen, and C. Anastasi, *Chem. Phys. Lett.*, **1988**, 146, 375.
35. P. Stevens and J. Anderson, *J. Phys. Chem.*, **1992**, 96, 1708.
36. J. Bozzelli and A. Dean, *J. Phys. Chem.*, **1993**, 97, 4427.
37. D. Stone and D.M. Rowley, *Phys. Chem. Chem. Phys.*, **2005**, 7, 2156.
38. W. Bloss, D. Rowley, R. Cox, and R. Jones, *Phys. Chem. Chem. Phys.*, **2002**, 4, 15, 3639.
39. E. Hamilton Jr, *J. Chem. Phys.*, **1975**, 63, 8, 3682.
40. E. Hamilton Jr and L. Ruey-Rong, *Int. J. Chem. Kinet.*, **1977**, 9, 875.
41. N. Donahue, R. Mohrschladt, T. Dransfield, J. Anserson, and M. Dubey, *J. Phys. Chem. A*, **2001**, 105, 1515.
42. D. Golden and G. Smith, *J. Phys. Chem. A*, **2000**, 104, 3991.
43. B. Bean, A. Mollner, S. Nizkorodov, G. Nair, M. Okumura, S.P. Sander, K. Peterson, and J.S. Francisco, *J. Phys. Chem. A*, **2003**, 107, 6974.
44. C.A. Taatjes and J.F. Hershberger, *Annu. Rev. Phys. Chem.*, **2001**, 52, 41.

Chapter 6

The BrO + BrO Reaction

The BrO radical is an important atmospheric species playing a major role in O_3 destruction and as an intermediate in the breakdown of bromine containing compounds. In both the polar and mid-latitude stratosphere catalytic cycles involving BrO, principally those involving the BrO + ClO reaction, have been shown to be critical when considering the O_3 budget.[1] In addition, relatively large springtime concentrations of atmospheric BrO have been observed in the Artic marine boundary layer (MBL),[2-4] as shown in Figure 6. 1, and more recently in the mid-latitude MBL,[5, 6] implying that O_3 losses in these regions result from BrO chemistry. Specifically, due to elevated BrO concentrations observed in such regions, the BrO self-reaction is expected to play an important role.

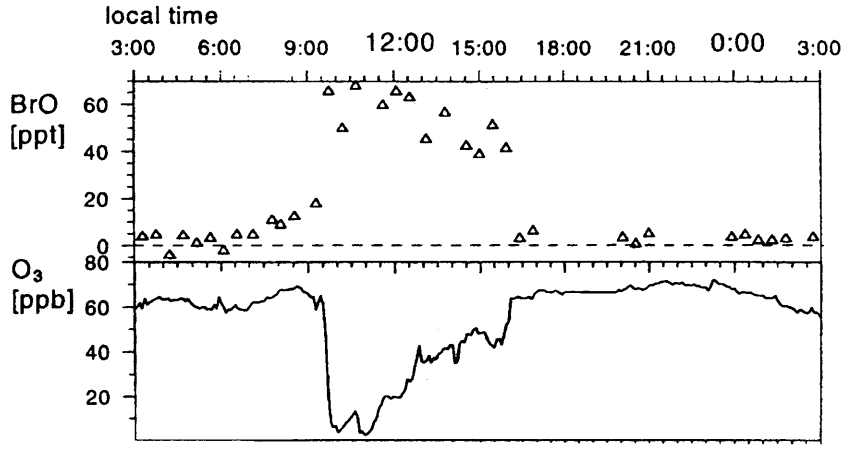

Figure 6. 1 Tropospheric mixing ratios of BrO and O_3 taken over the course of a day, recorded at the Arctic MBL. Taken from reference 3.

A number of mechanisms, all suggesting sea salt Br^- as the source of inorganic bromine, have been put forward as an explanation for the existence of elevated gas phase BrO concentrations in the MBL.[7-10] A widely accepted mechanism is that nighttime uptake of HOBr onto sea salt aerosol particles results in the production of gaseous Br_2. Subsequent daytime photolysis of Br_2 releases Br atoms, hence the production of BrO ensues with the concomitant loss of O_3, reactions (6. 1)-(6. 5).

(6. 1) $HOBr\ (g) + aerosol \leftrightarrow HOBr\ (aq)$

(6. 2) $HOBr\ (aq) + Br^-\ (aq) + H^+\ (aq) \leftrightarrow Br_2\ (aq) + H_2O$

(6. 3) $Br_2\ (aq) \leftrightarrow Br_2\ (g)$

(6. 4) $Br_2\ (g) + h\nu \rightarrow 2Br$

(6. 5) $2(Br + O_3 \rightarrow BrO + O_2)$

Net: $HOBr + Br^- + H^+ + 2O_3 \rightarrow 2BrO + 2O_2 + H_2O$

The resulting elevated local BrO concentrations cause further O_3 loss through the BrO self-reaction in the following catalytic cycle:

(6. 6a) $BrO + BrO \rightarrow 2Br + O_2$

(6. 5) $2(Br + O_3 \rightarrow BrO + O_2)$

Net: $2O_3 \rightarrow 3O_2$

Given the atmospheric importance of the BrO radical there have been many studies of its gas phase reactions such as BrO + ClO, BrO + HO_2 and BrO + BrO. Uncertainties do however still remain in the kinetics and mechanism of these reactions and in particular of the self-reaction. Accurate knowledge of the self-reaction kinetics is therefore required. Furthermore, knowledge of the reaction channels of the BrO self-reaction is essential, since any channel not resulting in Br atom production will significantly change the impact the BrO self-reaction has on the O_3 budget. Determination of all of these results, along with a knowledge of the rate coefficients of all other atmospheric reactions of the BrO radical, allows the most accurate model description of O_3 chemistry and partitioning between active and inactive bromine species possible. Furthermore, not only is the BrO self-reaction atmospherically important, but it is also a crucial pathway when undertaking laboratory studies of other gas phase systems involving BrO.

6. 1 Reaction channels

The BrO self-reaction proceeds *via* two known reaction channels:

(6. 6a) $BrO + BrO \rightarrow Br + Br + O_2$

(6. 6b) $BrO + BrO \rightarrow Br_2 + O_2$

Experimental evidence for this two channel mechanism is discussed in Section 6. 2 below. In the atmosphere, channel (6. 6a) is a direct source of O_3 destruction *via* the catalytic cycle:

(6. 5) $Br + O_3 \rightarrow BrO + O_2$

6. 2 Previous Studies

Early studies of the kinetics of the BrO + BrO reaction show little agreement, at 298 K reported rate coefficients range from (0.65-5.2) $\times 10^{-12}$ cm^3 $molecule^{-1}$ s^{-1}. The majority of these studies determined the absolute rate constant $k_{6.6}$ and utilised techniques including discharge flow coupled with UV absorption spectroscopy,[11, 12] discharge flow coupled with mass spectrometry[13] and flash photolysis coupled with UV absorption spectroscopy.[14, 15] For those latter studies that used UV absorption spectroscopy, discrepancies are likely to stem from a poor knowledge of accurate BrO absorption cross-sections. Confusion over the mechanism is apparent in these studies. Basco and Dogra[15] assumed channel (6. 6b) was the exclusive pathway whereas Clyne and Cruse[12] and Clyne and Watson[13] assumed channel (6. 6a) dominated. The two earliest temperature dependent studies did not report rate coefficients at sub-ambient temperatures.[12, 14] The results from all of these studies of the BrO self-reaction, as well as those from subsequent studies discussed below, are summarised in Tables 6. 1 and 6. 2 below.

The first study to investigate the branching of the different channels of the BrO + BrO reaction was that of Jaffe and Mainquist.[16] These authors reported quantum yields for

the bromine photosensitised decomposition of O_3 over the temperature range 258-333 K and showed channel (6. 6a) to dominate. It is somewhat surprising that the observed quantum yields of Br_2 photolysis reported in this work inexplicably decreased with increasing Br_2 concentration.

Sander and Watson[17] completed the first comprehensive study of the kinetics and mechanism of the BrO self-reaction. Sander and Watson employed flash photolysis coupled with UV absorption spectroscopy, as a function of temperature over the range 223-338 K and pressure over the range 50-475 Torr. BrO absorption cross-sections were determined for the (7, 0) band in the ($A^2\Pi_{3/2} \leftarrow X^2\Pi_{3/2}$) transition at 223 K, 298 K and 388 K. Using these experimental conditions, Sander and Watson determined the rate coefficient $k_{6.6}$ to be independent of pressure and to exhibit Arrhenius behaviour with a negative temperature dependence, assuming that the BrO decay was pure second order. For the first time two independent chemical systems were used in order to determine the reaction rates of both reaction channels (6. 6a) and (6. 6b). The overall rate constant $k_{6.6}$ was determined *via* photolysis of Br_2/O_2 gas mixtures:

(6. 7) $O_2 + h\nu\ (\lambda > 180\ nm) \rightarrow 2O$

(6. 8) $O + Br_2 \rightarrow BrO + Br$

In the second chemical system Br_2 was photolysed in the presence of excess O_3 which had the effect of singling out the kinetic signal for channel (6. 6b).

(6. 4) $Br_2 + h\nu\ (\lambda > 300\ nm) \rightarrow 2Br$

(6. 5) $Br + O_3 \rightarrow BrO + O_2$

O_3 rapidly reacts with Br atoms regenerating BrO and O_2 in reaction (6. 5), so the kinetic signature from channel (6. 6a) is effectively masked. As a result, the observed BrO decay under these conditions is solely due to channel (6. 6b). Since $k_{6.6} = k_{6.6a} + k_{6.6b}$ combination of results from the two chemical systems resulted in the determination of the branching ratio. At 298 K Sander and Watson determined $k_{6.6a}/k_{6.6}$ to be 0.84 ± 0.03.

Sander and Watson rationalised the formation of Br_2 in channel (6. 6b) by the formation of a vibrationally excited intermediate, BrOOBr*:

(6. 6c)	BrO + BrO	↔	BrOOBr*
(6. 9a)	BrOOBr* + M	→	BrOOBr + M
(6. 9b)	BrOOBr*	→	BrOO + Br
(6. 10)	BrOO	→	Br + O_2
(6. 9c)	BrOOBr*	→	[Br-O-O-Br]
(6. 11)	[Br-O-O-Br]	→	Br_2 + O_2

Turnipseed *et al.*[18] carried out a low pressure study of the BrO self-reaction using discharge flow coupled with mass spectrometry. The use of this detection technique meant that the results from this study did not depend on the determination of BrO absorption cross-sections. The temperature dependence determined over the range 253-400 K is in good agreement with that determined by Sander and Watson.

Lançar *et al.*[19] also used discharge flow coupled with mass spectrometry to measure the overall rate constant $k_{6.6}$ as well as that of the channel producing Br_2 and O_2, $k_{6.6b}$. An O + Br_2 chemical system was used to measure $k_{6.6}$ and an O_3 + Br system was used to record $k_{6.6b}$, where Cl + C_2H_3Br was the source of Br atoms. Results from the Lançar *et al.* study are in excellent agreement with Clyne and Watson and in good agreement with Turnipseed *et al.*, both of which used similar techniques. There is however disagreement between the results of Lançar *et al.* and the other previous studies that used UV absorption spectroscopy to monitor BrO.

Bridier *et al.*[20] used flash photolysis coupled with UV absorption spectroscopy in a 298 K study of the BrO self-reaction. As with many of the previous groups, photodissociation of Br_2 generated Br atoms which then reacted with O_3 to generate BrO radicals. Since use of this chemical system afforded the determination of $k_{6.6b}$ only, $k_{6.6}$ was determined by assuming the recommended branching ratio $k_{6.6b}/k_{6.6} = 0.16$ of the time. Using this assumption $k_{6.6}$ was found to be in excellent agreement with the

low pressure studies of Lançar *et al.* and Clyne and Watson, but in disagreement with Sander and Watson by approximately 36% despite Bridier *et al.* using the same technique as Sander and Watson. Bridier *et al.* carried out experiments at total pressures of 100, 500 and 650 Torr of He. Over the range studied, no pressure dependence, or dependence on O_3 concentration of $k_{6.6}$ was observed. If however N_2 was used as the carrier gas a small pressure dependence and a dependence of BrO kinetics on O_3 concentration was observed. This effect was attributed to the reaction:

(6. 12) $\quad Br + BrO + M \rightarrow \quad Br_2O + M$

At high O_3 concentrations no significant pressure dependence was observed since all the Br atoms were scavenged by O_3 and reaction with BrO could apparently not compete. Disagreement between this determination of $k_{6.6}$ and that of Sander and Watson, using the same technique, was attributed to the possibility that Sander and Watson may have overlooked the effect that reaction (6. 12) might have on BrO decay at the low O_3 concentrations used in this study and to discrepancies in BrO cross-sections used.

Mauldin *et al.*[21] carried out an extensive study of the kinetics and mechanism of the BrO self-reaction using flash photolysis coupled with UV absorption spectroscopy utilising both single wavelength PMT detection and broad band detection using a diode array. Rate coefficients were measured at 298 K and 220 K over the pressure range 75-600 Torr of He, N_2 and SF_6. The overall rate coefficient $k_{6.6}$ was determined using BrO absorption cross-sections from the literature[22] and was subsequently found to be independent of pressure at 298 K but dependent on pressure at 220 K. The branching ratio $k_{6.6a}/k_{6.6}$ was determined to be 0.84 and 0.68 at 298 K and 220 K respectively and independent of pressure. For the first time, in the low temperature experiments, an additional absorption feature was observed at 312 nm that was tentatively assigned to the BrO dimer, Br_2O_2.

Rowley *et al.*[23] used flash photolysis coupled with UV absorption spectroscopy in a 298 K study of the kinetics of the BrO self-reaction. This study was the first study to use a 2-dimensional CCD detector to monitor radicals in the gas phase. As with the study of Mauldin *et al.*, literature BrO absorption cross-sections[22] were used to determine $k_{6.6}$,

and the rate coefficient for channel (6. 6b). Results are in excellent agreement with previous studies.

Laszlo *et al.*[24] used 193 nm laser photolysis of $Br_2/N_2O/N_2$ gas mixtures to determine the kinetics of the BrO self-reaction at 295 K. The study measured BrO absorption cross-sections that were in good agreement with those used in previous studies, taken from the literature.[22] BrO radicals were generated in the following way:

(6. 13) $N_2O + h\nu \rightarrow O(^1D) + N_2$

(6. 14) $O(^1D) + N_2 \rightarrow O(^3P) + N_2$

(6. 8) $O(^3P) + Br_2 \rightarrow BrO + Br$

The measured rate coefficients from this study are in excellent agreement with previous studies.

Gilles *et al.*[25] also used 193 nm laser induced fluorescence of $Br_2/N_2O/N_2$ gas mixtures, coupled with UV absorption spectroscopy to measure the absolute BrO absorption cross-sections of the (7, 0) band and the rate coefficient $k_{6.6}$, over the temperature range 204-388 K at total pressures of 6-15 Torr. At 298 K results are in good agreement with previous studies. The temperature dependence exhibited negative linear Arrhenius behaviour.

By far the most extensive study of the kinetics and mechanism of the BrO self-reaction is that of Harwood *et al.*[26] This study was carried out over the temperature range 222-298 K and the pressure range 100-760 Torr of N_2 or O_2. Like previous studies photolysis of O_2 in the presence of excess Br_2 and photolysis of Br_2 in the presence of excess O_3 were both used such that the overall rate coefficient, and those of both reaction channels could be determined. As with many of the previous studies BrO absorption cross-sections were taken from the literature.[22] In agreement with Mauldin *et al.* the observed temperature dependence was negative over the entire temperature range and at temperatures below 250 K the rate coefficient $k_{6.6}$ was also found to be

dependent upon pressure. The rationale for this observed effect was that at low temperatures an additional termolecular channel, forming a Br_2O_2 dimer, occurs:

(6. 6c) $$BrO + BrO + M \leftrightarrow Br_2O_2 + M$$

Like Mauldin *et al.* at low temperatures an underlying absorption was observed. Harwood *et al.* attributed this absorption to the BrO dimer and subsequently the UV absorption spectrum of Br_2O_2 was recorded over the wavelength region 300-390 nm.

Reference	Technique	T / K	p / Torr	$k_{6.6}$ / 10^{-12} cm^3 molecule^{-1} s^{-1}	$k_{6.6a}/k_{6.6}$
Clyne and Cruse[12]	DF/UV	293-573	1	5.2 ± 0.6	
Basco and Dogra[15]	FP/UV	298	400-760	1.1 ± 0.2	
Clyne and Watson[13]	DF/MS	298		3.2 ± 0.7	
Jaffe and Manquist[16]	PD	258-333			0.84 ± 0.07
Sander and Watson[17]	FP/UV	223-338	50-475	2.17 ± 0.68	0.84 ± 0.03
Cox *et al.*[27]	MM/UV	298		4.1 ± 1.5	
Turnipseed *et al.*[18]	DF/MS	253-400	2	2.49 ± 0.26	
Lançar *et al.*[19]	DF/MS	298	1-2	3.2 ± 0.5	0.85
Bridier *et al.*[20]	FP/UV	298	760	3.1 ± 0.4	
Mauldin *et al.*[21]	FP/UV	298, 220	75-600	2.78 ± 0.25	0.84
Rowley *et al.*[23]	FP/UV	298	760	2.98 ± 0.42	
Laszlo *et al.*[24]	LP/UV	295	200	2.8 ± 0.5 [a]	
Gilles *et al.*[25]	DF/UV	204-388	6-15	3.4 ± 0.5	
Bedjanian *et al.*[28]	DF/MS	298	1	2.75 ± 0.35	0.84 ± 0.03
Harwood *et al.*[26]	LP/UV	222-298	100-760	2.88 ± 0.20	

[a] 295 K

Table 6. 1 Comparison of kinetic data describing the BrO self-reaction recorded at 298 K.

Reference	T / K	P / Torr	A / cm^3 molecule^{-1} s^{-1}	$(-E_a/R)$ / K
Clyne and Cruse[12]10	293-573	1	$(5.25 \pm 3.07) \times 10^{-11}$	-450 ± 300
Sander and Watson[17]15	223-338	50-475	9.58×10^{-13}	225 ± 195
Turnipseed *et al.*[18]16	253-400	2	$(1.06 \pm 0.20) \times 10^{-12}$	251 ± 56
Gilles *et al.*[25]23	204-388	6-15	$(1.70 \pm 0.45) \times 10^{-12}$	215 ± 50
Harwood *et al.*[26]24	250-298	760	$(5.31 \pm 1.17) \times 10^{-12}$[a]	211 ± 59[a]
			$(1.13 \pm 0.47) \times 10^{-14}$[b]	-983 ± 111[b]

[a](6. 6a) BrO + BrO → Br + Br + O_2, [b](6. 6b) BrO + BrO → Br_2 + O_2

Table 6. 2 Comparison of results of the temperature dependence of the BrO self-reaction, where $k_{6.6}(T) = A\exp\left(\frac{-E_a}{RT}\right)$.

In addition to these experimental studies, several *ab initio* studies of the reaction pathways have been carried out in broad support of a two channel mechanism with the BrO dimer lying *ca.* –60 kJ mol^{-1} relative to the BrO radical reactants.[29, 30] The most recent of these sudies, by Papayannis *et al.*[29] predicts a negligible energy barrier to reaction products, which suggests a weak overall temperature dependence. Possible weak stabilisation of a short-lived Br_2O_2 complex at low temperatures is expected to cause an increased probability of channel (6. 6b).

In summarising the previous studies of the BrO self-reaction, many aspects of the process, particularly at 298 K, are well established. The existence of a two channel mechanism is clear, and the branching ratio between the two channels at 298 K and at sub-ambient temperatures is very well characterised, perhaps partly because this ratio is fundamentally unaffected by the choice of BrO absorption cross-sections in spectroscopic studies. In the atmosphere, whilst the branching between channels of the BrO self-reaction will affect O_3 destruction, the rapid solar photolysis of Br_2 or indeed the BrO dimer is likely to compromise the effect of non-direct production of Br atoms in the self-reaction. Perhaps, therefore the most significant uncertainty remaining in the BrO self-reaction is simply the kinetics of the overall process at reduced temperatures. Of the many previous studies of this process, very few have detailed coverage of this temperature region, despite the obvious atmospheric significance, and this is reflected in the current uncertainty in the recommended rate coefficient for the BrO self-reaction in atmospheric modelling, rising from ± 15% at 298 K to ± 37% at 220 K.[31]

6. 3 This Work

This chapter presents results of a kinetic study of the BrO self-reaction. The reaction has been chosen, firstly as a test reaction at 298 K to show that the inclusion of laser flash photolysis into the experimental set-up has been successful and secondly to address discrepancies in the previous studies of the temperature dependence of the overall reaction.

6. 3. 1 Radical Generation

The production of BrO radicals was initiated following 193 nm photolysis of gaseous nitrous oxide, N_2O (BOC, 99.999%). This results in near 100% formation of electronically excited oxygen atoms:[32]

(6. 13) $N_2O + h\nu\ (193\ nm) \rightarrow O(^1D) + N_2$

Under all experimental conditions adopted here (p > 100 Torr) this process is then exclusively followed by collisional deactivation of $O(^1D)$ by the N_2 buffer gas:

(6. 14) $O(^1D) + N_2 \rightarrow O(^3P) + N_2$

Ground state oxygen atoms were then reacted with an excess of Br_2 to produce BrO radicals:[33]

(6. 8) $O(^3P) + Br_2 \rightarrow BrO + Br$

Some photolysis of Br_2 was also likely ($\sigma(BrO)_{193\ nm} \sim 2 \times 10^{-20}$ cm^2 molecule^{-1}), liberating further Br atoms:

(6. 4) $Br_2 + h\nu\ (193\ nm) \rightarrow 2Br$

Experiments were carried out over the temperature range 225-305 K and at 760 Torr. The instrument settings used for these experiments are given in Table 6. 3 below.

Spectrograph diffraction grating	300 grooves / mm
Entrance slit width	75 μm
Resolution	1.1 nm (FWHM)
Wavelength region	305-365 nm
CCD shift time	50 μs

Table 6. 3 Experimental instrument settings used for this study of the BrO self-reaction.

Photolysis of $N_2O/Br_2/N_2$ gas mixtures resulted in the production of BrO radicals, the distinctive spectrum of which, with vibronic structure, could be observed over the experimental wavelength region 305-365 nm. A typical post-photolysis absorption spectrum for this experimental system is shown in Figure 6. 2.

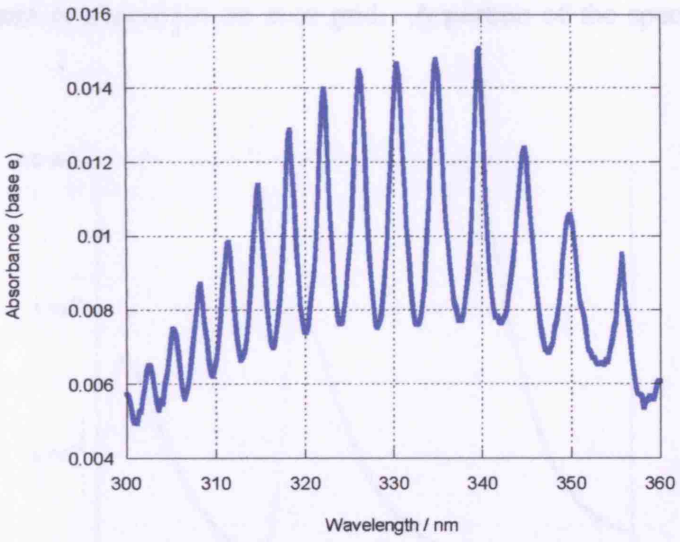

Figure 6. 2 Typical post-photolysis absorbance spectrum recorded for a $N_2O/Br_2/N_2$ gas mixture.

6. 3. 2 Quantification of BrO radical concentrations

From the observed experimental intensities, absorbances and subsequently concentrations were determined by applying Beer's law and the Beer-Lambert law as discussed in Section 3. 5. An integral part of this procedure requires the knowledge of absorption cross-sections, in this case for BrO, σ(BrO). The reference cross-section used for this analysis was that obtained from the very extensive study of Wilmouth *et al.*[34] This cross-section is of considerably higher resolution than that adopted in this

study (where wavelength coverage compromises experimental resolution) and therefore had to be smoothed down to match experimental resolution. Some complications arose from this however, as the reference cross-section had 10 cm^{-1} resolution on a wavenumber scale compared to the experimental resolution in this work of 1.1 nm on a wavelength scale. As a result the equivalent wavelength scale was non-linear and the resulting resolution non-uniform. However, over the entire reference wavelength range of 385.698-285.934 nm, the resolution *change* was 0.067 nm. This resolution change was no greater than 6% of the experimental resolution of 1.1 nm (FWHM) and was therefore considered negligible. In order to be able to smooth the reference spectrum to the experimental resolution it was necessary to convert the non-linear wavelength scale to an even grid. The average dispersion of the wavelength grid was 0.0225 nm, so this was the chosen dispersion for the even grid. The spectrum on the uneven grid was interpolated and re-plotted on an even grid. A portion of the spectrum is shown in Figure 6. 3.

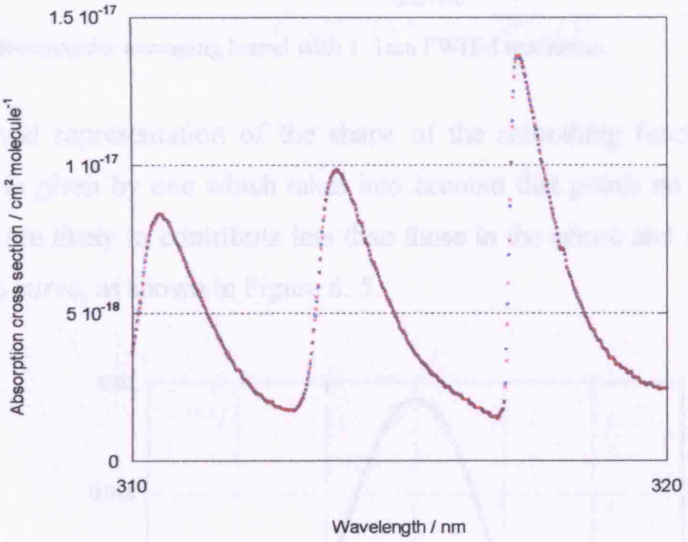

Figure 6. 3 310-320 nm portion of the reference BrO absorption cross-section on a non-linear grid (red) and a regular grid of 0.0225 nm dispersion (blue).

The reference spectrum, on an even wavelength grid, was now smoothed to the experimental resolution using a series of different sliding averaging kernels to examine which gave the best fit to the experimental spectrum. In each of these cases, an output (degraded) absorption cross-section was obtained using a normalised average of all the high resolution cross-sections at wavelengths across a width corresponding to the

spectral resolution. First, a rectangular averaging kernel was used. The width of the kernel was 49 points to give a resolution of 1.1 nm FWHM. A rectangular averaging kernel gives equal weighting to all points across the spectral resolution, as shown in Figure 6. 4.

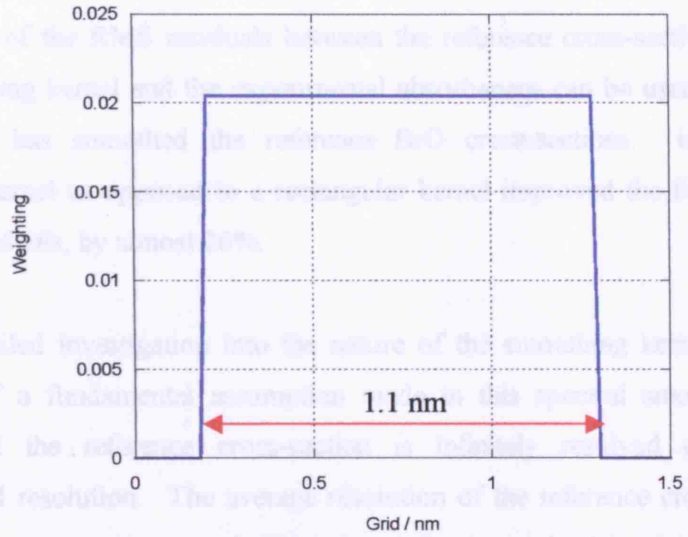

Figure 6. 4 Rectangular averaging kernel with 1. 1nm FWHM resolution.

An improved representation of the shape of the smoothing function to instrumental resolution is given by one which takes into account that points on the periphery of the resolution are likely to contribute less than those in the centre and is therefore given by a Gaussian curve, as shown in Figure 6. 5.

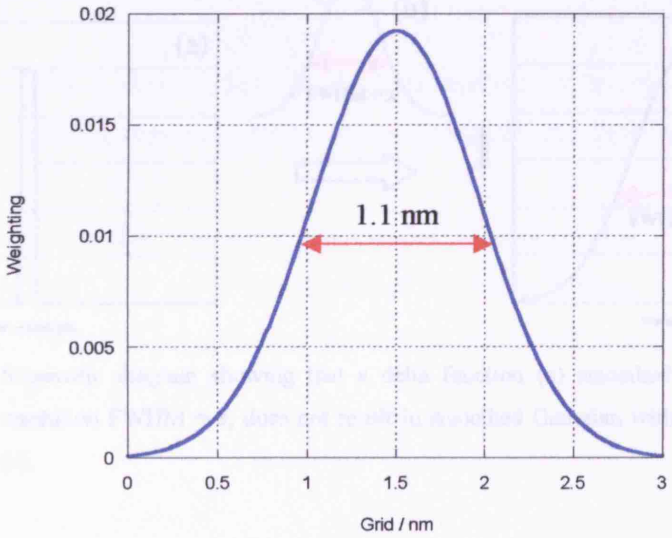

Figure 6. 5 Gaussian averaging kernel with 1.1 nm FWHM resolution.

As a result, the use of a Gaussian shaped averaging kernel with 1.1 nm resolution FWHM should give smoothed cross-sections more representative of the data. Taking the smallest points of the kernel to be approximately 1% of the total resulted in a 135 point kernel.

Comparison of the RMS residuals between the reference cross-sections generated for each smoothing kernel and the experimental absorbances can be used to see how well each kernel has smoothed the reference BrO cross-sections. Using a Gaussian smoothing kernel as opposed to a rectangular kernel improved the fitting, as shown in the fit to residuals, by almost 20%.

Further detailed investigation into the nature of the smoothing kernel highlighted the invalidity of a fundamental assumption made in this spectral smoothing technique, namely that the reference cross-section is infinitely resolved compared to the experimental resolution. The average resolution of the reference cross-section was in fact 0.1108 nm. Application of a Gaussian sliding averaging kernel with a resolution of 1.1 nm FWHM, termed the 'input FWHM', to a representative peak (either delta or Gaussian function) with resolution of 0.1108 nm resulted in a smoothed output peak of 1.1023 nm FWHM, now termed the 'output FWHM'. Consequently an averaging kernel with an input FWHM of 1.0976 nm was required to give a peak with an output FWHM of 1.1000 nm.

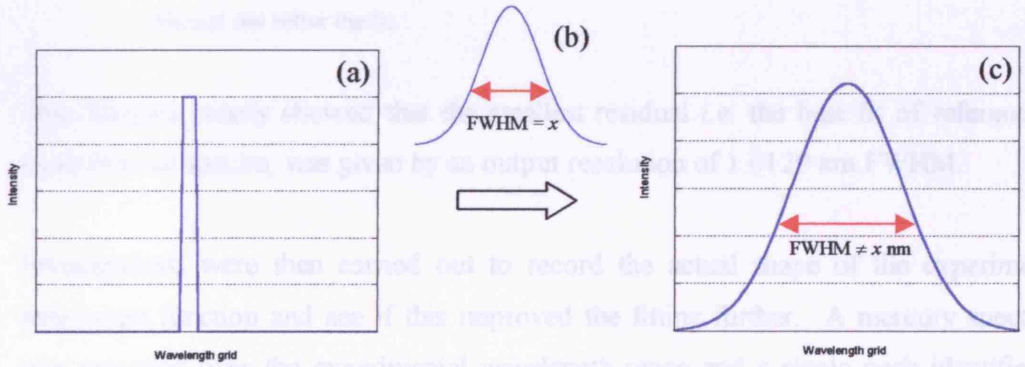

Figure 6. 6 Schematic diagram showing that a delta function (a) smoothed by Gaussian (b) with resolution FWHM = x, does not result in smoothed Gaussian with resolution FWHM = x (c).

This narrower averaging kernel was used as another improvement to the convolution of BrO cross-sections to the experimental resolution. During this procedure however, examination of the RMS residuals or 'goodness of fit' between the fitted, smoothed, reference cross-sections and experimental spectra indicated that the experimental resolution might indeed be less than 1.1 nm, as calculated from the reported spectrograph magnification and the entrance slit width (as well as previous studies in this laboratory). This is shown in Figure 6. 7 below, where the RMS residuals between fitted, smoothed, reference spectra and experimental spectra are plotted as a function of resolution of the averaged reference spectrum.

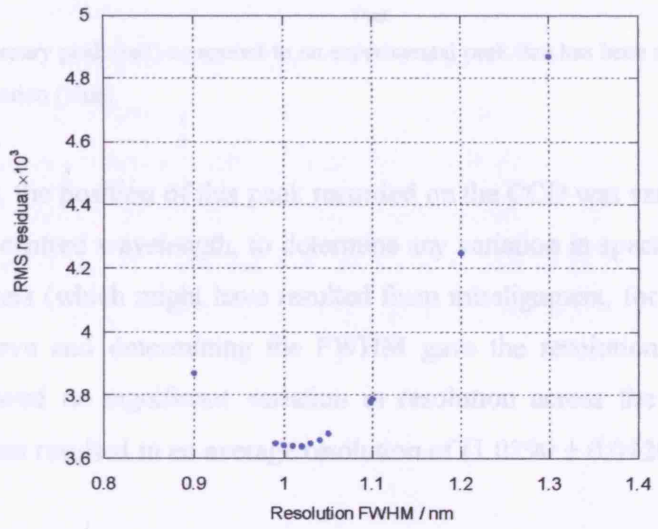

Figure 6. 7 RMS residual or 'goodness of fit' as a function of FWHM resolution. The smaller the RMS residual the better the fit.

This analysis clearly showed that the smallest residual *i.e.* the best fit of reference to experimental spectra, was given by an output resolution of 1.0129 nm FWHM.

Investigations were then carried out to record the actual shape of the experimental instrument function and see if this improved the fitting further. A mercury spectrum was recorded over the experimental wavelength range and a single peak identified at 334.148 nm, shown in Figure 6. 8.

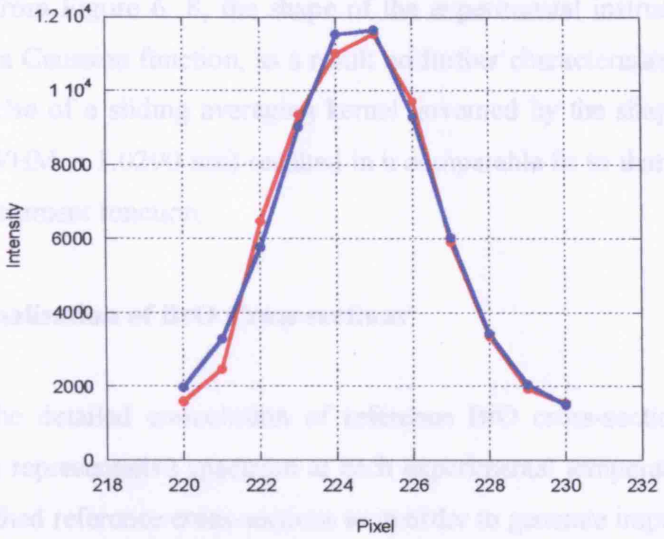

Figure 6. 8 Mercury peak (red) compared to an experimental peak that has been smoothed by a Gaussian function (blue).

Furthermore, the position of this peak recorded on the CCD was varied, by changing the value of the centred wavelength, to determine any variation in spectral resolution across the CCD pixels (which might have resulted from misalignment, for example). Fitting a Gaussian curve and determining the FWHM gave the resolution of the peak. This analysis showed no significant variation in resolution across the CCD, as shown in Figure 6. 9 but resulted in an average resolution of (1.0290 ± 0.0120) nm FWHM.

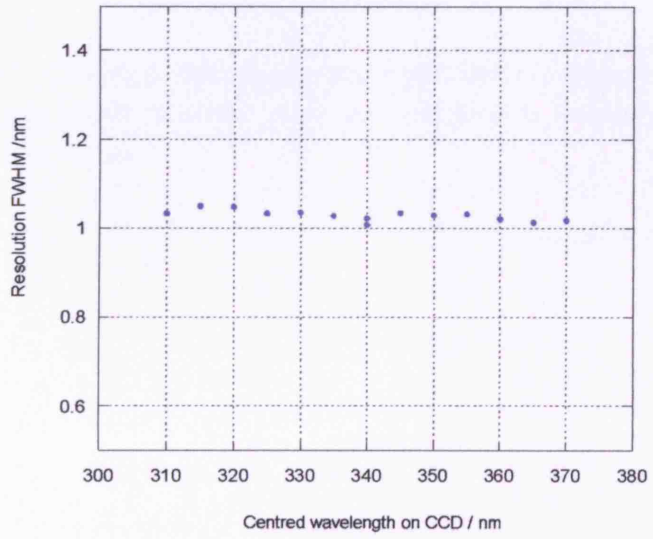

Figure 6. 9 FWHM resolution as a function of CCD pixel, which directly correlates to wavelength on the CCD.

As evident from Figure 6. 8, the shape of the experimental instrument function fitted very well to a Gaussian function, as a result no further characterisation of the shape was necessary. Use of a sliding averaging kernel governed by the shape of the instrument function (FWHM = 1.0290 nm) resulted in a comparable fit to that generated using the Gaussian instrument function.

6. 3. 3 Normalisation of BrO Cross-sections

Following the detailed convolution of reference BrO cross-sections to experimental resolution, a representative spectrum at each experimental temperature was normalised to the smoothed reference cross-sections to in order to generate improved reference BrO cross-sections. The effects of these improvements to the quality of the differential fitting of BrO reference to experimental cross-sections can be seen in Figure 6. 10 where the (offset) residual between fitted spectra is greatly reduced by improving the spectra convolution procedure. This improvement gives a change in returned concentrations of *ca.* 7% between the two cases shown in Figure 6. 10, and highlights the need for very careful convolution of reference spectra obtained from the literature.

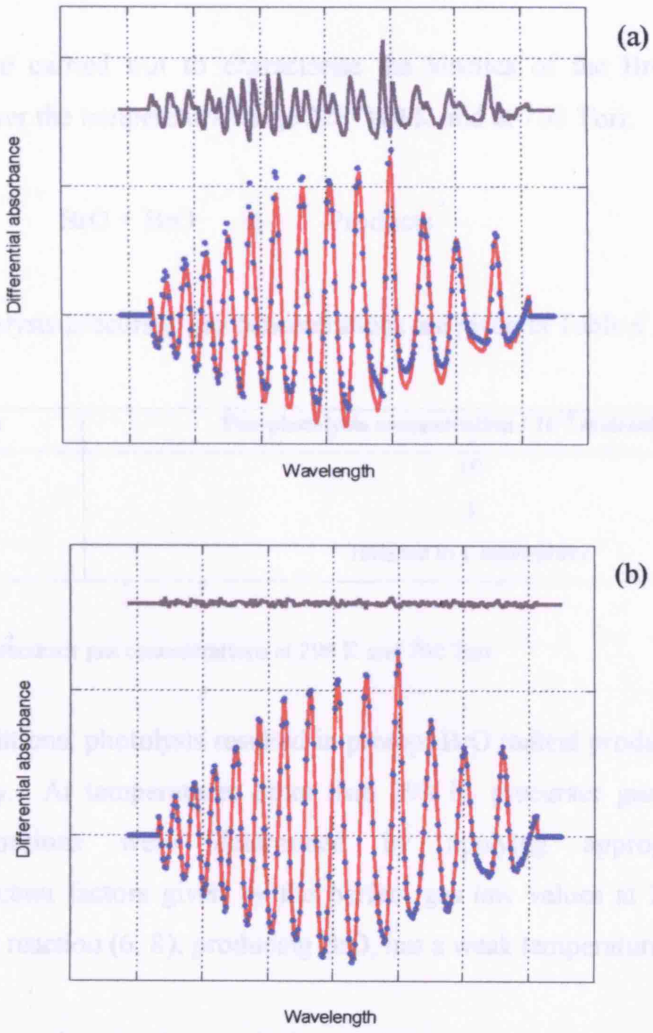

Figure 6. 10 (a) Experimental differential absorbance (red) fitted to a reference cross-section (blue). (b) Experimental differential absorbance (red) fitted to a normalised experimental cross-section (blue).

6. 3. 4 Kinetic Analysis

Experiments were carried out to characterise the kinetics of the BrO self-reaction, reaction (6. 6), over the temperature range 225-310 K and at 760 Torr.

(6. 6) $BrO + BrO \rightarrow$ Products

Typical pre-photolysis precursor gas concentrations are given in Table 6. 4 below.

Precursor gas	Pre-photolysis concentration / 10^{16} molecule cm^{-3}
N_2O	10
Br_2	3
N_2	Balance to 1 atmosphere

Table 6. 4 Typical precursor gas concentrations at 298 K and 760 Torr.

Under these conditions, photolysis resulted in prompt BrO radical production relative to subsequent decay. At temperatures other than 298 K, precursor gas flow rates and radical concentrations were determined by applying appropriate thermal expansion/contraction factors given by the perfect gas law values at 298 K. This is appropriate since reaction (6. 8), producing BrO, has a weak temperature dependence.[31]

In an identical procedure to that applied to ClO experimental data in Chapter 5, the application of Beer's law (described in Chapter 3) to post-photolysis data relative to pre-photolysis data resulted in 1000 time-resolved spectra, each of which were fitted to an appropriate differential cross-section, according to the Beer-Lambert law, resulting in BrO concentration as a function of time, $[BrO]_t$. The time dependent $[BrO]_t$ trace showed prompt BrO formation and decay, attributed to the BrO self-reaction. Figure 6. 11 shows an example of an experimental trace taken at 298 K, 760 Torr.

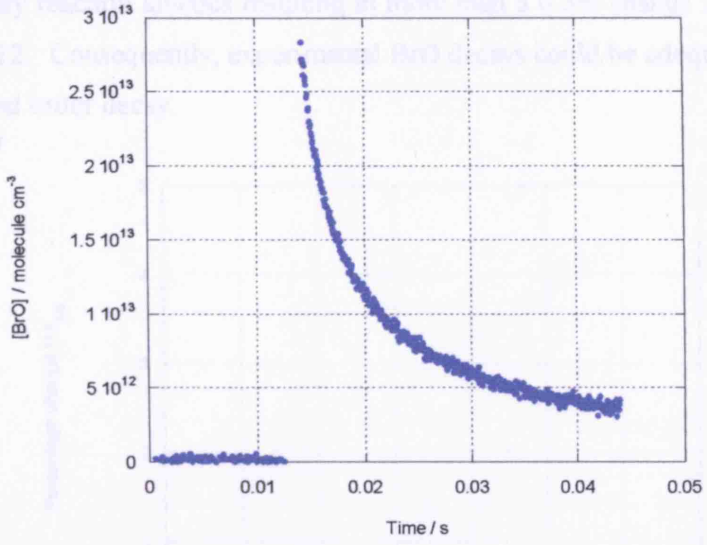

Figure 6. 11 Typical BrO concentration as a function of time trace recorded at 298 K and 760 Torr.

The extensive chemical reaction scheme shown in Table 6. 5, was modelled in the numerical integration and fitting program FACSIMILE[35] and used to conduct a sensitivity analysis at 298 K, 760 Torr.

Reaction number	Reaction	k / cm^3 molecule^{-1} s^{-1}
1	$Br_2 + O \rightarrow BrO + Br$	1.44×10^{-11}
2	$BrO + O \rightarrow O_2 + Br$	4.12×10^{-11}
3	$Br + BrO \rightarrow Br_2O$	1.89×10^{-12}
4	$Br + Br \rightarrow Br_2$	2.25×10^{-13}
5	$Br + Br_2O \rightarrow BrO + Br_2$	4×10^{-11}
6	$Br_2O_2 + Br \rightarrow Br + Br_2 + O_2$	4×10^{-10}
7	$Br_2O_2 \rightarrow 2BrO$	64.2[a]
8	$BrO + BrO \rightarrow$ Products	Optimised

[a] Units of s^{-1}

Table 6. 5 Reactions and rate coefficients included in sensitivity analysis for $Br_2/N_2O/N_2$ gas system.

For this sensitivity analysis, a simulated temporal trace was fitted to a representative experimental trace, allowing $k_{6.6}$ to optimise. Then in turn, each of the rate coefficients for the reactions in the model were doubled and halved in the model, and the percentage change in $k_{6.6}$ from refitting the model was noted. The results of this analysis showed that the observed BrO decay was only sensitive to the self-reaction, with no perturbation

in secondary reaction kinetics resulting in more than a 0.5% change in $k_{6.6}$, as shown in Figure 6. 12. Consequently, experimental BrO decays could be adequately described by pure second order decay.

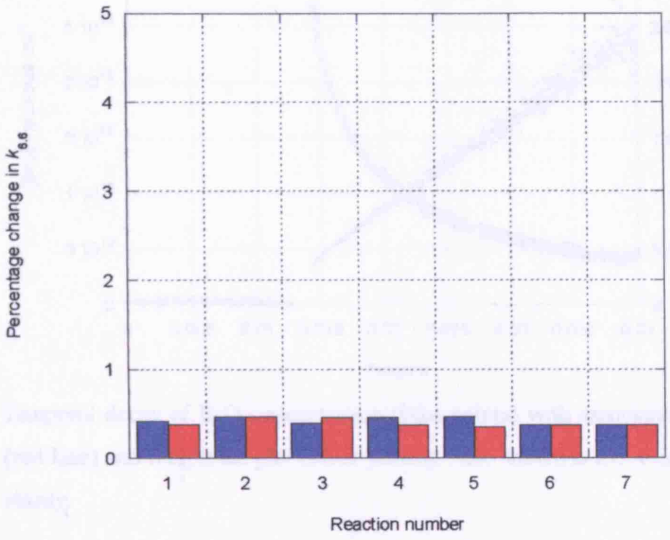

Figure 6. 12 Sensitivity analysis for $Br_2/N_2O/N_2$ gas system. Effect of doubling (blue) and halving (red) the given secondary rate coefficient. Reaction numbers refer to those in Table 6. 5.

BrO concentration *versus* time traces were well described by a second order kinetic scheme according to:

(E6. 1) $$-\frac{d[\mathrm{BrO}]}{dt} = 2k_{6.6}[\mathrm{BrO}]^2$$

Integration of this differential equation generates a linear solution:

(E6. 2) $$\frac{1}{[\mathrm{BrO}]_t} = \frac{1}{[\mathrm{BrO}]_0} + 2k_{6.6}t$$

Consequently, a plot of $1/[\mathrm{BrO}]_t$ *versus* t results in a linear plot with gradient $2k_{6.6}$. A typical BrO radical decay, along with second order model fit and associated reciprocal plot is shown in Figure 6. 13.

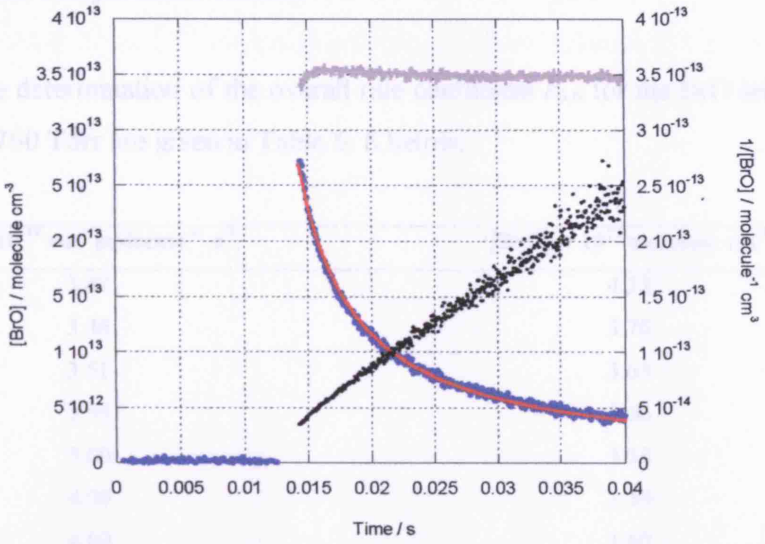

Figure 6. 13 Temporal decay of BrO concentration (blue points) with associated second order model fit (red line) and reciprocal plot (black points). Also shown is the residual (grey line) offset for clarity.

6. 3. 5 Ambient Temperature Results

Results for the determination of the overall rate coefficient $k_{6.6}$ for the BrO self-reaction at 298 K and 760 Torr are given in Table 6. 6 below.

$k_{6.6}$ / 10^{-12} cm^3 molecule^{-1} s^{-1}	$[BrO]_0$ / 10^{13} molecule cm^{-3}
3.47	4.25
3.46	3.70
3.51	3.63
3.59	3.56
3.60	3.38
4.09	1.59
4.03	1.60
3.99	1.59
4.09	1.61
4.05	1.59
3.45	5.37
3.52	4.86
3.54	4.61
3.62	4.23
3.86	2.14
3.89	2.13
3.82	2.40
3.85	2.29
3.79	1.94
3.83	1.87
3.97	1.71
3.97	1.67

Table 6. 6 Experimentally determined $k_{6.6}$ and $[BrO]_0$ at 298 K and 760 Torr.

Figure 6. 13 shows that the $Br_2/N_2O/N_2$ gas system is well described by the second order model and averaging the 22 results from Table 6. 5 gives $k_{6.6} = (3.77 \pm 0.45) \times 10^{-12}$ cm^3 molecule^{-1} s^{-1} at 298 K and 760 Torr. Errors are 2σ, statistical only.

Experiments were carried out as a function of Br_2 concentration and as a function of N_2O concentration. The rate coefficient for BrO decay was determined as described

above. $k_{6.6}$ showed no significant variation with Br_2 concentration over the range investigated (1.64-8.22) × 10^{16} molecule cm^{-3}, as shown in Figure 6. 14 below.

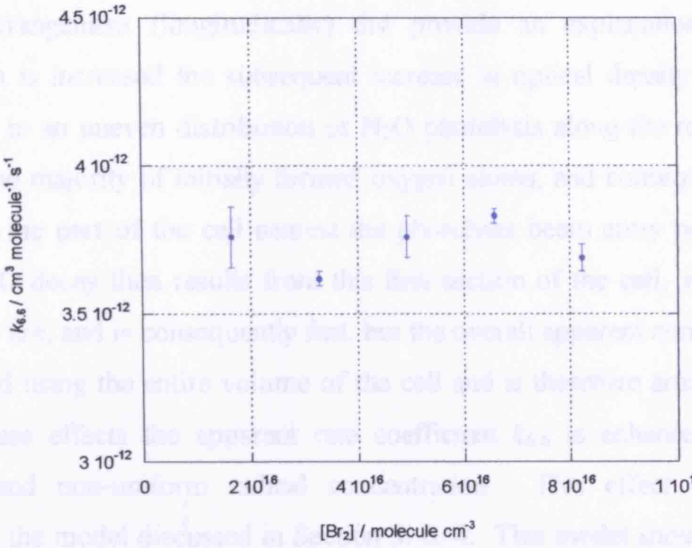

Figure 6. 14 Experimentally determined $k_{6.6}$ as a function of precursor Br_2 concentration.

This behaviour can be rationalised since Br_2 plays no further part in the gas phase chemistry after radical generation. Thus, provided Br_2 is in excess all oxygen atoms will be scavenged to generate BrO in reaction (6. 8). The rate coefficient $k_{6.6}$ did however show an enhancement with increasing N_2O concentration over the range (2.50-12.5) × 10^{17} molecule cm^{-3}, as shown in Figure 6. 15.

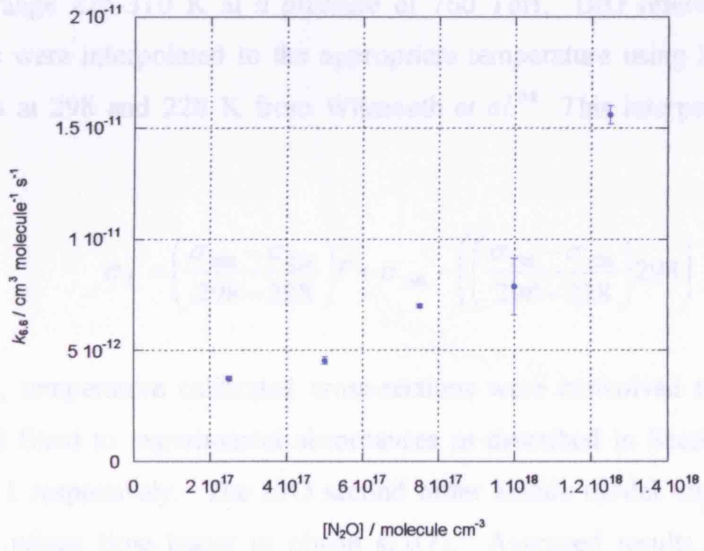

Figure 6. 15 Experimentally determined $k_{6.6}$ as a function of precursor N_2O concentration.

Whilst the increase in $k_{6.6}$ with increasing N_2O concentration, and therefore oxygen atom concentration was inexplicable on the basis of the gas phase chemistry in Table 6. 4, consideration of the optical density of the cell, coupled with the nature of the photolysis arrangement (longitudinally) did provide an explanation. As the N_2O concentration is increased the subsequent increase in optical density of the precursor gases results in an uneven distribution of N_2O photolysis along the reaction cell. This resulted in the majority of initially formed oxygen atoms, and consequently BrO, being generated in the part of the cell nearest the photolysis beam entry point. The rate of observed BrO decay then results from this first section of the cell, where most of the BrO radicals are, and is consequently fast, but the overall apparent concentration of BrO is determined using the entire volume of the cell and is therefore artificially low. As a result of these effects the apparent rate coefficient $k_{6.6}$ is enhanced because of an unrealistic and non-uniform radical concentration. This effect could indeed be simulated in the model discussed in Section 3. 6. 4. This model showed that keeping a cell optical depth of < 2.36 at the laser wavelength, requiring $[N_2O] << 2.5 \times 10^{17}$ molecule cm^{-3}, resulted in a < 10% distortion of the radical decay rate and therefore all kinetics data reported here were within this limit.

6. 3. 6 Temperature Dependence

Experiments to study the kinetics of the BrO self-reaction were conducted over the temperature range 225-310 K at a pressure of 760 Torr. BrO reference absorption cross-sections were interpolated to the appropriate temperature using literature cross-sections taken at 298 and 228 K from Wilmouth *et al.*[34] This interpolation took the form:

(E6. 3)
$$\sigma_T = \left(\frac{\sigma_{298} - \sigma_{228}}{298 - 228}\right)T + \sigma_{298} - \left(\left(\frac{\sigma_{298} - \sigma_{228}}{298 - 228}\right)298\right)$$

Appropriately, temperature calibrated cross-sections were convolved to experimental resolution and fitted to experimental absorbances as described in Section 6. 3. 3 and Section 3. 5. 1 respectively. The BrO second order kinetic model was then fitted to concentration *versus* time traces to obtain $k_{6.6}(T)$. Averaged results at each of the experimental temperatures are given in Table 6. 7.

T / K	$k_{6.6}$ / 10^{-12} cm^3 molecule^{-1} s^{-1}	Number of determinations (n)
225.0	6.17 ± 0.06	12
228.0	5.87 ± 0.03	6
235.0	5.09 ± 0.06	12
240.0	5.00 ± 0.06	8
245.0	4.79 ± 0.03	12
250.0	4.62 ± 0.05	12
260.0	4.431 ± 0.009	6
270.0	4.153 ± 0.009	6
280.0	4.13 ± 0.07	12
285.0	4.03 ± 0.07	12
290.0	4.05 ± 0.07	12
298.0	3.77 ± 0.10	22
305.0	3.83 ± 0.07	12
310.0	3.66 ± 0.04	12

Table 6. 7 Experimentally determined $k_{6.6}$ as a function of temperature at 760 Torr. Errors are 2σ, statistical only, and have been divided by $n^{1/2}$ to account for non-equivalence of sample sizes.

An example of typical BrO temporal traces at different temperatures is given in Figure 6. 16 below.

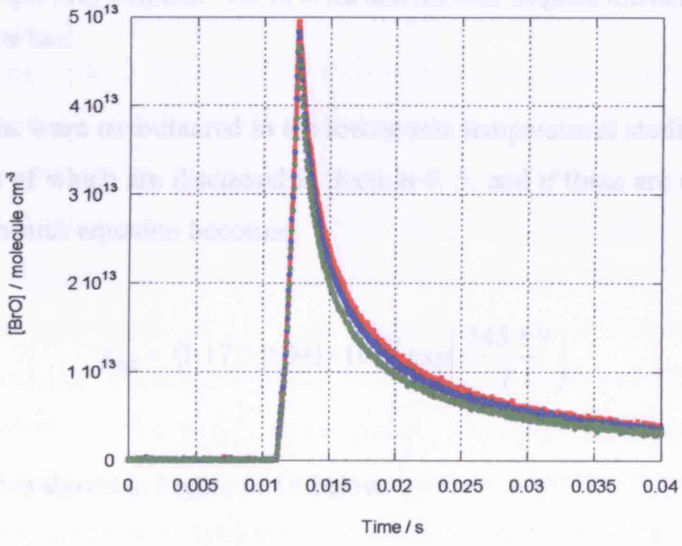

Figure 6. 16 Temporal decay of BrO concentration recorded at three different experimental temperatures, 270 K (red points), 250 K (blue points), 235 K (green points).

The weak temperature dependence of the BrO self-reaction is evident in the similarities of these traces and the temperature dependence data are described by linear Arrhenius behaviour according to:

(E6. 4) $$k_{6.6} = (8.19 \pm 0.20) \times 10^{-13} \exp\left(\frac{440 \pm 6}{T}\right)$$

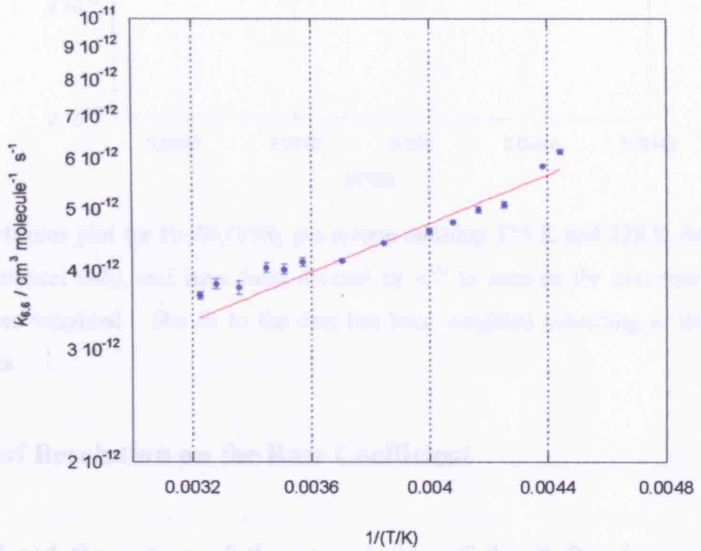

Figure 6. 17 Temperature dependent data for $Br_2/N_2O/Br_2$ gas system plotted in Arrhenius form. Errors are 2σ, statistical only, and have been divided by $n^{1/2}$ to account for non-equivalence of sample sizes weighted. The fit to the data has been weighted according to the size of the error bars.

Some problems were encountered in the lowest two temperatures studied (225 and 228 K), the details of which are discussed in Section 6. 5, and if these are omitted from the fitting the Arrhenius equation becomes:

(E6. 5) $$k_{6.6} = (1.17 \pm 0.04) \times 10^{-12} \exp\left(\frac{345 \pm 9}{T}\right)$$

a plot of which is shown in Figure 6. 18 below.

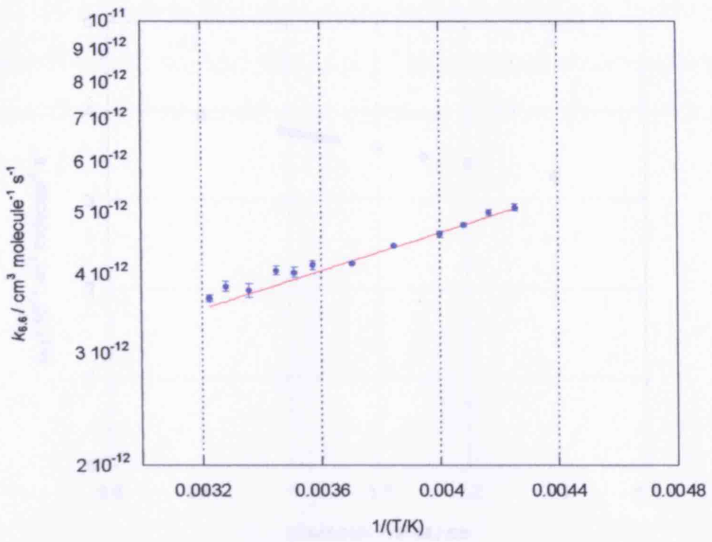

Figure 6. 18 Arrhenius plot for $Br_2/N_2O/Br_2$ gas system omitting 225 K and 228 K data. Errors are 2σ, statistical only, and have been divided by $n^{1/2}$ to account for non-equivalence of sample sizes weighted. The fit to the data has been weighted according to the size of the error bars.

6. 3. 7 Effect of Resolution on the Rate Coefficient

Having considered the nature of the convolution of the BrO reference cross-sections from the initially high resolution of Wilmouth *et al.*[34] to the lower resolution adopted in this study, further checks on the kinetic analysis of the BrO self-reaction traces were carried out to examine the sensitivity of the returned self-reaction rate coefficient to the instrumental resolution. Figure 6. 19 shows the results from such an analysis of a representative trace at 298 K. Clearly, a degree of anticorrelation between the returned rate constant and the width of the smoothing function is apparent. This is explicable, as the width of the smoothing kernel effectively defines the magnitude of the analysing absorption cross-section of the BrO radicals, which *via* the Beer-Lambert law has a linear effect on concentrations. It is also interesting to note that the nature of the smoothing kernel (*e.g.* rectangular *versus* Gaussian) had a minimal effect on the value of the rate constant returned at a given resolution. As shown above however, in Figure 6. 10, optimisation of this function did allow the clearest possible subtraction of the BrO contribution to absorbance, which in turn enabled examination of the time dependence of underlying absorption, observed in some cases, discussed in the following section.

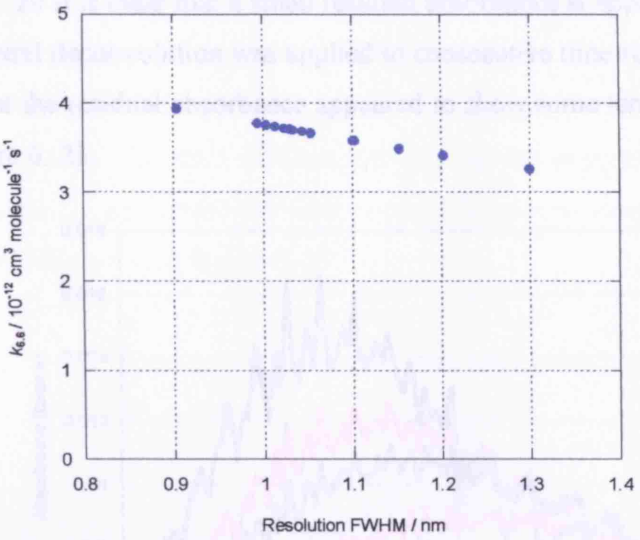

Figure 6. 19 Experimentally determined $k_{6.6}$ as a function of instrument resolution FWHM.

6. 3. 8 Identification of Multiple Absorbers

An advantage of the broad band spectra monitoring used in this work, aside from the quantification of the free radical concentrations using a wide spectral window, is the ability to monitor multiple potential absorbing species. Figure 6. 20 shows a typical time averaged experimental spectrum, along with the reference spectrum of BrO and the residual obtained from subtracting the BrO contribution to absorbance.

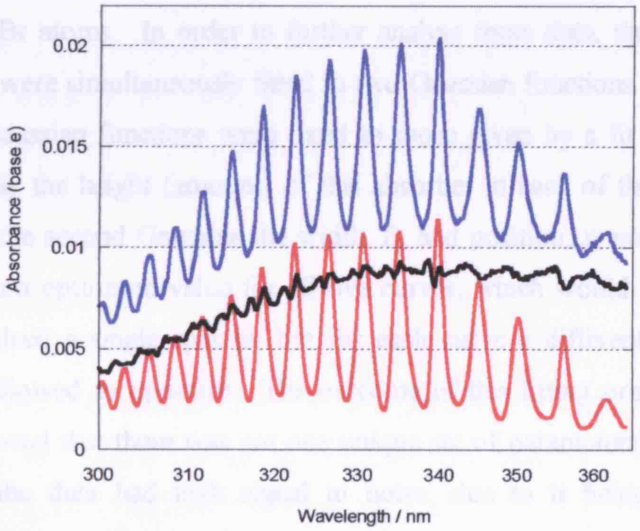

Figure 6. 20 Experimentally recorded absorbance spectrum (blue) compared to a BrO reference spectrum (red). If the reference spectrum is subtracted from the experimental spectrum a residual absorbance (black) remains.

From figure 6. 20 it is clear that a small residual absorbance is apparent. Furthermore, when this spectral deconvolution was applied to consecutive time-resolved spectra from one experiment the residual absorbance appeared to show some temporal behaviour, as shown in Figure 6. 21.

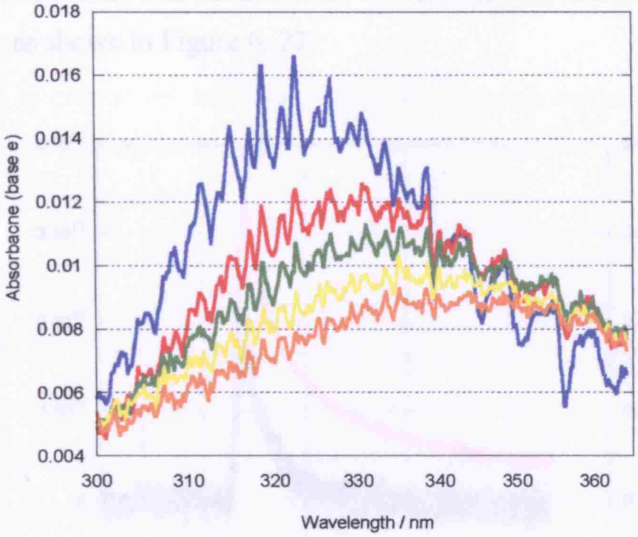

Figure 6. 21 Residuals from time averaged spectra recorded at (1-3.5) × 10^{-3} s (blue), (3.5-6) × 10^{-3} s (red), (6-8.5) × 10^{-3} s (green), (8.5-11) × 10^{-3} s (yellow) and (11-13.5) × 10^{-3} s (orange).

The apparent shift in the maximum wavelength of this absorbance is consistent with the presence of multiple absorbers. Absorbance at $\lambda > 340$ nm is likely to be due to Br_2 removed in the initial laser photolysis and regenerated in reaction (6. 1b), along with combination of Br atoms. In order to further analyse these data, the five consecutive residual spectra were simultaneously fitted to two Gaussian functions. The parameters of one of the Gaussian functions were fixed to those given by a fit to the Br_2 cross-section[36] and only the height (amount) of this absorber in each of the five curves was optimised. For the second Gaussian the width, B, and position, x, parameters were set to be one common optimised value for all five curves, which would be the case if this transient was indeed a single species, but for each curve a different height (amount) parameter was allowed to optimise. The outcome of this fitting proved inconclusive. The analysis showed that there was not one unique set of parameters that could fit the residuals. As the data had high signal to noise, due to it being a residual, this unconvincing fitting could not rule out the transient decay being due to absorbing species.

On further examination of the residual spectrum obtained from subtraction of the BrO differential spectrum from the experimental absorbance, the spectrum appeared to have some structure at high wavelengths (λ = 340-360 nm, Figure 6. 21). Furthermore, when this structured residual was itself differentially fitted to the experimental absorbance as a function of time the temporal behaviour of the residual was seen to show a plausible kinetic signature, as shown in Figure 6. 22.

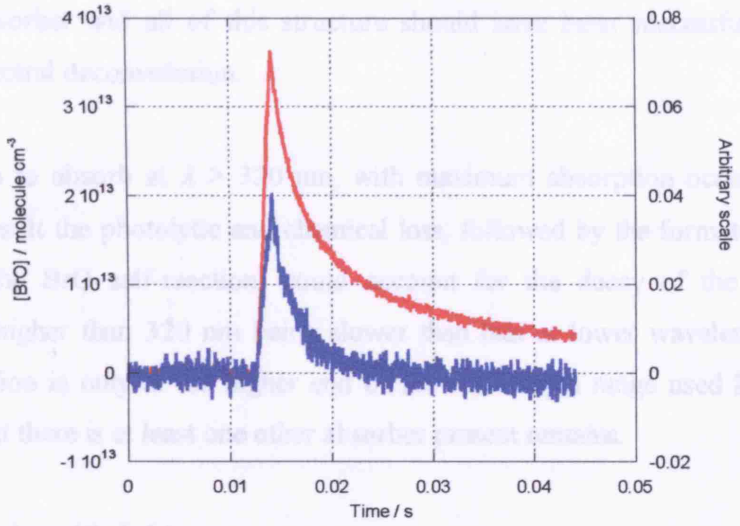

Figure 6. 22 Typical BrO radical concentration as a function of time (red) compared to temporal behaviour of residual (blue).

The existence of this kinetic signature for the residual is consistent with it being a chemical species. Furthermore, Figure 6. 22 shows that this kinetic signature was different to that observed for BrO, suggesting that it is due to a different transient molecule to BrO. All possible candidates for the 'unknown' absorber were therefore investigated, as discussed below.

6. 3. 9 Identification of Unknown Absorber

To identify the unknown transient absorber it is necessary to consider all the possible species that can be formed in the $N_2O/Br_2/N_2$ gas mixture. Simplistically, the permutations of species resulting from the BrO self-reaction can take the form of diatomics, triatomics or 4 atom molecules, each of which will be considered in turn below.

6. 3. 9. 1 Species with 2 Atoms

O_2 is a known product of the BrO self-reaction[31] but O_2 is categorically known not to absorb in this spectral region. Photodissociation of molecular oxygen occurs at much lower wavelengths ($\lambda < 200$ nm) than the experimental region.[31]

BrO absorption is present in this region but, as discussed extensively above, it is a structured absorber and all of this structure should have been successfully removed during the spectral deconvolution.

Br_2 is known to absorb at $\lambda > 320$ nm, with maximum absorption occurring at 410 nm.[36] As a result the photolytic and chemical loss, followed by the formation of Br_2, a product of the BrO self-reaction, could account for the decay of the transient at wavelengths higher than 320 nm being slower than that at lower wavelengths. Since this contribution is only at the higher end of the wavelength range used however, the possibility that there is at least one other absorber present remains.

6. 3. 9. 2 Species with 3 Atoms

Experimental evidence suggests that **BrOO** is unlikely to absorb in this experimental wavelength region. Mauldin *et al.*[21] photolysed Br_2 in excess O_2 and saw no evidence for the BrOO species. Similarly, Harwood *et al.*[26] looked for BrOO at 235 K over the wavelength region 270-390 nm but again no absorption was observed. By analogy with ClOO, BrOO might be expected to have a strong absorption in this wavelength region. However, as for ClOO, *ab initio* studies suggest that if formed BrOO would be very unstable as the energy barrier to products Br and O_2, is very small (5.0-7.1 kJ mol^{-1}).[37]

OBrO is known to absorb at much higher wavelengths ($\lambda > 500$ nm) than those of this experiment, so is a very unlikely candidate for the unknown transient. Furthermore, OBrO has been shown not to be a product of the BrO self-reaction.[23]

Br_2O is a known absorber in this experimental region, furthermore the formation of Br_2O *via* combination of Br and BrO, reaction (6. 12), has been proposed.[20]

(6. 12) $Br + BrO + M \rightarrow Br_2O + M$ $k_{6.12} = (2\text{-}4) \times 10^{-12}$ cm^3 molecule^{-1} s^{-1}

(Reference 23)

The Br_2O spectrum also has some structure at high wavelengths, which on first observation appear qualitatively similar to those observed experimentally. However, since the concentration of Br atoms in the system is high the secondary reaction (6. 15) is likely to convert any Br_2O formed back to BrO resulting in no net effect on the BrO self-reaction kinetics.

(6. 15) $Br + Br_2O \rightarrow Br_2 + BrO$ $k_{6.15} = 2 \times 10^{-10}$ cm^3 molecule^{-1} s^{-1}

(Reference 38)

Consequently, on this experimental timescale the observation of Br_2O is considered unlikely.[38] Furthermore, detailed comparison of the spectral features of the observed residual and the absorption cross-section of Br_2O appears to rule out this possibility, as shown in Figure 6. 23.

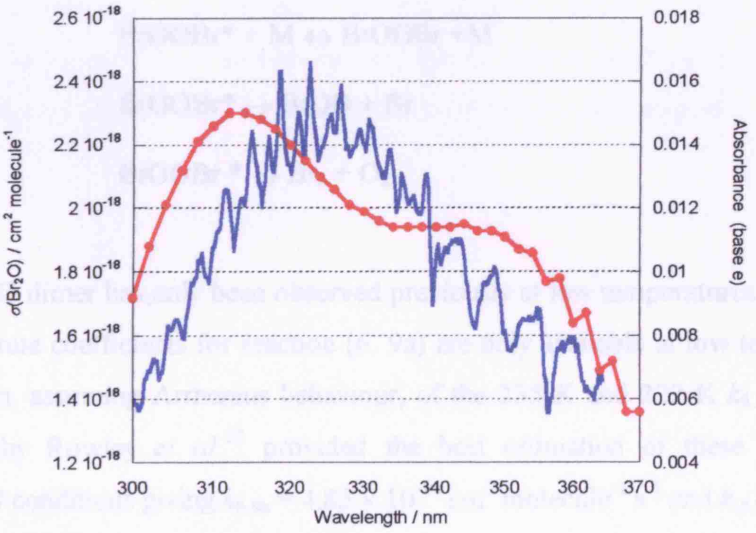

Figure 6. 23 Experimentally observed residual absorbance (blue) compared to the absorption cross-section of Br_2O (red) recreated from Rattigan *et al.*[39]

Numerical modelling of the Br_2O chemistry shows that, under typical experimental conditions, using the literature values of $k_{6.12} = 3 \times 10^{-12}$ cm^3 molecule^{-1} s^{-1} and $k_{6.15} = 2 \times 10^{-10}$ cm^3 molecule^{-1} s^{-1} at 298 K, cannot recreate the observed half life of the decay of the unknown. Furthermore, taking approximate experimental absorbance and absorption cross-section values for Br_2O at an example wavelength of 320 nm it is possible to approximate the concentration of the unknown species if it were indeed Br_2O. With an approximate absorbance value of 0.013 and taking $\sigma(Br_2O)_{320nm} = 2.2 \times 10^{-18}$ cm^2 molecule^{-1} from Orlando & Burkholder,[40] the concentration of Br_2O to account for the observed residual absorbance would have to be of the order 6×10^{13} molecule cm^{-3}, which is unfeasibly high compared to that predicted by modelling.

6. 3. 9. 3 Species with 4 Atoms

Formation of a **Br_2O_2** dimer has been discussed by Mauldin *et al.*[21] and Rowley *et al.*[23] who both observed absorbances underlying the BrO structure in Br_2/O_3 systems. These residuals were, however, only observed at low temperatures, $T < 235$ K. For these systems the proposed mechanism for dimer formation was:

(6. 6c) $\quad BrO + BrO + M \leftrightarrow BrOOBr^* + M$

(6. 9a) $\quad BrOOBr^* + M \leftrightarrow BrOOBr + M$

(6. 9b) $\quad BrOOBr^* \rightarrow BrOO + Br$

(6. 9c) $\quad BrOOBr^* \rightarrow Br_2 + O_2$

Since the BrO dimer has only been observed previously at low temperatures the forward and reverse rate coefficients for reaction (6. 9a) are only available at low temperatures. Extrapolation, assuming Arrhenius behaviour, of the 235 K and 222 K $k_{6.9a}$ values, as determined by Rowley *et al.*[23] provided the best estimation of these rates under experimental conditions giving $k_{6.9a} = 4.85 \times 10^{-14}$ cm^3 molecule^{-1} s^{-1} and $k_{-6.9a} = 3460$ s^{-1} at 760 Torr. Modelling this system did show the BrO dimer to have prompt formation and rapid decay, as observed for the unknown. The half-life of this decay was also comparable to that experimentally observed. The peak concentration of dimer predicted

by the model was however very low, of the order 5×10^9 molecule cm^{-3} which, taking into account the strength of the predicted absorption of the dimer *ca.* 1.5×10^{-17} cm^2 $molecule^{-1}$ would result in an absorbance of 7.5×10^{-6}, well below experimental detection limits. Furthermore, second order modelling of the BrO decay generated when these dimer kinetics were included in the model showed distortion, unlike that observed experimentally. Rowley *et al.* also predicted that the BrO dimer may react with Br atoms, in similar fashion to the chlorine dimer and Cl atoms:

(6. 16) $\quad Br + BrOOBr \rightarrow Br + Br_2 + O_2 \qquad k_{6.16} = 4 \times 10^{-10}$ cm^3 $molecule^{-1}$ s^{-1}

If however, reaction (6. 16) was included in the model no significant effect on the dimer formation or BrO decay kinetics was observed.

The observed structure in the residual underlying absorbance at higher wavelengths prompted the speculation that the absorbing species could be an excited form of BrO, **BrO ($v''> 0$)**. BrO has known hot bands in this high wavelength region with the vibrational transitions (4, 1) and (1, 1) (the only two bands not masked by $v''=0$ bands) at approximate wavelengths 364 nm and 385 nm respectively.[31] Although these bands are higher in wavelength than the structure observed experimentally, it does not rule out the possibility that higher energy hot bands may be present in the experimental wavelength region. As a result, the formation of vibrationally excited BrO radicals could result in the observed absorption and kinetic signature of the transient. BrO ($v''>0$) could be formed due to the exothermicity of the $O + Br_2$ reaction.

(6. 8) $\quad O + Br_2 \rightarrow BrO + Br \qquad \Delta_r H = -42.02$ kJ mol^{-1}

(Reference 31)

Production of excited BrO would result in the following channels being responsible for the observed BrO decay:

(6. 16) $BrO(v'>0) + M \rightarrow BrO(v'=0) + M$

(6. 17a) $BrO(v'=0) + BrO(v'=0) \rightarrow Products$

(6. 17b) $BrO(v'>0) + BrO(v'>0) \rightarrow Products$

(6. 17c) $BrO(v'>0) + BrO(v'=0) \rightarrow Products$

This chemical scheme was modelled using notional values of the rates of all of the BrO reactions to be $k_{6.6} = 3.25 \times 10^{-12}$ cm^3 molecule^{-1} s^{-1} taken from the literature.[31] For an initial model formation of BrO ($v'>0$) was taken to be 10%. In order to replicate the observed half life the vibrational relaxation of BrO ($v'>0$) would need to have a rate coefficient of 500 cm^3 molecule^{-1} s^{-1}. Using this model, although the modelled BrO decay did deviate from pure second order kinetics the observed departure was different to that seen experimentally. This value for the vibrational relaxtion is inconsistent with that observed experimentally by Ninomiya *et al.*[41] who showed BrO collisional relaxation with N_2 to occur at 1.5×10^{-13} cm^3 molecule^{-1} s^{-1} at 298 K. Under experimental conditions used in this work this corresponds to a first order rate of 3.75×10^6 s^{-1} and lifetime of 2.7×10^{-7} s, which would result in a much more rapid decay than observed for the unknown. Indeed, under no circumstances could the model recreate the observed transient decay in keeping with the BrO decay. Furthermore, Ninomiya *et al.* formed BrO *via* the Br + O_3 reaction, which is a much more exothermic reaction than Br_2 + O, ($\Delta_r H$ = -127.47 kJ mol^{-1}). Thus if anything, the possibility of forming excited BrO is much more likely in the experiments of Ninomiya *et al.* than in this work.

6. 3. 9. 4 Summary of Spectral Deconvolution

On the basis of extensive investigations into the nature of the underlying absorption the most likely, but inconclusive, candidate for the 'unknown' species involved is Br_2O. Spectral differences between the observed residual absorbance and the literature

spectrum of Br_2O are however apparent and are potentially due to poor characterisation and subtraction of the BrO spectral continuum. Indeed, in this system BrO is generated and exhibits underlying absorbances, which presumably are also present in other systems, such as that used to characterise the BrO reference spectrum.

Interestingly, a recent study of the absorption cross-section of OBrO by Fleischmann *et al.*,[42] using a $Br_2/O_2/O_3$ system also recorded an unknown absorption in the wavelength region 330-450 nm, with spectral structure to higher wavelengths. Although the peak of the Fleischmann *et al.* absorption is higher than observed in this experiment, 355 nm compared to 325 nm, the shape of the absorption is not dissimilar, as shown in Figure 6. 24. Fleischmann *et al.* could not rationalise the absorption with known absorbers and tentatively assign the absorption to Br_2O.

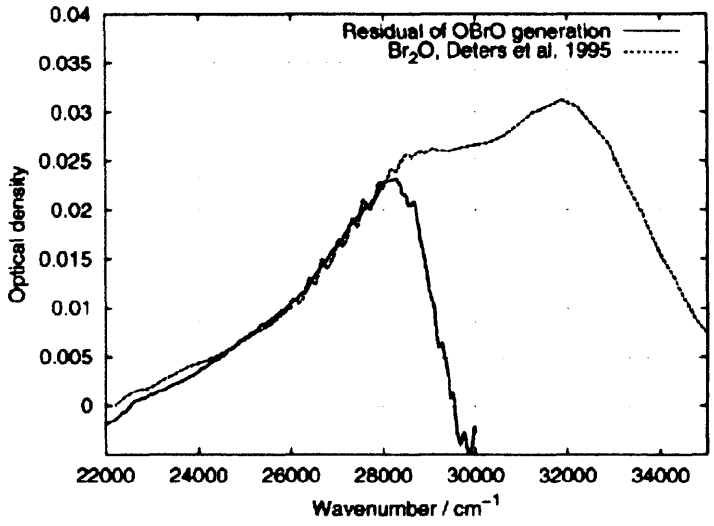

Figure 6. 24 Comparison of reference Br_2O absorption cross-section (dotted line) and experimentally recorded residual (solid line) from a $Br_2/O_2/O_3$ gas system.[42]

Certainly, on the basis of known rate constants, transient Br_2O formation and subsequent reaction with Br atoms does not affect the overall BrO self-reaction kinetics, but rather enhances the rate of Br atom recombination to Br_2. This kind of effect has indeed been observed by Laszlo *et al.*,[24] who saw unusually fast Br_2 build up in a study of the BrO self-reaction, inconsistent with third order bromine atom recombination.

6. 4 Experiments at Low Br_2 Concentrations

Analysis of a data set taken towards the end of an extensive experimental run revealed some curious results. A serious of successive experimental traces as a function of time under apparently identical conditions at 298 K, are given in Figure 6. 25 below.

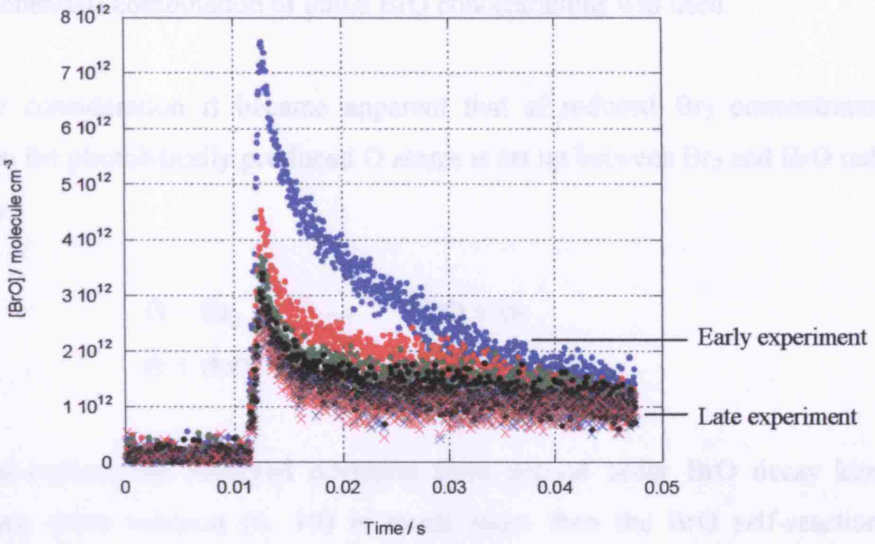

Figure 6. 25 BrO radical concentrations as a function of time recorded under conditions of low Br_2 concentration. Successive traces were recorded at later times during the course of an experiment. Blue points = earliest experiment and red crosses = latest experiment.

From these traces it was clear that not only had the initial BrO radical concentration dropped considerably, from *ca.* 3.5×10^{13} to (3-7) $\times 10^{12}$ molecule cm^{-3}, but there was obvious deviation from pure second order kinetics in the kinetic signature. As a result the second order model of BrO decay could no longer fit the traces with low initial BrO concentrations.

On closer examination of the experimental conditions it became apparent that in this sequence of experiments the liquid Br_2 had run low in the bubbler and as a result the N_2 carrier flow did not bubble through the liquid Br_2. Consequently, the degree of saturation and hence the Br_2 concentration reaching the cell was potentially reduced. Intuitively, this Br_2 concentration was also likely to have decreased with time as the meniscus of the liquid Br_2 systematically ran down. Since each experimental trace was

an average of 30 co-added experiments this decrease in Br_2 concentration could potentially have been present within, as well as between, each experimental run. Using the second order model of BrO decay it was not possible to reproduce the observed behaviour with a linear combination of traces with successively lower BrO concentrations (potentially demonstrative of decreasing Br_2). Moreover, this behaviour could not be replicated using successive model traces with decreasing BrO when a non-linear (exponential) combination of initial BrO concentrations was used.

On further consideration it became apparent that at reduced Br_2 concentrations a competition for photolytically produced O atoms is set up between Br_2 and BrO radicals themselves:

(6. 18) $O + Br_2 \rightarrow BrO + Br$

(6. 19) $O + BrO \rightarrow Br + O_2$

This could explain the observed deviation from second order BrO decay kinetics. Furthermore, since reaction (6. 19) is much faster than the BrO self-reaction the observed increase in decay rate with decreasing radical concentration can be rationalised. Upon reduction of the Br_2 concentration in the model containing the O + Br_2 reaction, using a linear combination of modelled traces with varying (decreasing) bromine concentrations, the experimental traces could indeed be replicated qualitatively, as shown in Figure 6. 26 below.

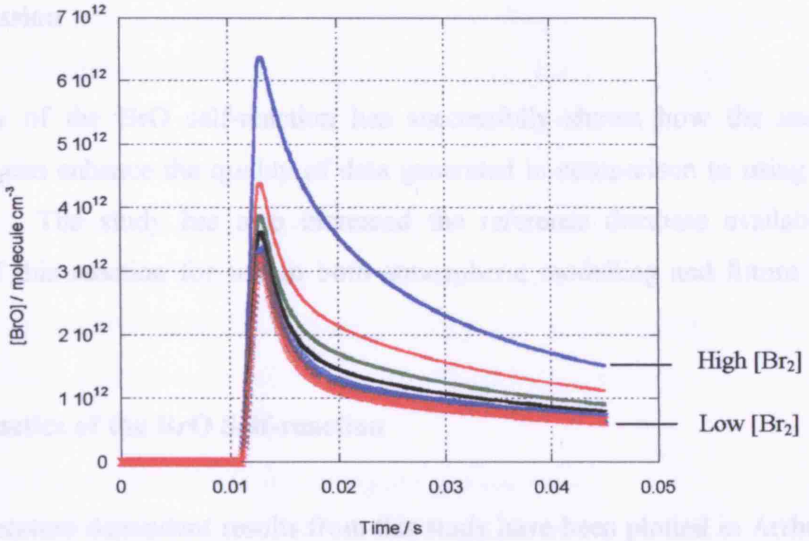

Figure 6. 26 BrO radical concentrations as a function of time generated using a numerical model. Traces were modelled using successively lower precursor Br_2 concentrations. Blue points = highest Br_2 concentration and red crosses = lowest Br_2 concentration.

Since the traces under these conditions are themselves a combination of data with varying radical concentrations no further useful kinetic analysis of them was viable. This (inadvertent) experiment does however serve to highlight the need to carry out kinetic experiments under carefully designed and controlled conditions.

6. 5 Discussion

This study of the BrO self-reaction has successfully shown how the use of laser photolysis can enhance the quality of data generated in comparison to using flashlamp photolysis. The study has also increased the reference database available for the kinetics of this reaction for use in both atmospheric modelling and future laboratory studies.

6. 5. 1 Kinetics of the BrO Self-reaction

The temperature dependent results from this study have been plotted in Arrhenius form and are compared to the Arrhenius parameterisations of the most recent previous studies in Figure 6. 27 below.

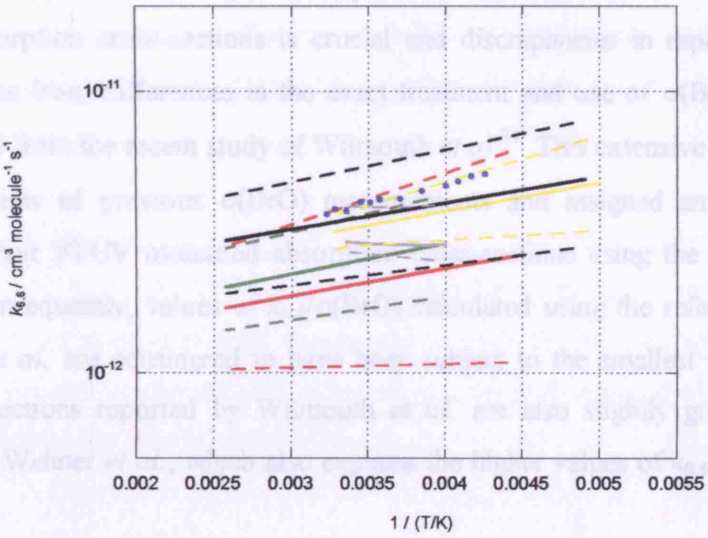

Figure 6. 27 Temperature dependent data determined in this study (blue points and error bars) plotted in Arrhenius form compared to the Arrhenius parameterisations determined by the previous studies of Sander and Watson (red), Turnipseed *et al.* (green), Gilles *et al.* (black), Harwood *et al.* (grey) and the current NASA recommendation (yellow), along with their associated regions of error (given by the dotted lines of the same colour).

The results form this study are in broad agreement with those of previous studies, showing a very similar overall trend, although results of this study lie towards the upper limit of the range defined by previous studies.

The lowest two data points (225 K and 228 K) have been omitted from the final data set presented from this study. This is appropriate since at low temperatures, experimental Br_2 concentrations were maintained low, in order to prevent liquid Br_2 condensing from the gas phase, a process governed by the vapour pressure of Br_2. At low Br_2 concentrations there is a possibility that competition for BrO radicals from the O + BrO reaction, as shown in Section 6. 4, may result in an observed rate enhancement. Furthermore, the remaining data points, at temperatures above 228 K, define a clearer Arrhenius trend inconsistent with the two lowest temperature points.

6. 5. 2 Use of Literature BrO Absorption Cross-sections

Since the determination of rate coefficients for second order reactions requires the knowledge of absolute concentrations of reactants or products, values determined using UV spectroscopy are strictly dependent upon σ(BrO) . As a result, accurate knowledge of BrO absorption cross-sections is crucial and discrepancies in reported results are likely to arise from differences in the exact treatment and use of σ(BrO). This study used σ(BrO) from the recent study of Wilmouth *et al.*[34] This extensive study included a detailed review of previous σ(BrO) measurements and assigned an absolute cross-section to their FTUV measured absorption cross-sections using the outcome of this review. Consequently, values of $k_{6.6}/\sigma$(BrO) calculated using the reference σ(BrO) of Wilmouth *et al.* are considered to have been subject to the smallest systematic error. The cross-sections reported by Wilmouth *et al.* are also slightly greater than those reported by Wahner *et al.*, which also explains the higher values of $k_{6.6}$ recorded in this work.

6. 5. 3 Advantages of Broad Band Spectroscopy

The observation of an underlying transient residual absorber in the spectra generated in this study would not have occurred if broad band spectroscopy had not been employed. The use of differential broad band spectroscopy negates the effect that any underlying absorbers have on the total experimental absorbance recorded. Furthermore, differential spectra generated using this analysis technique can be unequivocally assigned to a single absorber. Indeed, it is possible that the 'unknown' underlying absorber present in

the system used in this study was present in the chemical systems of some, if not all of the previous studies of the BrO self-reaction. If this were the case then the determination of rate coefficients in these studies could potentially have been compromised since previous determinations all relied on knowledge of the cross-sections of all absorbing species present. It is perhaps fortunate that the most likely candidate for the transient absorber observed in this work is Br_2O, the effect of which appears not to impact upon BrO kinetics, but simply to enhance the rate of bromine atom recombination.

6. 5. 4 Summary

Discrepancies between the results of this study and all previous studies using UV spectroscopy are likely to have arisen principally due to differences in the BrO absorption cross-sections used and the subsequent treatment of this cross-section. The scatter in the parameterisations of previous studies, especially those studies that used the same literature cross-sections, highlights the need for care when using cross-sections from the literature.

Overall, taking the differences in cross-sections into account, the kinetics of the BrO self-reaction are well established. Data reported here therefore verify the successful installation of the laser photolysis system and provide further data to characterise the temperature dependent overall rate coefficient, $k_{6.6}$, for both atmospheric models and for subsequent laboratory studies of the BrO radical.

6. 6 References

1. WMO, *Scientific Assessment of Ozone Depletion: 2002*, World Meteorological Association, Geneva, 1999, **2002**.
2. L.A. Barrie, J.W. Bottenheim, and W.R. Hart, *J. Geophys. Res.*, **1994**, 12, 25, 313.
3. M. Hausmann and U. Platt, **1994**, 12, 25, 399.
4. A. Richter, F. Wittrock, M. Eisinger, and J. Burrows, *Geophys. Res. Letts.*, **1998**, 25, 14, 2683.
5. A. Saiz-Lopez, J. Plane, and J. Shilito, *Geophys. Res. Letts.*, **2004**, 31, 3111.
6. V. Mateev, M. Peleg, D. Rosen, D. Tov-Alper, K. Hebestreit, J. Stutz, U. Platt, D. Blake, and M. Luria, *J. Geophys. Res. Atmos.*, **2001**, 106, 10375.
7. S. Fan and D. Jacob, *Nature*, **1992**, 359, 522.
8. M. Mozurkewich, *J. Geophys. Res. Atmos.*, **1995**, 100, 14199.
9. R. Sander and P. Crutzen, *J. Geophys. Res. Atmos.*, **1996**, 101, 9121.
10. R. Vogt, P. Crutzen, and R. Sander, *Nature*, **1996**, 383, 327.
11. M.A.A. Clyne and J.A. Coxon, *Proc. R. Soc. London, Ser. A*, **1968**, 303, 207.
12. M.A.A. Clyne and H.W. Cruse, *Trans. Faraday Soc.*, **1970**, 66, 2214.
13. M.A.A. Clyne and R.T. Watson, *J. Chem. Soc. Faraday Trans. 1*, **1975**, 71, 336.
14. J. Brown and G. Burns, *Can. J. Chem.*, **1970**, 48, 3487.
15. N. Basco and S.K. Dogra, *Proc. R. Soc. London, Ser. A*, **1971**, 323, 417.
16. S. Jaffe and W.K. Mainquist, *J. Phys. Chem.*, **1980**, 84, 3277.
17. S.P. Sander and R.T. Watson, *J. Phys. Chem.*, **1981**, 85, 4000.
18. A.A. Turnipseed and J.W. Birks, *J. Phys. Chem.*, **1990**, 94, 7477.
19. I.T. Lancar, G. Laverdet, G. LeBras, and G. Poulet, *Int. J. Chem. Kinet.*, **1991**, 23, 37.
20. I. Bridier, B. Veyret, and R. Lesclaux, *Chem. Phys. Lett.*, **1993**, 201, 563.
21. R.L. Mauldin, A. Wahner, and A.R. Ravishankara, *J. Phys. Chem.*, **1993**, 97, 7585.
22. A. Wahner, A.R. Ravishankara, S.P. Sander, and R.R. Friedl, *Chem. Phys. Lett.*, **1988**, 152, 107.
23. D.M. Rowley, M.H. Harwood, R.A. Freshwater, and R.L. Jones, *J. Phys. Chem.*, **1996**, 100, 3020.
24. B. Laszlo, R.E. Huie, and M.J. Kurylo, *J. Geophys. Res.*, **1997**, 102, 1523.

25. M. Gilles, A. Turnipseed, J. Burkholder, A. Ravishankara, and S. Solomon, *J. Phys. Chem.*, **1997**, 101, 5526.
26. M.H. Harwood, D.M. Rowley, R.A. Cox, and R.L. Jones, *J. Phys. Chem. A*, **1998**, 102, 1790.
27. R.A. Cox, D.W. Sheppard, and M.P. Stevens, *J. Photochem.*, **1982**, 19, 189.
28. Y. Bedjanian, G. LeBras, and G. Poulet, *J. Phys. Chem.*, **1998**, 102, 10501.
29. D. Papayannis, A. Kosmas, and V. Melissas, *Chem. Phys.*, **1999**, 243, 249.
30. Z. Li and G. Jeong, *Chem. Phys. Letts.*, **2001**, 340, 194.
31. S.P. Sander, R.R. Friedl, D.M. Golden, M.J. Kurylo, R.E. Huie, V.L. Orkin, G.K. Moortgat, A.R. Ravishankara, C.E. Kolb, and M.J. Molina, *Chemical Kinetics and Photochemical Data for Use in Atmospheric Studies*, JPL Publication 02-25, Jet Propulsion Laboratory, Pasadena, CA, **2002**.
32. H. Okabe, *Photochemistry of Small Molecules*, **1978**, John Wiley, New York.
33. J. Nicovich and P. Wine, *Int. J. Chem. Kinet.*, **1990**, 22, 379.
34. D. Wilmouth, H. TF, D. NM, and A. JG, *J. Phys. Chem. A.*, **1999**, 103, 45, 8935.
35. A.R. Curtis and W.P. Sweetenham, *FACSIMILE*. 1987, AERE Harwell Publication: Oxford.
36. Taken from: *Data Sheet PBr7*, http://www.iupac-kinetic.ch.cam.ac.uk,
37. L.F. Pacios and P.C. Gomez, *J. Phys. Chem. A*, **1997**, 101, 1767.
38. J.B. Burkholder, *Int. J. Chem. Kinet.*, **1998**, 30, 8, 571.
39. O.V. Rattigan, D.J. Lary, R.L. Jones, and R.A. Cox, *J. Geophys. Res.*, **1996**, 101, D17, 23021.
40. J.J. Orlando and J.B. Burkholder, *J. Phys. Chem.*, **1995**, 99, 1143.
41. Y. Ninoniya, S. Hashimoto, M. Kawasaki, and T.J. Wallington, *Int. J. Chem. Kinet.*, **2000**, 32, 3, 125.
42. O.C. Fleischmann, J. Meyer-Arnek, and J.P. Burrows, *J. Phys. Chem. A*, **2005**, 109, 5093.

Chapter 7
Conclusions and Final Remarks

The results reported in this thesis represent extensive studies of three reactions, namely the ClO + ClO and BrO + BrO self-reactions, as well as the ClO + HO_2 cross radical reaction. In the case of ClO + HO_2, this is the first study of this reaction to use broad band absorption spectroscopy. Some instrumental development, in the form of installing and testing a new laser photolysis source, has also been successfully completed.

The use of broad band absorption spectroscopy in this work confers clear advantages in the unequivocal monitoring of the halogen oxide radicals generated, by necessity, in the presence of other UV absorbing species. The strong vibronic structure evident in the spectra of the XO (X = Cl, Br) radicals has been exploited to extract a 'fingerprint' of that radical concentration, *via* so called 'differential' spectroscopy. This signal provides an indication of the time dependent concentration of the radical alone, irrespective of any changes in underlying absorbance, some of which may, in this and in other work, have resulted from unidentified absorbing species. The generation of a pure radical concentration temporal trace also allows such a trace to be compared directly with the simulated trace produced, either by classical rate equation solution or by numerical integration, for determining kinetic parameters. Not only is this very convenient, but such traces also show the maximum possible sensitivity to the kinetic parameters inherent in the temporal profile. As an example of this, consider the ClO dimerisation results reported in Chapter 4. The 'pure' ClO concentration *versus* time traces are readily fit to a classical solution of the dimerisation kinetics, giving excellent constraint on the forward and reverse rate coefficients. In principle, a similar analysis could be (and indeed has) carried out with a single wavelength absorbance *versus* time measurement. In such a measurement however, the decrease in the absorbance of ClO is compensated by an increase in the time-resolved absorbance of the Cl_2O_2 dimer, reducing the sensitivity. Furthermore, the changing contribution to absorbance from any ClO precursor species also needs to be taken account of in single wavelength monitoring, along with possible absorbances from secondary chemical reactions. *In extremis*, at a single wavelength where $\sigma(ClO) = 0.5 \times \sigma(Cl_2O_2)$, in the absence of any

other significantly changing absorbances, the decay of ClO absorbance would be perfectly compensated for by the build up of Cl_2O_2 product absorbance, resulting in a flat (isobestic) temporal trace containing no kinetic information. Of course such a wavelength would never be chosen for a kinetic study of ClO decay, and indeed such a wavelength does exist in the continuum part of the ClO absorption spectrum at *ca.* 251.5 nm. However, this does illustrate the inherent loss of kinetic information in single wavelength *versus* broadband monitoring. Another advantage of broad band monitoring may be evident when considering the wavelength stability of the 0.25 m spectrometer used in this work, which is a typical sized dispersing instrument for laboratory kinetics studies. As discussed in Chapter 4, over the course of a programme of experiments, small drifts in the wavelength calibration of the spectrograph were noted (always < 0.5 nm) which were readily accounted for in analysis by allowing small *x*-axis drifts in the high pass filtered reference spectra. These drifts might be unique to the apparatus used in this work and presumably arose from gradual change in the laboratory environment (*e.g.* temperature, vibrations). If such drifts affected single wavelength results analogously, however, where typically the top of a well resolved and therefore sharp vibronic absorption feature is chosen for monitoring, they would be very difficult to account for, and could if uncorrected affect results profoundly.

Whilst the kinetic studies reported in this thesis did benefit from broad wavelength monitoring, they also, since decays were not first order, relied upon the ability to measure absolute radical concentrations as a function of time. This therefore necessitated accurate determinations of radical absorption cross-sections, at the appropriate instrumental resolution and at the experimental temperature. For the measurement of ClO concentrations, in the ClO self-reaction and in the ClO + HO_2 reaction, measurement of the ClO absorption cross-section utilised a method developed previously in this laboratory. This method exploited a further advantage of the broad band spectral monitoring as the simultaneous recording of absorbance in the spectral continuum of ClO and in the vibronic structure was carried out. The continuum absorbances were then analysed to determine the ClO differential cross-section, as described fully in Section 4. 2. 1. 2. A subtle advantage of this was that the relative ClO temporal trace, obtained from fitting the (uncalibrated) reference spectrum of ClO to successive spectra, could be used to constrain the absorbance contribution of ClO to the continuum absorption and therefore better back extrapolate the continuum traces to

$t = 0$. This development of the method ensured that reliable analysis of continua traces was possible, and therefore the calibration of ClO absorption cross-sections in this way was optimised. A ClO absorption cross-section was therefore determined for each experiment, under the exact conditions adopted.

As an alternative spectral analysis procedure, carefully measured and high resolution BrO absorption cross-sections were available from the literature and carefully incorporated into smoothing routines to match the experimental resolution of this work. Again the broad band spectroscopy gave advantage in this, as the residuals between fitted reference and experimental spectra could always be compared. Furthermore, the successful subtraction of the contribution of BrO to the composite absorption spectra allowed examination of the deconvoluted spectrum to ensure that no BrO contribution remained, allowing investigation of a underlying absorption feature, as discussed in Chapter 6.

The kinetics of the ClO self-reaction were studied using two separate chemical systems, the first of which was used at high temperatures to investigate the thermochemistry of the dimerisation. This work showed that the exothermicity of the ClO association was somewhat greater than that reported in previous studies, notably those of Cox and Hayman.[1] On careful examination of the sensitivity of the ClO temporal traces used however, it was confirmed that in the work reported here, the Cl_2O_2 back reaction (*i.e.* thermal decomposition of Cl_2O_2) did not affect the ClO decay traces at low temperatures, which therefore imposed a minimum temperature for this study of 280 K. As discussed in Chapter 4, at temperatures lower than this, the ClO decay traces essentially revert to pure second order and so it is rather surprising, and impressive that Cox and Hayman were able to obtain dimerisation equilibrium constants down to temperatures as low as 233 K. Very careful analysis of the Cox and Hayman data also show a significant non linearity in the van't Hoff plot used to extract thermochemical parameters. This, as discussed more fully above, indicates that the Cox and Hayman work may have underestimated the exothermicity of ClO dimerisation. This assertion certainly brings the flash photolysis/molecular modulation results (using optical detection of ClO) into better agreement, and the very recent work of Plenge *et al.* is consequently very difficult to reconcile with this. One possibility in this respect arises from the very subtle deviation from linearity observed in the van't Hoff plot constructed

in this work. Successive exclusion of low temperature data from the fit showed that the dimerisation enthalpy determined did change (*i.e.* the van't Hoff plot was consistently curved) as discussed in Section 4. 2. 1. 6. One possible, speculative, interpretation of this is that the ClO dimerisation might proceed by one of two (or indeed more) pathways, with likely different thermochemistry. Thus, the observed ln K_p as a function of reciprocal temperature could contain contributions from two different van't Hoff plots with different gradients resulting in the observed behaviour. The existence of a minor channel to ClO dimerisation not producing ClOOCl has recently been suggested in theoretical work,[2] and the implications for polar O_3 loss could, if this multichannel reaction did occur, be profound, depending upon the atmospheric fate of a non-peroxide ClO dimer. Another implication of this could be that the assumption, in the analysis of the data reported by Plenge *et al.* that upon ionisation of Cl_2O_2 at low temperatures, ClO^+ detected has only originated from the ClOOCl isomer (despite the gas mixture containing only (83 ± 2)% ClOOCl) is false, and that the consequent analysis is flawed.

The low temperature study of the ClO self-reaction reported in this work was principally used so that the ClO association was well characterised in the subsequent analysis of experiments on the ClO + HO_2 reaction. This work showed excellent agreement with the very extensive study of the temperature and pressure dependence of the ClO association recently reported from our laboratory, and in turn, this verified the slight refinement in the analysis procedure used to determine σ(ClO), discussed above. It seems clear that this rate coefficient is somewhat more rapid, particularly at low temperatures, than earlier studies showed. Thus, the rate of O_3 loss through the ClO dimer cycle could be enhanced in sunlight, although this might be offset somewhat by the increase in the partitioning of the ClO to ClO dimer (of whatever nature) in polar O_3 loss. In similar fashion, the ClO + HO_2 kinetic study reported here, the most extensive (and problematic) study in this thesis, reported rate coefficients which were consistently higher than the, very scattered, dataset of previous work. In the atmosphere, at mid-latitudes, this would imply a shift towards the partitioning of ClO as HOCl, which in some cases (*i.e.* rapid photolysis of HOCl) could enhance chlorine mediated stratospheric O_3 loss. The ClO + HO_2 study also demonstrates the need for very careful experimental design and subsequent analysis. In principle, the method, allowing methanol to compete for excess chlorine atoms following Cl_2O photolysis, is very

simple and should quantify both free radicals provided usual flash photolysis conditions (rapid radical generation) are adhered to. In practice, as discussed in Chapter 5, this method became somewhat more complicated. Extensive studies did demonstrate that a ClO temporal trace alone did have sensitivity to the ClO + HO_2 cross-reaction, and temperature dependent data were obtained. The method also highlighted that allowing several kinetic parameters to vary (*e.g.* as in the work of Nickolaisen *et al.*[3]) will always allow temporal traces to be fit by a model, but that kinetic parameters obtained from this might be subject to cross-sensitivity. Perhaps most interestingly, the disparity between the initial HO_2 concentrations required by the model to fit the ClO temporal traces and the HO_2 concentrations inferred from back-to-back experiments might imply that some form of pre-equilibrium exists between ClO and HO_2 radicals. If this were the case, the radical association complex might be collisionally stabilised and a new HO_3Cl species might be produced in the atmosphere. Again, the fate of such a species, if formed, would depend upon the photochemical properties of the molecule, but again could significantly affect the atmospheric role of the ClO + HO_2 reaction. Detailed pressure dependent measurements of the ClO + HO_2 reaction, not possible in this work, are surely required to elucidate this.

The last chemical system studied, the BrO + BrO reaction, was partially done so as a benchmark system following the installation of the new excimer laser photolysis source. The BrO + BrO reaction is well characterised at ambient temperature and results from this work, using recently available absorption cross-sections, agree very well. The temperature dependence of BrO + BrO was confirmed to be negative, in agreement with previous studies. No dimerisation of BrO was explicitly studied in this work however, as the reaction was studied under conditions of excess bromine atoms. Previous work appears to show that the BrO dimer absorption spectrum is red shifted from the ClO counterpart, and along with the other possible product Br_2, rapid solar photolysis is therefore likely to liberate bromine atoms, allowing catalytic O_3 loss. Under such conditions the association of BrO radicals becomes rate limiting, and this study provides new data on this process as a function of temperature.

In conclusion, the results presented in this thesis provide significant new data on halogen oxide free radical reactions, as well as evidence for a number of unresolved issues which point the way to future studies. The results also illustrate the advantages

of time-resolved broad band UV spectroscopy in the investigation of the kinetics of these reactions, as provided for by the unique CCD detection system. In many ways, this system is an electronic reversion, with improvements, to the initial flash photolysis technique first developed by Porter and Wright. The ability to record an entire absorption spectrum at every time point is the most obvious and useful of these improvements and resulting spectra permit unprecedented accuracy in monitoring XO radicals and other gas phase species. The next step could be the exploitation of further technical advances, *e.g.* in IR spectroscopy to allow the simultaneous monitoring of other species and the full resolution of these complex and important reactions.

7. 1 References

1. R. Cox and G. Hayman, *Nature*, 1988, 322, 28, 796 .
2. R.S. Zhu and M.C. Lin, 2003, 118, 9, 4094.
3. S. Nickolaisen, R. Friedl, and S. Sander, *J. Phys. Chem.*, 1994, 98, 155.

Appendix 1

Effect of Instrument Function upon Absorption Cross-Section

According to Heisenberg's uncertainty principle the observed radiation associated with any electronic transition has a natural line width. If this radiation is observed using a dispersive detection system (as for the experiments in this dissertation) the magnitude and shape of this line width will be additionally directly influenced by the instrument function of the detection system. Consequently, even monochromatic light passed through a diffraction spectrograph will be spread over a range of wavelengths governed by this instrument function. The width of this spread is in turn dependent upon the spectral resolution. For the spectrograph/CCD detection system employed in this work, the entrance slit width and dispersion of the spectrograph determines the spectral resolution.

If the spectral resolution of a detection system is decreased this will be accompanied by an increase in the apparent line width of any observed spectral features. This effect becomes most significant for small molecules which often show distinct spectral features (vibronic structure) where a progression of individually resolved peaks are observed corresponding to transitions to discrete vibrational states below the dissociation threshold. The magnitude of such structural features is readily affected by the instrument function, since the natural line widths are somewhat smaller than the magnitude of the spectral resolution. Consequently, the magnitude and shape of experimentally determined absorption spectra are directly dependent upon the resolution of the apparatus used. In addition, the cross-sections determined from such spectra, or used to quantify absorbing species contributing to such spectra must also be dependent upon the resolution of the detection system. This phenomenon is illustrated in Figure A1. 1 which shows BrO absorption cross-sections recorded at spectral resolutions of 0.4 and 1.1 nm.

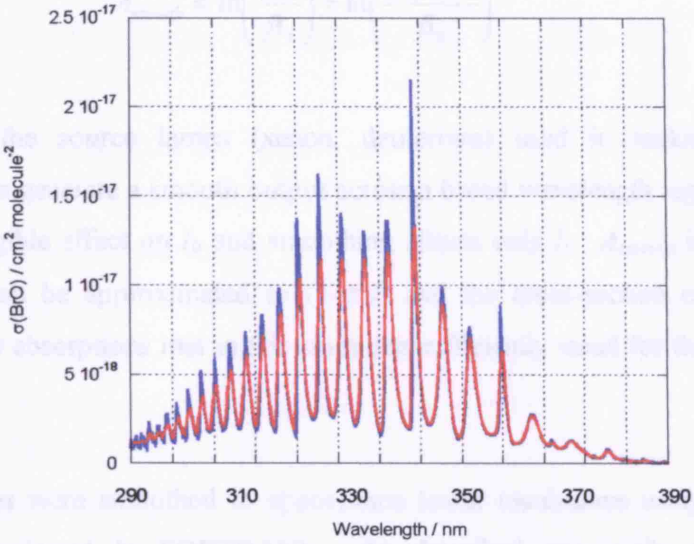

Figure A1. 1 BrO cross-sections illustrating the effect of spectral resolution on structured absorption spectra. The blue spectrum was recorded at 0.4 nm (FWHM) by Wilmouth *et al.* and the red taken on the experimental system used in this study with associated resolution of 1.1 nm (FWHM).

Since differential routines were used to determine radical concentrations by fitting the structural magnitude of the reference cross-sections to that of the recorded absorption spectra, it was vital that the respective resolutions were matched to ensure accurate determination of radical concentrations and subsequent kinetic parameters.

Reference absorption cross-section taken from the literature are often recorded at higher resolutions than those achieved in this work. The literature cross-sections therefore required smoothing before their use to quantify absorbing species present in the experimental spectra.

Theoretically, smoothing appropriate to the specific instrument function (f) must be applied to both the preflash intensity, I_0 and the postflash intensity, I_t used to generate the higher resolution spectrum prior to calculation of absorption and hence absorption cross-section at the lower resolution. In practice, however, it is often possible to smooth the higher resolution cross-section directly:

(EA1. 1) $$A_{smooth} = \ln\left(\frac{f I_0}{f I_t}\right) = \ln\left(\frac{f I_0 e^{-\sigma c l}}{f I_0}\right)$$

In general, the source lamps (xenon, deuterium) used in making cross-section measurements generate a smooth output across a broad wavelength regime. As a result f has a negligible effect on I_0 and smoothing affects only I_t. A_{smooth} is generally small hence $e^{-\sigma c l}$ can be approximated to $(1-\sigma c l)$ and the cross-section can be smoothed directly. The absorptions met in this study are sufficiently small for this approximation to apply.

Cross-sections were smoothed to appropriate lower resolutions using sliding average routines (developed in FORTRAN). As described previously (Chapter 6) the instrument function of the apparatus employed in this study is well described by a Gaussian function and an optimised function of this type, the width of which reflected the spectral resolution required, provided the basis for the smoothing kernel used in the averaging routine. The quality of the resolution match between the smoothed cross-section and the experimentally recorded spectrum could be investigated by subtraction of the fitted reference spectrum (fitted by optimising the species concentration according to the Beer Lambert law) from the experimentally resolved spectrum. The absence of systematic features in the resulting residual, across the whole wavelength region, confirmed that the resolutions were proportionate.

Appendix 2

Temperature Profile of the Reaction Cell

The internal temperature of the reaction cell was measured using a Pt-100 resistance thermometer. The thermometer itself had previously been calibrated against the literature temperatures associated with the triple point of water and a carbon dioxide/acetone bath. Measurements were taken at known points along the length of the reaction cell by removing the end piece from the effluent end of the reaction cell and inserting the thermometer into a bath gas flow of 1000 sccm (*i.e.* that of a typical experiment). The thermometer had been mounted into a plastic mesh disc to prevent the tip of the thermometer touching the internal walls of the reaction cell, which were in direct contact with the circulating cooling fluid. The thermometer was inserted, in random order, to 10 known intervals along the reaction cell and at each point the thermometer was given time to reach thermal equilibrium with its surroundings before the temperature was recorded. This procedure was repeated for a number of coolant fluid temperature settings. The results of this analysis are shown in Figure A2. 1, below.

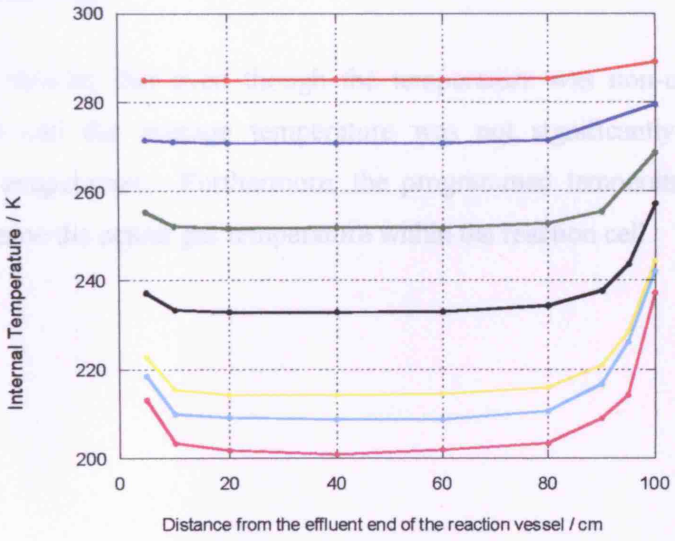

Figure A2. 1 Internal temperature profile of the reaction cell at different set coolant temperatures. 285 K (blue), 270 K (red), 250 K (green), 230 K (black), 210 K (yellow), 200 K (turquoise), 195 K (pink).

Figure A2. 1 shows that there is a non-uniform temperature profile along the reaction cell. The average temperature in the reaction cell was calculated by fitting a high order polynomial to each of the profiles and integrating the resulting function along the length of the cell. Figure A2. 2 shows a plot of the actual (averaged) temperature of the reaction cell against the programmed coolant temperature.

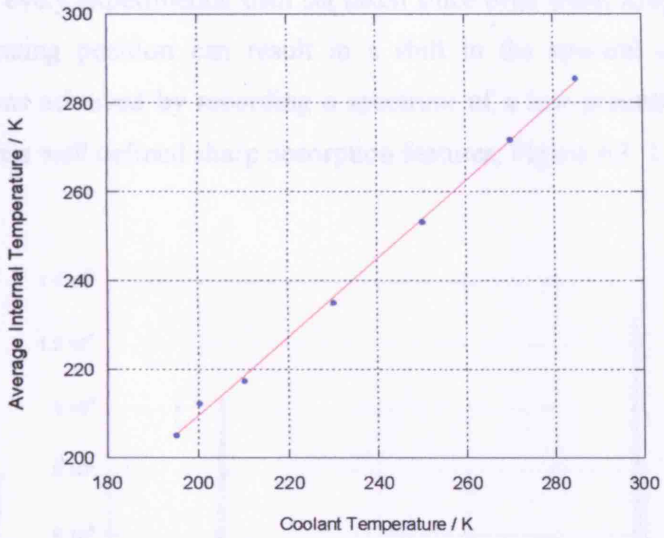

Figure A2. 2 Mean temperature of gas within the reaction cell *versus* the programmed temperature at the coolant bath.

This analysis showed that even though the temperature was non-uniform along the length of the cell the average temperature was not significantly different to the programmed temperature. Furthermore, the programmed temperature could also be used to determine the actual gas temperature within the reaction cell.

Appendix 3

Wavelength Calibration

Precise wavelength calibration was crucial to ensure that the correct absorption cross-sections were fitted to the experimentally observed absorbances. Such a calibration was necessary for every experimental data set taken since even small irreproducibility in the diffraction grating position can result in a shift in the spectral coverage recorded. Calibration was achieved by recording a spectrum of a low-pressure mercury pen ray lamp, which has well defined sharp absorption features, Figure A3. 1.

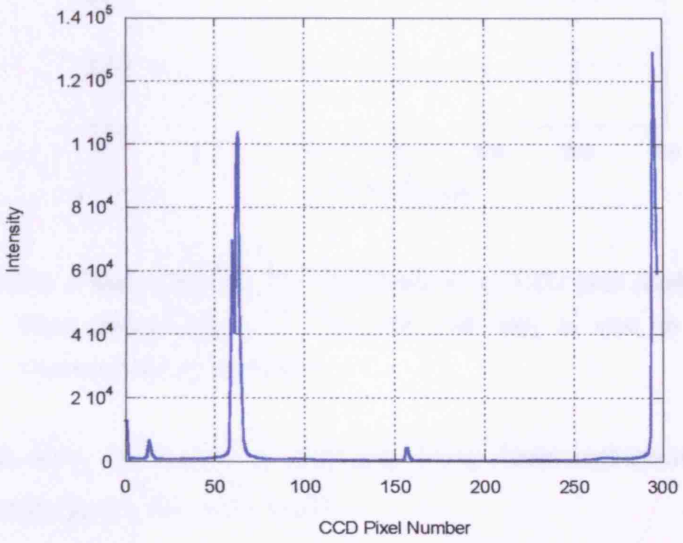

Figure A3. 1 Example of a typical mercury spectrum recorded experimentally.

By recording the CDD pixel number at which the mercury peaks occur and through knowing the exact wavelength that these peaks occur (well defined in the literature) a calibration plot can be produced, Figure A2. 2 below.

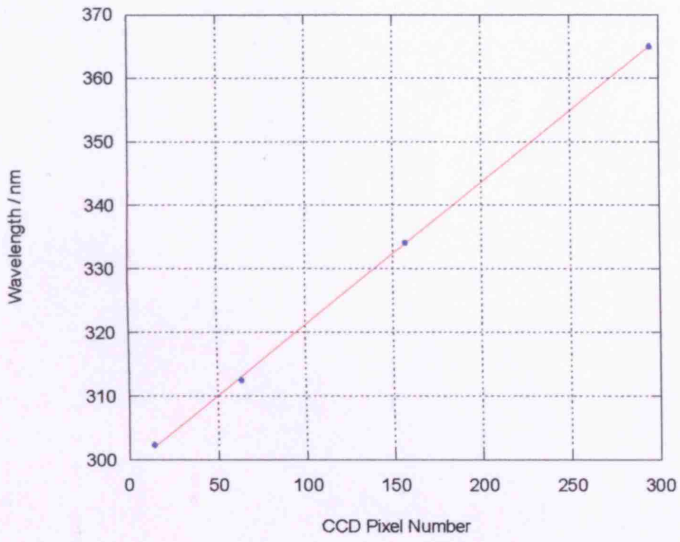

Figure A3. 2 Plot of known mercury peak wavelength *versus* CCD pixel number (blue points). The linear parameterisation of this plot (red line) is used to wavelength calibrate experimentally recorded spectra.

Such a calibration plot is readily analysed, using linear regression, to convert CCD column number (pixel) into wavelength.